Optical Hybrid Quantum Information processing

Hanna Le Jeannic

Hanna Le Jeannic. Optical Hybrid Quantum Information processing. Physics [physics]. Université Pierre et Marie Curie - Paris VI, 2016. English. NNT : 2016PA066596 . tel-01665496

HAL Id: tel-01665496
https://theses.hal.science/tel-01665496v1

THÈSE DE DOCTORAT
DE L'UNIVERSITÉ PIERRE ET MARIE CURIE

Spécialité : Physique

École doctorale : « Physique en Île-de-France »

réalisée

au Laboratoire Kastler Brossel

présentée par

Hanna Le Jeannic

pour obtenir le grade de :

DOCTEUR DE L'UNIVERSITÉ PIERRE ET MARIE CURIE

Sujet de la thèse :

Optical Hybrid Quantum Information Processing

soutenue le Mercredi 14 Décembre 2016

devant le jury composé de :

M^{me}	Sara DUCCI	Examinatrice
M.	Radim FILIP	Examinateur
M.	Eric LANTZ	Rapporteur
M.	Julien LAURAT	Directeur de thèse
M^{me}	Agnès MAITRE	Présidente du jury
M.	Christoph MARQUARDT	Rapporteur

Approche hybride du traitement quantique de l'information

Hanna Le Jeannic

Thursday 12th January, 2017

Remerciements

Comme la plupart des thèses, celle-ci n'est pas le fruit du travail d'une seule personne. Beaucoup de gens y ont contribuées de manière professionnelle, scientifique, ou plus personnelle. J'aimerais remercier ici toutes les personnes, merveilleuses et tellement importantes, que j'ai eu la chance de côtoyer pendant ces trois années de thèse.

Tout d'abord je tiens à remercier les examinateurs Sara Ducci et Radim Filip, les deux rapporteurs Christoph Marquardt et Éric Lantz ainsi que la présidente Agnès Maître d'avoir accepté de faire partie de mon jury de thèse, et ainsi d'avoir pu trouver du temps en cette période que je sais chargée. Je les remercie également pour les passionnantes questions, et remarques qu'ils ont pu me faire et qui ont contribué à améliorer ce travail.

En particulier je souhaiterais remercier Radim Filip, avec qui les discussions sur les possibilités offertes par nos expériences ont été nombreuses et fructueuses, et qui ont grandement contribuées au travail présenté dans cette thèse.

Ensuite, je tiens à remercier tout particulièrement Julien Laurat, mon directeur de thèse, pour son enthousiasme et sa rigueur. Je le remercie d'avoir une telle confiance en son équipe, et de nous laisser beaucoup de liberté et d'autonomie dans la vie de tous les jours.

Je souhaite ensuite remercier les gens qui ont travaillé avec moi sur l'expérience. Tout d'abord ceux qui m'ont accueillie: JianLi, Olivier et Kun. Olivier, je te remercie de m'avoir tout appris, merci d'être resté à l'écoute malgré ton départ vers d'autres horizons atomiques. Merci également pour tes réponses si rapides et efficaces à mes questions si stupides (et si nombreuses!!).

Je remercie également, Kun, pour m'avoir fait confiance pour garder son prénom français secret (que j'ai oublié!). "Xié xié"!

Un grand merci à Josselin aussi, en particulier pour son aide et ses conseils très précieux. Merci à Youn-Chang, pour son aide au jour le jour sur l'expérience.

Enfin je souhaiterais remercier mes deux ex-stagiaires Jérémy et Adrien. Même si le premier nous a fait des infidélités avec les atomes et les nanofibres, je tiens à lui souhaiter bonne chance dans sa thèse et dans sa vie professionnelle (ce dont je doute qu'il ait besoin). Je le remercie d'avoir été un super stagiaire, et de m'avoir fait me sentir moins vieille. Adrien, merci à toi d'avoir supporté une thésarde de troisième année survoltée. Merci pour ton sérieux, ta gentillesse ton humour, et ta musique bizarre qui m'a fait découvrir des choses que je ne soupçonnais pas. La manip est maintenant entre de bonnes mains :D.

Merci également à Yosuke, de passage pour seulement trois mois, pour son aide précieuse.

Je remercie également toute l'équipe du NIST et du JPL, et en particulier Varun Verma pour avoir fabriqué des dizaines de détecteurs pour notre expérience. Merci aussi à Francesco Marsili pour ses nombreuses réponses à mes nombreuses questions. Ce fut une collaboration riche en termes de science et de résultats.

Merci à Simon Berthou, Emmanuel Flurin et toute l'équipe de Benjamin Huard, à Laura Thévenard et Johan Biscaras pour m'avoir aidée à réparer lesdits détecteurs des dizaines de fois... Merci enfin au Service des Basses Températures d'avoir été si zen avec mon manque d'organisation.

Au sein de l'équipe « Quantum Networks », nous interagissons également beaucoup avec les autres collègues des autres manips, qui même s'ils travaillent un peu loin de nos OPOs, sont toujours là pour le soutien moral et le prêt de matériel.

Ainsi je tiens à remercier Lucile, Lambert, Adrien, Dominik, Christophe et Valentina pour les plus "anciens". Baptiste, Neil, Aveek, Pierre, Thomas, Laurent, Ming-Tao, et Sasha pour les "nouveaux". Merci à Lucile pour son accueil chaleureux et sa gentillesse quotidienne. Valentina, je te remercie pour ta gentillesse et ton support moral constant pendant ces trois années de thèse. Je suis tellement heureuse d'avoir été le témoin de ton retour au LKB. Dominik, merci pour ta gentillesse, les friday bars, les grandes conversations philosophiques, notamment sur la cuisson des tartes tatins, et pour ton miel! (délicieux!)

Baptiste, merci pour ton flegme naturel qui aide à dédramatiser les situations. Merci d'être à l'écoute, et d'une gentillesse et d'une générosité sans égal. Sasha, merci pour les pauses thés-gâteaux, je te souhaite des milliers de tartes aux framboises, et des milliers de chats!

Neil, muchas gracias amigo. Merci de pimenter autant la vie du labo que tes plats. Je te souhaite plein de bonheur con tu hija. Merci pour ton soutien moral en toutes circonstances, merci pour m'avoir nourri de tartes au citron durant toute ma rédaction. Je pense honnêtement que tu es une des plus belles personnes que j'ai pu rencontrer pendant ces 3 ans de thèse.

Pierre. Ah. Pierre. Merci pour tout. Je pense que je n'aurais jamais tenu pendant toutes les galères sans toi. Merci pour les prêts de matériel et les discussions sur mes galères de manips. Merci pour les pauses thés, les vidéos stupides, neko atsume, les pistaches et sucre safrané. Merci pour l'ambiance que tu instaures autour de toi. Merci d'être revenu de Kangourou-land. Merci. Merci. Merci. Le grand regret de ma thèse et que nous n'ayons pas eu le temps de faire la compilation "Quantum Optics".

Enfin mon collègue de salle mais non d'équipe: merci à Alexandre, pour partager mes gouts musicaux, et pour m'avoir nourri de clémentines pendant 3 ans.

Je remercie aussi les autres thésards que j'ai pu croiser pendant les pots, séminaires, et journées du labo: Davide, Chayma, Marion, Valentin, Théo, Tigrane, Dorian, Laura, Thomas, Hugo, Mickaël, Baptiste, ... merci pour votre présence lors des Fridays bars, et merci de m'avoir fait autant rire.

Un merci particulier à Mariane, ma consoeur-jumelle de galère et de thèse. Merci pour ton soutien 24h/24 et 7j/7. Je te dois tellement que des remerciements de thèse ne suffisent pas. Non seulement tu es une incroyable physicienne mais également une amie sur qui l'on peut compter au moindre souci ! Je pense que l'on ne se perdra pas de vue de sitôt.

Clément C., merci pour ton écoute ta gentillesse, ta bonne humeur, et pour avoir allégrement râlé et déprimé avec moi de concert pendant ces 3 ans au moindre souci :D. Je remercie Clément J. et Valérian, les deux inséparables, pour leur folie douce, et leurs douceurs sucrées salées. Merci à Jon le troisième comparse. Promis, je regarde "The Wire" bientôt.

Merci aux permanents du couloir 13-23, Samuel, Thibaut et mon parrain Tristan. Un merci particulier à Pierre-François pour son coaching quotidien et sa préoccupation de mes heures de travail. Je te dédie mes vacances! Un grand merci à Quentin, le maitre de l'azote liquide, pour son oreille attentive et sa gentillesse. Je le remercie moins pour ses blagues nulles (j'ai encore l'offre d'emploi chez CalTech avec moi)...

A Nicolas C., Delphine, pour l'organisation toujours surmotivée des meilleurs séminaires des doctorants du LKB. Delphine merci pour ta folie douce, ton humour, et ton envie de rendre le laboratoire toujours plus convivial. Je te souhaite beaucoup de bonheur dans la suite de ta vie professionnelle et personnelle. Je remercie Nicolas C. de sa gentillesse et de son écoute attentive des problèmes des thésards. Merci aussi de contribuer à l'ambiance du laboratoire!

Je remercie Nicolas Treps et Claude Fabre de m'avoir autorisée chaleureusement à squatter tous les pots de leur équipe.

Merci à tous les autres personnes que j'ai pu côtoyer, plus rapidement: Pauline, Maxime, Francesco, Pierre-Elie, Sanjib, Tony, Sandrine, Manu, Raphael, Thomas, Mathieu, Adrien D., Roman, Giulia, Cai Yin, Pu, Zhang, Young-Sik, Valentin.

Je remercie Laetitia, Michel, et Romain d'avoir supporté mes milliers de demandes pendant 3 ans avec patience et sourire. Je remercie également Monique, pour son efficacité et sa gentillesse. Merci à Nora d'avoir pris le relai de Monique et de s'être mobilisée pour certaines démarches qui prenaient du (trop de?) temps. Merci à Annick et Bintou, pour apporter du soleil et de grands sourires tous les matins.

Merci à l'atelier de mécanique pour leur travail, beaucoup trop rapide et efficace (et qui vont du coup plus vite que la manip!) !!

Merci à Loïc, Brigitte et Jean Pierre du service électronique. Merci Brigitte en particulier pour les conversations sans fin sur l'amélioration de l'état du monde, et pour son souci du bien être de chacun au sein du laboratoire.

Merci à Antoine, notre directeur, pour être, malgré son emploi du temps surchargé, si disponible et si facile d'approche. Merci pour son écoute et sa gentillesse.

Merci à Sylvain Gigan pour m'avoir orienté vers ce laboratoire.

Un grand merci à Nobuyuki Matsuda pour m'avoir fait plonger dans le monde de l'optique quantique. Merci à lui et Bill Munro pour m'encourager encore et toujours.

Enfin je remercie dans un ordre aléatoire: mes cherries, la relance, l'équipe de MadaNet, les piliers du Friday bar. Mais aussi tous mes amis, qu'ils fassent partie de la mafia PCéenne, Kastler-Brossienne, lycéenne, ou non. Je vais tenter d'en citer quelques-uns, mais il y en a que j'aurais forcément oublié : Amaury, Déborah, Edouard, Cloé, Mathieu, Roxanne, Romain, Beatriz, Rudy, Mélanie, Etienne, Quentin, Fanny, Bastien, Jean-Baptiste, Laura, Vincent, Camillo, Dorian, Marc, Charlène, Rémi, Simon, Amaury, Pierre, Rémi, Jean, Nicolas, Eloïse, Adrien, Marion, Annabelle, Eléonore, Alexis, Johan, mes parrains et mes fillot(e)s. Merci à Déborah pour les superbes dessins de chats qu'elle a fait pour ma présentation. Ma famille toute entière, Soizick, mon père, mon frère, ma maman, mes mamies.

Je dédie en particulier cette thèse à ma grand-mère Zohra, qui n'a pas pu en voir l'aboutissement, mais qui a toujours été un modèle de force et de volonté pour moi.

Merci à Sauron, Bilbo, Sherlock et Watson pour tout leur amour et leurs bêtises. Merci à Indiana pour son moelleux et ses ronrons. J'espère qu'il me remercie également de n'avoir pas tenté de le mettre dans une boîte, pour la science!

Maximilien, enfin, pour avoir supporté, écouté, et tenté de comprendre, toutes mes aventures. Pour être toujours aussi solide et immanquablement présent.

Contents

Introduction **x**

I Toolboxes for Quantum State Engineering and Characterization **1**

I Theoretical Tools **3**
- I.1 Field quantization . . . 4
  - I.1.1 Field description . . . 4
  - I.1.2 Quadrature operators . . . 4
- I.2 Density operator, matrices and criteria . . . 5
  - I.2.1 Density matrix representation . . . 5
  - I.2.2 Tools for state characterisation . . . 6
  - I.2.3 Tools for entanglement characterisation . . . 7
- I.3 Wigner representation . . . 9
  - I.3.1 Properties . . . 9
  - I.3.2 Continuous-variable tools . . . 10
- I.4 Some useful operators . . . 10
- I.5 Modeling experimental imperfections . . . 12
  - I.5.1 Losses or amplitude damping . . . 12
  - I.5.2 Phase noise . . . 13
- I.6 Zoology of quantum states . . . 14
  - I.6.1 Fock states . . . 14
  - I.6.2 Coherent state . . . 16
  - I.6.3 Squeezed vacuum state . . . 16
  - I.6.4 Cat state . . . 17
  - I.6.5 Squeezed cat state . . . 18
- I.7 Conclusion . . . 19

II Experimental tools **21**
- II.1 Optical parametric oscillators . . . 22
  - II.1.1 Spontaneous parametric down-conversion . . . 22
  - II.1.2 Principle of an optical parametric oscillator . . . 23
  - II.1.3 Phase matching . . . 24
  - II.1.4 Mode-filtering . . . 24
  - II.1.5 OPO specifications . . . 25

II.1.6 Phases 26
II.2 Homodyne detection 27
II.2.1 Tomography principle via homodyne detection 27
II.2.2 Temporal mode 29
II.3 Locking methods 31
II.3.1 Micro-controller based locking 32
II.3.2 Arduino 37
II.4 Conclusion 38

III Superconducting Nanowire Single Photon Detectors **41**
III.1 Context 42
III.1.1 The near-infrared range 42
III.1.2 History and different types of detectors 42
III.2 Characterizing a single-photon detector 43
III.3 SNSPD 43
III.3.1 Principle 43
III.3.2 Alignment: NIST's plug-and-play mounts 44
III.3.3 Cooling and apparatus 45
III.3.4 Measurement of the system detection efficiency 46
III.4 Detector optimization 48
III.4.1 Simulation 48
III.4.2 Fabrication 48
III.4.3 Results 49
III.5 Perspectives 50
III.5.1 A new superconducting material: MoSi 50
III.5.2 A new cryogen-free cryostat 50
III.6 Conclusion 51

II Quantum State Engineering **53**

IV Fock State Generation **55**
IV.1 Fast and high-purity heralded single photon 56
IV.1.1 Characterizing a single-photon source 56
IV.1.2 A single-photon source based on an OPO 57
IV.1.3 Experimental implementation 58
IV.1.4 Results 59
IV.1.5 Comparison with other photon sources 60
IV.2 Heralded two-photon Fock states 62
IV.3 Quantum state engineering with time-separated heraldings 63
IV.3.1 Temporal mode definition 63
IV.3.2 Experimental realization of Fock-state superpositions 65
IV.4 Conclusion 68

V Squeezing as a Tool for Quantum Engineering of Non-Gaussian States 69
- V.1 Transition between a thermal state and a squeezed state 70
  - V.1.1 Two-mode squeezed state and rotated basis 70
  - V.1.2 Experimental implementation 71
  - V.1.3 Modeling the transition 75
- V.2 Efficient generation of large squeezed Schrödinger cat states 77
  - V.2.1 Cat states in quantum optics and quantum information 77
  - V.2.2 Methods for their generation 78
  - V.2.3 Engineering modulo a gaussian operation - The core states . . . 79
  - V.2.4 The protocol 81
  - V.2.5 Experimental setup 82
  - V.2.6 Results 83
- V.3 Minimizing the decoherence by squeezing 86
  - V.3.1 From quantum to classical 86
  - V.3.2 Quantifying Decoherence 87
  - V.3.3 Experimental verification 92
  - V.3.4 A robust method for generating cat states 93
- V.4 Conclusion 95

III Hybrid Entanglement 97

VI Hybrid Entanglement of Light 99
- VI.1 Hybrid entanglement of light 100
  - VI.1.1 Schrödinger kitten states 101
  - VI.1.2 Entanglement generation 103
  - VI.1.3 Characterization 105
- VI.2 Increasing the dimensionality 107
  - VI.2.1 Hybrid qutrit entanglement: principle 107
  - VI.2.2 Results 109
- VI.3 Characterization of the hybrid entanglement via steering 111
  - VI.3.1 Steering inequality using homodyne detection 111
  - VI.3.2 Towards Bell-type violation 114
- VI.4 Remote state preparation 116
  - VI.4.1 Principle 116
  - VI.4.2 Results 119
- VI.5 Encoding conversion by hybrid teleportation 120
  - VI.5.1 Finding an optimal Bell measurement 122
  - VI.5.2 Implementation and expected results 123
  - VI.5.3 An analog-to-digital converter? 125
- VI.6 Conclusion 126

VII Micro-Macro entanglement of light 127
- VII.1 Additional local photon subtraction 128
  - VII.1.1 Even kitten state: an approximation 128
  - VII.1.2 Experimental setup 129

VII.1.3 Results . . . 130
VII.2 Squeezing-induced micro-macro entanglement of light . . . 132
VII.2.1 Experimental generation . . . 132
VII.2.2 Results . . . 133
VII.3 Macroscopicity witnesses . . . 136
VII.3.1 Pointer in phase space . . . 136
VII.3.2 Distance in phase space . . . 139
VII.3.3 Distinguishability in phase space . . . 141
VII.3.4 Amplitude and frequency of the Wigner fringes and purity decay 143
VII.3.5 Fisher information based criterion . . . 144
VII.3.6 Resume . . . 146
VII.4 Conclusion . . . 147

A Useful mathematical formulas **153**
A.1 Hermite polynomials . . . 153
A.2 Laguerre polynomials . . . 153
A.3 Gauss integral . . . 153

B ADUC7020 code for Maximum searching algorithm **155**

C Arduino code for Maximum searching algorithm **159**

D Hybrid entangled qubit state **161**

E Hybrid entangled qutrit state **163**

F Hybrid entangled qubit state with additional photon subtraction **165**

Bibliography **167**

Introduction

Light as a wave and a particle

Quantum light can only be fully described by taking into account its wave-particle duality. Einstein described this particular phenomenon as: *"We have two contradictory pictures of reality; separately neither of them fully explains the phenomena of light, but together they do"* [1]. This duality led to two historical ways of encoding information on light, the discrete-variable (DV) approach [2] and the continuous-variable (CV) approach [3], each of them focusing more on one side of the light's nature. In order to outperform classical computer (field of *quantum computation*) or to achieve spy-proof protocols (field of *quantum communication*), quantum optics groups have traditionally focused on one or the other of the two aforementioned approaches [4, 5].

The discrete-variable approach, analogous to the digital encoding in classical information *"0-1"*, encodes information on discrete degrees of freedom, such as the presence or absence of a single photon, orthogonal polarizations, spatial modes... The spanned Hilbert space has finite dimension. The resulting quantum state is called a quantum bit, shortened as *qubit*, and represented in the form of a superposition of two orthogonal states:

$$c_0|0\rangle + c_1|1\rangle. \tag{.0.1}$$

Discrete variables systems are usually easier to process, and large fidelities with targeted results are usually obtained. However, they mostly rely on probabilistic generation schemes and operations [6].

As an alternative to the discrete-variable encoding, the continuous-variable approach plays with the wave-nature of light. In this framework, the information is encoded onto the quadrature of a light field such as the phase and the amplitude. The spanned Hilbert space is therefore of infinite dimension. This approach can be seen as the quantum version of the analog encoding. Sometimes denoted as *qu-mode*, the paradigmatic quantum state can be represented as the superposition of two phase-opposite classical waves (called coherent states) of amplitude α:

$$c_\alpha|\alpha e^{i\varphi}\rangle + c_{-\alpha}|\alpha e^{i(\varphi+\pi)}\rangle. \tag{.0.2}$$

Continuous-variable systems allow deterministic operations, such as teleportation, or gates [7], and feature on-demand entanglement sources and efficient measurements such as homodyne detections (where efficiencies are higher than 99%). However they suffer from their loss sensitivity, and usually lead to smaller fidelities to targeted states and operations [6].

	Discrete variables	Continuous variables
Encoding	Particle state	Quadratures of light fields
Relation to classical computing	Digital	Analog
Hilbert space dimension	Finite	Infinite
Detector	Single photon detector	Homodyne detector
Universal Q-Computing via	CNOT gate	Cubic phase gate
Achieved fidelities	High	Finite
Generation/Operation type	Probabilistic	Possibly Deterministic

Table .1: Resume of the two traditional ways to encode information and their properties.

The hybrid approach of quantum information processing

The wave-particle duality of light has therefore led to two traditionally separated ways of generating quantum states and implementing protocols. However, recent works based on a hybrid approach showed new advantages by combining their methods and technologies [8, 9]. Implemented in a wide range of physical systems, going from optical states to superconducting and cavity QED systems, they aim at overcoming the intrinsic limitation of each field [10].

Bridging both approaches firstly enable the engineering of more complex quantum states, such as non-Gaussian states. Such states are main resources for a variety of quantum protocols and cannot be produced by the means of simple linear tools. An example in quantum optics can be the subtraction of a single-photon (DV operation) on a CV state, which leads to heralded non-Gaussian states [11, 12]. As an another example, in the fields of cavity- and circuit-QED, coupling a CV oscillator to a DV level, such as an atom, enables the deterministic generation of non-gaussian states [13, 14].

In order to achieve universal computing, operations such as CNOT gate for DV systems, or cubic phase gate for CV systems are required. The hybrid approach of quantum information processing may enable to experimentally implement them more efficiently. With discrete variables, schemes have therefore been proposed in order to implement CNOT gate in a nearly-deterministic manner while minimizing the necessary resources [15]. Other schemes proposed to implement a cubic phase gate by doing DV measurements and conditional gaussian operations on CVs [16–18].

New protocols, such as entanglement witnesses for single-photon entanglement [19] also have been based on such hybrid technique. The CV toolbox can also be used in a more general manner to make operations deterministic, such as for example the deterministic teleportation of a single-photon qubit [20].

In this manuscript we will review new techniques based on optical hybrid quantum information applied to quantum state engineering.

Context and structure of the manuscript

It is in this active context of hybridization of the processes that this PhD work took place. Light is a convenient media for the implementation of hybrid quantum information processing as having low decoherence at room temperature. We can also rely on mature optical technologies such as nonlinear optics crystal and efficient detectors. In addition, light is the natural carrier for quantum communication as the generated states can be freely propagating.

Recent quantum state engineering works based on the optical hybrid approach therefore impulsed new ways of designing quantum networks [21–24]. For example, heterogeneous networks, on which each operation is implemented with the most adequate encodings, could therefore be a way to overcome the current limitations. However, the nodes of a network need to be bridged together, in a quantum manner. Indeed, the quantum information hold by a DV qubit needs to be fully transferred to a CV-type state, for instance. A way to achieve such conversion is to perform teleportation based on a shared entangled state between the network nodes. The hybrid entanglement generation between CV and DV states achieved in the beginning of this thesis therefore paved the way for further study of such hybrid architectures [25]. The optical parametric oscillators used as main resources in this thesis were already well calibrated through the previous thesis of Olivier Morin, which led to the first generation of highly non-Gaussian optical states in the laboratory [26].

The present manuscript is organized as follows:

- **Part I** will first introduce the main toolboxes that will be used through all the manuscript. The first chapter will present the theoretical concepts and the adopted conventions. The second chapter will be devoted to the experimental resources, including non-linear crystals and detectors. The third chapter will be devoted to a certain type of detector, a superconducting nanowire single photon detector, which efficiency has been improved to the state-of-the art at our wavelength, through collaboration with the NIST and the JPL-NASA. The achieved close-to-unity efficiency enables to speed up our applications and we can therefore target more complex states through multiple conditioning schemes.

- **Part II** will then focus on quantum state engineering. Using the upgraded single-photon detectors, we will in Chapter IV demonstrate the high-purity and fast generation of single and two-photon states. The demonstrated figures of merit coupled to the achieved rate will enable us to target the generation of more complex states, such as squeezed Schrödinger cat states as presented in Chapter V. Such states will be generated with the help of a gaussian operation: squeezing. This method helps us to achieve complex states more easily as well as protecting them from decoherence.

- Finally **Part III** will focus on a certain type of hybrid state: the hybrid entanglement of light. Demonstrated at the very beginning of this PhD, hybrid entanglement of light enables to build a bridge between the different encodings.

Information can then be transferred through this bridge via quantum teleportation. Chapter VI will first introduce the experimental generation of remote hybrid entanglement, based on a non-local single photon subtraction. Demonstration of a new type of hybrid entanglement, i.e. qutrit entanglement, containing more entanglement due to a higher dimensionality will also be shown. Methods to characterize the non-locality features of hybrid entangled states will then be investigated. A first application of hybrid entanglement will be implemented via the remote generation of arbitrary continuous-variable qubits. This demonstration paves the way for the realization of a quantum encoding converter, and will therefore be followed by a short theoretical study on hybrid teleportation. Finally, Chapter VII will be devoted to a deeper study of hybrid entanglement in a more fundamental manner. Indeed, hybrid entanglement can be seen as entanglement between particle and waves, i.e. between microscopic states and *macroscopic* states. We will propose and implement a scheme to generate a micro-macro entangled state, by adding a local photon subtraction and increasing the mean photon number of the CV mode via a squeezing operation. We will then characterize this state through criteria proposed in the literature.

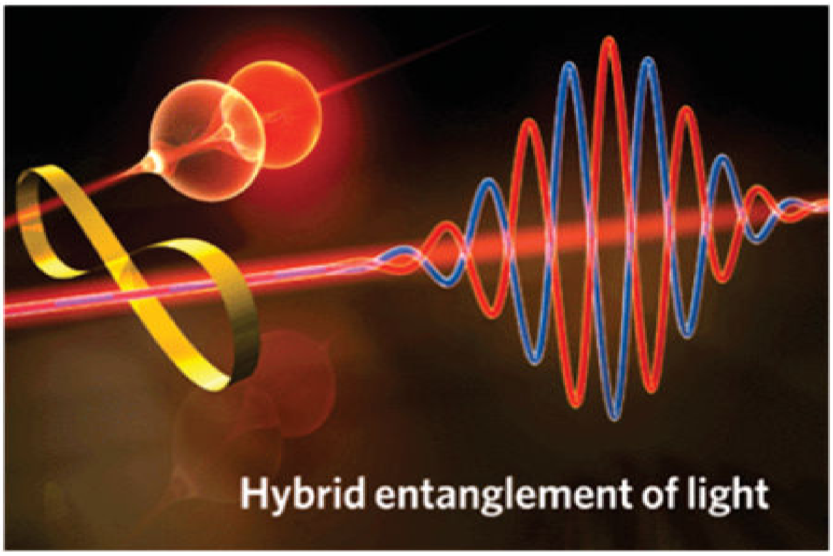

Credit: Nature Photonics cover.

List of publications

- *High-efficiency WSi superconducting nanowire single-photon detectors for quantum state engineering in the near infrared*
  H. Le Jeannic, V.B. Verma, A. Cavaillès, K. Huang, Y-C. Jeong, F. Marsili, M.D. Shaw, S.W. Nam, O. Morin, J. Laurat
  Opt. Lett. **41**, 22, pp. 5341-5344, doi.org/10.1364/OL.41.005341

- *Experimental quantum state engineering with time-separated heraldings from a continuous-wave light source: a temporal-mode analysis*
  K. Huang, H. Le Jeannic, V.B. Verma, M.D. Shaw, F. Marsili, S.W. Nam, E Wu, H. Zeng, O. Morin, J. Laurat
  Phys. Rev. A **93**, 013838 (2016), doi.org/10.1103/PhysRevA.93.013838

- *Optical synthesis of large-amplitude squeezed coherent-state superpositions with minimal resources*
  K. Huang, H. Le Jeannic, J. Ruaudel, V. B. Verma, M. D. Shaw, F. Marsili, S. W. Nam, E Wu, H. Zeng, Y.-C. Jeong, R. Filip, O. Morin, J. Laurat
  Phys. Rev. Lett. **115**, 023602 (2015), doi.org/10.1103/PhysRevLett.115.023602

- *Microcontroller-based locking in optics experiments*
  K. Huang, H. Le Jeannic, J. Ruaudel, O. Morin, J. Laurat
  Rev. Sci. Instrum. **85**, 123112 (2014), doi.org/10.1063/1.4903869

- *Remote creation of hybrid entanglement between particle-like and wave-like optical qubits*
  O. Morin, K. Huang, J. Liu, H. Le Jeannic, C. Fabre, J. Laurat,
  Nature Photon. **8**, 570-574 (2014), doi.org/10.1038/nphoton.2014.137

In preparation

- *Slowing decoherence by squeezing*
  H. Le Jeannic, A. Cavaillès, K. Huang, R. Filip, J. Laurat

- *Remote state preparation of continuous variable qubits via hybrid entanglement of light*
  H. Le Jeannic, A. Cavaillès, J. Raskop, J. Laurat

Part I

Toolboxes for Quantum State Engineering and Characterization

I | Theoretical Tools

Introduction

In this first chapter, basic notions of quantum optics will be described. From the field quantization to a description of the quantum states that will be found in this PhD work, formulas and basic models will be explained. Although all of these notions are detailed in textbooks [27–31], it is convenient for the reader to have them gathered here, in order to know the normalizations and notations used in all this manuscript.

Contents

I.1 Field quantization 4
  - I.1.1 Field description 4
  - I.1.2 Quadrature operators 4

I.2 Density operator, matrices and criteria 5
  - I.2.1 Density matrix representation 5
  - I.2.2 Tools for state characterisation 6
  - I.2.3 Tools for entanglement characterisation 7

I.3 Wigner representation 9
  - I.3.1 Properties 9
  - I.3.2 Continuous-variable tools 10

I.4 Some useful operators 10

I.5 Modeling experimental imperfections 12
  - I.5.1 Losses or amplitude damping 12
  - I.5.2 Phase noise 13

I.6 Zoology of quantum states 14
  - I.6.1 Fock states 14
  - I.6.2 Coherent state 16
  - I.6.3 Squeezed vacuum state 16
  - I.6.4 Cat state 17
  - I.6.5 Squeezed cat state 18

I.7 Conclusion 19

I.1 Field quantization

I.1.1 Field description

In classical optics, the field can be described using a basis made of orthogonal spatio-temporal modes of light. These different modes can be for example found by using a Fourier description. In quantum physics, the electric field can be described using the annihilation and creation operators, $\hat{a}$ and $\hat{a}^\dagger$. One mode of the electric field can therefore be noted as:

$$\hat{E}(\overrightarrow{r},t) = E_0(\hat{a}e^{-i(\omega t-\overrightarrow{k}\overrightarrow{r})} + \hat{a}^\dagger e^{i(\omega t-\overrightarrow{k}\overrightarrow{r})}). \tag{I.1.1}$$

Such mode lives in a given Hilbert space H. When several modes are involved, for example in the case of entanglement, it is possible to extend the description to a full Hilbert space denoted: $H = H_1 \otimes ... \otimes H_k \otimes ... \otimes H_n$. Each the Hilbert space H_i has either a finite or an infinite dimension.

The annihilation (respectively creation) operator removes (respectively adds) a quanta - here a photon - to a photon number state. Thus their effect is described as:

$$\hat{a}|n\rangle = \sqrt{n}|n-1\rangle \tag{I.1.2}$$

$$\hat{a}^\dagger|n\rangle = \sqrt{n+1}|n+1\rangle \tag{I.1.3}$$

where $|n\rangle$ is a photon-number state, also called Fock state, and $[\hat{a},\hat{a}^\dagger] = 1$ is their commutation relation.

The photon-number operator is defined by the product of the two operators:

$$\hat{n} = \hat{a}^\dagger\hat{a}. \tag{I.1.4}$$

I.1.2 Quadrature operators

In analogy to classical optics, the electric field can also be written in the Fresnel phase-space in terms of its real and imaginary parts, as shown in Fig I.1:

$$\hat{E}(\overrightarrow{r},t) = E_0\sqrt{2}(\hat{X}\cos(\omega t - \overrightarrow{k}.\overrightarrow{r}) + \hat{P}\sin(\omega t - \overrightarrow{k}.\overrightarrow{r}) \tag{I.1.5}$$

where $\hat{X}$ and $\hat{P}$ are called the quadrature operators of the field. They can also be written as:

$$\hat{X} = \sigma_0(\hat{a}+\hat{a}^\dagger) \tag{I.1.6}$$

$$\hat{P} = -i\sigma_0(\hat{a}-\hat{a}^\dagger) \tag{I.1.7}$$

with σ_0 the variance of the vacuum fluctuations. We usually choose the value $\sigma_0 = 1$ to normalize our systems. These two operators can also be named as position and momentum operators. Their commutation operator can be written as

$$[\hat{X},\hat{P}] = 2i\sigma_0^2. \tag{I.1.8}$$

$\hat{X}$ and $\hat{P}$ are conjugated variables, they follow the Heisenberg inequality:

$$\sigma_x\sigma_p \geq \sigma_0^2. \tag{I.1.9}$$

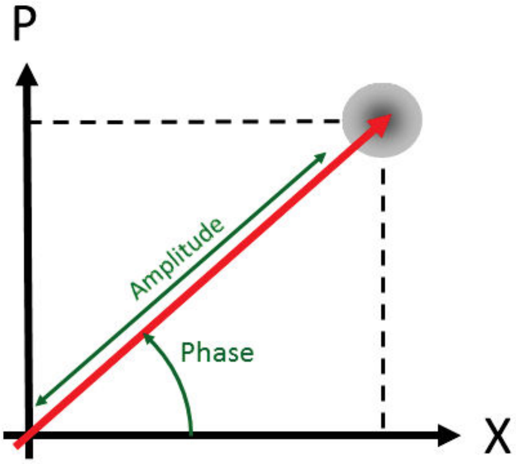

Figure I.1: Fresnel representation of the quantum field, also called phasor diagram. The grey area represents the associated quantum flucutations.

The quadrature operators are observables and are therefore Hermitian operators. They have orthonormal eigenvectors, $\hat{X}|x\rangle = x|x\rangle$, which satisfiy the completeness relation $\int |x\rangle\langle x|dx = \mathbb{1}$. The number operator can also be expressed using these operators as

$$\hat{n} = \frac{1}{4\sigma_0^2}(\hat{X}^2 + \hat{P}^2 - 2\sigma_0^2). \tag{I.1.10}$$

The quadrature operators can be generalized to any phase angle θ in the Fresnel representation:

$$\hat{X}_\theta = \sigma_0(\hat{a}e^{-i\theta} + \hat{a}^\dagger e^{i\theta}). \tag{I.1.11}$$

I.2 Density operator, matrices and criteria

The density operator enables to generalize the representation of states. For example when a state experiences losses it cannot be described using a pure state description (i.e. a ray description), it is becoming "mixed". In the following part, we will introduce the density matrix formalism as well as some useful criteria for state characterization.

I.2.1 Density matrix representation

To describe a quantum state and its features, one can use the matrix formalism and represent it as a density matrix. This matrix is the linear representation of the density operator and they are often interchanged. The density operator representation is especially used if the state is not a pure state, but a statistical mixture of states : it is always the case experimentally due to the interaction with the environment resulting from loss or phase damping. The density matrix may be infinite-dimensional. It is diagonalizable in a basis of orthogonal eigenvectors which means that the state can always be described as a sum of pure states $|\psi_i\rangle$:

$$\hat{\rho} = \sum_i p_i |\psi_i\rangle\langle\psi_i|. \tag{I.2.1}$$

This description is also called the spectral decomposition of the state. The diagonal elements of the density matrix are the probabilities of measuring each vector of the Hilbert space basis. Thus, due to the conservation of the probabilities, one has:

$$\mathrm{Tr}[\hat{\rho}] = 1. \tag{I.2.2}$$

A few properties also come from this representation.

- The density matrix is self-adjoint or hermitian:

$$\hat{\rho}^\dagger = \hat{\rho}. \tag{I.2.3}$$

- The density matrix is also positive semi-definite. All the eigenvalues are either positive or zeros:

$$\mathrm{rank}(\hat{\rho}) = \mathrm{rank}(\hat{\rho}^2). \tag{I.2.4}$$

- Given an operator $\hat{O}$, the expectation value is given by:

$$\langle \hat{O} \rangle = \mathrm{Tr}[\hat{\rho}\hat{O}]. \tag{I.2.5}$$

I.2.2 Tools for state characterisation

In this section, we will introduce criterions that are used to characterize the quantum features of a state. We will use them later in the manuscript to describe our experimental results.

- **Purity**
  If a state is pure, $\mathrm{Tr}[\hat{\rho}^2] = 1$. The purity is therefore measured as:

$$\mathcal{P} = \mathrm{Tr}[\hat{\rho}^2]. \tag{I.2.6}$$

- **Fidelity**
  The fidelity is related to the proximity between two states. It can be seen as the overlap between two states. In the most general case, it is defined as [32]:

$$\mathcal{F} = \left(\mathrm{Tr}[\sqrt{\sqrt{\hat{\rho}_1}\hat{\rho}_2\sqrt{\hat{\rho}_1}}]\right)^2. \tag{I.2.7}$$

  If one of the states is a pure state, it can be conveniently simplified as:

$$\mathcal{F} = \mathrm{Tr}[\hat{\rho}_1\hat{\rho}_2]. \tag{I.2.8}$$

  If the two states are pure, the fidelity can be written as the simple overlap:

$$\mathcal{F} = |\langle\psi_1|\psi_2\rangle|^2. \tag{I.2.9}$$

- **Pauli matrices**
  The Pauli matrices are also interesting to remind here, as they will be used

for entanglement witnesses. They can be defined in any basis of orthogonal eigenvectors:

$$\hat{\sigma}_x = \begin{pmatrix} 0 & 1 \\ 1 & 0 \end{pmatrix}, \hat{\sigma}_y = \begin{pmatrix} 0 & -i \\ i & 0 \end{pmatrix}, \hat{\sigma}_z = \begin{pmatrix} 1 & 0 \\ 0 & -1 \end{pmatrix} \tag{I.2.10}$$

More generally these pseudo-spin operators can be defined for any angle θ as:

$$\hat{\sigma}_\theta = \cos\theta\hat{\sigma}_x + \sin\theta\hat{\sigma}_y = \begin{pmatrix} 0 & e^{-i\theta} \\ e^{i\theta} & 0 \end{pmatrix}, \hat{\sigma}_z = \begin{pmatrix} 1 & 0 \\ 0 & -1 \end{pmatrix} \tag{I.2.11}$$

The expectation value of these operators is very commonly used as a tool when it comes to implement entanglement witnesses such as Bell-type or steering inequalities.

They can be extended to the full Hilbert space [33, 34], in which case they act upon the parity of the photons, and are therefore "parity-spin" operators:

$$\begin{aligned} \hat{\sigma}_x &= \sum_{n=0}^{\infty} |2n\rangle\langle 2n+1| + |2n+1\rangle\langle 2n| \\ \hat{\sigma}_y &= \sum_{n=0}^{\infty} i(|2n+1\rangle\langle 2n| - |2n\rangle\langle 2n+1|) \\ \hat{\sigma}_z &= \sum_{n=0}^{\infty} |2n+1\rangle\langle 2n+1| - |2n\rangle\langle 2n|. \end{aligned} \tag{I.2.12}$$

In such case, the operator $\hat{\sigma}_z$ is the opposite of the parity operator. $\hat{\sigma}_x$ and $\hat{\sigma}_y$ are called the parity-flip operators. Their commutation relations are analogous to the pseudo-spin operators ones.

I.2.3 Tools for entanglement characterisation

A counter-intuitive property which follows from the quantum mechanics theory is the possibility for states that contains several modes to be non-separable. A separable state is a state $\hat{\rho}$ living in a Hilbert space $H = H_A \otimes H_B$ that can be written in the form:

$$\hat{\rho} = \sum_k p_k \hat{\rho}_A \otimes \hat{\rho}_B \tag{I.2.13}$$

where $p_k \geq 0$.

Non-separable states can exhibit quantum correlations. These correlations are at the heart of quantum information and can lead to the implementation of various protocols, including for quantum computing, communication and metrology [27]. In the following will be reminded different measures that can be used to witness or quantify the entanglement of the states we are producing.

- **Concurrence**
  For a bipartite pure state $\hat{\rho}_{AB}$ and given the matrices
  $$\hat{\rho}'_{AB} = (\hat{\sigma}_y \otimes \hat{\sigma}_y)\hat{\rho}^*_{AB}(\hat{\sigma}_y \otimes \hat{\sigma}_y) \tag{I.2.14}$$
  where $\hat{\rho}^*_{AB}$ is the complex conjugation, $\hat{\sigma}_y$ the pauli operator and
  $$M = \sqrt{\sqrt{\hat{\rho}_{AB}}\hat{\rho}'_{AB}\sqrt{\hat{\rho}_{AB}}}. \tag{I.2.15}$$
  The concurrence is defined as:
  $$C(\hat{\rho}_{AB}) = max(0, \lambda_1 - \lambda_2 - \lambda_3 - \lambda_4) \tag{I.2.16}$$
  where $\lambda_1, ..., \lambda_4$ are the eigenvalues in decreasing order of the matrix M
  This definition is valid for qubit states (dimension 2).

- **Negativity**
  The negativity of entanglement is a measure given by:
  $$\mathcal{N}(\hat{\rho}_{AB}) = \frac{\|\hat{\rho}^{\Gamma_A}_{AB}\| - 1}{2} \tag{I.2.17}$$
  where $\hat{\rho}^{\Gamma_A}_{AB}$ is the partial transpose of $\hat{\rho}$ with respect to subsystem A. Equivalently, it can be defined as:
  $$\mathcal{N}(\hat{\rho}_{AB}) = \sum_i \frac{|\lambda_i| - \lambda_i}{2} \tag{I.2.18}$$
  where λ_i are the negative eigenvalues of $\hat{\rho}^{\Gamma_A}_{AB}$.
  This measure is monotone with entanglement and cannot increase under local operations. It will be mostly used in our experimental realizations.

- **Steering inequality**
  Steering is a phenomenon related to the Einstein Podolsky Rosen paradox which can be shown when two parts, Bob and Alice, share entanglement. Alice is trying to convince Bob by that they share entanglement by making a measurement on her side and telling her results to Bob. Steering inequalities stand between non-separability and non-locality Bell-type tests, and usually leads to higher technical difficulties. They are becoming more and more investigated as a new way to show strong entanglement features, and in particular "device-independent" cryptography scenario [35]. Steering inequalities will be furtherly described in Chapter VI.

- **Bell inequality**
  Bell-type measurements enable to violate an inequality that should be respected if the theory of quantum mechanics was local. When such an inequality is violated, it is possible to refute the presence of any hidden variables that would make the correlations local, showing the robustness of the quantum mechanics theory. When an assumption is made on the state for technical reasons, for example fair sampling (because of limited detection inefficiency), no-communication between the parties (because of limited distance), it forces us to trust one of the parties, making the violation without any loophole harder to achieve experimentally. Very recently, three loophole-free violations of such inequality have been reported [36–38].

I.3 Wigner representation

Another tool to represent a quantum state, oftenly used in the continuous-variable framework, is the Wigner representation. For a given state, the Wigner function can be defined as:

$$W_{\hat{\rho}}(x,p) = \frac{1}{2\pi\sigma_0} \int e^{\frac{iyp}{\sigma_0^2}} \langle x-y|\hat{\rho}|x+y\rangle dy \tag{I.3.1}$$

where for any Fock state $|n\rangle$,

$$\langle n|x_\theta\rangle = e^{in\theta} \frac{1}{(\sqrt{2\pi}\sigma_0 2^n n!)^{\frac{1}{2}}} H_n\left(\frac{x}{\sigma_0\sqrt{2}}\right) e^{-\frac{x^2}{4\sigma_0^2}}. \tag{I.3.2}$$

$H_n(x)$ are Hermite polynomials and are detailed in Appendix A. Thus, it is possible to calculate the Wigner function using the density matrix in the Fock state basis in the following way:

$$W_{\hat{\rho}}(x,p) = \sum_{k,l} \rho_{kl} W_{|k\rangle\langle l|}(x,p) \tag{I.3.3}$$

with

$$W_{|k\rangle\langle l|}(x,p) = \frac{(-1)^l}{2\pi\sigma_0^2}\sqrt{\frac{l!}{k!}}\left(\frac{x-ip}{\sigma_0}\right)^{k-l} e^{-\frac{x^2+p^2}{2\sigma_0^2}} L_l^{k-l}\left(\frac{x^2+p^2}{\sigma_0^2}\right) \tag{I.3.4}$$

if $k \geqslant l$ (otherwise: $W_{|k\rangle\langle l|}(x,p) = W_{|l\rangle\langle k|}(x,-p)$). $L_n(x)$ are Laguerre polynomials, detailed in Appendix A. The Wigner representation allows one to represent a state in terms of X- and P- distribution. It can be seen in quantum optics as the quantum noise quasi-probability distribution.

The Wigner function can have negative values. These negative values are often considered as a strong signature of non-classicality. Of course, this representation can be generalized for several modes:

$$W_{\hat{\rho}}(x_1,p_1,...,x_n,p_n) = \frac{1}{(2\pi\sigma_0^2)^n}\int_{\mathbb{R}^{2n}} \langle x_1-y_1|...\langle x_n-y_n|\hat{\rho}|x_1+y_1\rangle...|x_n+y_n\rangle dy_1...dy_n. \tag{I.3.5}$$

Using the same idea, any operators can be also transferred in terms of Wigner representation.

I.3.1 Properties

The Wigner function only has real values if the operator is hermitian. An obvious example can be the density matrix, i.e. the representation of a quantum state. The Wigner function is also linear.

In the following are detailed some other useful properties.

- The conservation of the probabilities gives:

$$\iint_{\mathbb{R}^2} W_{\hat{\rho}}(x,p)dxdp = 1. \tag{I.3.6}$$

- **Overlap**
  The overlap of two Hermitian operators is written using the Wigner representation as:
  $$\mathrm{Tr}[\hat{O}_1\hat{O}_2] = 4\pi\sigma_0^2 \iint dx dp W_{\hat{O}_1}(x,p) W_{\hat{O}_2}(x,p). \tag{I.3.7}$$
  This very general formula can be easily adapted to get the direct expression for the action of an operator on a quantum state as well as the fidelity between two states or the purity of a state [39].

- **Diagonal elements**
  In the Fock state basis, the sum of the density matrix diagonal elements, weighted by their parity, is related to the value of the Wigner function at the origin of phase-space:
  $$W_{\hat{\rho}}(0,0) = \frac{1}{2\pi\sigma_0^2}\sum_n (-1)^n \hat{\rho}_{nn}. \tag{I.3.8}$$

- **Transposition**
  Transposing the density matrix is equivalent of replacing p by $-p$ in the Wigner function of the quantum state.

- **Parity Operator**
  The Wigner function can also be written as the displacement of the parity operator $\hat{\Pi}$:
  $$W(\alpha) = \frac{2}{\pi}\mathrm{Tr}[\hat{D}(-\alpha)\hat{\rho}\hat{D}(\alpha)\hat{\Pi}] \tag{I.3.9}$$
  where $\alpha = (x+ip)/2\sigma_0$.

I.3.2 Continuous-variable tools

In continuous variable experiments, detection is usually implemented via homodyne detection. This type of detector, which will be furtherly described in Chapter II, can measure the quadratures of a light field. Therefore the marginal distribution, which is the density probability to measure x_θ with the quadrature observable $\hat{x}_\theta$, is often used. It can be extracted from the Wigner function as :

$$\mathcal{P}_{\hat{\rho}}(x_\theta) = \int dp_\theta W_{\hat{\rho}}(x_\theta\cos\theta - p_\theta\sin\theta, p_\theta\cos\theta + x_\theta\sin\theta). \tag{I.3.10}$$

I.4 Some useful operators

In this section will be listed the main operators that will be implemented experimentally in the rest of the manuscript in order to engineer quantum states.

- **Squeezing operator**
  The Heisenberg relation that constrains conjugate quadratures shows that the

overall uncertainty of a system cannot be bypassed. However it is possible to achieve a better knowledge on one quadrature while having more uncertainty on the other one. Such phenomenon is known as quadrature squeezing, where the fluctuations of one quadrature is decreased while the other quadrature gets "anti-squeezed" in phase space. The squeezing operator can be written as:

$$\hat{S}_\xi = e^{\frac{1}{2}(\xi \hat{a}^2 - \xi^* \hat{a}^{\dagger 2})} \tag{I.4.1}$$

where $\xi = re^{i\theta}$. The squeezing factor s is the compression ratio of the quadrature variance $\sigma^2_{\hat{x}_\theta}$ compared to its initial value, and can be written as:

$$s = e^{-2r}. \tag{I.4.2}$$

It is often given in the decibel scale. Additionally, parameters such as λ will be used in this PhD work, for the sake of formula simplification. This latest can be written as:

$$\lambda = \tanh r. \tag{I.4.3}$$

The factor s can be expressed in decibels as: $s_{dB} = -10\log_{10}(\frac{1-\lambda}{1+\lambda}) = \frac{20}{\ln 10} r$.

Experimentally, this operator can be implemented using non-linear processes such as parametric down conversion processes. Its action on the Wigner function of a quantum state can be seen as:

$$W_{\hat{\rho}}(x,p) \to W_{\hat{\rho}}(xe^{\xi}, pe^{-\xi}). \tag{I.4.4}$$

We have taken here the case where $\xi \in \mathbb{R}$ to simplify the expression. The general case is equivalent to to this change of coordinates on θ-rotated axes of the Wigner function.

- **Phase Shift Operator**
  This operator represents the phase shifting of a quantum state:

$$\hat{U}_\varphi = e^{i\hat{a}^\dagger \hat{a}\varphi}. \tag{I.4.5}$$

  In terms of Wigner representation it corresponds to a simple rotation in the phase-space plan, leading to the transformation:

$$W_{\hat{\rho}}(x,p) \to W_{\hat{\rho}}(x\cos\varphi - p\sin\varphi, x\sin\varphi + p\cos\varphi). \tag{I.4.6}$$

- **Displacement Operator**
  This operator enables to displace the state in phase space. Experimentally it is implemented by mixing the state with a coherent state field via an asymmetric beam splitter. It can be written as:

$$D(\alpha) = e^{\alpha a^\dagger - \alpha^* a} \tag{I.4.7}$$

  In terms of Wigner representation it corresponds to the transformation:

$$W_{\hat{\rho}}(x,p) \to W_{\hat{\rho}}(x + Re[\alpha], p + Im[\alpha]). \tag{I.4.8}$$

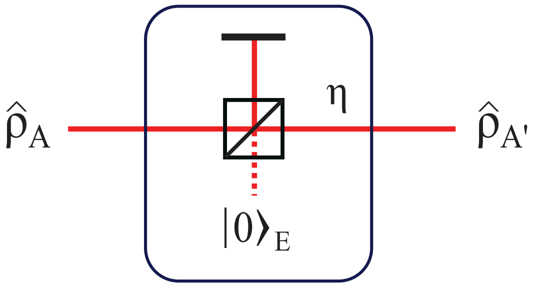

Figure I.2: Losses modeled by a damping channel

- **Beam Splitter Operator**
  Used to model losses (see below), splitting or mixing of modes, but also for conditional generation schemes, the beam splitter operator is a basic tool in quantum optics for quantum state generation as well as for protocol implementation. It is given by:
  $$\hat{B}(\theta) = e^{\theta(\hat{a}^\dagger\hat{b} - \hat{a}\hat{b}^\dagger)} \tag{I.4.9}$$
  where $\hat{a}$ and $\hat{b}$ are the anihilation operators for the two spatial modes A and B. It thus leads to an interesting way of reformulating the action of a beam-splitter on a mode:
  $$\begin{aligned} \hat{B}^\dagger(\theta)\hat{a}\hat{B}(\theta) &= \hat{a}\cos\theta + \hat{b}\sin\theta \\ \hat{B}^\dagger(\theta)\hat{b}\hat{B}(\theta) &= \hat{b}\cos\theta - \hat{a}\sin\theta \end{aligned} \tag{I.4.10}$$
  In the Wigner representation, its effect can be written as:
  $$W_{\hat{\rho}_{A\otimes B}}(x_A, p_A, x_B, p_B) \to W_{\hat{\rho}_{A\otimes B}}(tx_A + rx_B, tp_A + rp_B, tx_B - rx_A, tp_B - rp_A) \tag{I.4.11}$$

This latest operator will be used in order to model optical imperfection such as the optical loss of a system, as shown in the next section.

I.5 Modeling experimental imperfections

In this section we will detail the two main sources of imperfections that can be met in a quantum optics experiment. These imperfections are due to the interaction of the quantum state with its environnement, on which the experimentalist cannot have access. This leads therefore to a statistical mixture of the quantum state.

I.5.1 Losses or amplitude damping

In quantum optics, losses are seen as amplitude damping and can be modeled using a beam splitter operation on which the environment (vacuum) is mixed with the quantum state and then averaged with a partial trace operation on the environmental mode. The process is sketched in Fig. I.2.

Let's consider a state represented by its density matrix $\hat{\rho}$, losses in energy, with a value $(1 - \eta)$ (where η is called the efficiency of the system) can be represented as the action of a beam splitter with a transmission coefficient $\cos\theta = \sqrt{\eta}$:

$$\hat{\rho}_A \otimes |0\rangle_E\langle 0| \xrightarrow{\hat{B}(\eta)} \hat{B}(\eta)\hat{\rho}_A \otimes |0\rangle_E\langle 0|\hat{B}^\dagger(\eta), \tag{I.5.1}$$

where $|0\rangle_E$ is the vacuum in the environnemental mode. The experimentalists only have access to mode A, and cannot have access to the leakage of the photons due to losses. The resulting density matrix is therefore obtained by partially tracing the reflected output of the beam splitter:

$$\hat{\rho}'_A = \mathrm{Tr}_E[\hat{B}(\eta)(\hat{\rho}_A \otimes |0\rangle_E\langle 0|)\hat{B}^\dagger(\eta)]. \tag{I.5.2}$$

It is also possible to calculate amplitude damping using the Wigner formalism. By implementing a beam splitting operation of transmission corresponding to $\sqrt{\eta}$ and then integrating on the whole phase-space of E, one can find the expression for the new Wigner representation of the state:

$$W'_A(x_A, p_A) = \int W_{A,E}(\sqrt{\eta}x_A + \sqrt{1-\eta}x_E, \sqrt{\eta}p_A + \sqrt{1-\eta}p_E, \sqrt{\eta}x_E + \sqrt{1-\eta}x_A, \sqrt{\eta}p_E + \sqrt{1-\eta}p_A)dx_E dp_E. \tag{I.5.3}$$

I.5.2 Phase noise

Another source of imperfection can be the phase averaging coming from the lack of precision in phase measurement or from path instabilities. It leads to statistical mixing, but without affecting the probability of measuring eigenmodes. In other terms, it affects the anti-diagonal elements of the density matrix, i.e. the coherence terms, and leaves unchanged the diagonal elements of the density matrix.

In this manuscript, we have chosen a very simple model of gaussian phase noise (which may not be the case experimentally but can help to check the sensitivity of states to phase noise, and is very easy to calculate). Let us consider a state $\hat{\rho}$ written as the sum of states ρ_k:

$$\hat{\rho} = \sum_k c_k e^{i\varphi_k}\rho_k. \tag{I.5.4}$$

The phase averaging on each phase φ_k due to one or several gaussian noises of standard deviations σ_k leads to a new matrix $\hat{\rho}_\sigma$:

$$\hat{\rho}_\sigma = \frac{1}{\sqrt{2\pi}\sigma_1} \times \cdots \times \frac{1}{\sqrt{2\pi}\sigma_k} \int \cdots \int_{\mathbb{R}} e^{-\frac{\varphi_1^2}{2\sigma_1^2}} \dots e^{-\frac{\varphi_k^2}{2\sigma_k^2}} \hat{\rho} d\varphi_1 \dots d\varphi_k. \tag{I.5.5}$$

Such noise source is less commonly found in the literature as it happens only in the case of state superposition. We will therefore give here a short example of its consequences on one initial pure qubit of the form $|\Psi\rangle = c_0|0\rangle + c_1|1\rangle$. A gaussian noise on its superposition phase will lead to a mixed state:

$$\hat{\rho}_\sigma = \begin{pmatrix} c_0^2 & c_0^* c_1 e^{-\frac{\sigma^2}{2}} \\ c_0 c_1^* e^{-\frac{\sigma^2}{2}} & c_1^2 \end{pmatrix} \tag{I.5.6}$$

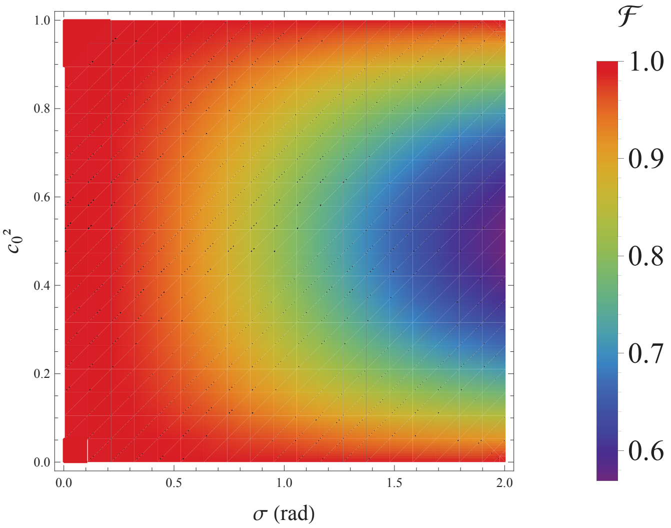

Figure I.3: Fidelity between the qubit state $|\Psi\rangle$, and a qubit $\hat{\rho}_\sigma$ under gaussian phase noise of standard deviation σ for different probabilities of the vacuum state c_0.

The fidelity between the decohered state and the initial one decreases and is reduced to:

$$\mathcal{F} = \frac{c_0^4 + 2c_0^2 c_1^2 e^{-\frac{\sigma^2}{2}} + c_1^4}{\left(c_0^2 + c_1^2\right)^2}. \tag{I.5.7}$$

This fidelity is plotted in Fig. I.3 as a function of σ and c_0. The state is more sensitive to phase noise when the superposition is equally weighted, i.e. for $c_0^2 = 0.5$. When σ becomes large, coherence terms fully disappear. Hence $\mathcal{F} \to 0.5$.

Now that we have presented our main toolboxes, we will review in the following the quantum states that will be present in this PhD work.

I.6 Zoology of quantum states

In this section will be listed common quantum states that can be found in the manuscript, for which it exists two main categories. Depending on their quadrature fluctuation distributions, quantum states are qualified as gaussian or non-gaussian. The Hudson-Picquet theorem [40] states that a gaussian state cannot have a negative Wigner function. Non-gaussian states exhibiting negative values of the Wigner function are therefore considered as strongly non classical. We will give in this section a few examples of such states and show their Wigner functions.

I.6.1 Fock states

A first class of quantum states used in quantum optics are the Fock states or photon-number states $|n\rangle$. They are eigenvectors of the number operator $\hat{a}^\dagger\hat{a}$. They are a class

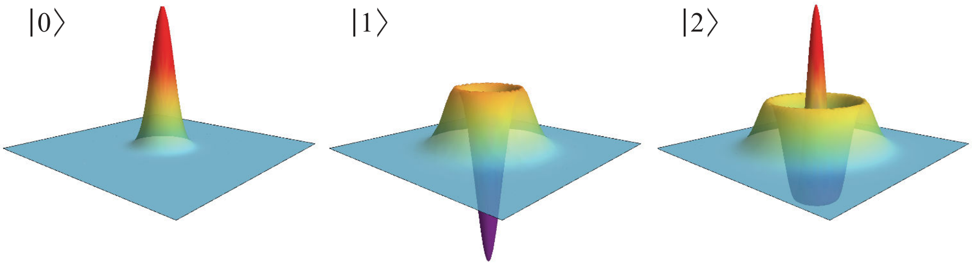

Figure I.4: Wigner function of vacuum, single-photon, and two-photon Fock states.

of orthonormal vectors. Their Wigner functions can be written as:

$$W_{|n\rangle}(x,p) = \frac{(-1)^n}{2\pi\sigma_0^2} e^{-\frac{x^2+p^2}{2\sigma_0^2}} L_n\Big(\frac{x^2+p^2}{\sigma_0^2}\Big). \tag{I.6.1}$$

The Wigner function of different Fock states are represented in I.4. The parity of a Fock state is related to the sign of its Wigner function at the origin of the phase space. The decoherence of Fock states under photon losses, scales with the power of the photon number. For example, the fidelity with a Fock state $|n\rangle\langle n|$, given an efficiency η, can be expressed as:

$$\mathcal{F}_{|n\rangle,\eta} = \eta^n. \tag{I.6.2}$$

Figure I.5 gives the evolution of the fidelity with losses of different Fock states. The higher the photon number is, the faster a Fock state decoheres. This means that it is technically very challenging to generate high-number Fock states. In Chapter IV, we will see how to generate single photon and two-photon Fock states with high purity. However their sensitivity to losses prevents the use of the same protocols to generate three-photon Fock states with high purity.

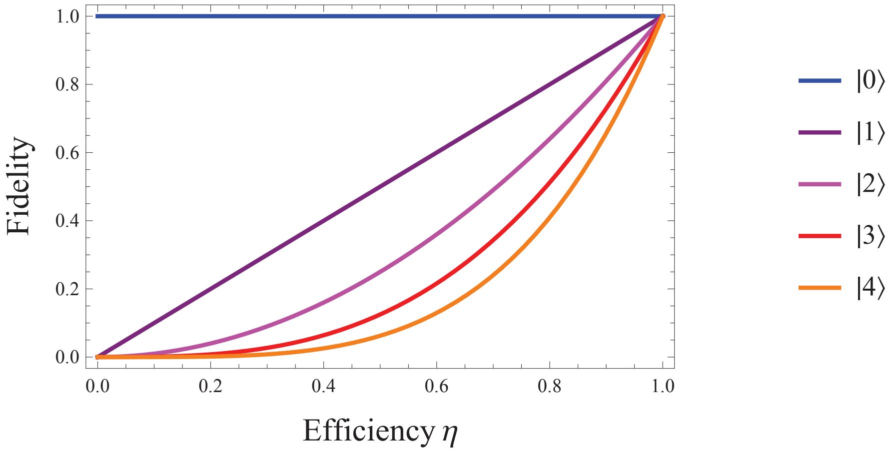

Figure I.5: Fidelity with the efficiency of the channel, for different Fock states. This fidelity corresponds directly to the vacuum admixture for single-photon state $|1\rangle$.

I.6.2 Coherent state

Considered as quasi-classsical states, coherent states $|\alpha\rangle$ are the closest to an attenuated laser field. Coherent states exhibit a Poissonian distribution of their photon number. As a consequence, they are gaussian states. They are as well eigenvectors of the annihilation operator:

$$\hat{a}|\alpha\rangle = \alpha|\alpha\rangle. \tag{I.6.3}$$

The "simplest" form of coherent state is the vacuum. Any other coherent states can be seen as a displaced vacuum state.

$$\hat{D}(\alpha)|0\rangle = |\alpha\rangle. \tag{I.6.4}$$

Coherent states can be expressed in the Fock state basis as:

$$|\alpha\rangle = e^{-\frac{|\alpha|^2}{2}} \sum_{n=0}^{+\infty} \frac{\alpha^n}{\sqrt{n!}} |n\rangle. \tag{I.6.5}$$

Their mean photon number is related to their amplitude α:

$$\langle\alpha|\hat{n}|\alpha\rangle = |\alpha|^2. \tag{I.6.6}$$

Their Wigner function can be written as:

$$W_{|\alpha\rangle\langle\alpha|}(x,p) = \frac{e^{-\frac{1}{2\sigma_0^2}\left((x-\alpha_x)+(p-\alpha_p)^2\right)}}{2\pi\sigma_0^2} \tag{I.6.7}$$

where $\alpha = \alpha_x + i\alpha_p$.
Finally, the overlap between two coherent states $|\alpha\rangle$ and $|\beta\rangle$ is:

$$|\langle\alpha|\beta\rangle|^2 = e^{-|\beta-\alpha|^2}. \tag{I.6.8}$$

I.6.3 Squeezed vacuum state

It results from the application of squeezing operator on the vacuum state.

$$\hat{S}|0\rangle = (1-\lambda^2)^{1/4} \sum_{n=0}^{\infty} \binom{2n}{n}^{\frac{1}{2}} \left(\frac{\lambda}{2}\right)^n |2n\rangle. \tag{I.6.9}$$

Due to this operation, the variance of the vacuum σ_0^2 is reduced by the factor $s = \frac{\sigma^2}{\sigma_0^2}$ on the $\hat{x_\theta}$ quadrature, where $\theta = \arg(\xi)$. The noise variance is increased of $\frac{1}{s}$ on the conjugated quadrature.

The Wigner function of squeezed vacuum can be written, in the case where $\theta = 0$, as:

$$W_{\hat{S}|0\rangle}(x,p) = \frac{e^{-\frac{1}{2\sigma_0^2}\left(e^{-2\xi}p^2+e^{2\xi}x^2\right)}}{2\pi\sigma_0^2} \tag{I.6.10}$$

Wigner functions of several squeezed states are given in Fig. I.6.

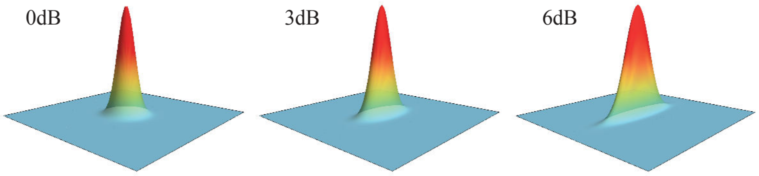

Figure I.6: Wigner functions of vacuum, 3 dB- and 6 dB-squeezed vacuum states.

Two-mode squeezed vacuum

This particular two-mode state is obtained when mixing two single-mode squeezed vacuum states on a 50/50 beam-splitter. Sometimes called "EPR-entangled" state, it can be written in the form:

$$|\Psi\rangle = (1-\Lambda^2)^{1/2}\sum_{n=0}^{\infty}\Lambda^n|n\rangle_s|n\rangle_i \tag{I.6.11}$$

and exhibits photon number correlations between the two modes.

I.6.4 Cat state

The famous thought experiment of Erwin Schrödinger [41] underlines the strangeness of quantum mechanics, in which theoretically a macroscopic state, as a cat, could be in a quantum superposition. The experiment involves entanglement between an atom obeying to the laws of quantum mechanics and a cat dead or alive. The overall system is inside a black box, avoiding any measurement that could be performed by the observer. A simplified version mainly used in quantum physics considers only the cat part. A "cat-like Schrödinger state" usually refers to the superposition of two classical macroscopic states. In Chapter VII, we will come back to the foundation of the idea and try to reproduce the entanglement of the though experiment, whereas in Chapter V, we will only consider cat-like states as superposition of classical states. In quantum optics, as coherent states are seen as quasi-classical states, an analogy to this thought experiment would be to have a coherent-state superposition defined as:

$$\begin{aligned}|\mathrm{Cat}+\rangle &= \frac{1}{N_+}(|\alpha\rangle + |-\alpha\rangle) = \frac{2}{N_+}e^{-|\alpha|^2/2}\sum_{n=0}^{+\infty}\frac{\alpha^{2n}}{\sqrt{2n!}}|2n\rangle \\ |\mathrm{Cat}-\rangle &= \frac{1}{N_-}(|\alpha\rangle - |-\alpha\rangle) = \frac{2}{N_-}e^{-|\alpha|^2/2}\sum_{n=0}^{+\infty}\frac{\alpha^{2n+1}}{\sqrt{(2n+1)!}}|2n+1\rangle\end{aligned} \tag{I.6.12}$$

with $N_\pm = \sqrt{2(1\pm e^{-2|\alpha|^2})}$ the normalization factor.

Depending on the phase between the two components, the cat can either be called "even" or "odd". This is due to the resulting parity of the photon number components due to the superposition. Indeed $|\mathrm{Cat}+\rangle$ can be written as a sum of even photon number state and is thus called even cat states whereas its counterparts is called odd.

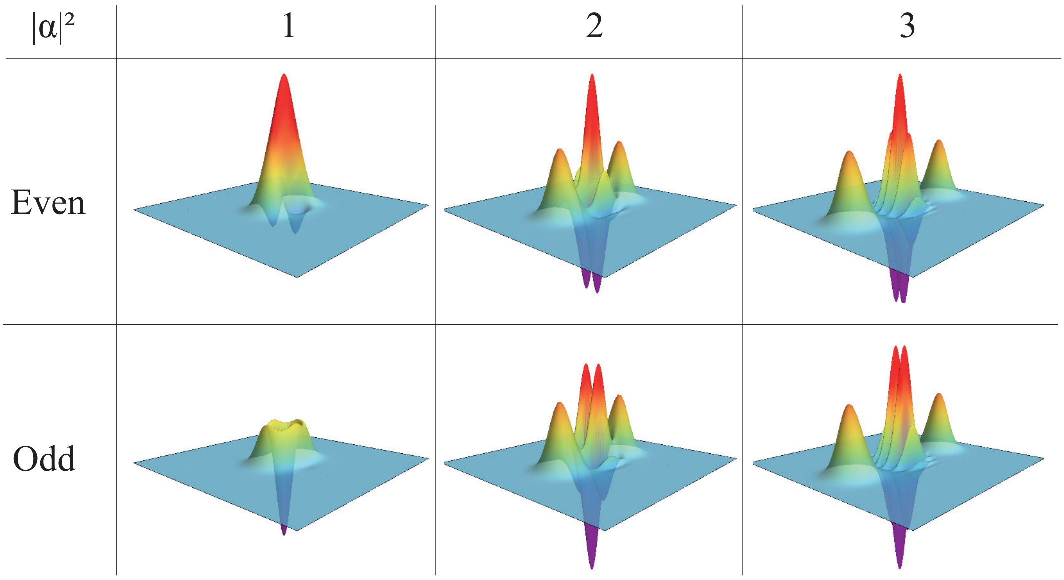

Figure I.7: Wigner function of cats states. The top row is for even cat states, the lower one is for odd cat states. The first colum gives the mean photon number $|\alpha|^2$ from 1 to 3.

Their Wigner functions are of the form:

$$W_{|\mathrm{Cat}\pm\rangle}(x,p) = \frac{e^{-\frac{x^2+p^2}{2\sigma_0^2}}\left(\pm\cos(\frac{2\alpha p}{\sigma_0}) + e^{-2\alpha^2}\cosh(\frac{2\alpha x}{\sigma_0})\right)}{2\pi\sigma_0^2\left(e^{-2\alpha^2}+1\right)}. \tag{I.6.13}$$

They are represented in Fig. I.7. The size of a cat states scales as the mean photon number $|\alpha|^2$.

I.6.5 Squeezed cat state

Squeezed cat states are states resulting from the action of the squeezing operator on a cat state. They will be experimentally generated and studied later in the manuscript. The squeezing operation is a gaussian operation, and therefore does not introduce additional non-gaussianity features on the state. The Wigner function of such states can be written as:

$$W_{\hat{S}|Cat\pm\rangle}(x,p) = W_{|Cat\pm\rangle}(xe^{\xi}, pe^{-\xi}). \tag{I.6.14}$$

Such states are interesting as the squeezing operation allows one to reduce the mean photon number without changing the maxima values of the Wigner function, i.e. the contrast of the oscillations in phase-space. The decoherence of a cat state can therefore be reduced by squeezing its means photon number while the Wigner function negativity, signature of strong non-classicality, is preserved. This phenomenon will be deeply studied in Chapter V.

I.7 Conclusion

In this chapter we briefly introduced the optical field quantization and defined the resulting quadrature operators. As this thesis is based on the combination of discrete-like and continuous-like types of variable in quantum information, we have shown the two descriptions that can be used for a quantum state, i.e. the density matrix and the Wigner function. Definitions of useful parameters and operators were given, as well as a list of quantum states that will be used in the following work. To generate such quantum states, and to experimentally build the useful operators, one has to use specific tools. These experimental tools will be described in the next chapter.

II | Experimental tools

Introduction

In this chapter we will review several tools used in the experiments realized during this thesis.

Firstly, non-linear materials are one of the main ingredients used to generate optical quantum states. In these materials, parametric conversion can be used to initially get photon-number correlations or squeezing at their output. In this work, non-linear crystals are inserted into resonant cavities realizing optical parametric oscillators.

Secondly, once such quantum states are generated, the detection plays an important part to characterize their quantum features. A section of this chapter will be devoted to a typical continuous-variable detection scheme: the homodyne detection. This very efficient detection enables to measure the quantum fluctuations of an optical field.

Finally, another requirement is the implementation of path stabilization and mode-filtering via resonant cavities. For this we will describe the recent improvement made on the setup to enhance the long-term stability, via configurable micro-controller locking [42].

Contents

II.1 Optical parametric oscillators 22
  II.1.1 Spontaneous parametric down-conversion 22
  II.1.2 Principle of an optical parametric oscillator 23
  II.1.3 Phase matching 24
  II.1.4 Mode-filtering 24
  II.1.5 OPO specifications 25
  II.1.6 Phases 26
II.2 Homodyne detection 27
  II.2.1 Tomography principle via homodyne detection 27
  II.2.2 Temporal mode 29
II.3 Locking methods 31
  II.3.1 Micro-controller based locking 32
  II.3.2 Arduino 37
II.4 Conclusion 38

II.1 Optical parametric oscillators

In this section we will quickly review the main principles of parametric down-conversion, and apply them to parametric oscillators. We will also give the experimental specification of the devices used during this PhD work.

II.1.1 Spontaneous parametric down-conversion

In our experiments, we use a continuous-wave Nd:YAG laser, with two outputs, one at 532 nm that we will use as a pump laser, and another at 1064 nm that will be used as a seed to lock the different paths and cavities and as local oscillator for the homodyne detection. The green laser output is obtained via a doubling of the infrared beam thanks to an external cavity. This laser is sent onto non-linear crystals where a pump photon at 532 nm can be converted into two photons (signal and idler) at 1064 nm, as sketched in Fig. II.1(a). This down-conversion process only happens when two conditions are fulfilled:

- the energy conservation: $\omega_p = \omega_i + \omega_s$
- the momentum conservation (phase-matching): $\vec{k}_p = \vec{k}_i + \vec{k}_s$.

To fulfill the phase-matching condition, it is necessary to have birefringence in the medium. The tailoring of the birefringence can allow to reach the relation: $n_p\omega_p \approx n_i\omega_i + n_s\omega_s$. The Hamiltonian of the process can be written as:

$$\mathcal{H} = i\frac{\hbar g}{2}\hat{a}_s^\dagger \hat{a}_i^\dagger \hat{a}_p + h.c. \tag{II.1.1}$$

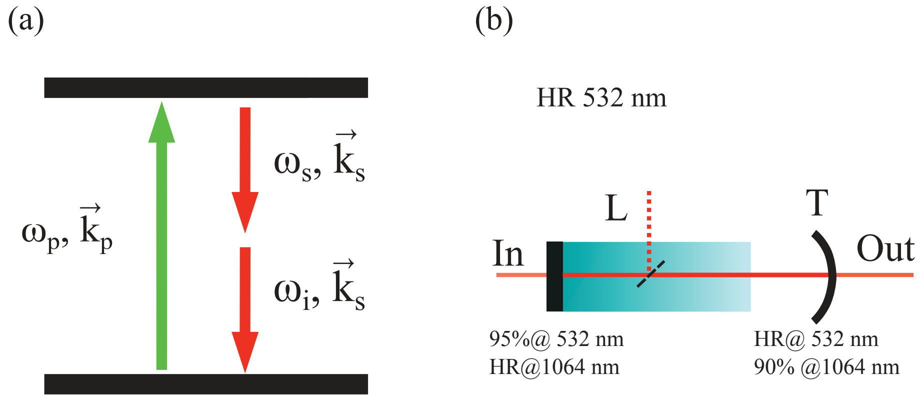

Figure II.1: (a) Scheme of the spontaneous parametric down-conversion phenomenon, where a pump photon with frequency ω_p and wave vector $\vec{k}_p$ is converted into two photons, signal and idler, with frequencies ω_s and ω_i, and wave vector $\vec{k}_s$ and $\vec{k}_i$ respectively. The specific case of degenerate wavelengths $\omega_s = \omega_i$ is represented. (b) Scheme of the OPO cavity and of the specific parameters of the cavity mirrors for both pump and signal wavelengths. L stands for the losses of the cavity and T for the transmission of the output coupler. HR stands for highly-reflective, with reflexion above 99%. The other facet of the crystal is anti-reflection coated.

In our system we will always use the degenerate wavelengths for signal and idler. By approximating the pump by a coherent state $|\alpha_p\rangle$, it is possible to write the annihilation operator evolution as:

$$\hat{a}(t) = \hat{a}(0)ch(\kappa t) - \hat{a}^\dagger(0)sh(\kappa t). \tag{II.1.2}$$

This gives the quadratures of the output field evolution to be:

$$\begin{aligned} \hat{x}' &= e^{-\kappa t}\hat{x} \\ \hat{p}' &= e^{\kappa t}\hat{p}. \end{aligned} \tag{II.1.3}$$

by writing $\xi = \kappa t = g\alpha_p t$, we find back the squeezing operator seen in Chapter I:

$$\hat{S}(\xi) = e^{\frac{\xi}{2}(\hat{a}_i\hat{a}_s - \hat{a}_i^\dagger\hat{a}_s^\dagger)}. \tag{II.1.4}$$

Physically, t will be related to the interaction time of the photon with the non-linear crystal.

In this work, the process occurs in a resonant cavity, as detailled in the following.

II.1.2 Principle of an optical parametric oscillator

An optical parametric oscillator (OPO) is a cavity in which a nonlinear crystal is inserted. The presence of the cavity makes the process much more efficient, as the probability for a pump photon to be converted is increased by the cavity-enhancement power. The cavity also "cleans" the output modes and allows a well-definition in frequency and space of the output state. It also induces a threshold effect, i.e., a pump power at which the oscillation can start.

One can write equations about what is happening during a single round-trip, for an triply-resonant OPO (for pump, idler and signal), and deduce the mode loop equations under the assumption of low loss L and low transmission T [26, 43].

$$\begin{aligned} \tau\frac{d\hat{a}_s}{dt} &= -\frac{T+L}{2}\hat{a}_s + 2g\mathcal{L}\hat{a}_p\hat{a}_i^\dagger + \sqrt{L}\hat{a}_{sL} + \sqrt{T}\hat{a}_{sIn} \\ \tau\frac{d\hat{a}_i}{dt} &= -\frac{T+L}{2}\hat{a}_i + 2g\mathcal{L}\hat{a}_p\hat{a}_s^\dagger + \sqrt{L}\hat{a}_{iL} + \sqrt{T}\hat{a}_{iIn} \end{aligned} \tag{II.1.5}$$

where $\mathcal{L}$ is the length of the cavity.

From such equations the threshold power:

$$P_{th} = \frac{(T+L)^2}{16g^2\mathcal{L}^2} \tag{II.1.6}$$

can be extracted, which is the pump power when the gain compensates the losses and some oscillation process starts. Importantly, this threshold expression shows that it scales as T^2, the square of the output coupler transmission.

Another important parameter used to characterize an OPO is its escape efficiency, i.e., the probability that a generated photon has to be transmitted by the OPO. It can be linked to the intra-cavity losses, and the transmission by the expression

$$\eta = \frac{T}{T+L}. \tag{II.1.7}$$

This parameter directly defines the maximal amount of squeezing that can be achieved close to the threshold, or the maximal purity one can obtain in the case of heralded single-photon generation, which will be developed in Chapter IV. To achieve quantum states with high purity, an OPO must have its escape efficiency close to unity. In our OPOs, this escape efficiency is around $\eta_{OPO} \sim 0.96$. For given intracavity losses, increasing the escape efficiency requires to increase the transmission of the output coupler, at the expense, as seen just before, of a quadratic increase in the threshold.

II.1.3 Phase matching

Two situations to fulfill the momentum conservation requirement can be found depending on the type of crystal and its birefringence properties.

Type-I phase matching: Single-mode squeezed vacuum

In this case, the pump is polarized along the ordinary axis of the crystal, and it leads to the generation of signal and idler, on the extraordinary axis: $o \longleftrightarrow e + e$. The emitted photons are therefore degenerate in polarization. The squeezing operator can be re-written, for photon pairs of the same wavelength, in the form:

$$\hat{S}(\xi) = e^{\frac{\xi}{2}(\hat{a}^2 - \hat{a}^{\dagger 2})}. \tag{II.1.8}$$

This operation therefore leads to single-mode squeezed vacuum of the form:

$$|\Psi\rangle = (1-\lambda^2)^{1/4} \sum_{n=0}^{\infty} \binom{2n}{n}^{\frac{1}{2}} \left(\frac{\lambda}{2}\right)^n |2n\rangle \tag{II.1.9}$$

with $\lambda = \tanh|\xi|$. This OPO will be used for the generation of continuous-variables states, such as squeezed light or Schrödinger cat-like states.

Type-II phase matching: Two-mode squeezed vacuum

In this case, the pump is polarized along the extraordinary axis of the crystal, and it leads to the generation of signal and idler, on the two different axes: $e \longleftrightarrow o + e$. The output infrared photons are thus orthogonally polarized. This situation leads to two-mode squeezed-vacuum of the form:

$$|\Psi\rangle = (1-\Lambda^2)^{1/2} \sum_{n=0}^{\infty} \Lambda^n |n\rangle_s |n\rangle_i. \tag{II.1.10}$$

The two modes can be separated with their polarization, and the resulting modes are EPR-entangled, exhibiting photon number correlations. This situation will be the one we use most of the time in order to create discrete-like states such as Fock states.

II.1.4 Mode-filtering

The free spectral range of the OPO is smaller than the acceptance window of the phase matching, leading to the emission of pairwise correlated photons but with separated spectral modes $f_0 + \Delta f$ and $f_0 - \Delta f$ as shown in II.2(a), where the emission spectrum

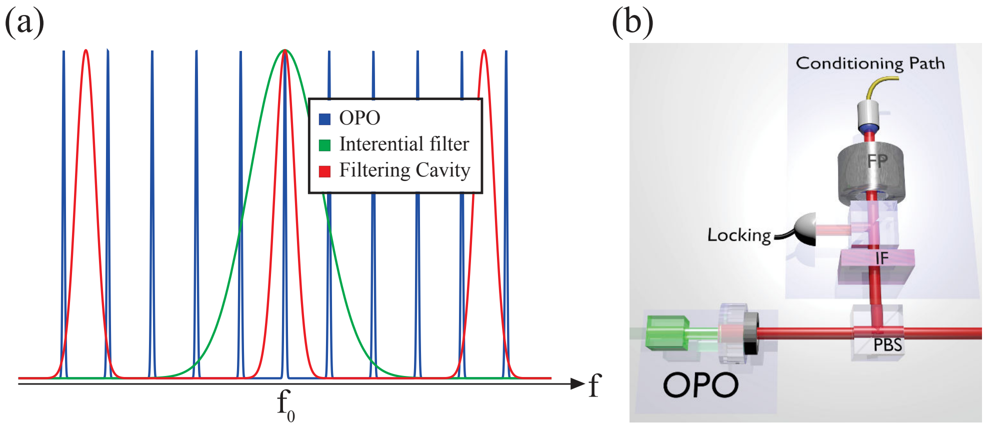

Figure II.2: (a) Frequency modes at the output of the OPO cavity (in blue), the interferential filter (in green), and the high-finesse cavity (in red). The action of the two filtering elements results in a 25 dB rejection of the non-degenerate modes.(b) Scheme of the experimental filtering path, where the beam is first sent to an interferential filter (IF) and then to a Fabry-Pérot cavity (FP). The resulting beam is then coupled to a single-mode fiber.

is schematized. In order to implement conditioning based on single photon detection of the idler mode, and to detect on the same mode the signal photons, the non-degenerate modes due to the OPO cavity must therefore be filtered out. To do so, we first implement a broad filtering of the conditioning path via an interferential filter of 0.5 nm bandwidth. Its effect is plotted in green in II.2 (a). We then send the conditioning mode to a homemade Fabry-Pérot cavity of 0.4 mm length, with a 330 GHz free spectral range, and 300 MHz bandwidth (the finesse of this cavity is therefore around 1000). The cavity effect is plotted in red color in II.2(a). The combination of the two aforementioned filtering elements leads to 25 dB of rejection of the non-degenerate modes. However this filtering path, shown in II.2(b) also induces optical losses. After the coupling of the cavity output to a single-mode fiber, the overall transmission of the conditioning path is 50%.

II.1.5 OPO specifications

As shown in Fig II.1 (b), our OPOs are made of a semi-monolithic cavity, where one of the mirror is coated on the OPO itself and is highly reflective for 1064 nm while being 95% reflective for the pump laser. The crystal is anti-reflection coated for both wavelengths on the opposite side. The other curved mirror is on the contrary HR-coated for 532 nm and has a transmission of $T = 90\%$ for signal and idler at 1064 nm. Both OPOs are based on $KTiOPO_4$ material, shortened as KTP. The type-I crystal is made of periodically-poled KTP crystal (PP-KTP), while the type-II is made of KTP crystal. The mount on which the crystal is set is shown in II.3(a) and, a picture is given in II.3(b). To ensure the resonance of signal, idler and pump, a Peltier element is set on the crystal for temperature tuning. Our OPO being semi-monolithic, it is not possible to tune the angle of the crystal to achieve such resonance. In the particular case of the type-II OPO, the idler and signal beams are non-degenerate. Therefore a

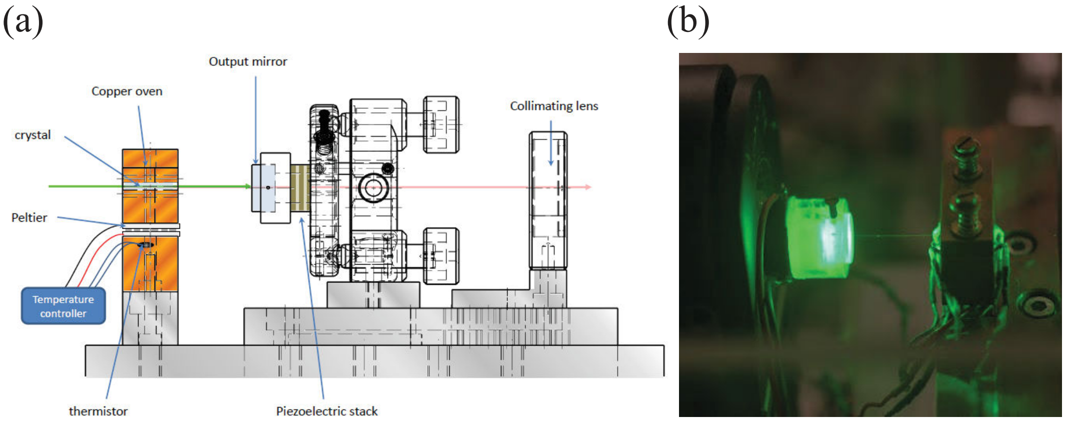

Figure II.3: (a) Scheme of the mount of the type-I OPO. (b) Picture of the similar type-II OPO mount.

resonance for the three beams, the pump, the idler and the signal must be achieved. In this endeavor, the wavelength of the laser have additionnally to be adjusted. Changing the point on which the light is focused can also help to find stable configurations. The free spectral range of our OPOs is equal to $\Delta\omega = 4.3$ GHz, and its bandwidth are around 50 MHz. A collimating lens is set at the output of the OPO to have a size of beam around 1 mm. The type-I phase-matched OPO has been used before this thesis to generate squeezed vacuum of 10.5 dB of noise reduction at 5 MHz central frequency, as shown in the measured noise spectra given on Fig. II.4 [44].

II.1.6 Phases

In order to measure phase-dependent states, it is necessary get a phase reference. For this purpose, an infrared seed beam is sent through the OPO cavity, to lock the relative phase between the pump and the idler and signal beams, via the resulting amplification of the infrared field. By using a piezoelectric transducer (PZT) at the input of the OPO, the phase of the seed beam can be controlled, in order to reach maximum amplification. However locking on the maximum of the amplification of the seed is precise at a π offset. Indeed if we write the phase equation of the OPO for the amplification/de-amplification process:

$$\Delta\varphi = \varphi_p - \varphi_s - \varphi_i. \tag{II.1.11}$$

Our signal and idler having the same frequency and being issued from the same seed, they experience the same dephasing:

$$\Delta\varphi = \varphi_p - 2\varphi_{s,i}. \tag{II.1.12}$$

To get amplification, one needs to have: $\Delta\varphi = \frac{\pi}{2}$, which is the targeted locking value. However, this point is defined at a π constant offset on the signal phase. Indeed, the π dephasing counts twice for idler and signal and is finally equivalent to a 2π phase shift on the overall phase. Thus, if the PZT gets out of range and relocks automatically, it can relock at a point which can be dephased of π for the signal.

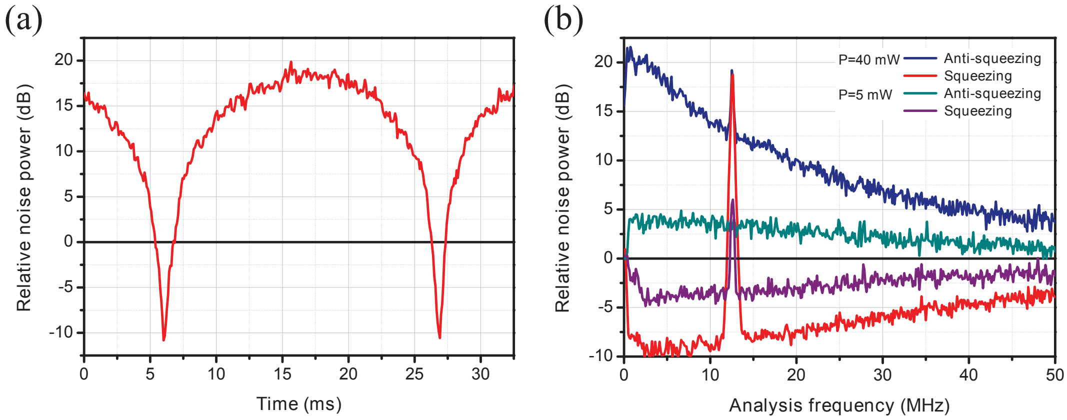

Figure II.4: Measured noise spectra of squeezed vacuum states generated by the type-I phase-matched PP-KTP OPO. All the data are recorded by a spectrum analyzer with a resolution bandwidth of 300 kHz and a video bandwidth of 300 Hz. Spectra are normalized to the shot noise limit.(a) Noise variance as a function of the local oscillator phase, at a pump power of 40 mW and an analysis frequency of 5 MHz. (b) Broadband squeezing up to 50 MHz for a pump power of 5 mW and a pump power of 40 mW. The peak at 12 MHz results from the electro-optic modulation used to lock the cavities.

This offset has no consequences on the detection because the homodyne detector that we used and which will be developed in the next section is π-periodic, but it can be sometimes noticed experimentally by a "jump" of π on the fringe signal.

This phase reference via amplification process enables us to get a reference to implement phase-dependent tomography process via homodyne detection. We will detail in the next section this type of continuous-variable detector.

II.2 Homodyne detection

In order to characterize a quantum state, two categories of detectors exist. Photon detectors such as avalanche photodiodes (APDs), superconducting single photon detector (SSPD), transition edge sensors (TES),..., are sensitive to the presence or absence of a photon or their photon number. However these detectors are insensitive to the phase features of the quantum state. Homodyne detection is a scheme used in the field of continuous variable, which has the advantages of being very efficient and sensitive to the phase space structure of the state. This detector records the quantum fluctuations of the optical field [39].

II.2.1 Tomography principle via homodyne detection

How does it work?

The quantum state $\hat{\rho}_s$ interferes with a laser beam called local oscillator $|\alpha_{LO}e^{-i\theta}\rangle$, on a 50/50 beam splitter (Fig II.5 (a)). In terms of operator this operation can be translated as:

$$(\hat{a}_S, \hat{a}_{LO}) \rightarrow (\frac{\hat{a}_S + \hat{a}_{LO}}{\sqrt{2}}, \frac{\hat{a}_S - \hat{a}_{LO}}{\sqrt{2}}). \tag{II.2.1}$$

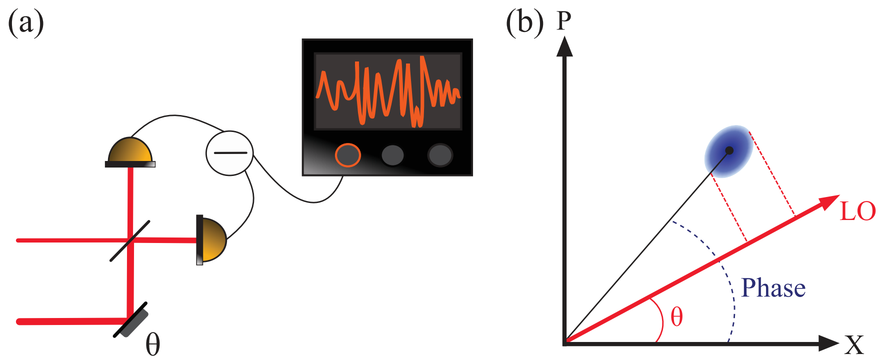

Figure II.5: (a) Experimental scheme of optical homodyne detection (b) Homodyne detection effect in the Fresnel plane: the state is projected onto the local oscillator (LO). By sweeping the phase of the later, all the quadratures values can be measured

The two outputs of the beam splitter are then sent on two photodiodes, whose photocurrents are subtracted. Under the assumption of a bright local oscillator field, the operator of the local oscillator can be replaced by its expected value α_{LO}. Assuming a perfect detection efficiency, i.e. each photon gives an electron, the resulting photocurrent can be writen as:

$$\Delta i \propto \Delta \hat{n} = \hat{a}_S \hat{a}^{\dagger}_{LO} + \hat{a}^{\dagger}_S \hat{a}_{LO} \approx |\alpha_{LO}|(e^{-i\theta}\hat{a}_s + e^{i\theta}\hat{a}^{\dagger}_s)) \tag{II.2.2}$$

where θ is the phase of the local oscillator. The detected photocurrent is thus directly proportional to the measurement of the quadrature $\hat{Q}_\theta = \hat{X}cos\theta + \hat{P}sin\theta$. This detection is phase sensitive, and by recording the quadrature values for each phase of the local oscillator (Fig II.5 (b)), it is possible to reconstruct via a maximum likelihood tomography the full density matrix of the quantum state.

Detection efficiency

The overall efficiency of our detection is 85%. This is firstly due to the efficiency of our photodiodes (Fermionics,FD500N-1064 - $\eta_{PD} \approx 98\%$). The visibility of the fringes between the signal and the local beam also induces some losses ($\eta_{Vis} = V^2 = (99\%)^2$). Finally, the electronic noise of the homodyne detection can be translated in terms of equivalent losses. Our electronics exhibits 20 dB between vacuum shot noise at the central frequency and electronic noise. By taking an overall 50 MHz bandwidth, the equivalent efficiency can be calculated to be $\eta_{noise} = 96\%$ [45].

On top of these losses intrinsic to the detection system, we have to add the losses due to the propagation of light through optical elements. The total transmission from the OPO output to the detection system, $\eta_{prop} = 93\%$ is mainly limited by an optical isolator used to prevent backscattering photons from the bright local oscillator beam.

Maximum-likelihood algorithm

Shortened as "MaxLike" algorithm, this reconstructing tool, widely used in quantum optics experiments, enables to find the closest density matrix compatible with the measured quadrature values [46, 47]. The quadratures values x_k corresponding to an angle θ_k of the local oscillator are rearranged in terms of occurrences frequencies f_k. Using these data sets, we construct the iteration operator:

$$\hat{R}(\hat{\rho}) = \sum_k \frac{f_k}{Tr[\hat{\Pi}(\theta_k, x_k)\hat{\rho}]}\hat{\Pi}(\theta_k, x_k) \tag{II.2.3}$$

where $\hat{\Pi}(\theta_k, x_k)$ is the projector $|x_k, \theta_k\rangle\langle x_k, \theta_k|$. Initialized by the identity matrix, this operator is used to iterate the generation of the density matrix

$$\hat{\rho}^{(i+1)} = N(\hat{R}\Big(\hat{\rho}^{(i)})\hat{\rho}^{(i)}\hat{R}(\hat{\rho}^{(i)})\Big) \tag{II.2.4}$$

where N is the normalization factor in order to keep the trace equal to 1. When the algorithm converges $Tr[\hat{\Pi}(\theta_k, x_k)\hat{\rho}] \rightarrow f_k$ and therefore $\hat{R}(\hat{\rho}) \rightarrow \mathbb{1}$, giving the closest, i.e. the most likely, density matrix. As the MaxLike algorithm returns the density matrix, it is then easy to calculate the associated Wigner function.

This reconstruction process always gives physical states thanks to always positive diagonal elements. It also enables to easily correct from detection losses, by changing the measurement operator [26]. Moreover this reconstruction process is also the most accurate. Easy to implement, this algorithm requires at least 50 000 acquisitions for single-mode tomography and 100 000 for two-mode reconstruction. Assumptions on the size of the Hilbert space must also be given to the algorithm. Typically we will choose a size of 10 for most of the states, and will limit the chosen size to 7 for single-photon Fock states, in order to save iteration time during two-mode reconstruction processes.

In the context of heralded quantum states, the homodyne detection is triggered on the detection of a conditioning event. Therefore, the temporal structure of the quantum state comes into play.

II.2.2 Temporal mode

The temporal mode of a photon can be seen as the probability of the photon to be emitted at a certain time. It can also be seen as the "duration" of the photon. The temporal mode of a photon emitted by an OPO is related to the OPO cavity bandwidth. Indeed it corresponds to the "lifetime" of the photon inside the cavity, before it gets out. It can be written [26]:

$$f(t) = \sqrt{\pi\gamma}e^{-\pi\gamma|t|} \tag{II.2.5}$$

where γ is the OPO bandwidth. This mode is plotted in Fig II.6(a), for a 50 MHz bandwidth OPO cavity.

In the pulsed regime, the time of emission of the photon can be precisely defined, thanks to the repetition frequency of the pump laser. One particularity of continuous-wave experiments is the difficulty to localize in time a photon probabilistically emitted by the OPO.

Heralded generation

In the case of heralded experiments, where the detection of an idler photon heralds the generation of its correlated counterparts, it is possible to use a temporal mode

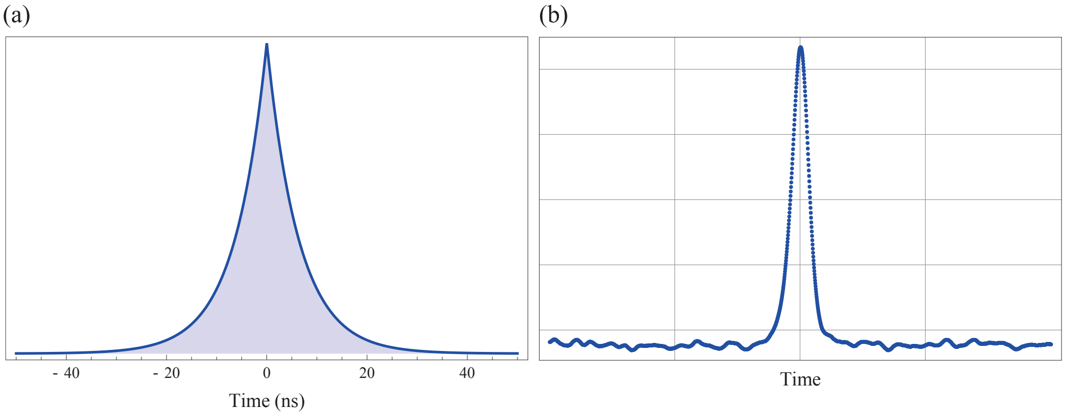

Figure II.6: (a) Temporal mode of a single photon out of an OPO cavity of 50MHz bandwidth. (b) Acquisition of the variance on each time for several samples of the homodyne detection signal, corresponding to a heralded single photon generation.

based method to localize the generated state. To localize precisely the time of photon emission, given a heralding event, one can simply check the variance of the homodyne signal [48]. This experimental acquisition is shown for a heralded single photon in II.6(b). Indeed the variance of a single photon, or any other states, is higher than the one of the vacuum. Therefore, in experiments, we make several acquisition of the homodyne signal for which we compute the variance. The maximum of the variance enables us to localize the center of the temporal mode.

Extracting quadrature values

Given the knowledge of the shape of the temporal mode, and of the emission time, quadrature values of the generated state can be extracted via homodyne detection. Given $x(t)$ the recorded signal of the homodyne detection, its integration by the temporal mode gives the measurement of the quadrature value:

$$x_\theta = \int x(t) f(t) dt. \tag{II.2.6}$$

This operation can be realized numerically, or directly by shaping the local oscillator mode.

Combining several OPOs

For experiments involving several OPOs, like the generation of hybrid entanglement, in order to achieve indistinguishability between the emitted photons, it is necessary to realize a matching of the temporal mode of the photons. This has been achieved by building the two OPO cavities with the closest possible geometry and coupler transmission. By measuring the temporal modes of each OPO cavity output and numerically computing the overlap, a value of 99% is found, showing the strong similarity between the emitted photons. By using the same filtering cavity to filter out the non-degenerate modes of both OPOs, we additionally ensure to get similar filtering on the conditioning path of our setups. Given a heralding event detected at the output of the conditioning path, the two generated states will therefore be in the same temporal mode.

Playing with the temporal mode can also highlight interesting effects on state generation as described in Chapter IV.

We have introduced how to detect quantum states generated with continuous-wave OPOs. Homodyne detection being sensitive to the phase of an optical field, it is necessary to ensure the path stability of the overall setup. In the following section we will describe our methods in order to ensure the locking of relative optical path, phases and optical cavity lengths.

II.3 Locking methods

Experimental setups in optics usually rely on various locking for path or cavity stabilizations. In our experiments, a seed beam is sent for 50 ms, during which we lock all the necessary optical paths by sending a voltage to piezo electric transducers (PZTs). Then, the seed beams are switched off, using mechanical shutters, and the positions of the PZT are hold for 50 ms, during which our quantum states are generated and detected.

Various methods based on analog locking have been extensively studied. These lockings require an error signal, which is fed into an analog proportional-integral controller (PI) towards a PZT to ensure a continuous and fast correction of the transducer.

We will first give a few examples and a quick description of techniques used to generate such an error signal in our experimental setup:

- The Dither and Lock method [49] consists in the low frequency modulation (a few kHz) of the length of an optical path via a PZT. We then detect and demodulate the signal, with a lock-in amplifier. This method could be used in order to lock the phase between the pump and the seed of the OPOs, or other relative phases in the experimental setup.

- In the Pound-Drever-Hall method [50], used to lock cavities, the modulation frequency is higher than the bandwidth. A beating note between the mean field and the side bands is obtained via phase modulation of the signal. When the cavity is at resonance the demodulation leads to a zero signal. When the cavity is out of resonance, the two lateral bands do not have the same phase, and thus lead to an amplitude modulation. This creates an error signal that can be locked. This method is used to lock the OPOs cavities, by using the laser modulation at 12 MHz. Despite the fact that 12 MHz is smaller than the bandwidth of our OPO cavities, the parasite bands that could appears are small enough, and we can implement a correct locking of the system.

- The tilt-locking [51] method also relies on the interference of the mean field and a phase reference directly reflected by the cavity. However, the phase reference is given here by spatial modes and not sidebands. For this purpose, the signal is slightly misaligned to ensure the presence of the TEM01 mode, coexisting with the TEM00. The TEM01 will be totally reflected by the cavity, its lobes exhibit a π phase difference. The two modes are then sent to a photodiode with two detection area. When at resonance the interference of TEM00 and TEM01 will then give the same intensity on both photodiodes and the photocurrent difference will be zero. When the cavity is out of resonance, the phase of TEM00 is changing, but not the TEM01 one, leading to a difference in each part of the photodiode, and a non-zero photocurrent. This signal has a different sign depending on the side of the resonance. This leads to an error signal that can be fed into a PI. This locking method was employed to lock the high-finesse filtering cavity which is at the direct 1064 nm output of the laser. This cavity is used to filter out all the possible parasite spatial modes that would exist in the laser output and ensure a "cleaned" local oscillator for the homodyne detection as well as all the seed beams used to lock cavities and paths.

However these techniques require some materials, such as lock-in amplifier, PI, and do not contain any automatic relocking features when the PZT transducer is out of range or when a strong vibration or the cutting of the light produce an unlocking of the signal. For complicated experiments in quantum optics, where multiple locking are required (up to 9 in some of our experiments), it is necessary to achieve robust and good phase lockings.

In this endeavor we have implemented the locking of several optics system by the use of only cheap micro-controllers (ADUC7020 and Arduino Due), sometimes coupled with a PI [42], as now detailed.

II.3.1 Micro-controller based locking

The idea of a micro-controller locking is to avoid the use of an error signal. For this purpose, it is possible to use a maximum (or minimum) searching algorithm. In this algorithm, the micro-controller registers an initial value of the signal. The microcontroller then sends a voltage to the PZT, of a certain step value (the step can be adapted to achieve either fast or very precise locking). The micro-controller registers then the new value of the signal and compares it to the previous one. If the voltage is higher (lower), it means the maximum (minimum) has not been reached, the microcontroller register this value and keep on incrementing the voltage sent to the PZT by one step. If the voltage is smaller, it means the previous value was already the maximum, the direction of the step is then reversed.

In the following, we will show some experimental applications of this simple algorithm, by using an Analog Device ADUC7020 micro-controller.

Phase locking of an interferometer

A phase locking system can be applied to a certain number of elements. For example, such system will be used in our experiments to lock an optical path, an interferometer, or the local oscillator phase of the homodyne detection. In order implement such locking, one needs to only have access to an interference fringe signal. In the case of an OPO, the amplification-deamplification process occuring between the pump and a signal beam creates an interference-like signal, depending on the phase of the seed beam. It is then easy to implement a maximum, or minimum locking algorithm, and lock the fringes at a maximum or a minimum point (or any phase value by adding an offset, see in Chapter VI).

In the following we will show experimental results of the locking of a 1.5 meter long Mach-Zender interferometer, using a maximum-searching algorithm. Figure II.7(a) gives the scheme of the experimental setup as well as the flowchart of the algorithm in (b). The signal of the interference is recorded on the photodiode A, and shown in Fig II.7(c). A fast-Fourier transform algorithm is then performed on this signal in order to get the frequency spectrum of the locking, which is compared to a non-locked system, where the position of the PZT is manually adapted to stay close to the maximum. The spectra resulting from the two locking methods, for an acquisition time of 100s, are presented in II.7(d). The smallest angle that can be locked, is determined by the smallest step achievable i.e. the resolution of the ADC. Indeed at the equilibrium, only fluctuations larger than its resolution can be detected by the micro-controller. For the ADUC 7020, this resolution is of 12 bits. With a reference voltage of 2.5V, this leads to a minimal signal fluctuations $\delta_{ADC} = 2.5V/2^{12} \approx 0.61mV$, corresponding to a minimum detectable phase change $\Delta\theta_0$:

$$\Delta\theta_0 = N \times n \times 2\pi/2^{12} \approx 1.8^\circ \tag{II.3.1}$$

with N the step size, and n the number of periods for a full scanning. Experimentally, by optimizing the parameters of the lock, such as the step size ($N = 1$), the number of periods ($n \sim 1.5$), or the delay between two corrections (depending on the speed of the PZT), we obtained a standard deviation of 0.50 mV, corresponding to $\Delta\theta_0 = 1.7^\circ$ as shown in II.7(c).

Cavity Locking

Locking of low-finesse cavity can be applied by locking for example on the maximum of transmission of the resonant light. In order to lock such cavity, the maximum (or minimum) phase-locking algorithm must be complexified. Indeed, the position of the peak of resonance must be found in order to start the locking algorithm. To do that, we implemented one (or two- for high finesse cavities) voltage scanning, fed on the PZT of the cavity, to identify the rough voltage where the peak is localized. The microcontroller first sweeps the cavity length and subsequently defines a high and low threshold (Y_{th1} and Y_{th2}). It then sweeps again the length to reach an initial starting point above the high threshold. If the locked signal becomes smaller than the low threshold, the microcontroller will get out of the locking mode and go back to the scanning mode. Once this range is identified, the maximum (or minimum) locking algorithm can be triggered. This simple locking method can be enhanced by implementing some proportional feedback using more sophisticated programming. For instance, one can numerically calculate the corresponding derivative of the signal, or simply use the signal difference between the sequential steps, as the gain of the feedback signal. We call this method the PI-like algorithm.

The flowchart is presented in Fig II.8(a). We implemented such algorithm on one of our OPO cavities, with minimum-locking of the pump reflection. The finesse is around 100 for the pump light. The resulting signal acquisition is shown in Fig II.8(b). The simple maximum searching algorithm, and the PI-like method are compared with the

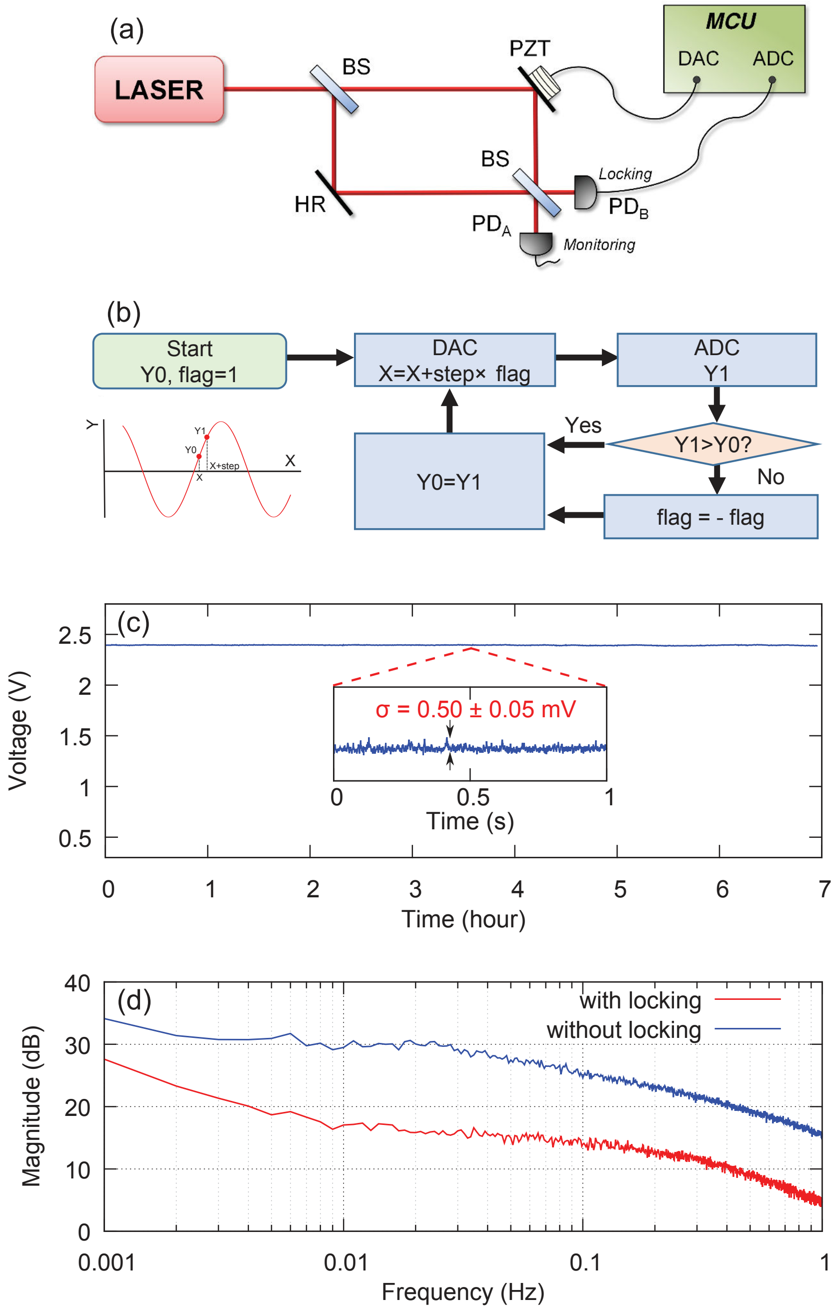

Figure II.7: (a) Experimental setup: locking a 1.5-meter-arm Mach-Zehnder interferometer with a microcontroller unit. HR stands for high-reflective mirror, BS for beam-splitter, PZT for piezoelectric transducer and PD for photodiode. (b) Flowchart of the program execution for the maximum-searching algorithm. (c) Long-term stability. The inset gives a one-second zoom and the associated standard deviation. (d) Noise spectrum at low frequencies with and without locking, acquired by processing fast-Fourier transform on the recorded signal of PD$_A$.

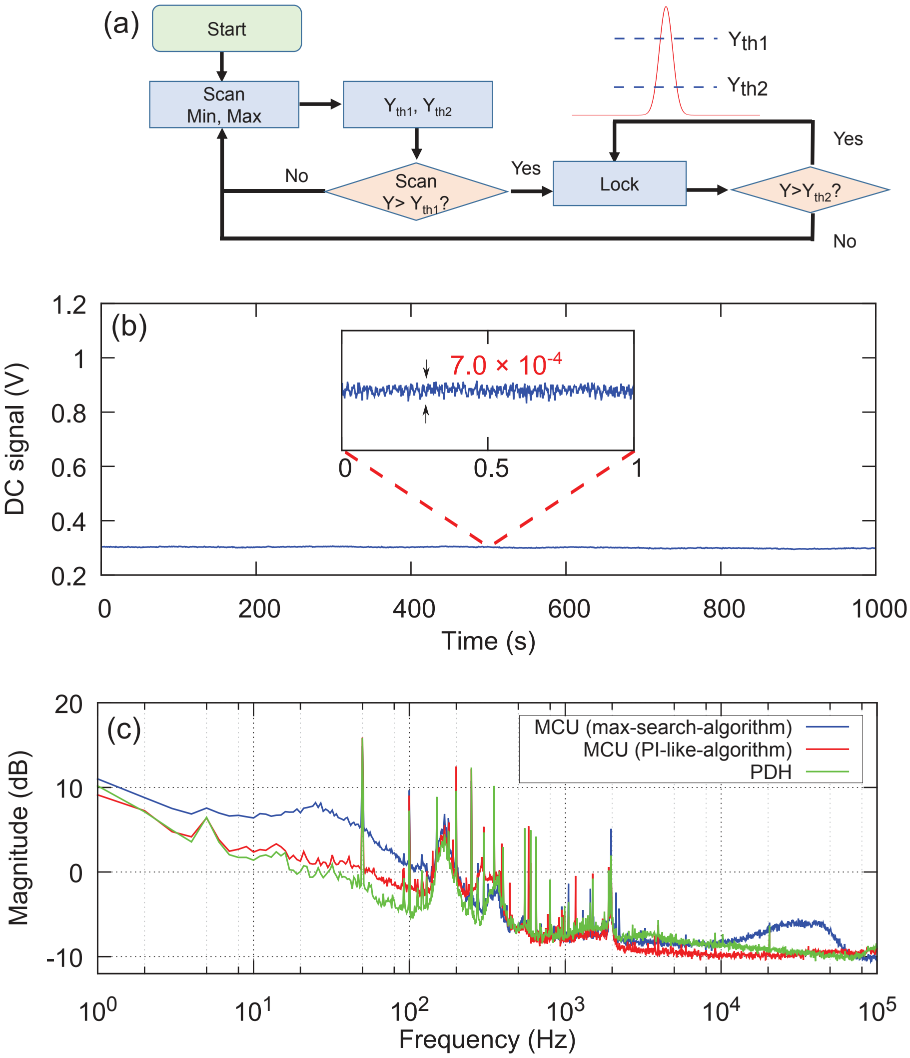

Figure II.8: (a) Flowchart of the program execution to lock a low-finesse cavity, including peak searching and automatic relocking. (b) Long-term stability. The inset gives a one-second zoom. The standard deviation is normalized to the cavity peak height. (c) Noise spectra for maximum-searching locking, PI-like locking and for locking with the standard analog Pound-Drever-Hall technique.

previously used Pound Drever Hall (PDH) method in Fig II.8(c). Using the PI-like algorithm, we obtain a standard deviation equivalent to the one obtained by PDH locking: 7.0×10^{-4} to compare with 6.6×10^{-4}. By using the simple maximum searching algorithm, the standard deviation: 8.0×10^{-4}, is still very close to the previous methods and can therefore be used in many applications.

High-finesse cavities

High finesse cavities (of finesse ≈ 1000) are used on our experiment to filter out parasitic modes. For example, the filtering cavity at the 1064 nm output of the laser enables to clean the laser from all spatial or spectral undesired modes. In order to filter out the non-degenerate modes of the OPO cavities, as previously explained, we also use micro-cavities, of a few mm long, to ensure the detection of a single photon on a well-defined frequency mode, for the generation of heralded quantum states.

To lock such cavities, we implemented the same type of algorithm developed for low-finesse cavities. However, due to the limited resolution of the DAC, it is not possible to use exactly the same algorithm. For a finesse of 1000 for example, $\frac{4096}{1000} \approx 4$ is the number of points that will cover the whole peak. This number is obviously not sufficient. To overcome this problem, we combine two 12-bits DAC in order to get a 24-bits DAC. Another way to see this, is that we use two different scanning voltages: a long scan (DAC1) to cover the whole range and localize roughly the peak position, and a shorter one (DAC0), to scan around the peak position and to lock the signal. The two outputs are summed up with different gains. As there is four DACs available in the microcontroller development board, this method is easy to implement without the need of any additional electronic building.

We give here an experimental application of such locking by locking the micro-cavity used for the heralding path filtering. A seed beam is sent through this cavity. The micro-controller first starts a long range scanning, where it finds a rough start point corresponding to the peak position. Then, a second smaller voltage is added to the starting point and is used in order to lock the cavity using the same algorithm as used for low-finesse cavities. The flowchart of the algorithm and locking process scheme are given in Fig. II.9(a) and (b). The resulting long-time acquisition of the locked signal is given in Fig. II.10(a). The simple maximum searching locking is enhanced by a PI-locking algorithm, and both methods are compared to an implemented Dither and Lock method (DTH). A fast-Fourier transform is performed on the three resulting signals and are shown in II.10(b). The measured standard deviation for one second 4.8×10^{-3} for the PI-like, being slightly higher than the DTH method: 5.6×10^{-3}. The maximum-searching algorithm gives 6×10^{-3}. For 15 minutes, the normalized standard deviation reaches 8×10^{-3}. These results show the suitability and efficiency of the microcontroller-based locking with high-finesse cavities.

Requirements for an adequate micro-controller

The requirements that are needed for such lockings are listed in the following. Firstly, it is very convenient to have several analog inputs and outputs. Implementing an analog to digital converter would require the need of synchronization systems that can take time and money. Several inputs and outputs also enable us to have several lockings on the same card. For example with the ADUC7020, it is possible to lock 2 OPOs (2 phase locking + 2 low-finesse cavity locking = 4 locking systems), or two high-finesse cavities with only one board. Also we wanted this micro-controller to be cheap, and it is: around 50 euros. The micro-controller must also be fast enough: the ADC and DAC are at 1 MHz, and the internal clock of the system is 60 MHz. This is sufficient enough for our applications as the main limitation of the locking is the PZT bandwidth, which is around a few kHz.

This micro-controller can also be coupled to an analog PI, in particular for cavity locking. In that case, the micro-controller is used to search the starting voltage, corresponding to the peak of the signal, and to start the PI system. Automatic relocking

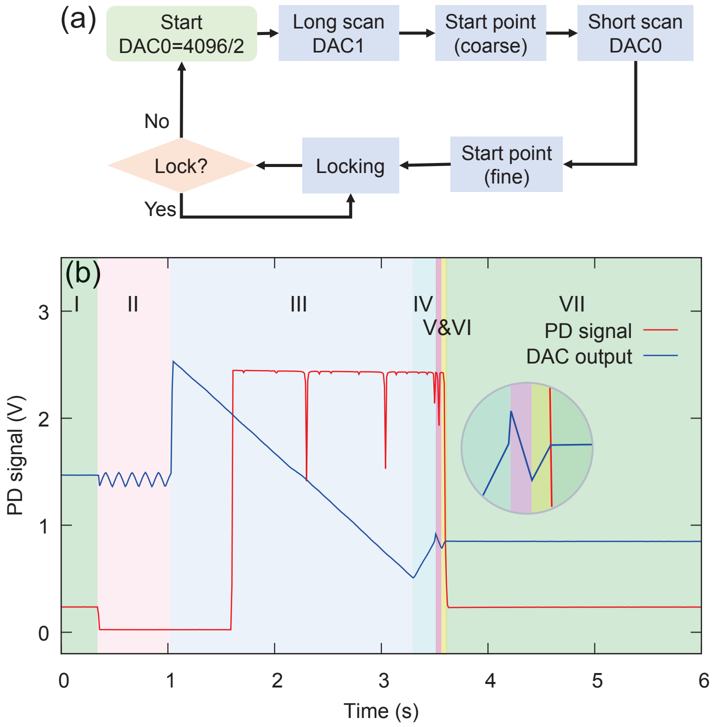

Figure II.9: (a) Flowchart of the program execution to lock a high-finesse cavity. This scheme includes two different scanning modes controlled by two outputs in order to use the full DAC resolution. (b) Experimental locking process of a cavity with a finesse equal to 1000. The light is measured in reflection. (I) Cavity is locked. (II) Light is blocked to disrupt the lock and the program goes thus to the short-scan mode.(III) As the short-scan did not enable the relocking in this specific example, the long-scan is started in order to learn the rough peak position. (IV) The output is set at a rough start point determined in the previous step. (V) A short-scan is started to find the precise peak position. (VI) The output is set to the precise start point. (VI) Locking is on.

of the system can be also implemented. This method is taking advantage of the high-quality obtained by analog PI-locking as well as of the digital automatic re-locking enabled by micro-controller. Because of the weight of the historical mount of the type-II OPO, the OPO-cavities are locked using this hybrid method in our experiments.

The codes for the ADUC7020 micro-controller phase-locking algorithm can be found in Appendix B.

We also used another type of micro-controller which met the aforementioned requirements. This micro-controller is easier to find and can be bought in larger quantities.

II.3.2 Arduino

Recently, Arduino came out with a new model that possesses analog outputs: the Arduino Due, with a slightly faster internal clock (84MHz) than the ADUC7020. Its ADC and DAC roughly have the same speed (500k-1MHz and $\sim$ 1.5 MHz, respectively) which will be the limitation. It is also simpler to write code with it, user-friendly, and

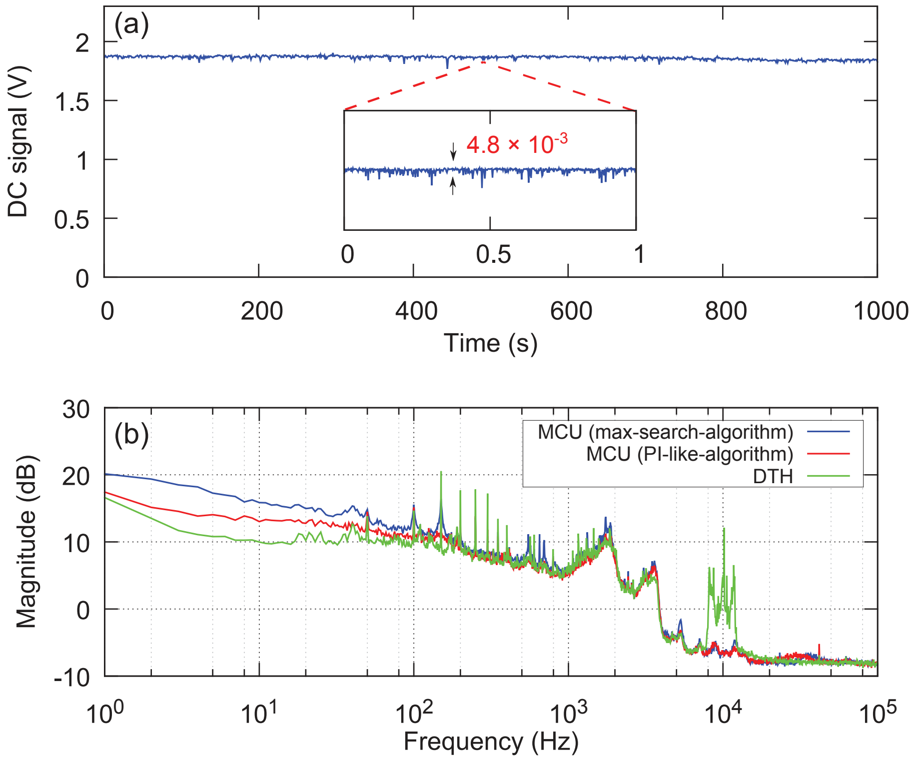

Figure II.10: (a) Long-term stability for the high- finesse cavity. The inset gives a one-second zoom. The standard deviation is normalized to the cavity peak height. (b) Noise spectrum for maximum-searching locking, PI-like locking and the traditional analog dither-and-lock technique.

a large amount of free libraries already exists. However unlike the ADUC7020, it has only two outputs. It is also slightly cheaper (≈ 30 euros).

Using this micro-controller, we implemented the locking of an interferometer at any phase difference, i.e. at any position on the fringe signal. The idea is to implement a first scan to measure the maximum and the minimum of the fringe. Using this measurement, it is possible to target a specific voltage corresponding to a certain phase. Using a feedback gain proportional to the difference between the targeted signal and the detected signal, we can lock the interferometer at any phase. We have used this method to lock the local oscillator phase of our homodyne detection at any desired point. This will be used in Chapter VI, for remote state preparation and steering.

The codes for locking a Mach-Zender interferometer with the Arduino Due can be found in Appendix C.

II.4 Conclusion

This chapter has detailled the general tools used in our quantum optics experiments. The central non-linear system here is an OPO based on a crystal inserted into a cavity. Depending on its phase matching properties, such device can generate either single or two-mode squeezed vacuum states. Both are available on our experimental setup. To detect and characterize the generated quantum state, we use homodyne detections as they are phase-sensitive, can achieve full tomography of a state and have a high efficiency. Such detectors also need a correct knowledge of the temporal mode features of the state [48]. This aspect will be furtherly investigated for Fock states in Chapter IV.

A new way of locking optical paths and cavities has also been implemented as the generation of complex states requires many locking systems. We implemented a reconfigurable, automatically re-locking, cheap, and efficient method thanks to different micro-controllers [42].

In the next chapter we will focus on another type of detector we did not develop so far: a single-photon detector, often used in discrete-variable schemes. In our case, we rely on superconducting nanowire single photon detectors, which can reach close to unity quantum efficiency and combined variety of figures of merits.

III Superconducting Nanowire Single Photon Detectors

Introduction

In this chapter, we will show the optimization at 1064 nm of superconducting nanowire single-photon detectors (SNSPDs) that we will use in our quantum state engineering experiments. Based on a fruitful collaboration with V. Verma and S. W. Nam, from the National Institute of Standard and Technology (NIST), and F. Marsili and M. D. Shaw from the Jet Propulsion Laboratory (JPL), the WSi-based SNSPDs reached an efficiency of 93% with a dark noise below Hz level. We will firstly provide a brief review of the different types of existing detectors, and then focus on SNSPDs. We will then discuss about the WSi-based SNSPDs that we optimized, characterized and used.

Contents

III.1 Context **42**
  III.1.1 The near-infrared range 42
  III.1.2 History and different types of detectors 42
III.2 Characterizing a single-photon detector **43**
III.3 SNSPD **43**
  III.3.1 Principle 43
  III.3.2 Alignment: NIST's plug-and-play mounts 44
  III.3.3 Cooling and apparatus 45
  III.3.4 Measurement of the system detection efficiency 46
III.4 Detector optimization **48**
  III.4.1 Simulation 48
  III.4.2 Fabrication 48
  III.4.3 Results 49
III.5 Perspectives **50**
  III.5.1 A new superconducting material: MoSi 50
  III.5.2 A new cryogen-free cryostat 50
III.6 Conclusion **51**

III.1 Context

III.1.1 The near-infrared range

The near-infrared wavelength range has been an important playground for a large community in quantum optics, in particular at $\lambda = 1064$ nm. At this wavelength that corresponds to Nd:YAG lasers, narrow-linewidth and ultra-stable lasers are available, as well as ultralow-loss optical coatings and photodiodes with close-to-unity efficiency. Pioneering [52] and world-record [53] demonstrations of squeezed light [54] have been performed at this wavelength, as well as quantum teleportation [55] and enhanced quantum metrology, including for gravitational wave detection [56].

In contrast to these realizations, the preparation of single-photon states or more complex states involving larger photon-number components generally requires single-photon detections to herald their preparations [25, 57, 58]. Indeed, combining several photon detection lead to a drastic decrease in the count rate which can prevent from using several protocols at a row [59]. It as well adds technical difficulties due to the stability over long time of the experiment.

In the case of multiple heralding events, as targeted in this thesis work, or also to implement successive protocols, the implementation of fast and highly efficient single photon detectors is therefore a fundamental and demanding requisite for these investigations [60].

III.1.2 History and different types of detectors

Detecting efficiently single photons at 1064 nm has been a long standing issue. The first available detectors were avalanche photodiode detectors (APDs), where the detection of a photon triggers an avalanche multiplication of the current. Two materials are used in this endeavor. Si-based APDs have low efficiency ($< 2\%$) while having a dark count rate from 50 Hz to 1 Hz. InGaAs/InP ones, even though large improvements have been obtained in the recent years with these devices, exhibit limited efficiency for this specific wavelength and often suffer from large dark count rates if used in free-running mode. In addition their dead-time is usually around the μs scale, too long for our targeted applications.

For all these reasons people started to go towards superconducting-nanowire single-photon detectors that could reach high efficiency, with low dead-time and jitter, and below Hz dark noise. Such parameters will be detailed in the following section. Historically, the first generation of such detectors was based on NbN material and could reach up to 30% detection efficiency [61]. The first detectors used in the group a few years ago were based on such material. Published works reported efficiency larger than 50% [62], but were considering only photons coming onto the area of the detector and not an overall system detection efficiency. Despite recent progresses [63, 64], their efficiency is limited by the intrinsic nature of the material. Indeed, due to the lack of compatibility between NbN and the others materials helping on the increase of the system efficiency, only a small choice of substrates can be used to fabricate the NbN nanowire. Moreover, NbN being crystalline, it is affected by crystal defects, which limits the fabrication of large-area devices to maximize the absorption probability of a photon, and to be able to play widely with design parameters to enhance the absorption.

Recently, the development of SNSPDs based on tungsten silicide (WSi) [65, 66] enabled to outperform other infrared single-photon detectors. In addition to a better internal efficiency than other materials, the amorphous nature of WSi facilitates the fabrication of large sensitive area and the embedding of the material inside an optical stack to enhance absorption. System detection efficiency greater than 90% has been achieved in the wavelength range $\lambda = 1520 - 1610$ nm [67].

III.2 Characterizing a single-photon detector

In this section will be briefly described the important parameters for different types of single-photon detector.

- **System detection efficiency (SDE)**
  The system detection efficiency quantifies the capacity for one input photon to generate a detectable electronic pulse. This value includes coupling and fiber losses and provides an overall effective quantum efficiency.

- **Dark count rate**
  Dark counts are events appearing despite the absence of light. They can be very detrimental in quantum state engineering. False-detection events will indeed degrade the fidelity of heralded states.

- **Jitter**
  The jitter is the deviation from a periodic signal, which produces some uncertainty on the photon detection time. The jitter can be of hundreds of picoseconds for Transition-Edge Sensors (TESs) or APDs and is closer to tens of picoseconds for SNSPDs. This parameter is therefore not relevant for the experiments presented in this thesis.

- **Dead-time**
  The dead time is the time it takes for detector to come back at its operating state after a detection event. During this time, it cannot sense any other excitation. This duration is around a few μs for TES while reaching few ns for SNSPDs.

SNSPDs combine large system detection efficiencies, low dark count rates, limited jitter and dead time. This combination makes them one of the best detectors for quantum optics experiments. The next section will focus on SNSPDs, their principle and operation apparatus. The protocol used to measure their quantum system detection efficiency will also be detailed.

III.3 SNSPD

III.3.1 Principle

The detector is cooled down to cryogenic temperature in order to achieve a superconducting behavior of the material. A current called the bias current I_B is sent to the detector. This current must be small enough, below the switching current I_{SW}, to

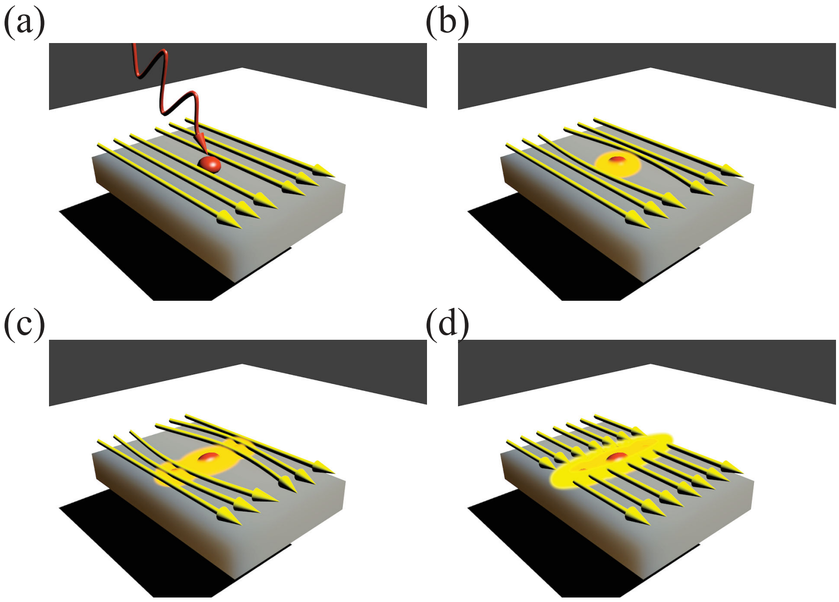

Figure III.1: (a) A single photon is absorbed by the nanowire. (b) Creation of a hotspot making the material locally resistant. (c) The density of current increases as the current tries to bypass the resistance. (d) Complete phase transition. The material becomes locally resistant and a voltage pulse is detected.

keep the detector in the superconducting state. When a photon is absorbed by the nanowire (Fig. III.1(a)), it creates a hotspot that makes the material locally resistant (Fig. III.1(b)). The current then tries to bypass this resistance and the resulting increase in the current density leads to a phase complete transition (Fig. III.1(c)). It results in a resistance of a few $k\Omega$ (Fig. III.1(d)), and a measurable voltage pulse.

Depending on the material, the necessary cooling temperature can vary. In the first experiments conducted at NIST, the operating temperature of the cryostat was set to 800 mK. However, more recently, operations above 2K were also demonstrated for detection at 1310 nm [68].

III.3.2 Alignment: NIST's plug-and-play mounts

It is important to check the overall system detection efficiency and not only the probability for one photon impinging on the surface to create a pulse, which is determined by the material's intrinsic nature. Indeed, what can be tricky when one wants to efficiently detect all the photons is to be able to send them correctly onto a very small area.

For example, for NbN-based device the efficiency is in part limited by the difficulty of fabricating large areas, without defects, leading to a difficulty to couple them with optical fibers. Drifting of alignment with time can therefore also be an issue.

To simplify the alignment and prevent from misalignment issues with time, NIST has developed a self-alignment technique. A keyhole shape is etched though the wafer around each detector as shown in Fig III.2(a). Each detector can then be removed and self-aligned to a single mode fiber, using a fiber ferrule of the same diameter [69]

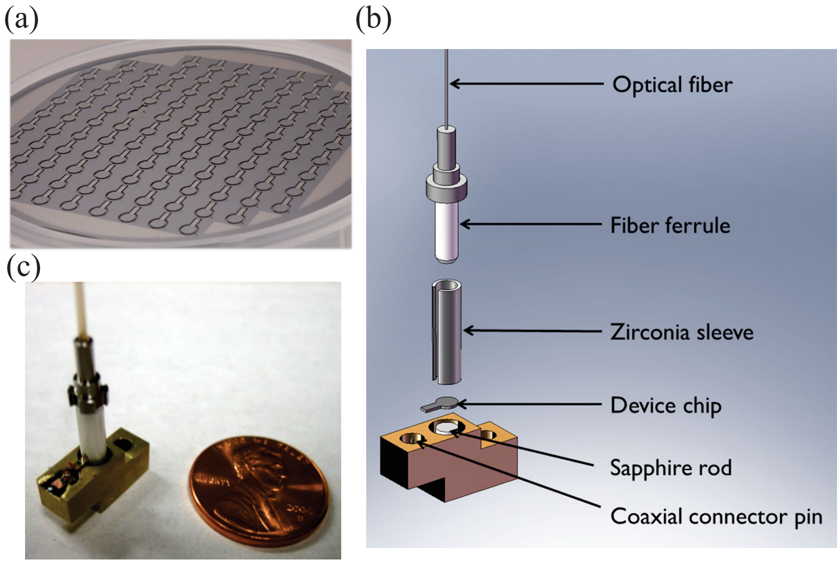

Figure III.2: (a) Photography of a wafer containing several detectors. (b) Detector assembly and fiber connection. The single-mode fiber is self-aligned via a zirconia sleeve. The 16 μm × 16 μm active area of the SNSPD is larger than the 10 μm mode field diameter of a standard single mode fiber, to allow for slight misalignment. (c) Photography of the SNSPD mount.

as shown in Fig III.2(b). Thanks to an adequate mount holding the overall system, the alignment is made stable, efficient and very reproducible. A picture of the usually used mount is shown in Fig III.2(c).

III.3.3 Cooling and apparatus

In our case, the SNSPD is mounted at the bottom of a double-wall dipstick. This dipstick is immersed into a liquid Helium dewar while the vacuum inside is pumped, in order to decrease the temperature slightly below 2K by the Joule-Thomson effect. The apparatus is shown in Fig. III.3(a).

A 1-meter-long single-mode fiber is connected to the detector and to the top of the dipstick. The fiber end face is anti-reflection coated for 1064 nm (OZ-Optics). The resulting voltage pulses are sent through a coaxial wire to the top of the dipstick.

To enhance the signal-to-noise ratio, we filter the signal using a 100 MHz low-pass filter, and amplify it with a chain of two 1 GHz amplifiers of 24 dB gain each (Minicircuits ZFL-1000LN+). All the electronics is implemented at room temperature. The overall electronic scheme is presented in Fig. III.3(b). An additional filter is added on the oscilloscope settings in order to ease a precise triggering by smoothing the signal. The signals of the SNSPD with and without this additional numerical filter are shown in Fig III.3(c). Usually, a value of 20 MHz for the scope filter is chosen.

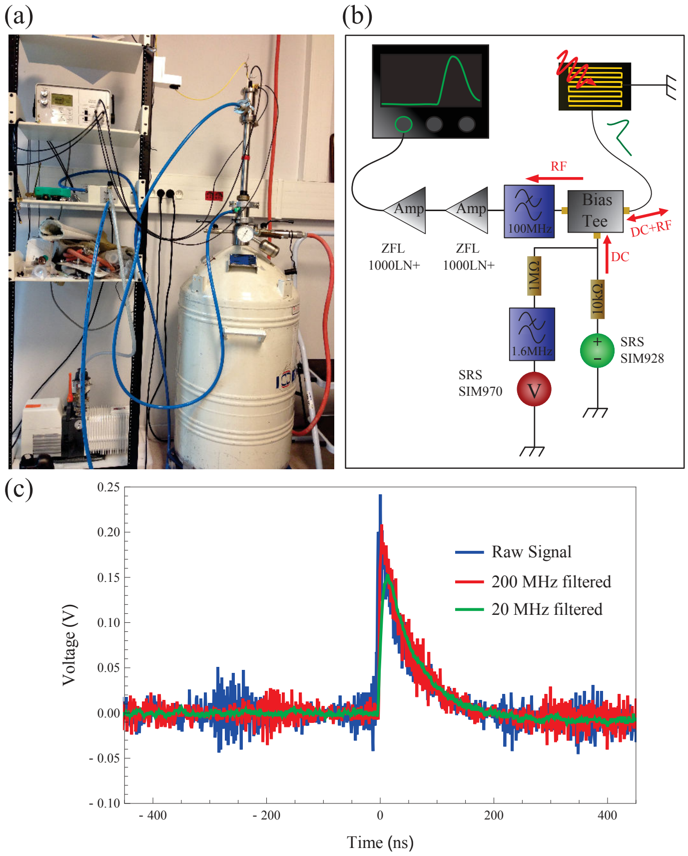

Figure III.3: (a) Photography of the dipstick immersed into the liquid Helium dewar. (b) Scheme of the electrical circuit used to recover the pulse. A small DC current is sent via a SRS SIM928 source (1 mV on the voltage source corresponds to 0.1 μA in current) to the detector. In order to check the current sent do the detector we use a SRS SIM970 voltmeter. This voltmeter also enables us to check that the detector stays in its superconducting state, i.e. that it does not become resistant because of the sent DC current. The voltage pulse resulting on the absorption of a photon is a high frequency signal. This signal (in green) is recovered thanks to a bias tee. The signal is frequency-filtered using a 100 MHz low pass filter, and then amplified using two Minicircuits amplifiers ZFL-1000LN+ of 24 dB gain each. (c) In blue is given the voltage pulse of the SNSPD after amplification. In Red is given the SNSPD pulse, filtered on the oscilloscope via a 200 MHz numerical low pass filter. In green is given the SNSPD pulse, filtered numerically by a 20 MHz low pass filter. This configuration is usually used in the experiments for a facilitated triggering.

III.3.4 Measurement of the system detection efficiency

To quantify the overall system detection efficiency (SDE) including fiber and coupling losses, we sent a strongly attenuated laser at 1064 nm in a fiber, in order to reach a mean photon number of about 100,000 photons/s. The detector is polarization-sensitive (typically up to 10% difference in efficiency) due to the anisotropic nature of the material. The polarization of the probe light is thus optimized in order to maximize the number of counts.

Then, to quantify the efficiency, we follow the steps shown in Fig III.4:

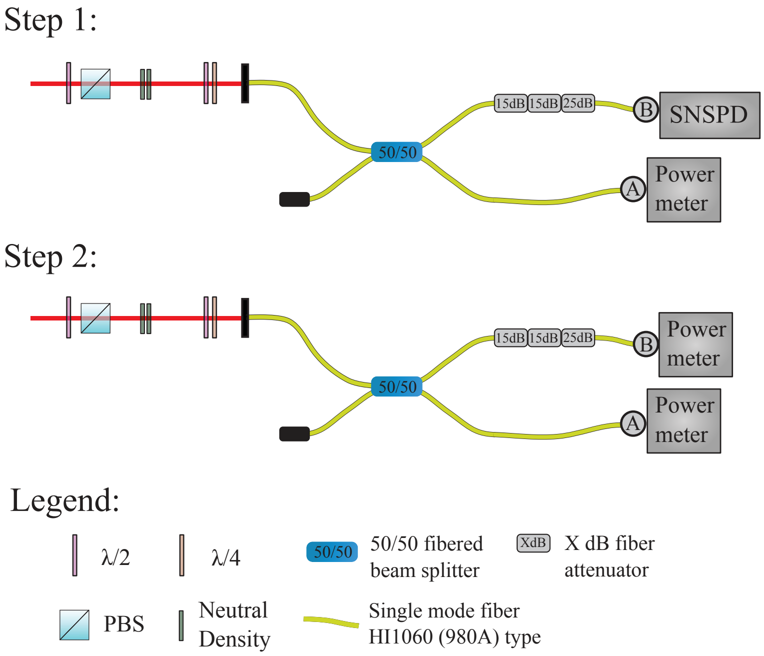

Figure III.4: SDE measurement, consisting in two main steps. The light of a 1064-nm continuous-wave laser is sent to a single-mode fiber and a 50/50 beam splitter. The first step consists in finding the good combination of fiber attenuator to reach the range 5 nW-200 pW at point A with the power meter, and a photon number of 10^5 photons/s at point B, i.e. at the SNSPD side. The polarization is optimized using a half-wave plate and a quarter-wave plate at the input of the fiber. The ratio between the count number in B, and the laser power in A is calibrated. The second step consists in the precise calibration of the power attenuation between A and B. The light power is finally increased until the same power meter at point B reaches the range 5 nW-200 pW, and 1 μW-30 μW at point A.

Step 1:

- The light of a 1064-nm continuous-wave laser is sent to a single mode fiber and attenuated until the power meter measures at point A in the range $5nW - 200pW$. Fiber attenuators are added on B to reach at point B, i.e. on the detector side, a photon number of 10^5 photons/s.
- The polarization is optimized using a half-wave plate and a quarter wave plate at the input of the fiber.
- The ratio between the count number in B, and the laser power in A is calibrated (Fig III.4 step 1).

Step 2:

- The light power is finally increased until the power meter in B reaches the range 5 nW-200 pW, and 1μW-30 μW on A. This step enables to calibrate the power attenuation between A and B (Fig III.4 step 2).

The steps must be repeated several times to ensure a correct calibration of the quantum efficiency, and with other attenuators. It is then necessary to pay attention to some uncertainty sources such as:

- The intensity fluctuations of the light, due to the technical fluctuations of the laser intensity and the light shot noise. These fluctuations have been estimated to be below ±0.5%.
- The calibration uncertainties, due to the curve fitting of the data point to get the ratios. They can be minimized by taking a sufficient number of points and by repeating the steps several times. These uncertainties have been estimated to be below ±0.5%.
- The precision of the power meter (Ophir PD300-IRG): due to two different sources. The first one is the precision of the power meter itself, and its calibration with a standardized source. The second one is the non-linearity between two different ranges of the power meter. These uncertainties sum up to be below ±3%, according to the constructor data.

Thus the total uncertainty on the system detection efficiency is governed by the one of the power meter and is equal to ±3%.

We can with this method achieve a trustful calibration of our SDE.

III.4 Detector optimization

We will now turn to the work done on the development and optimization of the SNSPDs at the wavelength 1064 nm [70].

III.4.1 Simulation

Because the crystal structure of WSi is amorphous, WSi-based nanowires are more robust to structural defects than NbN nanowires. Moreover, its nature allows it to be embedded in a variety of substrates, enabling to enhance its absorption. The $W_{0.8}Si_{0.2}$ detectors were then optimized for maximum absorption at 1064 nm. Simulations were performed via a Matlab© program running RCWA (rigorously coupled-wave analysis) to optimize the layer thicknesses, given the optical constants of the materials. A scheme of the different layers is shown in Fig III.5(a). The simulated spectra of absorption, reflexion and transmission can be found in Fig III.5 (b).

III.4.2 Fabrication

The first step of the fabrication process consists in the deposition of an 80 nm-thick gold mirror on a 3”*Si* wafer by electron beam evaporation and lift-off, with a 2 nm Ti adhesion layer below and above the mirror. A quarter-wave spacer layer (152 nm of SiO_2) was then deposited by plasma-enhanced chemical vapor deposition, and Ti/Au contact pads were patterned by electron beam evaporation and lift-off. The $\sim$ 4 nm-thick superconductor layer was deposited by DC magnetron co-sputtering from separate W and Si targets at room temperature. It was then capped with 2 nm of

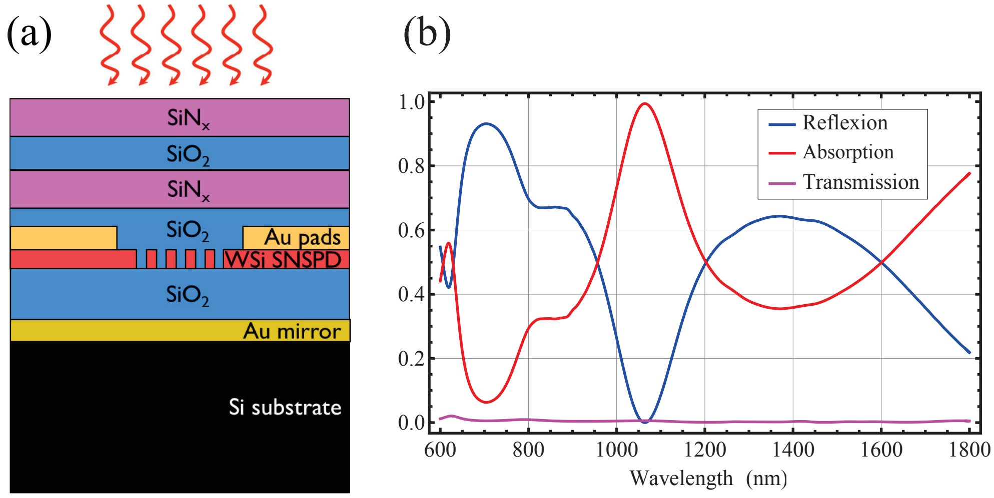

Figure III.5: (a) Scheme of the different layers of WSi-based SNSPDs. The WSi meander is embedded inside an optical stack deposited on a Si substrate. The layers have been optimized to enhance absorption at 1064 nm. An antireflection coating is deposited on the top surface and a quarter-wave spacer layer is realized between the meander and the bottom gold mirror. (b) Theoretical absorption, reflection and transmission spectra for the optimized layers using an RCWA analysis.

amorphous Si to prevent oxidation. Photolithography and etching in an SF6 plasma were used to define a 20 μm-wide strip between gold contact pads. Electron beam lithography using PMMA resist and etching in SF6 were then used to define nanowire meanders with a width of 140 nm and a pitch of 245 nm within the 20 μm-wide strip. An SEM image of the meander is shown on Fig III.6.

An antireflection coating was finally deposited on the surface with 102 nm SiO_2, 137 nm SiN_x, 171 nm SiO_2, and 192 nm SiN_x.

III.4.3 Results

Many detectors were tested with different pitches and gaps. Their efficiencies usually varied from 70% to close-to-unity efficiency. Figure III.7 provides the measurement of the best detector's SDE and dark count rate as a function of the bias current. As it can be seen, at this operating temperature the system reaches the inflection current, leading to a saturated efficiency, before reaching the switching current, $\sim 2\mu A$, for which the device switches to its resistive, non-superconducting state. At a bias current of $1.8\mu A$, an SDE of $93 \pm 3\%$ is obtained with a dark noise limited to 3 counts per second (cps). For bias currents closer to the switching current, the dark count rate increases rapidly.

A recent improvement consisted in replacing the gold mirror by a dielectric one. This operation led to an increase of the critical current by a factor of 2 and therefore an enhancement of the signal to noise ratio.

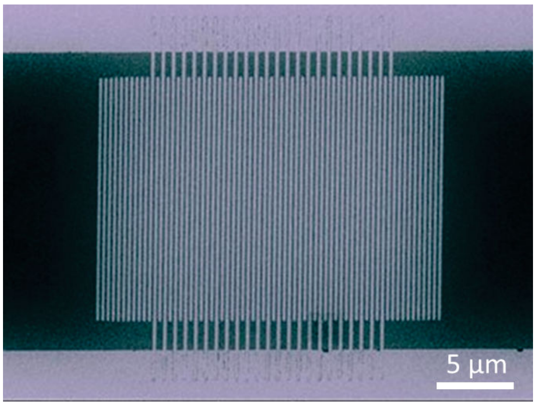

Figure III.6: SEM image of the meander. The nanowire has a width of 140 nm and pitch of 245 nm

III.5 Perspectives

We conclude this chapter by discussing two main on-going evolutions of this work.

III.5.1 A new superconducting material: MoSi

A new material based on molybdenum silicide is currently tested and optimized for our wavelength. MoSi detectors are interesting because they work at higher temperature, which enables to have higher switching current, and therefore have a larger voltage response around $1.8K$. The resulting increase is a strong incentive in the signal-to-noise ratio. Moreover this high switching current enables us to almost always reach the plateau region, where the SDE saturates. Therefore we can fully reach the maximal intensity of each detector. This direction will therefore be followed in the future.

However it requires another fabrication process that our collaborators at NIST recently started to develop. First batches enable to reach detection efficiencies around 70%. It should be feasible to target close-to-unity efficiency for this material as well, with a greatly improved signal-to-noise ratio.

III.5.2 A new cryogen-free cryostat

Problems concerning the lifetime of the detectors were found and were an important issue during this thesis. Indeed from one cooling cycle to another one, the surface coating is peeling off, resulting on unbounding of the aluminum micro-wires and deterioration of the quantum efficiency. Even though the surface can be cleaned with alcohol and the wire rebounded, after some time, the efficiency is still decreasing and the surface get so dirty that it is almost impossible to reconnect the wires.

These issues are related to our cooling process. Two hypotheses were made. When the pump is stopped, the detector is still immersed in boiling helium that can cause mechanical action and damage the surface and the aluminum boundings. Alternatively, when the pump is stopped and the dipstick is taken out of the helium, either some air is getting back in it and can easily turn into ice, or some impurities in the helium itself

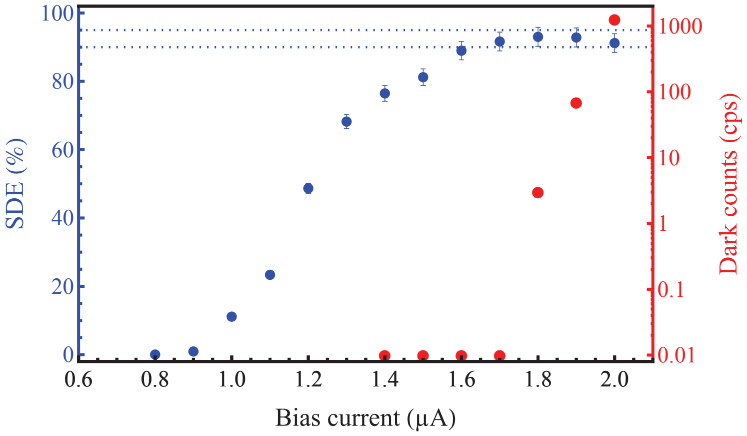

Figure III.7: System detection efficiency (SDE) at 1064 nm (blue) and dark counts (red) as a function of the bias current. For a bias current of $1.8\mu A$, a value equal to 0.9 times the switching current, a SDE of $93 \pm 3\%$ is obtained with a dark noise of 3 cps. These measurements are obtained at an operating temperature of 1.8 K.

crystallize on the detector. We saw sometimes crystalline-like dirt on the surface, and very often had water in the dipstick, comforting us to assume such hypothesis.

To prevent these damages from occurring again, a new helium free cryostat based on charcoal sorption cooling will be arriving soon. Cooling at 4 K with some liquid Helium make the charcoal adsorb gas and decrease the pressure enabling further cooling below 2 K.

III.6 Conclusion

The fruitful collaboration with NIST and JPL resulted in the most-efficient single-photon detectors at 1064 nm so far using superconducting nanowire single-photon detectors. The amorphous nature of the WSi material enables to grow large areas and facilitates its embedding inside an optical stack. The detectors are easy to connect with an optical fiber, and requires only an operating temperature around 2 K. The achieved detection efficiency of detection was $93\% \pm 3\%$, with dark counts at the Hz level. In the future, we can expect that the signal to noise ratio will even be further enhanced by the fabrication of MoSi-based devices.

The unique combination of such close-to-unity efficiency single-photon detectors and our high-quality non-linear sources opens the path to a variety of quantum state engineering experiments, as detailed in the following of this work.

Part II

Quantum State Engineering

IV Fock State Generation

Introduction

Fock states, i.e. photon-number states, are often used in the world of discrete variables as carriers of information. In particular, building reliable single-photon sources is a critical requirement for the implementation of quantum optics protocols. Fock states are also main resources for the engineering of non-gaussian states. Indeed, one cannot build a non-gaussian state by solely using gaussian operation and resources. Generating non-gaussian states requires at the minimum either non-gaussian operation or to start with non-gaussian states, such as Fock states.

In this chapter, we will describe an efficient method for generating heralded Fock states, based on spontaneous parametric down-conversion (SPDC) in an OPO. We will demonstrate that our single-photon source shows high performances, such as one of the largest spectral brightness to date for SPDC sources and a large heralding efficiency. We will then use the same source to demonstrate high-purity two-photon Fock state generation. Thanks to the achieved large generation rate, we will also study the temporal mode structure of two-photon state and show how it can be used as an additional degree of freedom for quantum engineering.

Contents

IV.1 Fast and high-purity heralded single photon 56
  IV.1.1 Characterizing a single-photon source 56
  IV.1.2 A single-photon source based on an OPO 57
  IV.1.3 Experimental implementation 58
  IV.1.4 Results 59
  IV.1.5 Comparison with other photon sources 60
IV.2 Heralded two-photon Fock states 62
IV.3 Quantum state engineering with time-separated heraldings 63
  IV.3.1 Temporal mode definition 63
  IV.3.2 Experimental realization of Fock-state superpositions 65
IV.4 Conclusion 68

IV.1 Fast and high-purity heralded single photon

IV.1.1 Characterizing a single-photon source

At the heart of many protocols, high-purity single-photon sources are a central resource for the development of quantum information [71]. In linear optical quantum computing protocols, such as in the KLM scheme [72] where universal quantum computing is achieved with linear optics tools and single-photon detectors, single photons are used as information carrier. This approach is based on interferometric transformation and high-efficiency single-photon detection and highly relies on the quality of the single-photon source. High-quality single-photon source is at the heart of a large number of groups' working themes [73], ranging from quantum-key distribution schemes, boson sampling approach, or Bell type violation of locality [36–38].

In all these developments, the need of a low admixture of vacuum is a crucial requirement and is directly linked to the overall optical losses of the system. The generation of high-purity and ultrafast single-photon is thus an active topic nowadays. Depending on what is required for the protocols, the source need to reach different figures of merit that will be described in the following.

Heralding efficiency

The heralding efficiency corresponds to the probability P_1 to have one and only one photon, given the detection of a heralding event. It is thus directly linked to the purity of the source. Definitions may vary whether it is with or without correction from detection losses. In this study, we chose to give it with correction from detection losses as it quantifies the limit our source can target, and the quality of the photon used in subsequent protocols. In our case, the detection losses are a technical issue and not intrinsically limiting the purity nor preventing its direct use in subsequent protocols, as the photon is emitted in a very well-defined spatio-temporal mode. Such losses will thus be given separately.

Second-order correlation

The second-order intensity correlation $g^{(2)}(0)$ is proportional to the ratio of the 2-photon population with the overall population:

$$g^{(2)}(0) = \frac{\langle((\hat{a}^\dagger)^2\hat{a}^2\rangle}{\langle(\hat{a}^\dagger\hat{a}\rangle^2} \approx \frac{2P_2}{(P_1+2P_2)^2} \tag{IV.1.1}$$

where P_1 is the heralding efficiency, i.e. the probability to find one photon, and P_2 the probability to find two photons, in a well-defined spatio-temporal mode. It quantifies the multi-photon character of the source. The autocorrelation function is an important though incomplete parameter. Indeed, $g^{(2)}(0))$ criterion is insensitive to losses.

Spectral Brightness

The spectral brightness is the number photons emitted per unit of time and per unit of bandwidth per mW. The effective count rate, deriving from the spectral brightness of the source, is important if one wants to use these photons on subsequent protocols.

Also the spectral brightness shows how many photons are emitted in a well-defined spectral mode. If ones want to store these states in a quantum memories, the mode size needs to meet the atomic bandwidth and thus needs to be well-defined and of a few MHz large.

Brightness
Another parameter, which can be applied to pulsed sources, and which characterizes also the speed and efficiency of the source is the brightness. Definition may vary. It can be seen as the spectral brightness integrated over all wavelengths. But also as the probability, given one pump photon, to emit a single-photon as referred in [74]. This latest definition is hard to apprehend for our continuously-pumped OPO and we will therefore here only focus on the spectral brightness of our source.

In order to meet all this requirements, we will detail in the following how each of these criteria depends on the parameters of an OPO.

IV.1.2 A single-photon source based on an OPO

Our single-photon source will be based on a type-II phase-matched OPO, as detailed in Chapter II. Two mode-squeezed states, which will be furtherly studied in the next chapter, are emitted at the output of the device. The output state can be written in the Fock basis as:

$$|\Psi\rangle \approx \sum_{0}^{\infty} \Lambda^{2n} |n\rangle_i |n\rangle_s. \tag{IV.1.2}$$

The resulting idler and signal modes are therefore photon-number correlated. Moreover, the modes being orthogonally polarized, they can be separated using a simple polarization beam splitter (PBS) and a half wave-plate (HWP). Then, by implementing a single-photon detection on the idler mode, it is possible to herald the generation of its twin on the signal mode.

In an OPO, the two main parameters on which the user can play are the system escape efficiency η_{OPO}, and the threshold power P_{th}. These parameters are given by the cavity features: the intra-cavity losses $\mathcal{L}$, the transmission for the pump T_p of the input coupler and the transmission of the infrared photons T of the output coupler of the cavity. Indeed the escape efficiency can be written as: $\eta_{\text{OPO}} = \frac{T}{T+\mathcal{L}}$, and the threshold power as: $P_{\text{th}} \propto T_p \frac{T^2}{\mathcal{L}^2}$.

More specifically, the heralding efficiency P_1 is limited by the escape efficiency, as $1 - \eta_{\text{OPO}}$, which is the minimal admixture of vacuum than cannot be avoided. Then P_1 also depends on the distance of the pump power to the threshold. Indeed $\frac{P}{P_{\text{th}}} \propto \Lambda^2$. Therefore the P_2 component increases with the pump power while the P_1 component will decrease. Consequently, the $g^{(2)}(0)$ function is determined by the distance to the pump power.

The spectral brightness is independent of the pump power. To achieve a large spectral brightness, one must have a narrow mode bandwidth. Narrow bandwidth are also necessary for photon coupling to atomic systems, and in particular for atomic quantum memories. This bandwidth is defined by the cavity bandwidth of the OPO and therefore depends on the output coupler of transmission T. The longer time the

Parameter	Depends on	Play with
P_1	P_{th}, η_{OPO}	T, L, P_p
$g^{(2)}(0)$	P_{th}	P_p
Sp. Brightness	η_{OPO}	T

Table IV.1: The parameters of a single-photon source in the first column depend on the parameters of the OPO source, in the second column. In order to optimize the single-photon source, one can play with the experimental parameters of the third column.

photon "spends" in the cavity, the narrower will be its bandwidth. Therefore the smaller T is, the narrower the mode is. However the bandwidth scales in the inverse way than the escape efficiency η_{OPO}, and thus than the heralding efficiency P_1. The output coupler of the OPO must be chosen as a trade-off between a narrow bandwidth and a high heralding efficiency.

Table IV.1 summarizes the dependency of each figure of merit of the source with the OPO parameters, and how they can be experimentally tuned.

In our system, we chose for the mirrors the values detailed in Chapter II, leading to: $\eta_{\text{OPO}} \approx 96\%$, $P_{th} \approx 50$ mW and a bandwidth of around 50 MHz.

IV.1.3 Experimental implementation

The experimental setup is shown in Fig. IV.1. The non-linear crystal is a type-II phased-matched KTP crystal pumped by a continuous-wave Nd: YAG laser at 532 nm. The crystal is 1 cm-long. The transmission of the output coupler is of $T = 90\%$ for 1064 nm and highly reflective for 532 nm. This OPO is made triply-resonant for the pump and the two polarizations of idler and signal at 1064 nm by tuning the temperature of the crystal and the pump wavelength. This enables the generation of orthogonally-polarized photon pairs at 1064 nm, which can be split using a polarizing beam splitter. The idler non-degenerate modes are then filtered using the combination of a 0.5 nm-wide interferential filter followed by a Fabry-Pérot cavity of 300 MHz bandwidth. The resulting idler photons are then detected via a superconducting nanowire single-photon detector (SNSPDs). The combination of these filtering elements is used in order to make sure that the emitted signal photon will be in the same, well-defined, mode than the heralding idler photon (see Chapter II for details and values). The overall transmission of this conditioning path is of $\eta_{\text{cond}} \approx 50\%$.

We then analyzed the emitted photons using homodyne detection. However due to backscattering of the local oscillator on the optical elements and the photodiodes, we have to use an optical isolator made of a Faraday rotator and two polarized beam splitters on the detection path. The additional elements create some losses that we can correct from when we reconstruct the density matrix. The detection losses sum up to be 15%, which details can be found in Chapter II. For each event, the homodyne signal is recorded and multiplied by the temporal mode of the photon [48], which is a double decaying exponential profile with a bandwidth of 53 MHz, as detailed in Chapter II.

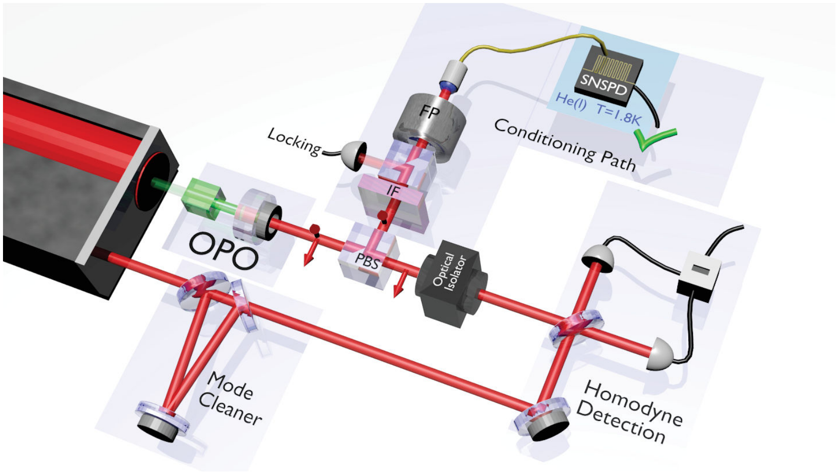

Figure IV.1: Experimental setup for the heralded single-photon source. A polarization non-degenerate and triply-resonant OPO is pumped far below threshold by a continuous-wave laser at 532 nm. Due to the cavity enhancement, the pump power is in the mW range. At the output of the OPO, photons pairs are separated via a polarizing beam splitter. Single-photon detection on the conditioning path heralds the emission of its twin, which is then characterized by homodyne detection. The overall transmission of the conditioning path, which includes frequency filtering (interferential filter IF and resonant cavity), reaches 50%. An optical isolator enables to avoid any backscattering from the detection system.

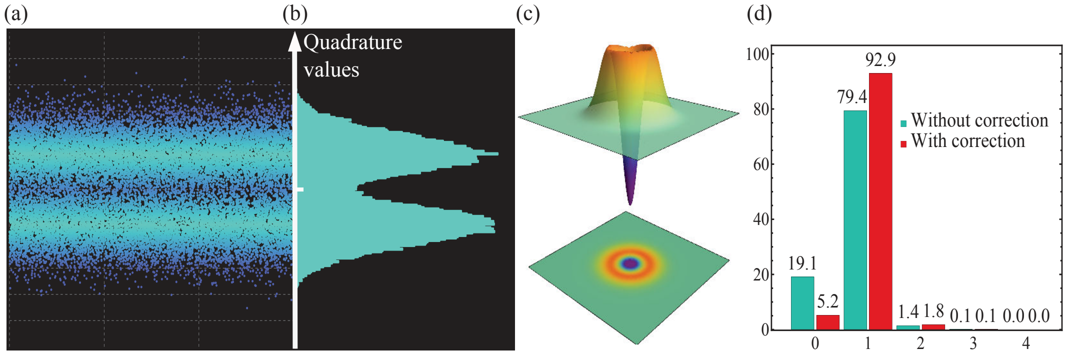

Figure IV.2: (a) Quadrature values and (b) distribution measured via the homodyne detection for the heralded state. (c) Wigner function of the heralded state corrected from detection losses (15%). (d) Photon-number distribution for a 1 mW pump power, with and without correction from detection losses (15%). The heralding efficiency, i.e. the probability of obtaining a single photon at the output of the OPO per heralding event, reaches 93%. The vacuum admixture is limited to 5%.

IV.1.4 Results

The recorded quadrature values and the experimental Wigner function are given in Fig. IV.2. Using a maximum likelihood algorithm, the density matrix is reconstructed and its diagonal elements (photon number probabilities) are given in Fig IV.2(d), with and without correction from detection losses (15%). We reach a heralding efficiency as high as 93%, with a vacuum component limited to 5% [75]. This is in agreement with

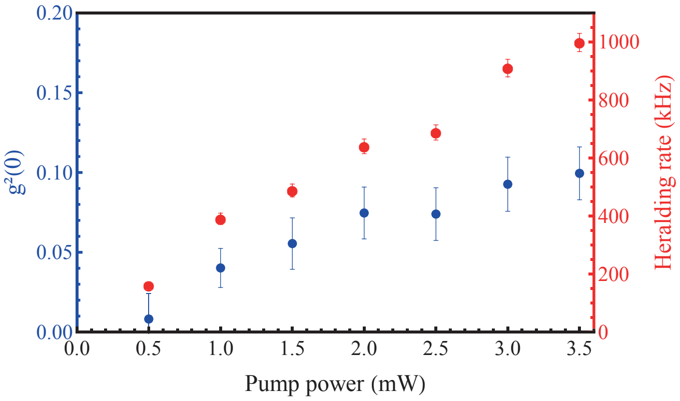

Figure IV.3: Heralding rate and conditional autocorrelation function $g^{(2)}(0)$ as a function of the pump power. A spectral brightness as large as 0.6×10^4 photons/(s·mW·MHz) is obtained, close to the maximal achievable value in this parametric down-conversion system.

the escape efficiency of the OPO which is around $\eta = 96\%$. Figure IV.3 provides the $g^{(2)}(0)$ values with the pump power. $g^{(2)}(0)$ values from 0.008 to 0.1 for a heralding rate going from 150 kHz to 1 MHz are obtained. The rate is proportional to the single-photon probability and thus depends linearly on the pump power: $R_H \propto \Lambda^2 \propto P_{\text{pump}}$ [70] Thanks to the high-efficiency SNSPDs, we thus can reach a spectral brightness of 0.6×10^4 photons/(s·mW·MHz). This value is very close to the maximum achievable by our source 1.2×10^4 photons/(s·mW·MHz) if one assumes a perfect single-photon detector and no loss in the heralding path (50% overall losses currently).

IV.1.5 Comparison with other photon sources

In this section we will briefly review some of the best photon sources based on SPDC published in the literature. A comparison table of several parameters can be found in Table IV.2. Many sources lack of the presence of good detectors while others have problems in terms of the mode definition of the emitted photons because of the absence of a cavity. Our source has the advantage to reach high values for many figures of merits, being one of the best in each category. This can be resumed by its high spectral brightness while having a heralding efficiency greater than 90%.
Recently, new sources such as in reference [74], based on enhanced Purcell effect due to the presence of a quantum dot embedded in a cavity, are starting to reach high figures of merits, and in particular a very high brightness.

We demonstrated the generation of high-brightness single-photon source. In the following, using the same source we will demonstrate the generation of highly-pure two-photon Fock states, via multiple conditioning events.

Sources	λ (nm)	H_R (kHz)	H_η	$g^2(0)$	$\Delta\nu$ (MHz)	SP detector and wavelength (nm)	η_{det}	Spectral Brightness (pairs/(s·mW·MHz)
This work	1064	390	0.79	0.04	53	SNSPD, 1064	0.92	$0.61.2 \times 10^4$
Jin [76]	1584	45	≤ 0.02	0.02	-	SNSPD, 1584	0.6	-
Ramelow [77]	810	6	0.82	-	230×10^3	TES, 810	≥ 0.95	2.6×10^{-3}
Krapick [78]	1575	105	0.6	0.4	330×10^3	APD, 800	0.55	~ 3
Pomarico [79]	1550	4400	0.45	0.18	375×10^3	APD, 800	0.50	~ 3
-	-	94	0.80	0.018	-	-	-	~ 3
Ngah [80]	1540	2100	0.42	0.023	200×10^3	SSPD, 1550	0.17	2.5×10^2
Neergaard-Nielsen [81]	860	12.8	0.625	-	8	APD, 860	0.44	$\sim 9 \times 10^2$
Wakui [82]	860	~ 50	0.58	-	9.3	APD, 860	-	10^2
Scholz [83]	894	5	0.55	0.012	3	APD, 894	-	1.4×10^4
Fortsch [84]	1064	-	-	< 0.2	$7.2 - 13$	APD, 1064	0.075	10^6
Luo [85]	890	-	-	< 0.02	66	APD, 890	-	3×10^4

Table IV.2: Comparison of different heralded single-photon sources based on spontaneous parametric down conversion

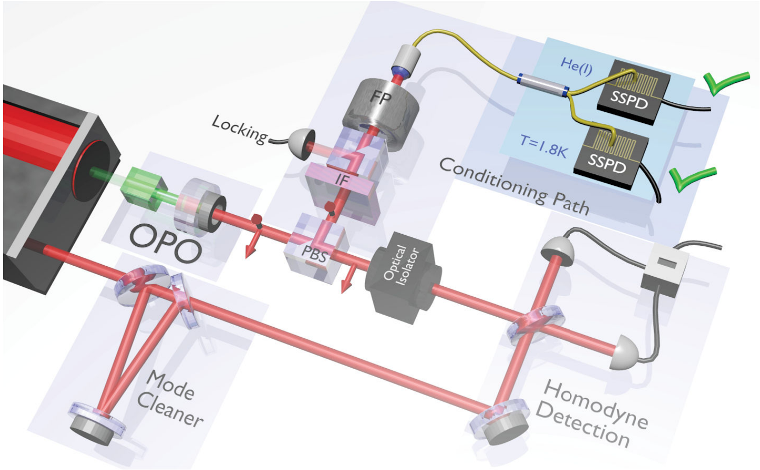

Figure IV.4: Experimental setup for the generation of high-purity and fast two-photon Fock state. The presented setup is the same as the one developed for single-photon generation, but with an additional photon detection, in order to detect two-photon as heralding events. The accepted coincidence window between the two heralding triggers is set to 1 ns, much smaller than the typical time given by the inverse of the OPO bandwidth.

IV.2 Heralded two-photon Fock states

Based on the same source, i.e. a high-escape efficiency OPO, it is also possible to generate two-photon Fock state with the addition of another single-photon detection, as shown in Fig IV.4. This double-detection is implemented using a fibered beam splitter at the output of the micro-cavity and plugged into two SNSPDs of efficiency 85%. For coincidences arriving within a time window of 1 ns, smaller than the typical time of the system, which is the inverse of the OPO bandwidth, the homodyne signal is detected. The density matrix is then reconstructed using the same technique used for the heralded single-photon state. The experimental quadrature values and marginal distribution are given in Fig. IV.5(a) and (b). The results in the form of the Wigner function and the photon number elements are given in IV.5(c) and (d). Due to the high escape efficiency of our OPO and the efficiency of the detectors, we manage to achieve a generation of 80% purity two-photon Fock state (60% without correction for detection losses), at a rate of 200 Hz. The achieved purity is consistent with the OPO escape efficiency. The achieved preparation rate is the largest obtained so far, when other experiments are around the Hz level, and the purity of our two-photon Fock state is also the highest demonstrated heretofore.

We demonstrated fast two-photon source based on two-photon detection heraldings. We considered here the case when the two heralding events arrive in a time much smaller than the OPO typical time. In the next section, thanks to the achieved rate, we will study as an additional degree of freedom, the generation of Fock state superposition via time-separated heralded single photon detection.

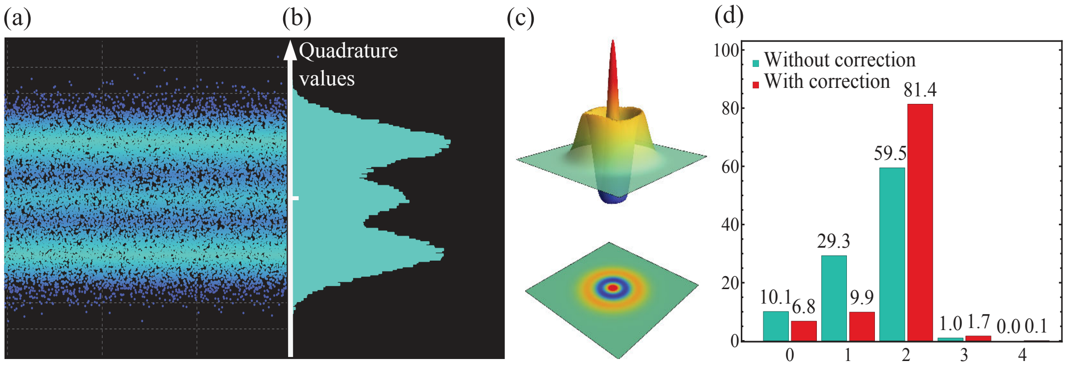

Figure IV.5: (a) Quadrature values and (b) distribution measured via the homodyne detection for the heralded state. (c) Wigner function of the generated two-photon Fock state with correction from detection losses (15%). (d) Photon number probabilities of the generated two-photon Fock state, with and without correction from detection losses (15%).

IV.3 Quantum state engineering with time-separated heraldings

In contrast to the pulsed regime where the acceptance window of the heralding events is defined by the pulse temporal profile itself, in the continuous-wave regime these events can occur at different times. Such time separation of the conditioning detections is an additional degree of freedom and can strongly affect the heralded states by introducing a multimode temporal structure [48, 86–88]. For example, large-amplitude coherent-state superpositions have been obtained by time-separated two-photon subtraction operated on a continuous-wave single-mode squeezed vacuum [89, 90]. Similarly, considering two-mode squeezed vacuum, A. E. B. Nielsen and K. Mølmer have theoretically investigated how the fidelity of the generated states can be affected by the time separation and have defined optimal temporal modes for Fock-state generation [86].

We experimentally investigated such scheme, using two-mode squeezed vacuum out of our type-II OPO and two photon detections, where now the delay between the events can be tuned. We have shown in the previous section that a small delay (typically 1 ns) between two conditioning events does not compromise the two-photon fidelity [58]. Thanks to our newly-developed high-efficiency SNSPDs, an unprecedented preparation rate was achieved. Here, this feature enables us to acquire a sufficient amount of data in a reasonable time to cover temporal separation between the two heralding clicks in a range much longer than the width of the temporal mode defined by the OPO cavity. Therefore, we can post-select the temporal delay between triggers within this range, and then explicitly demonstrate the behavior of the resulting state with this delay.

IV.3.1 Temporal mode definition

In the following, we consider the general case where the heralding detections have a temporal delay and we investigate how this delay affects the modal structure of the

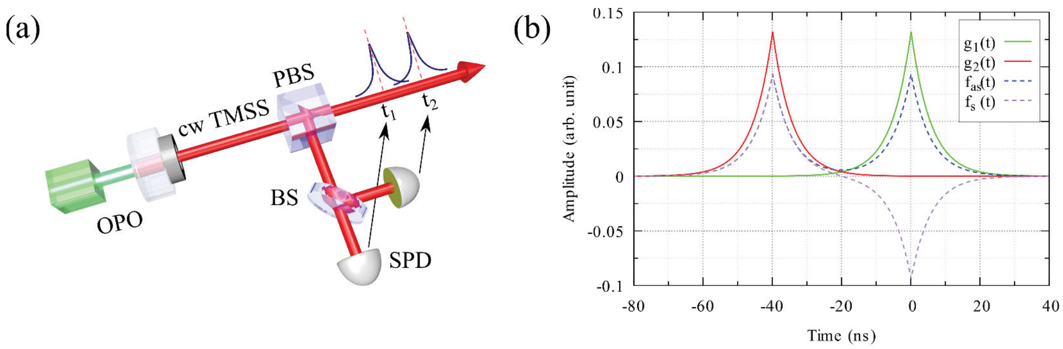

Figure IV.6: (a) Generation of two-photon state with time-separated conditional detections. OPO: nondegenerate optical parametric oscillator, SPD: single-photon detector, PBS: polarization beam-splitter, BS: beam-splitter, cw TMSS: continuous-wave two-mode squeezed vacuum state. (b) Temporal mode functions for an OPO cavity bandwidth $\gamma = 53$ MHz. The time separation of the heralding events is set to 40 ns here.

heralded state. The generation of two-photon state with time separated conditional detections is sketched on Fig. IV.6 (a). This scheme is the same as the setup presented for the two-photon Fock state generation, but we can now play on the acceptance window between the two photon detections.

For each single photon detected at the time $t_{1,2}$, the temporal modes can be defined as:

$$g_{1,2}(t) = \sqrt{\pi\gamma}e^{-\pi\gamma|t-t_{1,2}|}. \tag{IV.3.1}$$

These two modes are given in Fig. IV.6(b). The overlap I between the two modes, g_1 and g_2, depends on $\Delta t = |t_1 - t_2|$, the delay between the two detections, and can be written as

$$I = \int g_1(t)g_2(t)dt = e^{-\pi\gamma|\Delta t|}(1 + \pi\gamma|\Delta t|). \tag{IV.3.2}$$

The heralded two-photon state can thus be written:

$$|\Psi\rangle = \frac{1}{\sqrt{1+I^2}} \int\int dtdt' g_1(t)g_2(t')a^\dagger(t)a^\dagger(t')|0\rangle_1|0\rangle_2. \tag{IV.3.3}$$

where $\hat{a}^\dagger(t)$ corresponds to the operator associated with the idler photon in the mode in which the heralding detection took place. It is possible to rewrite the state $|\Psi\rangle$ in the form of two orthogonal temporal modes, a symmetric and an antisymmetric ones:

$$\begin{aligned} f_s(t) &= \frac{1}{\sqrt{2(1+I)}}[g_1(t) + g_2(t)], \\ f_{as}(t) &= \frac{1}{\sqrt{2(1+I)}}[g_1(t) - g_2(t)]. \end{aligned} \tag{IV.3.4}$$

These last modes are plotted in Fig IV.6 (b). The expression of the heralded state using these two modes enables to simplify the expression of the heralded state as:

$$|\Psi\rangle = \frac{1}{\sqrt{2(1+I^2)}}\Big((1+I)|2\rangle_s|0\rangle_{as} - (1-I)|0\rangle_s|2\rangle_{as}\Big). \tag{IV.3.5}$$

where $|x, y\rangle_{s,as} = |x\rangle_s \otimes |y\rangle_{as}$ and $|x\rangle_{s/as}$ corresponds to x photons in the mode $f_{s/as}(t)$.

IV.3.2 Experimental realization of Fock-state superpositions

As the experiment is performed in the continuous-wave regime, the two heralding events can occur at different times. The outputs of the two SNSPDs are connected to a fast digital oscilloscope (Lecroy Wavepro 7300A), offering a dual A-B triggering. By playing on the delay Δt, it is possible to play on the photon number distribution of the generated state.

The photocurrent $x(t)$ of the homodyne detection is recorded with an oscilloscope at a sampling rate of 10 Gs/s during 500 ns. As the local oscillator is continuous, post-processing is used to extract the heralded state in a given temporal mode $h(t)$. For each realization, we get a single outcome of the quadrature measurement as

$$x = \int h(t)x(t)dt. \tag{IV.3.6}$$

In our experiment, one million measurements are accumulated over the 65 ns acceptance window to obtain sufficient quadrature values for quantum state tomography with a maximum likelihood algorithm.

In the following, we discuss the different cases, from small delay, to large delay.

a Small acceptance range: generation of two-photon state

When Δt is small, and in particular for $\Delta t = 0$, i.e. the generation of a two-photon state, the situation is the one developed in the previous section. As seen later, a small delay $\Delta t = 1ns$ do not affect too much the fidelity of the heralded state.

b Large acceptance range: generation of two independent single photons

In this part, the time delay between the coincident triggers is set to be in an acceptance range much longer than the temporal mode duration defined by the OPO cavity bandwidth: $1/\gamma \approx 20$ns. In this situation, the generated states is made of two independent single photons, occupying the two temporal mode $g_1(t)$ and $g_2(t)$.

For example when the delay between two triggers is set to 40 ns, depending on which mode is used to reconstruct the state, different Fock-state superpositions can be generated. The photon number distributions are shown in Fig IV.7, for different temporal mode functions $g_1(t)$, $g_2(t)$, $f_s(t)$, and $f_{as}(t)$, used for the reconstruction of the density matrix.

For the temporal modes $g_i(t)$, adapted to a single-photon state, the single-photon fidelity is about 76%. This value gives an expected optimal two-photon fidelity about $0.76^2 \approx 0.58$ when heralded by zero-delay coincident triggers. This value is in agreement with the one measured in the small delay case.

c Intermediate acceptance range: from single-mode to two-mode structures

We now investigate the general case with an intermediate delay Δt.

Figure IV.8 gives the evolution of the photon number components depending on this delay, for the temporal mode $g_1(t)$. The solid lines are the theoretical evolutions of

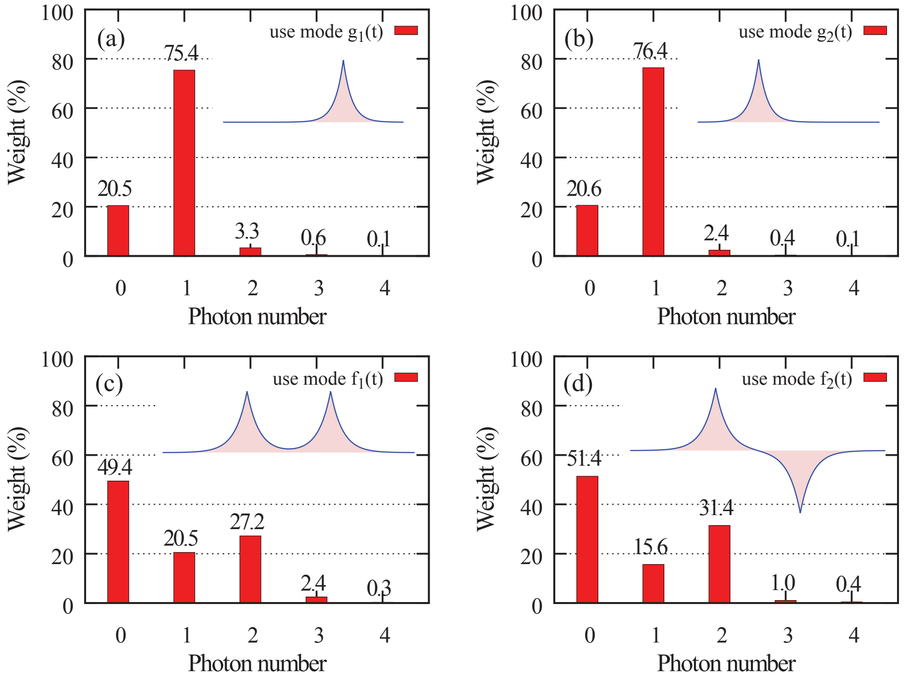

Figure IV.7: Photon-number distributions of the reconstructed states for the different temporal mode functions $g_1(t)$, $g_2(t)$, $f_s(t)$, and $f_{as}(t)$ shown in the insets. The distributions are not corrected for detection losses. The delay is set to 40 ns.

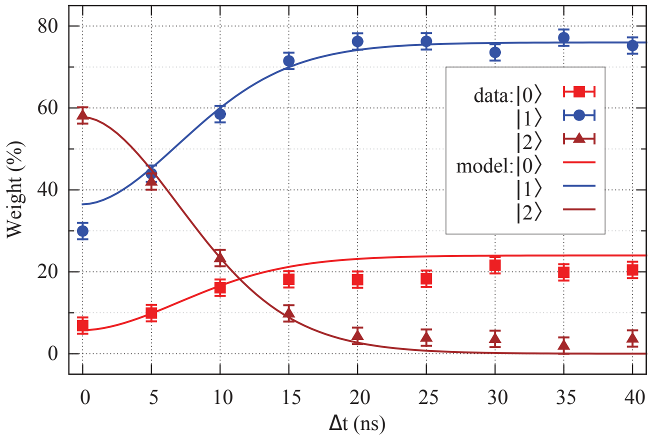

Figure IV.8: Photon-number weights of the reconstructed states for the fixed temporal mode $g_1(t)$ as a function of the delay Δt. The two parameters for the model are the OPO bandwidth $\gamma = 53$ MHz and the overall intensity transmission $\eta = 0.76$.

such components, by using $\gamma = 53$ MHz and $\eta = 0.76$ as the overall system efficiency. The slight discrepancy between the theory and the experiment is due to larger photon-number components that are not taken into account in the theory and were minimized in the experiment by using a very low pump power. The last data point corresponds to the previous case with large delay.

Figure IV.9 finally provides the two-photon component of the resulting state, when using the temporal mode $f_s(t)$. Using this mode, we can witness the degradation of the fidelity with the delay: this illustrates the transition from single mode to two-mode structure.

Interestingly, we can also observe that there is, in the case where the used temporal mode is $f_s(t)$, a plateau for the fidelity to two-photon Fock state at small delays. This favors the practical generation of two-photon Fock states.

Finally, in the case where the temporal mode $g_1(t)$ is used, the decay of the two-photon state fidelity with the delay Δt is faster than in the case where $f_s(t)$ is used. This is because $f_s(t)$ is the optimal temporal mode for a two-photon Fock state.

d Fidelity with a two-photon Fock state: best strategy

The two-photon fidelity for the mode $f_{s/as}(t)$ can be written by calculating the norm square of the weight coefficients of the state $|\Psi\rangle$:

$$\mathcal{F} = \frac{(1 \pm I)^2}{2(1+I^2)} = \frac{1}{2} \pm \frac{I}{1+I^2} \tag{IV.3.7}$$

where ± corresponds to the modes $f_s(t)$ and $f_{as}(t)$ respectively. The fidelity is maximized when the mode $f_s(t)$ is used. This mode is therefore the optimal temporal mode for two-photon Fock state generation.

In the case where the time delay is much bigger than the bandwidth of the OPO, the overlap I goes to zero. Therefore the fidelity to the two-photon Fock state when using the mode $f_s(t)$ is limited to $1/2$. This two-photon fidelity should therefore be in this case $0.58/2 = 0.29$, which is in good agreement with the measurements given in Fig. IV.7(c) and (d).

In the limit $\Delta t \to 0$, when the optimal mode $f_s(t)$ is used, the fidelity with a

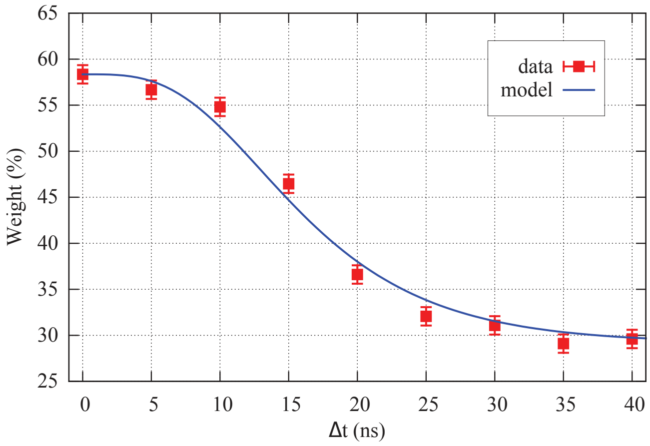

Figure IV.9: Weight of two-photon component for the optimal temporal mode $f_s(t)$ as a function of the delay between the two triggers. The blue line corresponds to the model taking into account the overall loss and the OPO bandwidth.

two-photon Fock state can be written:

$$F \approx 1 - (\frac{\pi\gamma\Delta t}{2})^4. \tag{IV.3.8}$$

When the mode $g_1(t)$ is used, the fidelity with a two-photon Fock state is:

$$F \approx 1 - (\frac{\pi\gamma\Delta t}{\sqrt{2}})^2. \tag{IV.3.9}$$

Therefore in the case where $f_s(t)$ was used, the fidelity is equal to 1 minus a small correction of fourth order, whereas in the case where $g_1(t)$ is used, the small correction is of second order. For a fixed temporal mode, the acceptance window should be thus reduced relative to the optimal adapted case.

This result confirms that a small delay can indeed be used without compromising the state fidelity but should be reduced in the second case. This highlights the importance of temporal modes when working with continuous-wave sources. When one wants to use a generated state in a quantum circuit, it is important to have a precise knowledge of its modal structure. Efficient methods have been developed recently to experimentally access the optimal mode via raw homodyne data without initial assumptions on the state [48, 91].

IV.4 Conclusion

We demonstrated a bright single-photon source that gathers a heralding efficiency larger than 90%, a low $g^{(2)}(0)$ and a narrowband spectrum. The unique combination of large escape efficiency OPOs, which enable a very low admixture of vacuum, and SNSPDs with close-to-unity efficiency, is making protocols based on multiple-photon conditioning more accessible and scalable. Based on this high quality source, we have therefore generated two-photon Fock states with the largest fidelity and the highest count rates so far.

Due to the continuous-wave light source used here, the possible delay between multiple conditioning events introduces a multimode temporal structure. The two-photon state fidelity achieved with the optimal temporal mode has therefore been measured as a function of the delay between the heralding events. We showed that in continuous-wave generation protocols, this temporal mode structure plays a central role and must be carefully studied.

Using this efficient source enables us to generate more exotic states like cat states based on multiple conditioning. This is the topic of the next chapter.

V Squeezing as a Tool for Quantum Engineering of Non-Gaussian States

Introduction

Squeezed light is commonly used in quantum information protocols based on gaussian resources [54]. In this chapter, we will describe quantum state engineering experiments where this gaussian resource can also help in the generation of complex non-gaussian states [92]. More specifically, we will show the engineering of large Schrödinger cat-like states where squeezing plays a central role [58]. The squeezing operation also helps to better protect these cat states from decoherence. We will finally demonstrate and characterize such protection.

Contents

V.1 Transition between a thermal state and a squeezed state 70
  - V.1.1 Two-mode squeezed state and rotated basis 70
  - V.1.2 Experimental implementation 71
  - V.1.3 Modeling the transition 75

V.2 Efficient generation of large squeezed Schrödinger cat states 77
  - V.2.1 Cat states in quantum optics and quantum information . . . 77
  - V.2.2 Methods for their generation 78
  - V.2.3 Engineering modulo a gaussian operation - The core states . 79
  - V.2.4 The protocol 81
  - V.2.5 Experimental setup 82
  - V.2.6 Results 83

V.3 Minimizing the decoherence by squeezing 86
  - V.3.1 From quantum to classical 86
  - V.3.2 Quantifying Decoherence 87
  - V.3.3 Experimental verification 92
  - V.3.4 A robust method for generating cat states 93

V.4 Conclusion 95

V.1 Transition between a thermal state and a squeezed state

Squeezing can find applications in a variety of continuous-variable protocols for quantum computing [17, 93–95], communication [96, 97], as well as in metrology [98] or in imaging [99]. It can also be useful, to improve the sensitivity of the main interferometer in the new generation of gravitational wave detectors [100, 101]. Experiments can now reach squeezing larger than 15 dB noise reduction [102].

Squeezed light is the most common non-classical Gaussian state. Thermal light, on the contrary, is a classical state, with gaussian distribution in phase-space. Two recent papers by G. Leuchs, R.J. Glauber and W. P. Schleich [103] focused on the link between the distribution in phase space of a state, related to its dimensionality, and its second-order intensity correlation [104]. They apply this method to three gaussian states: a coherent state, a thermal state and a squeezed state. This study opened a question about the evolution in between those three *"isolated islands"*. In the following we will experimentally and theoretically investigate the transition between a squeezed and a thermal state. Such study can be seen as an introduction in order to help the reader to understand the technique used for the engineering of large cat states, which will be developed in the next section, as the required main resource will be identical.

V.1.1 Two-mode squeezed state and rotated basis

The resources that will be used for this generation is a type-II phase matched OPO, already detailed in Chapter II and used in Chapter IV as a high-purity Fock state generator. In this system, under the absence of a conditioning event, the output can be written as the state:

$$|\psi\rangle_{i,s} = \hat{S}_{i,s}|0\rangle = e^{\frac{\xi}{2}(\hat{a}_i\hat{a}_s - \hat{a}_s^\dagger\hat{a}_i^\dagger)}|0\rangle \tag{V.1.1}$$

where a squeezing operator is applied to the vacuum. The generated state exhibits photon-number correlation called EPR-entanglement and can be written in the form:

$$|\Psi\rangle \propto \sum_{n=0}^{\infty} \Lambda^{2n}|n\rangle_i|n\rangle_s. \tag{V.1.2}$$

If one of the modes is traced out, a thermal state, which is a statistical mixture of photon number states, is generated on the other mode:

$$\hat{\rho}_{th} \propto \sum_{n=0}^{\infty} \Lambda^{4n}|n\rangle\langle n|. \tag{V.1.3}$$

In type-II phase matching crystals, signal and idler photons have orthogonal polarizations. When rotating the polarization basis of 45°, each annihilation and creation operator can be re-written as:

$$\begin{aligned} \hat{a}_s &= \hat{a}_1 + i\hat{a}_2 \\ \hat{a}_i &= \hat{a}_2 - i\hat{a}_1. \end{aligned} \tag{V.1.4}$$

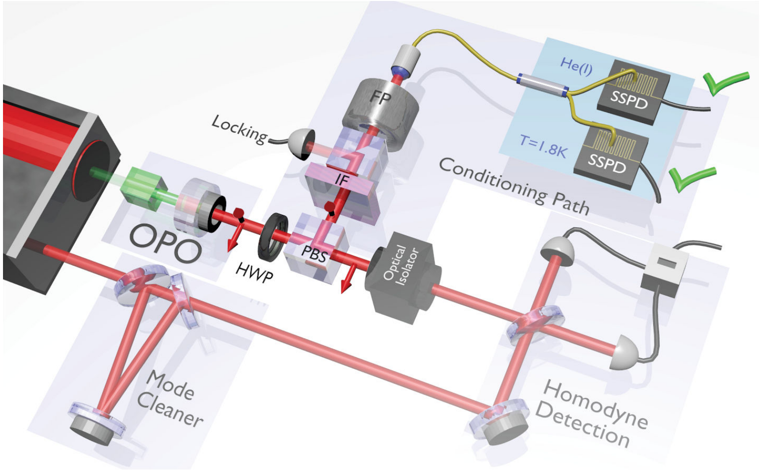

Figure V.1: Experimental setup: a type-II OPO is continuously pumped with a 532 Nd:YAG laser. The output modes are mixed using a polarized beam splitter (PBS) and a half-wave plate (HWP). A two-photon detection is implemented on one output of the polarized beam splitter, while the other output is analyzed via a homodyne detection for full quantum state tomography. This setup is equivalent to the one used for two-photon Fock state generation, at the difference of a HWP and a PBS, in order to play with the mixing of idler and signal modes.

The squeezing operator can therefore be re-written in the form of two single-mode squeezing operators:

$$\hat{S}_{si}(\xi) \rightarrow e^{\frac{\xi}{4}((\hat{a}_2+i\hat{a}_1)(\hat{a}_2-i\hat{a}_1)-h.c)} = e^{\frac{\xi}{4}(\hat{a}_1^2+\hat{a}_2^2-h.c.)}) = \hat{S}_1\hat{S}_2 \tag{V.1.5}$$

This corresponds to two uncorrelated squeezed vacuum states on each of the spatial modes 1 and 2:

$$|\Psi\rangle \propto \left(\sum_{n=0}^{\infty} c_n|2n\rangle_1\right)\left(\sum_{n=0}^{\infty} c_n|2n\rangle_2\right) \tag{V.1.6}$$

Depending on the half-wave plate angle (HWP), it is possible to either generate EPR-entanglement, leading to thermal states in each spatial mode, or to de-correlate the modes, which leads to independent squeezed vacua on each mode. This situation corresponds to the transition of one amplifier phase-insensitive to two independent amplifiers, which are phase-sensitive. In the following, we will therefore be able to study the transition between a squeezed state and a thermal state by simply changing the HWP angle. In particular, we will study the evolution of the quadrature variances and of the second-order correlation function.

V.1.2 Experimental implementation

The setup is presented in Fig V.1. This setup is similar to the one used in Chapter IV for two-photon Fock state generation. We use a type-II KTP triply-resonant optical parametric oscillator, pumped by a continuous-wave Nd:YAG laser at 532 nm. As shown previously, the output polarization modes can be mixed using a half-wave plate and a polarized beam splitter. One output of the beam splitter is frequency-filtered

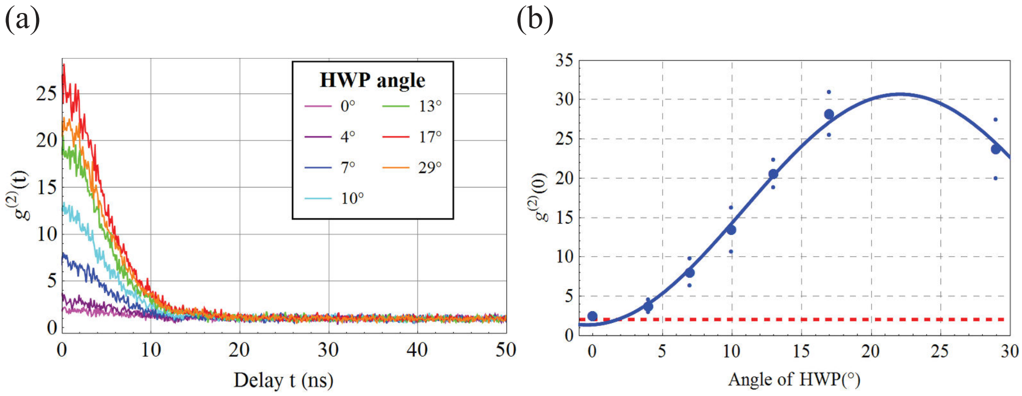

Figure V.2: (a) The coincidences rates of single-photon detections happening at different delays, normalized by the uncorrelated ($t \to \infty$) coincidences means, gives $g^{(2)}(t)$. This parameter is displayed for several angles of the HWP. A strong bunching effect happens at 0 ns delay. (b) $g^{(2)}(0)$ for different angle of the HWP. The solid line represents the theoretical fitting of the experimental data points with the model $f(t) = a \times \cos((x+b)\frac{\pi}{45})^2 + c$, where x is the angle of the HWP, and $\{a, b, c\}$ are the fitting parameters. 0° corresponds to a thermal state, while 22.5° corresponds to squeezed vacuum. The dotted red line corresponds to $g^{(2)}(0) = 2$.

via an interferential filter and a cavity. This path is then split on a fibered beam splitter, and the outputs are detected via two SNSPDs (see Chapters III and IV for more details). This configuration will enable us to check the second-order correlation function $g^{(2)}(t)$. The other output of the beam splitter is measured via a homodyne detection, enabling therefore to reconstruct the density matrix and the associated Wigner function, in order to study the quantum fluctuation variances.

For one angle of the HWP, we can record the second-order correlation function $g^{(2)}(t)$ of a state, and the density matrix of its complementary. However, the two recorded states only differs by a rotation in phase space. Therefore their quadrature variances and $g^{(2)}(t)$ are the same.

We will now give the results obtained independently for the $g^{(2)}(t)$ and the quadrature variances.

a Second-order correlation function

The filtered path enables to measure the second-order correlation function. For this purpose, we acquire, for an acceptance window between two detection events of 50 ns, the time of the two single-photon detections. The distribution of the photon coincidences depending on the delay normalized by the uncorrelated coincidences gives the $g^{(2)}(t)$ function, and is shown in Fig V.2(a) for several wave-plate angles. The zero angle of the HWP corresponds to the perfect separation of the two orthogonally polarized modes. A strong bunching effect appears at 0 ns delay, corresponding to $g^{(2)}(0)$.

The evolution of $g^{(2)}(0)$ with the angle of the HWP is shown in Fig V.2(b). The angle corresponding to the generation of EPR entanglement is 0°. Indeed for this

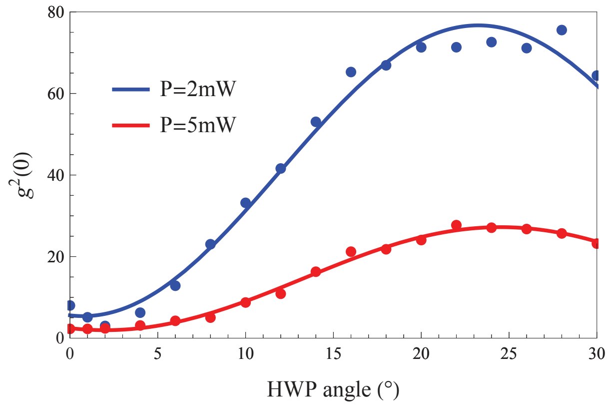

Figure V.3: Evolution of the $g^{(2)}(0)$ as a function of the angle of the wave plate, for two different input pump powers, 2 mW and 5mW, corresponding respectively to 0.7 and 1.6 dB of squeezing.

angle the output is made of two correlated thermal states, and their $g^{(2)}(0) = 2$ [105]. However, for a squeezed vacuum state, $g^{(2)}(0) > 2$ and more precisely, for a pure squeezed vacuum:

$$g^{(2)}(0) = 3 + \frac{1}{\langle \hat{n} \rangle}, \tag{V.1.7}$$

leading to $g^{(2)}(0) = 3$ for infinitely squeezed vacuum. Our two uncorrelated squeezed states, i.e. resulting from the perfect separation of the two parts of the two-mode squeezed state, corresponds thus to an angle of 22.5°. Our squeezing is voluntarily small here, close to 1.3 dB, in order to avoid any damage on the crystal. This value explains that we are far away from 3.

Evolution with the squeezing

Two sets of data have additionally been acquired for 2 mW and 5 mW of pump power, corresponding respectively to 0.7 and 1.6 dB of squeezing. They are shown in Fig V.3. A higher squeezing means that more photons are involved in the correlations. The obtained values are consistent with the mean photon number 0.0074 and 0.04, leading respectively to $g^{(2)}(0) = 75.5$ and $g^{(2)}(0) = 27.7$.

b Wigner function and evolution of the variances

Using our homodyne detection, for the same wave plate angle, we can reconstruct the full density matrix of the state and plot the associated Wigner function. We can thus witness the transition from a squeezed state, where one quadrature has smaller fluctuations than the other, to a thermal state. The data are given in Fig. V.4. From these Wigner functions, we can extract the variances of each quadratures and compare them to the expected values.

To deduce the quadrature variances, we fit the Wigner functions by a gaussian

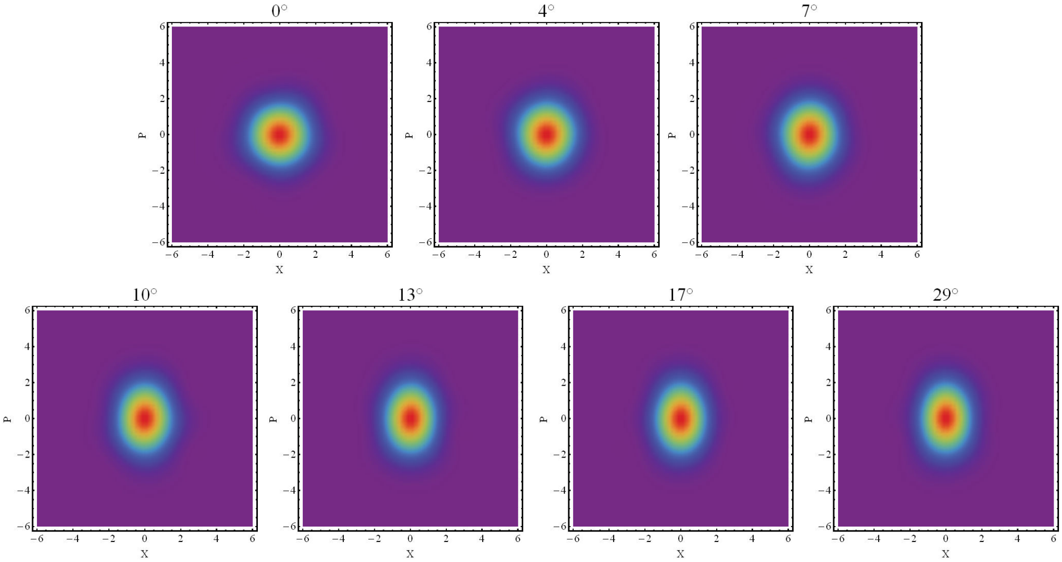

Figure V.4: Wigner functions for several HWP angles showing the transition from a thermal state corresponding to the angle 0° to a squeezed vacuum state.

distribution model:

$$W(x,p) = W_0 e^{\left(-x^2\left(\frac{\cos^2(\theta)}{2\sigma_x^2}+\frac{\sin^2(\theta)}{2\sigma_p^2}\right)-2xp\sin(2\theta)\left(\frac{1}{4\sigma_p^2}-\frac{1}{4\sigma_x^2}\right)-p^2\left(\frac{\sin^2(\theta)}{2\sigma_x}+\frac{\cos^2(\theta)}{2\sigma_p^2}\right)\right)}. \tag{V.1.8}$$

We can then deduce σ_x and σ_p, the standard deviation of the fluctuations of quadrature $\hat{X}$ and its orthogonal counterpart $\hat{P}$. They are plotted for different HWP angles in Fig V.5.

Therefore, for the same angles of the HWP, using one path we get the evolution of the variances, and using the other path we get the evolution of the second-order correlation function. In the following, we will show how these two evolutions can be

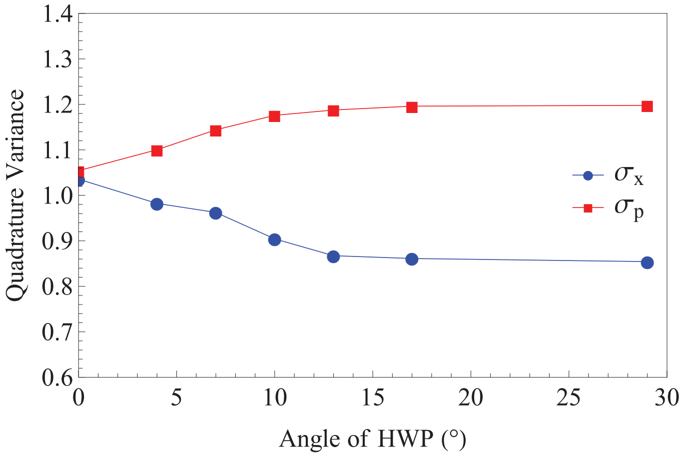

Figure V.5: Variances of the quadratures $\hat{X}$ and $\hat{P}$ extracted from the fitted Wigner function for different HWP angles.

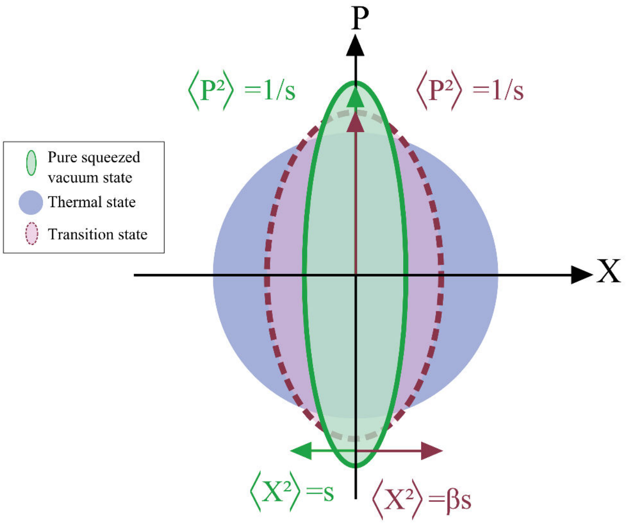

Figure V.6: Evolution of the phase space distribution of the state, from a pure squeezed vacuum state, in green, where $\beta = 1$, to a thermal state, in blue, where $\beta = \frac{1+s^2}{2s^2}$.

related, and theoretically model the transition.

V.1.3 Modeling the transition

Following these experimental results, we are now going to show how the correlation function and the variances evolution are related to each other. To do so, we will find a theoretical model for the evolution of the $g^{(2)}(0)$ function using the variances of the state.

To quantify the evolution between the two states, we introduce the transition parameter β as:

$$\langle \hat{X}^2 \rangle = \beta s, \tag{V.1.9}$$

where s will be here related to the variance of the quadrature $\hat{P}$: $\langle \hat{P}^2 \rangle = \frac{1}{s}$. β evolves from 1 to $\frac{1+s^2}{2s^2}$ during the transition from a squeezed vacuum state to a thermal state, as sketched in Fig. V.6. The correlation function can be written as follows:

$$g^{(2)}(0) = \frac{\langle \hat{a}^\dagger \hat{a}^\dagger \hat{a} \hat{a} \rangle}{\langle \hat{a}^\dagger \hat{a} \rangle^2} = \frac{\langle \hat{n}^2 \rangle - \langle \hat{n} \rangle}{\langle \hat{n} \rangle^2}. \tag{V.1.10}$$

The expression can be re-written with the variances of the quadratures $\hat{X}$ and $\hat{P}$ [106]. Indeed, for states with a Gaussian Wigner function of the form : $W(x,p) = W_0 e^{-ax^2-bp^2}$, we have:

$$\begin{aligned} \langle \hat{n} \rangle &= \frac{1}{4\sigma_0^2}(\langle \hat{X}^2 \rangle + \langle \hat{P}^2 \rangle - 2\sigma_0^2) \\ \langle n^2 \rangle &= \frac{1}{\sigma_0^4}(3\langle \hat{X}^2 \rangle^2 + 2\langle \hat{X}^2 \rangle \langle \hat{P}^2 \rangle + 3\langle \hat{P}^2 \rangle^2) - \langle \hat{n} \rangle - \frac{1}{2} \end{aligned} \tag{V.1.11}$$

where the quadrature variances can be expressed as a function of our experimental standard deviation:

$$\begin{aligned} \langle \hat{X}^2 \rangle &= \sigma_x^2 \\ \langle \hat{P}^2 \rangle &= \sigma_p^2. \end{aligned} \tag{V.1.12}$$

For a pure squeezed vacuum state, the variances of the quadratures are linked by the squeezing parameter as $e^{-2\xi} = s$. Therefore, $\beta = 1$, and:

$$\begin{aligned} \langle \hat{X}^2 \rangle &= s \\ \langle \hat{P}^2 \rangle &= \frac{1}{s}. \end{aligned} \tag{V.1.13}$$

The mean photon number can be written as:

$$\langle \hat{n} \rangle = \frac{1}{4}(s + \frac{1}{s} - 2). \tag{V.1.14}$$

The auto-correlation function $g^{(2)}(0)$ form for a squeezed vacuum can be finally deduced:

$$g^{(2)}(0) = 3 + \frac{1}{\langle \hat{n} \rangle}. \tag{V.1.15}$$

For a thermal state, $\langle \hat{X}^2 \rangle = \langle \hat{P}^2 \rangle$, directly leads to $g^{(2)}(0) = 2$[*]. In this case $\beta = \frac{1+s^2}{2s^2}$

It is then possible to write the correlation function in function of the transition parameter β:

$$g^{(2)}(0) = 3 + \frac{1}{\langle \hat{n} \rangle} - \frac{(\beta - 1)}{4\langle \hat{n} \rangle^2}. \tag{V.1.17}$$

β can be deduced from the standard deviation parameters extracted from the fitting of the Wigner function. We can then compare the $g^{(2)}(0)$ values obtained from this method to the ones obtained by direct coincidence detection.

The results are plotted in Fig. V.7. The results are globally consistent with each other. However the indirect method to acquire $g^{(2)}(0)$, by using the parameter β and the variances, seems to slightly minimize the correlation function compared to the direct acquisition by photon counting.

The perspectives of this work will be to study these methods for different squeezing, i.e. for different pump power, and to evaluate their $g^{(2)}(0)$ using different continuous variable measurements. A thinner precision, with better time resolution, and more squeezing points must be conducted in the future. In particular, it could be interesting to compare those results with the measurement of the Husimi-Q function, as

---

[*] Note that the starting hypothesis are different in the case of the coherent state. Indeed, in the case of the thermal state, we can write $\hat{X} = 0 + \Delta\hat{X}$, and $\hat{Y} = 0 + \Delta Y$. Therefore:

$$\langle \hat{X}^2 \rangle = \langle \Delta\hat{X}^2 \rangle = \langle Y^2 \rangle = \langle \Delta Y^2 \rangle. \tag{V.1.16}$$

In the case of a coherent state, we can write for example $\hat{X} = \hat{X}_0 + \Delta\hat{X}$, and $\hat{Y} = 0 + \Delta Y$. Therefore, the formula given for $\langle n^2 \rangle$ is different.

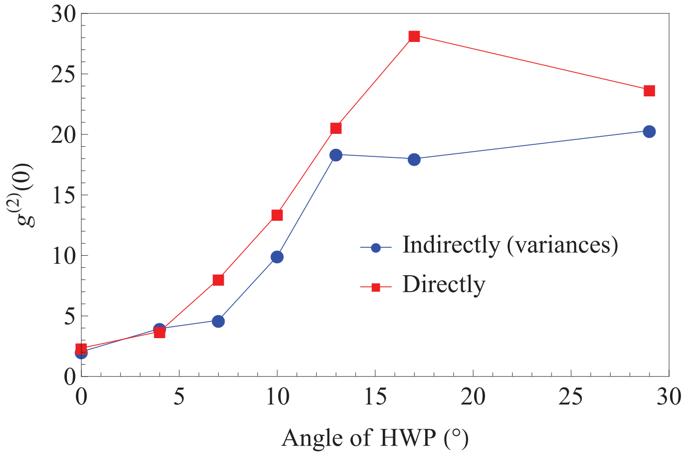

Figure V.7: Evolution of the $g^{(2)}(0)$ of the one output of the PBS as a function of the angle of the wave plate. The indirect method of evaluating the $g^{(2)}(0)$ using homodyne detection and Wigner function reconstruction is given in blue, while the direct method, using two single-photon detectors and coincidence counts is given in red.

pointed by C. R. Müller and co-workers [107]. This latest function is generally used to represent results obtained via heterodyne detection, while the Wigner function often characterizes homodyne detection results.

As a conclusion, we studied here the evolution between a thermal state and a squeezed vacuum state by using a type-II phase-matched OPO, a half-wave plate and a beam splitter. We are going to use this transition as a technique in order to generate squeezed Schrödinger cat states.

V.2 Efficient generation of large squeezed Schrödinger cat states

We studied on the previous section how to play with the output of a type-II OPO. We will demonstrate in this section that this ingredient enables to generate a "core state" for a variety of large squeezed Schrödinger cat states [58]. A core state is a state that can be transformed into the targeted state by only applying one or several gaussian operation [92]. By slightly mixing the idler and signal modes of the OPO output, we will generate superposition of 0 and 2 photon Fock states that have a very high fidelity to large squeezed cat states.

V.2.1 Cat states in quantum optics and quantum information

In the context of hybrid quantum information processing, a considerable effort has been dedicated to the generation of highly non-Gaussian states of light [10]. Specifically, free-propagating coherent-state superpositions, also referred as optical Schrödinger cat states, are an essential resource. Such states of the form

$$|\mathrm{Cat}\pm\rangle = \frac{1}{N_\pm}(|\alpha\rangle \pm |-\alpha\rangle) \tag{V.2.1}$$

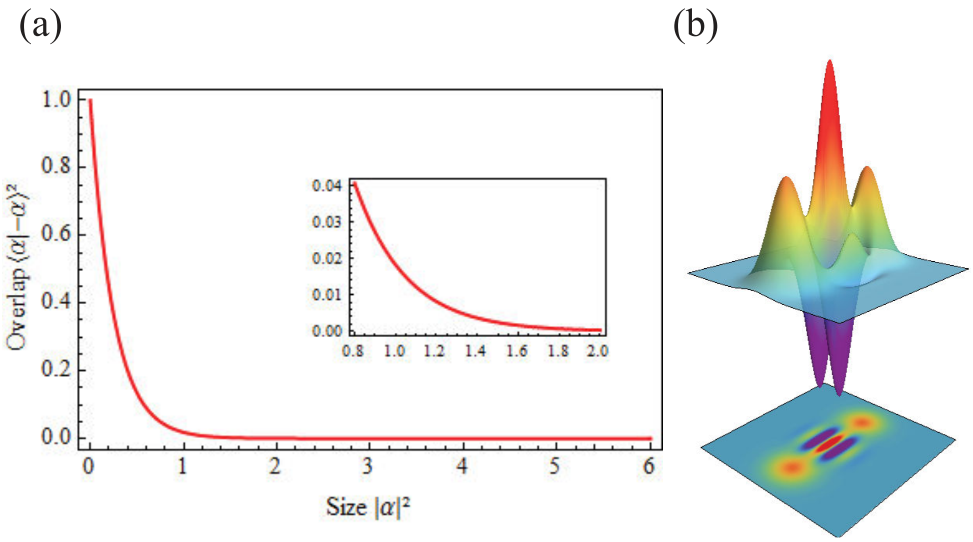

Figure V.8: (a) Overlap of two coherent states $|\alpha\rangle$ and $|-\alpha\rangle$ for several mean photon number $|\alpha|^2$. The inset gives a zoom on the 1 to 2 range. (b) Wigner representation of an even cat state of size $|\alpha|^2 = 3$.

consist in a superposition of two coherent states with opposite phases and mean photon number $|\alpha|^2$. They play the central role of qubits in the coherent state basis [4, 93, 108, 109], as an analogy with the $|0\rangle$ and $|1\rangle$ of the discrete-variable approach. However, in order to really encode the information onto a CV qubit, it is necessary to achieve orthogonality of the two coherent-state components. The overlap directly relates with the size of the superposition, i.e. the number of photon of the state $|\alpha|^2$, as :

$$|\langle\alpha|-\alpha\rangle|^2 = e^{-4|\alpha|^2}. \tag{V.2.2}$$

A theoretical plot of the overlap with the size of the superposition is shown in Fig V.8(a). The Wigner function of an even large cat state is given as an example in Fig. V.8(b). For example, fault-tolerant protocols require to reach a minimal size of $|\alpha|^2 = 1.2$ [110]. The generation of cat states with this minimal size and a generation rate large enough to allow subsequent operations will open a wealth of possible protocols and gate implementations [10, 111, 112]. However, such generation remains very challenging.

V.2.2 Methods for their generation

In cavity- or circuit-QED systems, size larger than $|\alpha|^2 \geq 2$ has already been reached [13, 113]. However, large free-propagating optical cat states that can be transferred through optical fibers are hard to generate. In this endeavor, various optical circuits have been developed to generate cat states using non-Gaussian resources. They are presented in Fig. V.9. The first seminal scheme consisted in subtracting a single-photon from a single-mode squeezed vacuum [11, 12, 82]. This operation can be performed by tapping a small part of squeezed light and by detecting it with a single-photon detector (Fig. V.9-M1). This process results in heralding a squeezed single-photon, which exhibits a high fidelity with an odd cat state with $|\alpha|^2 \sim 1$. Two-photon subtraction

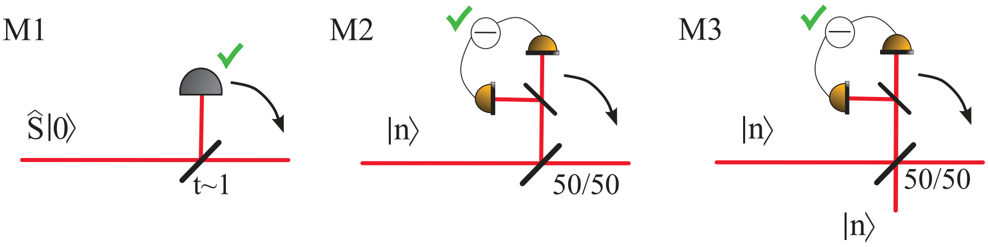

Figure V.9: Probabilistic methods to generate cat states. M1: photon subtraction on squeezed vacuum: a small part of the initial resource is tapped on a beam splitter, and detected via one or several single-photon detector. M2: Quadrature measurement on photon number states. An n-photon Fock state is sent onto a 50/50 beam splitter. On one output of the beam splitter is implemented a homodyne detection. The detection of a certain quadrature heralds the generation of a large cat state. M3: Variant of the M2 method. Several Fock states are mixed on a beam splitter. On one of the input of the beam splitter a quadrature measurement via homodyne detection is performed.

operated on squeezed light, with [89] or without [114] time-separation, has led to values $|\alpha|^2$ close to 2. An alternative method has provided a 3 dB-squeezed cat state with $|\alpha|^2 = 2.6$ [115]. For this purpose, a two-photon Fock state was first heralded, split on a beam splitter, and one output was measured by homodyne detection. A quadrature measurement within a given acceptance window is used as third conditioning (Fig. V.9-M2).

Up to now, cats of size $|\alpha|^2$ larger than 2 have been obtained with a very limited preparation rate, in the Hz level. In all cases this limited rate is coming either from photon subtraction on single mode squeezed light, where experimentally only a very small part of the beam can be tapped, or from the cascading of several conditioning operations. Recently, a similar approach based on the interference of two single-photons and homodyne conditioning has led to the same result (Fig. V.9-M3) [116, 117]. In all these experiments, the low generation rate precludes their use in subsequent protocols.

In this context, we implemented a new method for the generation of large optical Schrödinger cat states, based on two-mode squeezed vacuum and a n-photon detection performed on one of the modes, as explained in the following [58]. Importantly, rates two orders of magnitudes larger than obtained in previous experiments are demonstrated.

V.2.3 Engineering modulo a gaussian operation - The core states

As one cannot obtain non-gaussian states by using only gaussian operations and gaussian resources, generation of states that exhibits strong non-gaussianity is technically tricky. Indeed, non-gaussian resources such as highly pure single-photon are tricky to implement experimentally, and cascaded non-gaussian operations such as photon subtraction decrease a lot the count rate. Thus to overcome the difficulty of generating such states, one can find help in the addition of a gaussian operation. This operation will help to target the size, i.e. a certain number of photons, while the non-gaussianity will be realized by the implementation of a minimized number of non-gaussian operations.

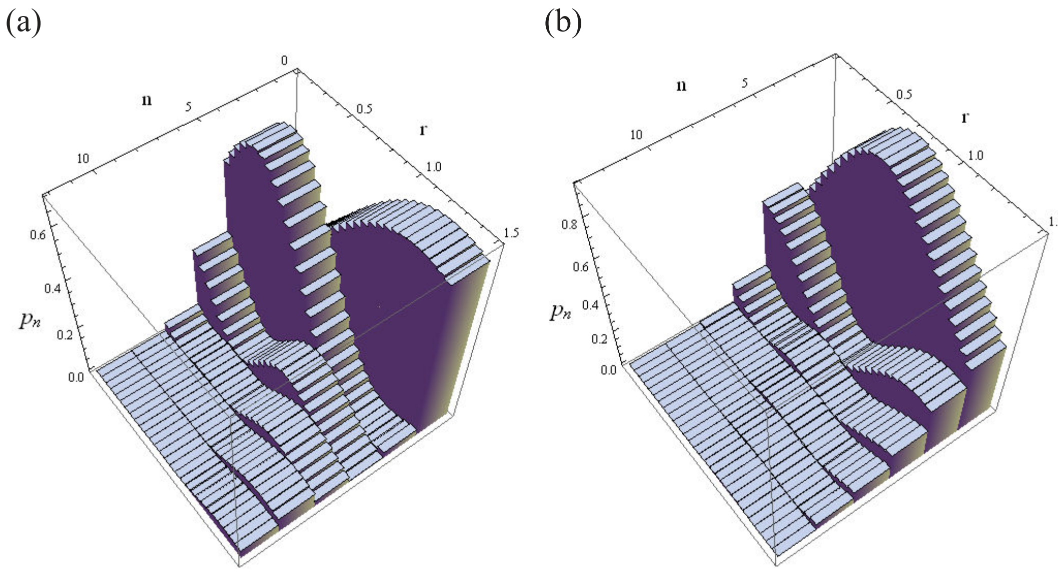

Figure V.10: Representation of the core states of two cat states of size $|\alpha|^2 = 3$. Each core state is labeled by a different squeezing $r = |\xi|$ and have a different photon number distribution, characterized by the photon number n, and the weight p_n. The even cat state core states are shown in (a), and the ones for the odd-parity cat are shown in (b). This figure is extracted from the work of D. Menzies and R. Filip [92].

In this spirit, the idea of the protocol we built is based on optimizing the state engineering by focusing all the non-gaussian resource and operation in generating the non-gaussian part of the state. Then, by using a gaussian operation such as displacement or squeezing, it is possible to target the desired size of the state. By identifying the minimal non-gaussianity needed in the targeted state, this strategy leads to better results while requiring less photon detections.

Figure V.10 shows different core states for even and odd cat states with $|\alpha|^2 = 3$, corresponding to different squeezing operations. The core state which has the smaller photon number will also be the one minimizing the number of non-gaussian resources or operations. By building this core state, and then implementing the optimal squeezing operation [118], it is thus easier to experimentally target larger cat states.

For example, as shown in Fig. V.10(a), a squeezed even cat state with squeezing parameter $|\xi| \approx 0.5$, is a superposition of $|0\rangle$ and $|2\rangle$. Therefore, if we are able to generate any superposition of $|0\rangle$ and $|2\rangle$ photon state, by using a subsequent unsqueezing operation such as described in [118], it is possible to target a large variety of even cat state.

Generally, in order to generate the core state with the minimal number of photons, we can check theoretically what is the optimal squeezing. For example, for an even cat state, to check which squeezing is more adapted to a given cat of size $|\alpha|^2$, we can check when the coefficient c_4 of the 4-photon component of a squeezed cat states gets cancelled:

$$c_4 = \frac{\sqrt{\lambda^4}\left(\frac{8\alpha^4\left(1-\lambda^2\right)^2}{\lambda^2} - \frac{48\alpha^2\left(1-\lambda^2\right)}{\lambda} + 24\right)}{8\sqrt{6}} \qquad \text{(V.2.3)}$$

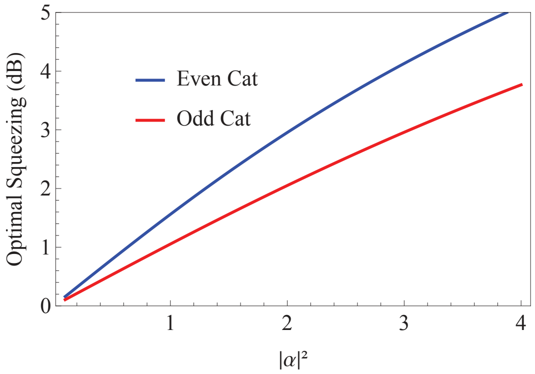

Figure V.11: Theoretical plot of the optimal squeezing with α for even (blue) and odd (red) cat state.

where $\lambda = \tanh|\xi|$. We get several solutions for this equation, and for each of those, we can plot the probability of having 6-photon and 8-photon components. The optimal squeezing, to erase all higher components in the desired range ($\alpha < 1.7$) is given by the solution:

$$\lambda_{\mathrm{E,Opt}} = -\frac{-\sqrt{4\alpha^4 + 6\sqrt{6} + 15} + \sqrt{6} + 3}{2\alpha^2}. \tag{V.2.4}$$

In order to simplify the expressions given in the following we will sometime use this specific squeezing. The same idea can be applied for an odd cat state, by cancelling its 5-photon component, we can find a physical solution for the optimal squeezing:

$$\lambda_{\mathrm{O,Opt}} = \frac{\sqrt{4\alpha^4 + 10\sqrt{10} + 35} - \sqrt{10} - 5}{2\alpha^2}. \tag{V.2.5}$$

In figure V.11 is plotted the optimal squeezing with the size of the cat state, for even and odd cat states.

V.2.4 The protocol

To generate a superposition of $|0\rangle$ and $|2\rangle$, one can mix two squeezed vacua and implement an n-photon detection. Two squeezed vacua of form $\hat{S}(\xi)|0\rangle$ are first overlapped with a $\pi/2$ phase-shift on a tunable beam splitter. The beam splitter here is slightly asymmetric with the asymmetry $\epsilon = \sin(2\theta) \ll 1$. Depending on the squeezing level, the detection of n photons in the conditioning channel heralds the following state:

$$|\Psi\rangle = \frac{1}{\sqrt{n(n-1)\epsilon^2 + \lambda^2}}(\epsilon\sqrt{n(n-1)}|n-2\rangle + \lambda|n\rangle) \tag{V.2.6}$$

with λ the squeezing parameter and $r = \sqrt{(1+\epsilon)/2}$ the reflection of the beam splitter. This expression is valid in the limit of small squeezing ($\lambda \ll 1$, where three-photon components are therefore ignored), and where the multiplexing of several on-off single-photon detectors is equivalent to a photon number resolving detector.

Equivalently this scheme can be realized using a two-mode squeezed state instead of two single-mode squeezed state, as shown in Fig. V.12. The output modes of

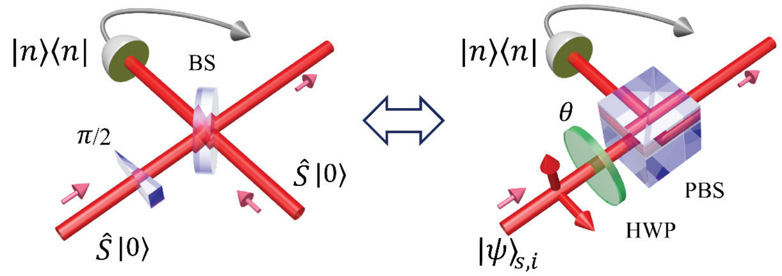

Figure V.12: Schemes for generating the superposition $\alpha|n-2\rangle+\beta|n\rangle$. (a) Two squeezed vacua are mixed on a tunable beam splitter. The detection of n photons in one of the outputs heralds the generation. (b) Equivalently, the scheme can be implemented directly from a two-mode squeezed vacuum. The two orthogonally-polarized modes are separated with a tunable mixing ϵ induced by a rotated half wave plate and a polarizing beam splitter, with $\epsilon = \sin(2\theta)$. The angle $\theta = 0°$ corresponds to the perfect separation, leading to the generation of a n-photon state.

our OPO are orthogonally polarized. The mixing can be realized by separating the beams after a small polarization rotation induced by a half-wave plate (HWP). Such implementation will be realized experimentally here, where as detailed in Section V.1, two independent squeezing modes can be mixed and exit an EPR-entangled state. In this case the mixing parameter is given by $\epsilon = sin(2\theta)$. To control the phase between the two components, it is possible to add birefringent elements before the polarized beam splitter.

Given a two-photon detection it is thus possible to herald any superposition of $c_0|0\rangle + c_2|2\rangle$ which can have a high fidelity with an even squeezed cat. A three-photon detection would herald superpositions $c_1|1\rangle + c_3|3\rangle$, which have high fidelities with odd squeezed cat. Numerical simulations of the fidelity with squeezed cat states depending on the number of photon detection are given in Fig. V.13. Squeezed cat states can be written:

$$\hat{S}(\xi)|Cat\pm\rangle = \frac{1}{\sqrt{2(1 \pm e^{-2|\alpha|^2})}}\hat{S}(\xi)(|\alpha\rangle \pm |-\alpha\rangle) \tag{V.2.7}$$

and their Wigner function can be found in the Chapter 1. For each point, the fidelity has been optimized by the size $|\alpha|^2$ and the squeezing applied to the cat. Fidelities higher than 98% can be obtained with cats of size as large as $|\alpha|^2 = 3$ for a two-photon detection, and as large as $|\alpha|^2 = 5$ for three-photon detection.

V.2.5 Experimental setup

To generate this superposition state, we use the same type-II phase-matched OPO, with a two-photon detection on the conditioning path, as shown in Fig. V.1, of section V.1. This time, the two-photon detection will be used as herald for the generation of squeezed cat states. If the two modes are perfectly separated like in Chapter IV, given a two-photon detection event, the generation of two-photon Fock state is obtained. However if one add a very small angle to the half-wave plate before the polarized beam splitter, states with high fidelity with squeezed Schrödinger cat states are produced.

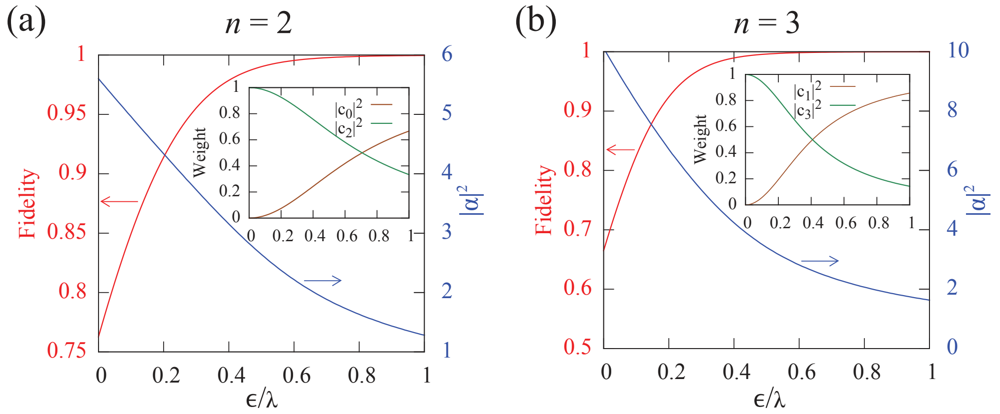

Figure V.13: (a) Two-photon detection: fidelity with a squeezed even cat state as a function of the ratio ϵ/λ. The fidelity is optimized by the size $|\alpha|^2$ and the squeezing of the target state. The inset gives the weights of the vacuum and two-photon components. (b) Three-photon detection state and fidelity with a squeezed odd cat state.

This experiment is performed in the continuous-wave regime, thus two events can occurs at different time. The acceptance coincidence windows is the same that set in the case of two-photon Fock state generation in Chapter IV, i.e. 1 ns.

V.2.6 Results

For an angle of the wave plate enabling the perfect separation of the signal and idler modes, i.e. $\theta = 0°$, a two-photon Fock state is generated, as described in Chapter IV. The angle of the plate is then increased up to 4.4°. The associated Wigner functions for different angles are given in Fig. V.14. The mixing strongly influences the output states which start to exhibit phase dependency and cat-like behavior. The larger the angle is, the smaller the generated cat is, up to a squeezed state.

We will focus now on two of the generated squeezed cat states corresponding to the angles $\theta = 1.6°$ and $\theta = 2.4°$. Marginal distributions, photon number probabilities, and Wigner functions (with correction from detection losses, 15%) are given in Fig. V.15.

Fidelities with cat state are also the highest reported to date, reaching 80% as

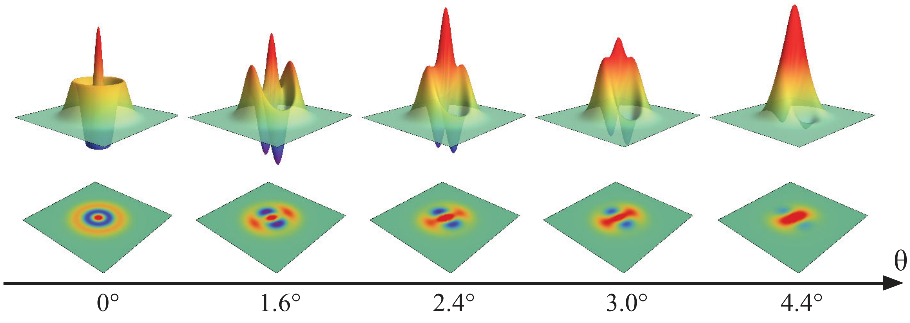

Figure V.14: Wigner function of the generated cats for angles going from 0° to 4.4°

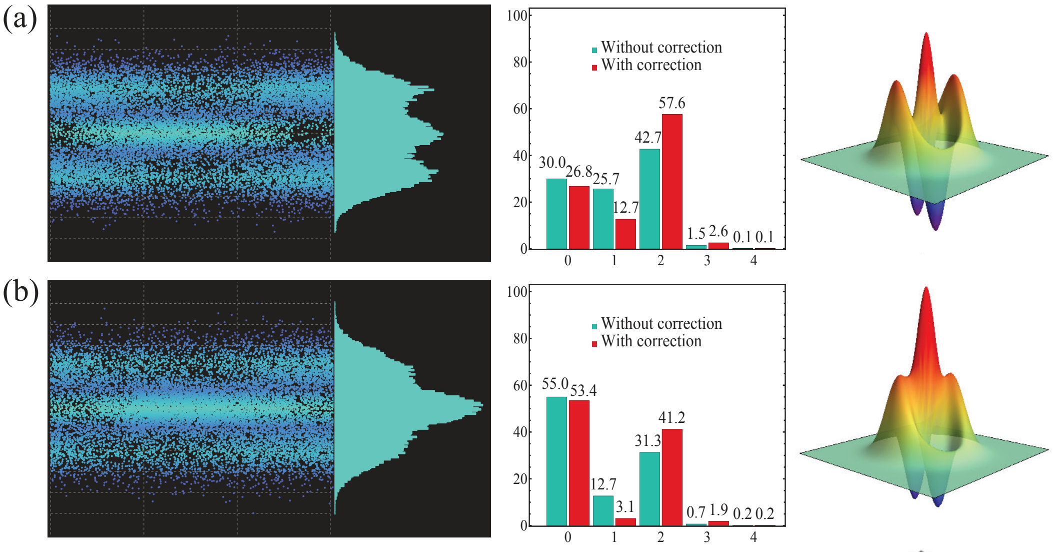

Figure V.15: From left to right, Homodyne detection acquisition for different phases, Marginal, and photon number probabilities of two generated squeezed cat states and Wigner function, for (a) $\theta = 1.6°$ and (b) $\theta = 2.4°$, with correction from detection losses (15%).

shown in Fig V.16, where the fidelity with cat states of different sizes and for different squeezing is displayed. The main limitation of this fidelity is due to the escape efficiency of the OPO.

It is important to note that these states are very phase-sensitive. Indeed due to insufficient sampling of the fringes of the homodyne detection, the first version of the experiment that we published only reached a 68% fidelity. These errors in the sampling of the homodyne detection are equivalent in introducing wrong phases for the state in phase-space. An ideal squeezed even cat state, shifted by certain phase φ can be written as:

$$|\Psi\rangle_\varphi \propto \hat{S}(\lambda)(|\alpha e^{i\varphi}\rangle + |-\alpha e^{i\varphi}\rangle) \propto \sum c_{2n} e^{in\varphi}|2n\rangle \tag{V.2.8}$$

where:

$$c_n = \sqrt{\frac{\lambda^n}{2^n n!}}\left(H_n\left(\sqrt{\frac{1-\lambda^2}{2\lambda}}\alpha\right) + H_n\left(-\sqrt{\frac{1-\lambda^2}{2\lambda}}\alpha\right)\right). \tag{V.2.9}$$

By modeling the phase noise by a gaussian noise, the resulting state is slightly phase-averaged, and can be written as:

$$\hat{\rho} = \frac{1}{\sigma\sqrt{2\pi}} \int |\Psi\rangle_\varphi \langle\Psi| e^{-\frac{\varphi^2}{2\sigma^2}}. \tag{V.2.10}$$

An example of the evolution with the gaussian noise standard deviation σ of the fidelity to a targeted squeezed cat state of size $|\alpha|^2 = 3$ is given in Figure V.17, for different losses. The bigger $|\alpha|^2$ is, the more two-photon component there is, and the more sensitive to phase noise the state is. To estimate this noise experimentally, it is possible to record the deviation between two fitted fringes on the continuous signal

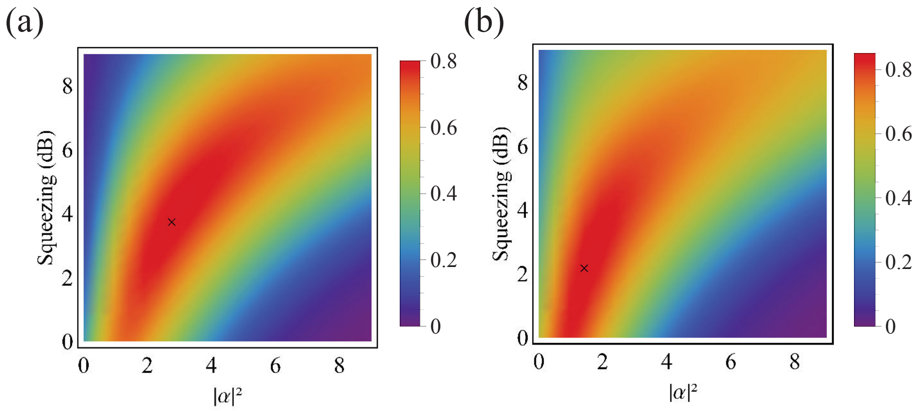

Figure V.16: Fidelity between the generated state and a squeezed even cat state, for(a) $\theta = 1.6°$ and (b) $\theta = 2.4°$. The plots give the calculated fidelity as a function of $|\alpha|^2$ and the squeezing in dB. The black crosses indicate the maximal fidelities. For $\theta = 1.6°$, the fidelity reaches 0.79 with an even cat state of size $|\alpha|^2 = 2.82$ and a 3.8 dB squeezing. For $\theta = 2.4°$ it reaches 0.84 with an even cat state of size $|\alpha|^2 = 1.54$ and a 2.3 dB squeezing.

of the homodyne signal. This amount of noise measured must then be multiplied by a factor of 2. Indeed, an angle of π for the fringes is equivalent to an angle of 2π in phase space, meaning that the sensitivity to the phase noise is twice bigger in phase space. An important work on the optimization of this noise has been realized, by better stabilizing the optical table and isolating the mechanical shutters used to block the light. We now manage to get a deviation noise under $\sigma \sim 0.1$ rad in phase space during an overall acquisition of 30 min, instead of $\sigma \approx 0.2 - 0.4$ rad in the previous work [58]. We also increased the sampling rate in order to determine more accurately the homodyne detection phase angle. This helped us to reach the fidelity of 80% for all

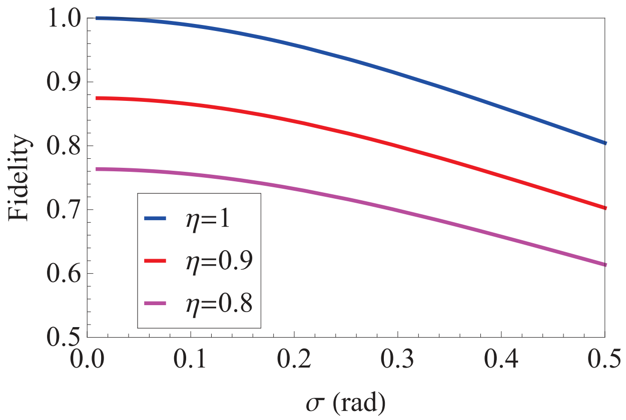

Figure V.17: Evolution of the fidelity between an ideal squeezed cat state and a squeezed cat state of size $|\alpha|^2 = 2.8$, and 4 dB squeezing, i.e., the generated cat corresponding to the angle $\theta = 1.6°$, with gaussian phase noise of standard deviation σ, for different system losses: 0% in blue, 10% in red and 20% in pink.

our generated squeezed cats instead of the limited 68% efficiency we initially published.

Importantly, the achieved rate is higher than 200 Hz, thanks to the combination of this mixing technique and high-efficiency SNSPDs: we only have two costly operations (single-photon detections) that we realize very efficiently. This rate is two orders of magnitude larger than previous experiments. Furthermore this scheme is versatile and allows to easily adapt the parameter ϵ (linked to the HWP angle) in order to produce many types of squeezed cat states. The fidelity is the best achieved so far for free propagating cat states. These free-propagating cats are ready to be used in subsequent protocols thanks to the achieved rate.

In the next section we will show that this method to generate the core state with the smaller number of photons is also a way to produce cat states robust to decoherence. This means that by the help of a gaussian operation, i.e. squeezing, we can better protect such states from decoherence.

V.3 Minimizing the decoherence by squeezing

Non-gaussian states, and specifically the paradigmatic Schrödinger cat state, are well-known to be very sensitive to losses. When propagating through damping channels, these states quickly lose their non-classical features. However, by optimally squeezing the superposition states, the decoherence process can be qualitatively changed and substantially slowed-down [119].

In this section, we experimentally observe the reduced decoherence of squeezed coherent-state superpositions through an amplitude damping channel. In particular, we will show that the core state which minimizes the photon number is the most robust squeezed cat state against a damping. It is therefore the most suitable for the transmission and storage of non-Gaussian states. To quantify the robustness of states, we introduce and measure a speed of decay of the Wigner function negativity.

V.3.1 From quantum to classical

Preserving the quantum nature of a state is a key point towards the implementation of quantum protocols and the expansion of quantum technologies. When a quantum state travels through a network, it suffers from its interaction with the environment, whether it comes from dephasing or from optical losses (10 km of fiber is equivalent to 20% loss). The quantum state interacts with its environment leading to correlations that cannot be measured and have to be traced out: information about the quantum state is lost.

This decoherence effect increases with the dimension of the system. For example the more photons a superposition state contains, the faster it will lose its coherence: a n-photon Fock state will lose its n-photon component on a scale η^n, where η is the system efficiency. The idea behind this effect leads back to the famous *gedankenexperiment* of Schrödinger [41], where the likeliness of having a macroscopic superposition decreases with the size of the system. This property makes the situation of having a macroscopic state (a real cat) in a quantum superposition impossible to witness. The simple fact that the cat breathes (or not), i.e. its interaction with our environment, would already collapse the quantum superposition onto a classical state.

The main idea that will be developed here, is to make macroscopic superpositions more robust to losses by optimally squeezing them, until the minimal mean number of photon is achieved, i.e. by going back to the core state of the cat. Then, as the state has less photons, it also suffers less from decoherence. Theoretical studies have already shown this effect on different parameters such as purity, or on non-classical parameters [120, 121]. Here we study particular parameters linked to the negativity of the Wigner function. Importantly, we will then experimentally check our method by adding losses to squeezed cat states, then performing homodyne measurement to reconstruct their density matrices, and following their decoherence.

V.3.2 Quantifying Decoherence

Decoherence is a very general term, often seen as a decrease in terms of fidelity or purity of a state. However the fidelity and the purity are very general tools and only give a wide quantification of an overall decoherence process. To characterize the evolution of decoherence, people often use as well the evolution of the Wigner function [13], and in particular of its negativity. The negativity of the Wigner function is a criterion of quantumness and non-classicality. The number of Wigner function negativities, often used as a characteristic of the quantumness of a state, can also be related to the number of non-gaussian operation implemented. The main fringe of the cat state's Wigner function is related to the phase relationships between the two main parts of the cat, i.e. the two coherent states, and represents the quantum feature of the superposition.

When going through a lossy channel, the contrast of the central fringe of a cat state decreases, leading a comparable reduction in the negativity of the Wigner function. However, when the mean number of photon is smaller, typically when a cat state is squeezed, the contrast and the negativity are the same for no losses while their robustness to losses is very different. A theoretical plot of the Wigner function and the central fringe of an even cat state and its optimally-squeezed counterpart is shown in Fig. V.18. If this state is going through an 80% transmission channel, such as 10 km of optical fiber, the negativity and the contrast of the Wigner function are much better preserved for a squeezed cat state.

Following the idea of the core state method developed and experimentally illustrated in the previous section, the most robust squeezed cat state will be the one with the fewer photon number. In order to simplify the mathematical expressions given in the following, we will sometimes give them for optimal squeezing, which expression was developed in the previous section.

a A decoherence quantification: the speed of decay

In atomic system, the decoherence is observed in the time scaling, and it is often characterized by the lifetime of the quantum system. Following the same idea, we propose a criterion that is based on "how fast" a quantum property decoheres. This work is based on a collaboration with R. Filip.

The quantum property, which will be observed here, is the negativity of the Wigner function, as it can be easily accessed via our experimental process of homodyne tomography. It corresponds to the minimal value of the Wigner function.

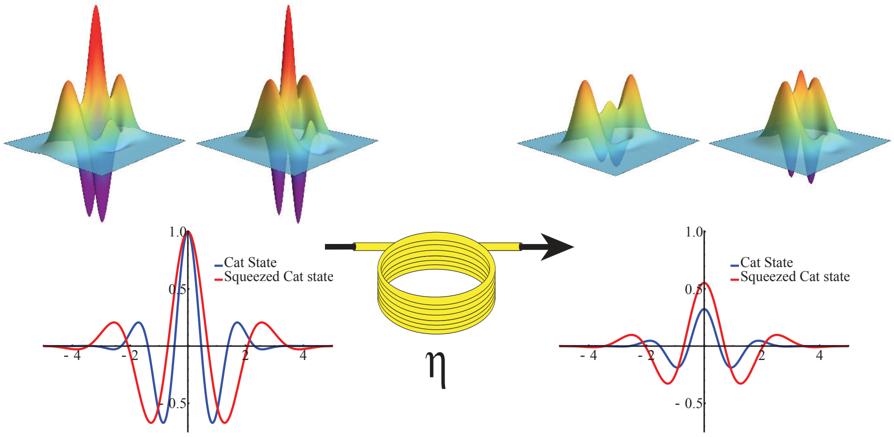

Figure V.18: Illustration of the decoherence process. The Wigner functions of an even coherent-state superposition ($|\alpha|^2 = 3$) and of its squeezed counterpart (4 dB-squeezing) are displayed before and after propagation through an amplitude-damping channel (transmission $\eta = 0.8$). The 2D plots give the cross-sections of the Wigner functions along the imaginary axis. The oscillations are damped with the loss but the contrast is better preserved for the squeezed version.

We introduce therefore the speed of decay of the Wigner function negativity, as the normalized derivative of the negativity of the Wigner function with the efficiency:

$$SD_W(\eta) = \frac{1}{W(x_{min}, p_{min}, \eta)} \frac{\partial W(x,p,\eta')}{\partial \eta'}\bigg|_{x_{min}, p_{min}, \eta}. \tag{V.3.1}$$

In the following, we will introduce a few examples of the evolution of this criterion.

- **For a single-photon state**

$$\begin{aligned} W_{|1\rangle}(0,0,\eta) &= \frac{1-2\eta}{2\pi} \\ SD_{W,|1\rangle}(\eta) &= -\frac{2}{1-2\eta} \end{aligned} \tag{V.3.2}$$

For a perfect transmission: $SD_{W,|1\rangle}(1) = 2$.

- **For a two-photon Fock state**

$$\begin{aligned} W_{|2\rangle}(0,p_{min},\eta) &= -\frac{e^{\frac{\sqrt{12\eta^2-8\eta+2}-6\eta+2}{2\eta}}\,\eta\left(\sqrt{12\eta^2-8\eta+2}-2\eta\right)}{\pi} \\ SD_{W,|2\rangle}(\eta) &= \frac{(2\eta-1)\left(\sqrt{12\eta^2-8\eta+2}-2\eta+1\right)}{\eta^2\left(\sqrt{12\eta^2-8\eta+2}-2\eta\right)} \end{aligned} \tag{V.3.3}$$

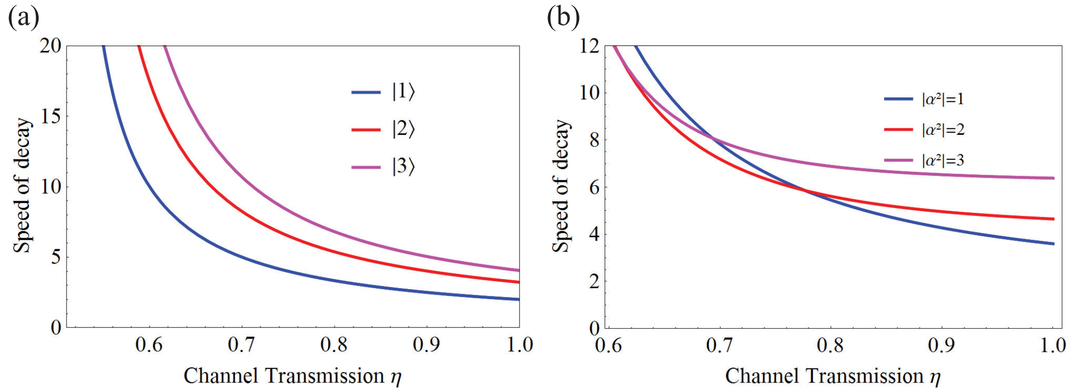

Figure V.19: (a) Theoretical plot of the evolution of the speed of decay of different Fock States with the transmission η of the channel. (b) Theoretical plot of the evolution of the speed of decay of cat states of different sizes with the transmission of the channel.

with $p_{min} = \sqrt{-\frac{\sqrt{12\eta^2-8\eta+2}-6\eta+2}{\eta}}$.
For a perfect transmission : $SD_{W,|2\rangle}(1) = \frac{1}{2}(4+\sqrt{6}) \approx 3.22$.

In Fig V.19(a) is shown the theoretical evolution of the negativity and speed of decay for different Fock states.

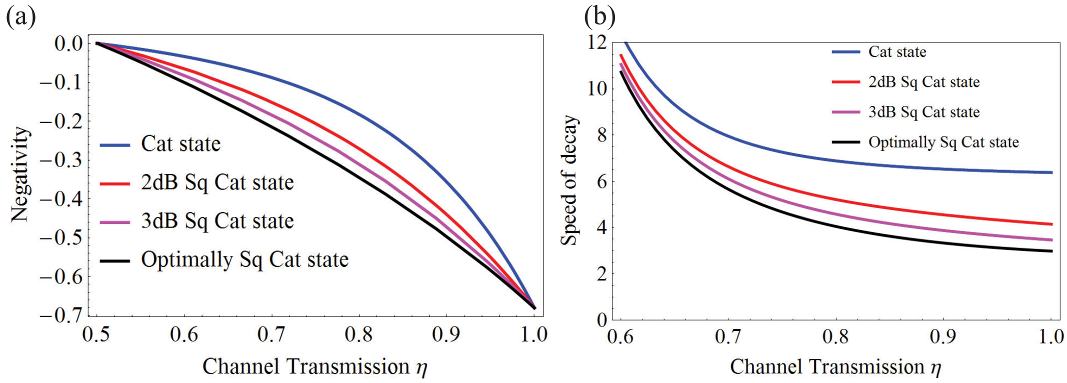

Figure V.20: Theoretical plots of the evolution of (a) the negativity of the Wigner function and (b) the resulting speed of decay of a cat state without and with different squeezing, as a function of the transmission of the channel. The considered size is $|\alpha|^2 = 3$.

- **For a cat state:**

$$W_{|cat+\rangle}(x,p,\eta) = \frac{e^{-\frac{x^2+p^2}{2}-2\alpha^2(\eta-1)-2x\alpha\sqrt{\eta}}\left(2e^{2\alpha\left(\alpha(2\eta-1)+\sqrt{\eta}x\right)}\cos\left(2\alpha\sqrt{\eta}p\right)+e^{4\alpha\sqrt{\eta}x}+1\right)}{4\pi\left(e^{2\alpha^2}+1\right)} \tag{V.3.4}$$

For simplification purpose, the expression for the speed of decay will be given for $x = 0$ (given a rotation in phase space, the final expression remains the same):

$$SD_{W,|cat+\rangle}(\eta) = -\frac{\alpha\left(4\alpha\sqrt{\eta}-4\alpha\sqrt{\eta}e^{2\alpha^2(2\eta-1)}\cos\left(2\alpha\sqrt{\eta}p\right)+2pe^{2\alpha(2\alpha\eta-\alpha)}\sin\left(2\alpha\sqrt{\eta}p\right)\right)}{\sqrt{\eta}\left(2e^{2\alpha^2(2\eta-1)}\cos\left(2\alpha\sqrt{\eta}p\right)+2\right)} \tag{V.3.5}$$

where $|cat+\rangle = \frac{1}{N_+}(|\alpha\rangle + |-\alpha\rangle)$. Fig V.19(b) gives the speed of decay of cat states of different sizes. The larger the cat is, the higher the speed of decay for a perfect transmission $\eta = 1$ will be.

- **For a squeezed cat state**

$$W_{\hat{S}|cat+\rangle}(x,p,s,\eta) = \frac{A\times\left(e^{\frac{2\alpha s\left(\eta^{3/2}s^2x+\alpha(2\eta-1)s-(\eta-1)\sqrt{\eta}x\right)}{\left((\eta-1)s^2-\eta\right)\left(\eta\left(s^2-1\right)+1\right)}}\left(e^{\frac{4\alpha\sqrt{\eta}sx}{\eta-\eta s^2+s^2}}+1\right)+2\cos\left(\frac{2\alpha\sqrt{\eta}ps}{\eta(s^2-1)+1}\right)\right)}{4\pi\left(e^{2\alpha^2}+1\right)\sqrt{\eta+\frac{1-\eta}{s^2}}\sqrt{\eta-(\eta-1)s^2}} \tag{V.3.6}$$

where $A = e^{\frac{p^2\left(\eta-(\eta-1)s^2\right)+s^2\left(4\alpha^2\eta\left((\eta-1)s^2-\eta\right)+x^2\left(\eta\left(s^2-1\right)+1\right)\right)}{2\left((\eta-1)s^2-\eta\right)\left(\eta\left(s^2-1\right)+1\right)}}$.
The expression for the speed of decay can then be deduced from this one. By optimizing the squeezing, it is possible to target the minimal speed of decay. This optimal squeezing is the one which provides the core state with the minimized photon number. Indeed, in Fig. V.20(a), the negativity of the Wigner function is better preserved for the optimally squeezed cat state than for the original cat. In Fig. V.20(b), we can

see that it is possible to optimize the squeezing to minimize the speed of decay. This squeezing is the same as the one which minimizes higher photon number components.

In the two last part of this section, we will show that the minimization of the speed of decay of a state can have effects on other more general criterion such as the fidelity to the targeted state, or the overlap between two coherent states.

b Fidelity

The fidelity between an initial cat state and his decohered counterpart after a lossy channel, is also better preserved when one use the squeezed (and then unsqueezed) method, than when one directly sends the cat state, as shown in Fig. V.21(a). However sometimes the fidelity can be a deceptive criteria as being an overall measurement. For this reason, we showed here that both fidelity and negativity are protected.

c Overlap

A more important parameter to preserve is the orthogonality between the two different parity cat states. To quantify precisely the ability to really discriminate the two parts of the superposition, we can plot the theoretical fidelity between an odd and even cat state, i.e. the overlap, and its evolution through the transmission channel, depending if we optimally squeeze the two cats, transfer them, and then unsqueeze them, or if the two cats are directly sent through a lossy channel. In Fig V.21(b), we can see that this overlap $\mathrm{Tr}[\hat{\rho}_{Cat+}\hat{\rho}_{Cat-}]$ is smaller when optimal squeezing for both even and odd cat state is applied.

The orthogonality between the cats, and thus the phase difference is better preserved. Even though the size stays the same, the preservation of the overlap shows that the important parameter to preserve is the Wigner function central fringe. This fringe is the only part which is different depending on the parity of the cat. The size is itself more related to the two gaussian "bumps" around the fringe.

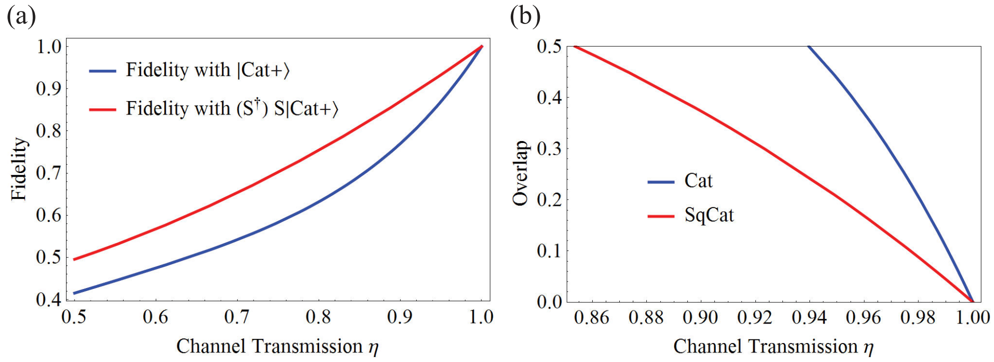

Figure V.21: (a) Theoretical plot of the evolution of the fidelity with the initial even cat state, for a cat state sent directly through the lossy channel (in blue), and a squeezed, transferred, and then unsqueezed cat state (in red). The considered size is $|\alpha|^2 = 3$.(b) Theoretical plot of the evolution of the overlap between two initial even and odd cat states, for cat states sent directly through the lossy channel (in blue), and two optimally squeezed, transferred, and then unsqueezed cat states (in red). The considered size is $|\alpha|^2 = 3$.

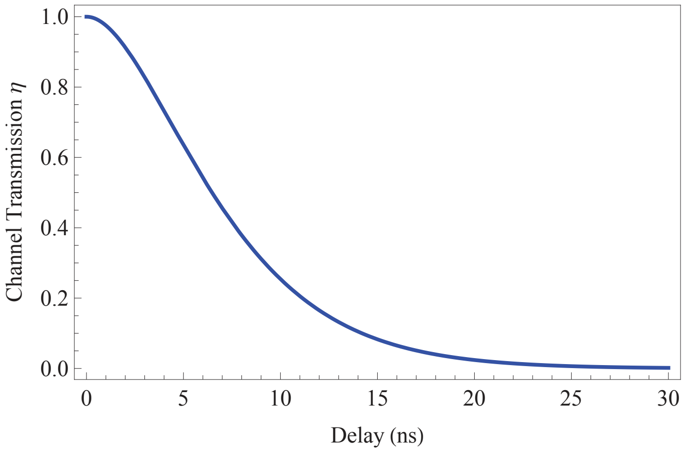

Figure V.22: Efficiency of the detection with temporal mode delay in ns.

V.3.3 Experimental verification

We choose two squeezed cat states corresponding to the angle $\theta = 1.6°$ and $\theta = 2.4°$ of the HWP, as shown in the previous section. They correspond respectively to a 4 dB squeezed cat state with $|\alpha|^2 = 2.8$ and a 2.5 dB squeezed cat state with $|\alpha|^2 = 1.7$. Then, to add quantifiable losses on the state we use the following method: by shifting the temporal mode of the state by an artificial delay in the reconstruction algorithm, we decrease the quantum efficiency of the detection and add losses that we can quantify. The introduced delay can be related to the introduced losses using the formula:

$$\eta(\tau) = \left(\int f(t)f(t+\tau)\, dt)^2 = ((1+\pi\gamma|\tau|)e^{-\pi\gamma|\tau|} \right)^2. \tag{V.3.7}$$

It is plotted in Fig. V.22.

The evolution of the Wigner functions under decoherence are compared for the two squeezed cat states experimentally prepared and for cat states of same amplitude but without squeezing. Figure V.23 shows the evolution of the Wigner functions for one of our experimental squeezed cat state, corresponding to $\theta = 1.6°$, corrected from detection losses (15%), and a cat state onto which we add the same initial system losses (10%). In particular, the cross section of the Wigner functions along the imaginary axis corresponding to the quadrature $\hat{P}$ is shown. This comparison confirms that the Wigner function oscillations preserved a much better contrast for the squeezed version of the cat state.

Figure V.24(a) finally provides the maximal Wigner function negativity as a function of the channel transmission η. As it can be seen, the negativity stays larger for the squeezed cat state, whatever the amount of loss experienced by the state. By fitting the experimental points by a third-order polynomial, we can finally estimate the derivative of the negativity of the Wigner function, and therefore the speed of decay as a function of the transmission η. These results are shown in Fig. V.24(b). Even though the speed of decay is smaller for the squeezed cat state than for the cat state, the difference between the two cat states is not so obvious. The mean photon numbers of the two states are 0.92 and 1.37, for $\theta = 2.4°$ and $\theta = 1.6°$ respectively, which is

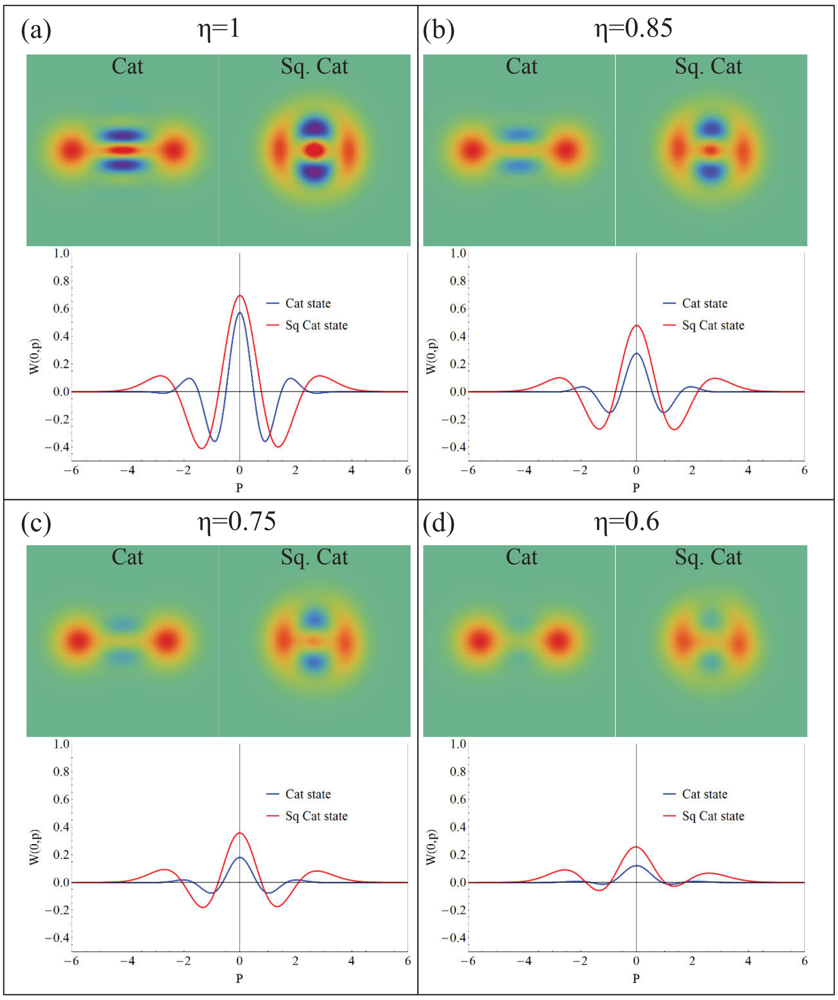

Figure V.23: Each block corresponds to a certain transmission of the channel: (a) $\eta = 100\%$, (b) $\eta = 85\%$, (c) $\eta = 75\%$, and (d) $\eta = 60\%$. For each block, the two top figures represent the simulated Wigner function of a cat state of size $|\alpha|^2 = 2.8$, on which is applied 10% losses, corresponding to the losses intrinsic to our resource (left), the experimental Wigner function of a squeezed cat state of the same size, with 4 dB of squeezing (right). In the lowest part of the block is plotted the corresponding central fringes.

quite close and can explain this proximity. This difference remains inside the error bars of the measurement.

V.3.4 A robust method for generating cat states

We have shown the slowed-down decoherence of the Wigner function negativity of squeezed cat states compared to cat states. We characterized this decrease of non-classicality using a speed-of-decay criterion. The method we use to generated squeezed cat state already makes us generate their core state i.e. their minimized-photon-number state, which means that no other operation is necessary to generate the minimally-

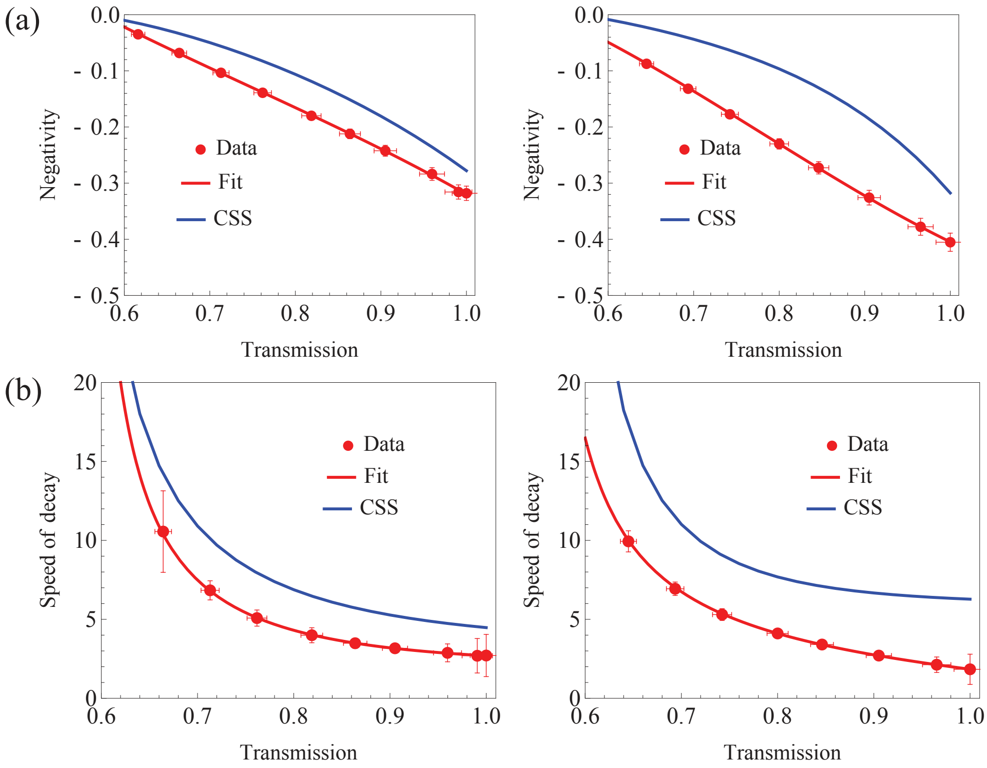

Figure V.24: Experimental results. Left and right figures correspond to an initial squeezed coherent-state superposition with $|\alpha|^2 = 1.5$ and $S = 2.8$ dB and with $|\alpha|^2 = 2.8$ and $S = 3.8$ dB, respectively, with correction from detection losses (15%). The blue line corresponds to a simulated cat state of the same size, on which is added 10% losses, corresponding to the intrinsic losses of our source. (a) Negativity of the Wigner functions. The red line is a third-order polynomial fit. (b) Estimated speed of decay of the negativity. The red line is the corresponding speed of decay of the third-order polynomial fit.

decohering core state. The cats are ready to be used and to be sent through a transmission channel, at the output of which one can implement unsqueezing operation in order to retrieve the "real" cat state. One must point out that unsqueezing the cat will not decrease non-classical effects (the Wigner function negativity is preserved), nor undermine fault-tolerant continuous variable protocols (it consists only in a division and multiplication of each quadrature).

This work opens therefore the question whether squeezed cat states could be sufficient for quantum information schemes, instead of the use of costly “real” large cat states, which can only be found for the moment in superconducting qubits [113, 122] or cavity QED experiments [13, 123], and where the generated cats are not freely-propagating, unlike optical ones.

In a recent study by J. P. Home’s group [124], it was also shown that measurement where easier and more efficient on squeezed cats states, than on their larger counterparts, although the main reason for it (i.e. the slowed decoherence) is not explicitly described.

V.4 Conclusion

We have extensively studied some effects that can happen out of a type-II OPO, where not only the situation when the idler and signal modes are perfectly separated is experimentally interesting for quantum state engineering, but also the transition towards two independent squeezed vacuum states. This transition enabled us to realize Fock states superposition, which can be seen as core states containing the minimal non-gaussian features to target the generation of high fidelity large cat states. This new method of generating large optical squeezed Schrödinger cat states enables to reach high count rates, two orders of magnitude higher than up-to-now protocols, and the highest fidelity so far. Moreover, these core states are more robust to loss, as they contain the minimum number of photons. Their fidelity, and non-classicality (characterized here by the negativity of the Wigner function and its evolution through losses) are shown to be preserved thanks to the use of the squeezing operation. Thus, in order to use them in communication protocols, it is more advantageous to use squeezed cat states as main resources than to directly send large cat states through a lossy channel. Our method already generates squeezed cat states with the minimal non-gaussian cost and can then be implemented in communication channels or continuous-variable protocols.

This work, which uses squeezing as an ancillary Gaussian resource, opens new possibilities to obtain, preserve and manipulate quantum superpositions at the macroscopic level.

Part III

Hybrid Entanglement

VI Hybrid Entanglement of Light

In this chapter, we will first introduce hybrid entanglement. The first demonstration was published at the beginning of this thesis [25, 26, 125]. We will show how this complex photonic state can be heralded using two different OPOs. In this thesis, we have pushed further this work by first generating a hybrid entangled state with a potentially higher degree of entanglement, by increasing the dimensionality. We will also focus on the possibility to characterize such hybrid entanglement via steering inequality and non-locality Bell tests. Finally, we will demonstrate a first application of such entanglement: it consists in the remote state preparation of any continuous-variable qubits. This experiment is the first step towards the achievement of hybrid teleportation of a discrete-variable qubit to a continuous-variable one, analog to the conversion of a "digital" signal to an "analog" one, at a distance. Several schemes will be proposed and discussed.

Contents

VI.1 Hybrid entanglement of light 100
VI.1.1 Schrödinger kitten states 101
VI.1.2 Entanglement generation 103
VI.1.3 Characterization 105
VI.2 Increasing the dimensionality 107
VI.2.1 Hybrid qutrit entanglement: principle 107
VI.2.2 Results 109
VI.3 Characterization of the hybrid entanglement via steering 111
VI.3.1 Steering inequality using homodyne detection 111
VI.3.2 Towards Bell-type violation 114
VI.4 Remote state preparation 116
VI.4.1 Principle 116
VI.4.2 Results 119
VI.5 Encoding conversion by hybrid teleportation 120
VI.5.1 Finding an optimal Bell measurement 122
VI.5.2 Implementation and expected results 123
VI.5.3 An analog-to-digital converter? 125
VI.6 Conclusion 126

VI.1 Hybrid entanglement of light

The discrete- [2] and the continuous-variable approaches [126] are often applied to different protocols in quantum information processing, due to their intrinsic advantages and drawbacks. In the context of future heterogeneous networks, sketched in Fig. VI.1, where some protocols are based on continuous variables and some others on the discrete counterpart, the realization of a quantum converter would be a key ingredient. Such converter would build a bridge between the different encodings of light and can be achieved via the teleportation of the state, from one encoding, hold by Alice, to another one hold by Bob, at a distance. It require in this case a quantum link, which can be provided by hybrid entanglement of light, i.e. entanglement of the form $|0\rangle|\alpha\rangle+|1\rangle|-\alpha\rangle$ between particle-like and wave-like optical qubits [127].

Such entanglement can also be useful for hybrid communication, such as cryptography protocols [128, 129]. Recently proposed schemes also hold the promise of nearly deterministic universal gate operations [130], thanks to the use of a hybrid entangled state as a double-encoded qubit. Hybrid entanglement is also the central resource of the quantum bus approach [8, 131], in which direct qubit-qubit interactions are avoided by the means of a common CV state.

In this section, we will show the first demonstration of hybrid entanglement, achieved at the beginning of this thesis [25] The discrete-variable qubit is encoded in the absence or presence of a single-photon, as expressed by $c_0|0\rangle + c_1|1\rangle$. The continuous-variable qubit will be encoded in Schrodinger cat states of different parities, $c_+|\text{Cat}+\rangle + c_-|\text{Cat}-\rangle$. Therefore the final hybrid entangled qubit state, shared between Alice and Bob, will be of the form:

$$|\Psi\rangle_{AB} = \frac{1}{\sqrt{2}}|0\rangle_A|\text{Cat}+\rangle_B + |1\rangle_A|\text{Cat}-\rangle_B. \tag{VI.1.1}$$

As a first step, we will detail how to generate the continuous resource, i.e. Schrödinger cat states of size $|\alpha|^2 \approx 1$ and with different parities.

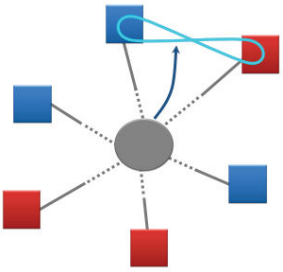

Figure VI.1: Scheme of an heterogeneous network where distant nodes of a quantum network can rely on different information encodings, i.e. continuous (CV) in blue or discrete (DV) variables in red.

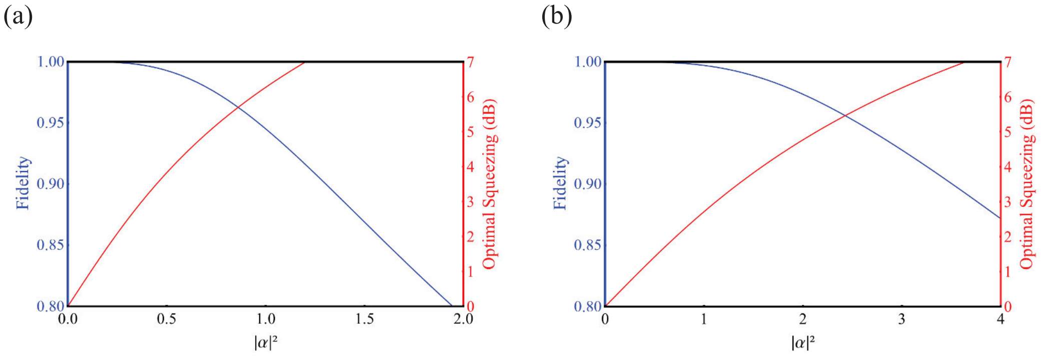

Figure VI.2: (a) In blue is given the fidelity between an even cat state of size $|\alpha|^2$ and a squeezed vacuum state for different optimized squeezing. The optimal squeezing to achieve the maximal fidelity for a given size is represented in red. (b) Fidelity (in blue) between odd cat state of size $|\alpha|^2$ and a single-photon-subtracted squeezed vacuum of optimal squeezing (in red).

VI.1.1 Schrödinger kitten states

We have seen in Chapter V a new method to generate large optical cat state via the core state method. However here, it is not possible to use the same method. Indeed, using this method would force us to have two type-II OPOs, while having limited degrees of freedom to ensure two triple-resonances at the same time. We will therefore here describe a more traditional approach to generate small Schrödinger cat states, also sometimes called *kittens*, with a size $|\alpha|^2$ close to 1. This generation is based on squeezed vacuum and single-photon detection.

In order to generate such states, we will use this time a type-I phase-matched OPO made of a PP-KTP crystal, as presented in Chapter II . This OPO can provide up to 11 dB of squeezing. However, here, to achieve good fidelity with the targeted states, only 3 dB of squeezing will be required.

Even kitten

The output of the OPO is a single-mode squeezed vacuum. As a first approximation, we will use in the following:

$$|\mathrm{Cat}+\rangle \approx \hat{S}|0\rangle \tag{VI.1.2}$$

This approximation is valid for small cat states, as show in Fig VI.2(a), and is deterministic, since it does not rely on the probabilistic detection of a heralding event.

Odd kitten

In order to generate odd kitten states, the most common scheme, initially proposed by Dakna *et al.* [132] relies on one (or more) photon subtraction operated on squeezed vacuum [11, 44, 81]. As shown in Fig. VI.2(b), the fidelity of a single-photon subtracted squeezed vacuum with different odd cat states can be closed to unity for $|\alpha|^2 \leq 1$. For one photon subtraction, it is possible to have the approximation:

$$|\mathrm{Cat}-\rangle \approx \hat{a}\hat{S}|0\rangle. \tag{VI.1.3}$$

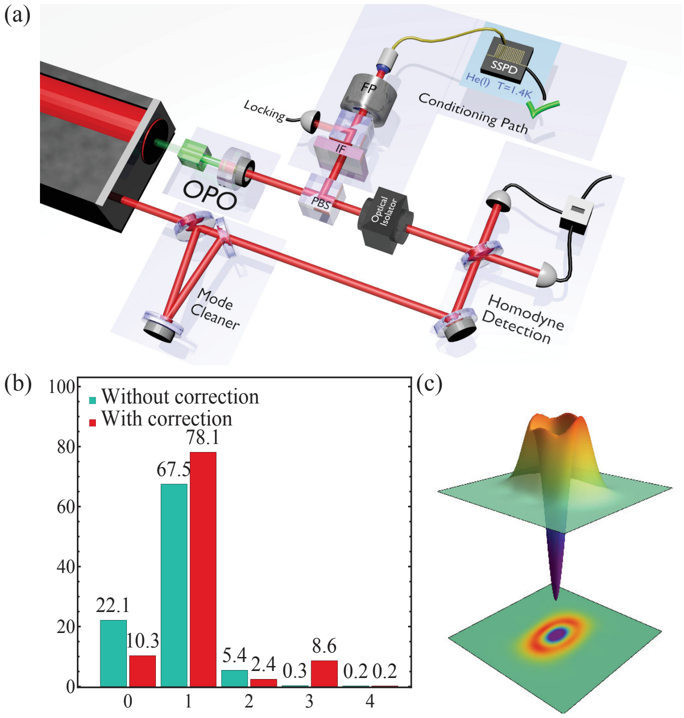

Figure VI.3: (a) Experimental setup for the generation of small odd kitten. A type I phase-matched PP-KTP OPO is pumped by a continuous-wave laser. A small part ($\approx 3\%$) of the output single-mode squeezed state is reflected by a beam splitter. This reflected path is frequency-filtered and sent to a superconducting single-photon detector (SNSPD). Given the detection of a single photon, a single-photon subtracted squeezed vacuum state, which has a high fidelity with an odd Schrödinger kitten state of size $|\alpha|^2 \approx 1$, is heralded. (b) Experimental photon number probabilities and (c) associated Wigner function corrected from detection losses (15%).

With the help of the relation:

$$\hat{S}^\dagger \hat{a} \hat{S} = \hat{a} \cosh|\xi| - \hat{a}^\dagger \sinh|\xi|, \tag{VI.1.4}$$

this state can also be seen as a squeezed single photon:

$$|\mathrm{Cat}-\rangle \approx \hat{a}\hat{S}|0\rangle = \hat{S}\hat{S}^\dagger \hat{a}\hat{S}|0\rangle = -\sinh|\xi|\hat{S}|1\rangle. \tag{VI.1.5}$$

A squeezed vacuum is a superposition of even photon- number states. Subtracting a single photon leads therefore to a superposition of odd photon-number states,

$$|\mathrm{Cat}-\rangle \approx \frac{(1-\lambda^2)^{3/4}}{\lambda} \sum_{n=1} \frac{\sqrt{(2n)!}}{n!} (\frac{\lambda}{2})^n \sqrt{2n} |2n-1\rangle. \tag{VI.1.6}$$

where $\lambda = \tanh|\xi|$ The experimental setup is presented in Fig. VI.3(a). The subtracting operation can then be realized by taping a small fraction of the beam ($\approx 3\%$) with a beam splitter. The detection of a single photon on the conditioning path will herald the generation of a single-photon subtracted squeezed vacuum, reaching a high fidelity with an odd Schrödinger kitten. The heralding mode is frequency filtered via an interferential filter followed by a Fabry-Pérot cavity (see Chapter II). The resulting states are phase-dependent and will therefore be detected via homodyne detection.

The resulting state is presented in Fig VI.3(b) and (c) and reaches a fidelity of 87% with an odd cat state of size $|\alpha| = 0.9$.

In this section, we have described the resources that will be used to generate the continuous basis of our hybrid entanglement. Using our type-I phase-matched OPO, we can indeed generate two orthogonal continuous-variable qubits, $\{|\text{Cat}+\rangle, |\text{Cat}-\rangle\}$, with a size $|\alpha|^2 = 0.8$. In the following section we will use such resources for the generation of hybrid entanglement of light.

VI.1.2 Entanglement generation

a Principle

We have defined the basis $\{|\text{Cat}+\rangle, |\text{Cat}-\rangle\}$ that we will use in the continuous-variable mode of our hybrid entanglement. The discrete-variable basis that is going to be used for the other mode is the presence or absence of a single photon, $\{|0\rangle, |1\rangle\}$. In order to generate single photon, we use a type-II phase-matched OPO, pumped far below threshold, exhibiting EPR-entangled state. This single-photon source is detailed in Chapters IV and V.

Given these two resources, a type-I and a type-II phase-matched OPO, we aim at generating a state of the form:

$$|\Psi\rangle_{AB} = \frac{1}{\sqrt{2}}|0\rangle_A|\text{Cat}+\rangle_B + |1\rangle_A|\text{Cat}-\rangle_B \tag{VI.1.7}$$

The experimental setup is given in Fig. VI.4. Bob's side consists in a type I-OPO, generating either even or odd Schrödinger kitten state, depending on the absence or presence of a single-photon detection event. The pump power is of 5 mW, in order to have 3 dB of squeezing at the output of the OPO. On Alice's side, a type II-OPO is used: the state is either a single-photon state or a thermal state, very close to vacuum, depending on the probabilistic detection of a single-photon on the idler mode.

Our scheme for the generation of entanglement relies on mixing the two conditioning paths, in an indistinguishable fashion: the tapped mode and the idler mode are interfered on a beam splitter, and then frequency-filtered by an interferential filter and a Fabry-Pérot cavity. Therefore, the detection of a single photon heralds either an odd cat state on Bob's side, and vacuum on Alice's side, or a single photon on Alice's side, and an even cat state on Bob's side. Giving a single-photon detection event, it is impossible to know from which mode the photon has been subtracted, leading to the heralded generation of the hybrid state:

$$|\Psi\rangle_{AB} \propto |0\rangle_A \hat{b}\hat{S}_B|0\rangle_B + e^{i\varphi}|1\rangle_A\hat{S}_B|0\rangle_B \approx |0\rangle_A|\text{Cat}-\rangle_B + e^{i\varphi}|1\rangle_A|\text{Cat}+\rangle_B. \tag{VI.1.8}$$

The normalization is omitted here. Such a state can also be written in the rotated $|\pm\rangle_A$ basis:

$$|\Psi\rangle_{AB} \propto |+\rangle_A|\alpha\rangle_B - |-\rangle_A|-\alpha\rangle_B \tag{VI.1.9}$$

where $|\pm\rangle_A = \frac{|0\rangle_A \pm e^{i\varphi}|1\rangle_A}{\sqrt{2}}$. The full theoretical derivation for the generated hybrid entangled state can be found in Appendix D.

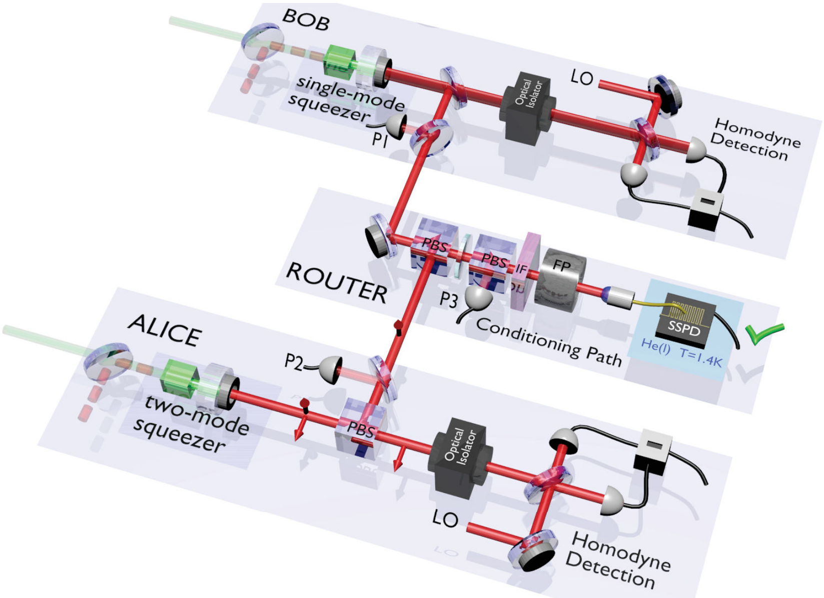

Figure VI.4: Experimental setup for the generation of hybrid entanglement. Alice and Bob locally generate the required resources by using continuous-wave optical parametric oscillators operated below threshold. A type-II and type-I phase-matched OPO are used respectively on Alice's and Bob's node. A small fraction of Bob's squeezed vacuum, which is a good approximation of an even cat state for $|\alpha|^2 \leq 1$, is tapped (3%) and mixed at a central station to the idler beam generated by Alice. The resulting beam is then frequency filtered (conditioning path) and detected by a superconducting single-photon detector (SSPD). Given a detection event, which heralds the entanglement generation, the hybrid entangled state is characterized by two high-efficiency homodyne detections. Two-mode tomography is performed and the density matrix is reconstructed via a MaxLike algorithm. Photodiodes P1, P2 and P3 are used for phase control and stabilization. The beam splitter ratio in the central station enables to choose the relative weights in the superposition. FP stands for Fabry-Pérot cavity, IF for interferential filter, PBS for polarizing beam splitter and LO for local oscillator.

In order to achieve such entanglement, the superposed beams must be indistinguishable in any degree of freedom. Therefore a fine tuning of the OPO bandwidth cavities must also be operated in order to achieve as close as possible temporal-mode shapes.

The phase and weight of the components can be fully tuned to engineer a variety of hybrid entangled states. The phase φ between the two components can be chosen by adapting the locking point of the fringes signal between the two paths. We usually lock on the maximum signal of the fringes, i.e. when $\varphi = \pi$, leading to the heralded generation of:

$$|\Psi\rangle \propto |0\rangle_A|\mathrm{Cat}-\rangle_B - |1\rangle_A|\mathrm{Cat}+\rangle_B. \tag{VI.1.10}$$

The weights of the superposition can be tuned by adapting the count rate ratio between the two heralding paths of the setup.

The fidelity is not affected by the loss in the conditioning path, equivalent to 80 km of fiber, which only affects the count rate of the generation. This entanglement can

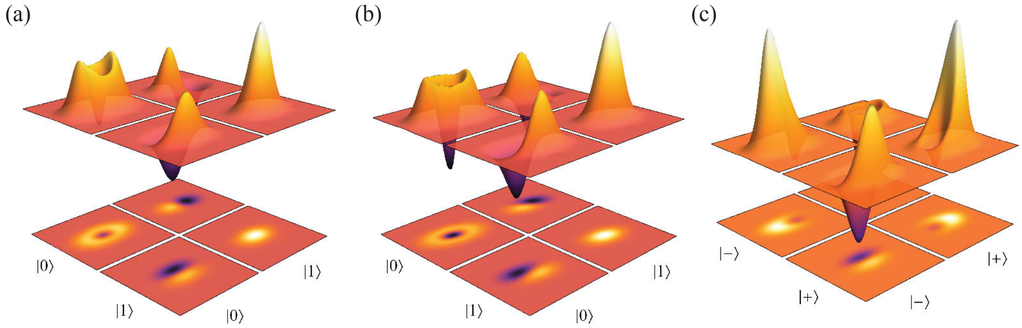

Figure VI.5: Experimental Wigner functions associated with the reduced density matrices $\langle k|\hat{\rho}|l\rangle_A$ with $k, l \in \{0, 1\}$, without (a) and with (b) correction for detection losses (15%). The components with $k \neq l$ being not Hermitian, the corresponding Wigner functions are not necessarily real, but conjugate. The plot gives therefore the real part in the back corner ($k < l$) and the imaginary part in the front corner ($k > l$). The relative phase is set to $\varphi = \pi$ and the beam splitter ratio in the central station is adjusted to generate a maximally entangled state, i.e. with equal weights. (c) Wigner functions associated with the reduced density matrices $\langle k|_A\hat{\rho}|l\rangle_A$ with $k, l \in \{+, -\}$, corrected for detection losses. $|+\rangle$ and $|-\rangle$ stand respectively for the rotated basis $\frac{1}{\sqrt{2}}(|0\rangle_A + |1\rangle_A)$ and $\frac{1}{\sqrt{2}}(|0\rangle_A - |1\rangle_A)$.

therefore be realized in a network where the two nodes are distant from each other. The single-photon detector used is a superconducting single-photon detector (SNSPD, NIST-JPL) working at cryogenic temperature, detailed in Chapter III. The low dark count of such detectors allows to avoid false detection events and therefore to achieve high-fidelity in the state generation.

VI.1.3 Characterization

To represent in a convenient way the results, we decided to use a hybrid representation. In the discrete-variable framework, the results are generally shown in form of the density matrix, while in continuous variable, the Wigner representation is privileged. Therefore, we chose to represent the Wigner function of the reduced density elements $\langle k|_A\hat{\rho}|l\rangle_A$ with $k, l \in \{0, 1\}$, i.e. of the continuous mode of the state, of the experimental state generated $\hat{\rho}$.

The experimental results are given in Fig. VI.5(a) without and (b) with correction for detection losses, for a phase set to $\varphi = \pi$ and a beam splitter ratio tuned to balance the detection probability from each node. Higher photon number components are limited to 2% and are therefore not represented in Fig. VI.5. In this subspace, the two first diagonal elements, namely the projections $\langle 0|\hat{\rho}|0\rangle_A$ and $\langle 1|\hat{\rho}|1\rangle_A$, correspond respectively to a photon-subtracted squeezed state and to a squeezed state. The non-zero off-diagonal terms witness the coherence of the superposition.

The generated state can also be represented using as another projection basis the rotated one $|+\rangle_A = (|0\rangle_A + |1\rangle_A)/\sqrt{2}, |-\rangle_A = (|0\rangle_A - |1\rangle_A)/\sqrt{2}$ (Fig. VI.5(c)). As it can be clearly seen from the contour plots, the two projections $\langle +|\hat{\rho}|+\rangle_A$ and $\langle -|\hat{\rho}|-\rangle_A$ exhibit an opposite displacement in phase space, corresponding with large fidelity to the two states $|\alpha\rangle_B$ and $|-\alpha\rangle_B$. Corrected for detection losses, we obtain a fidelity

$77 \pm 3\%$ with the targeted state with $\varphi = \pi$ and $|\alpha| = 0.9$. The demonstrated size is already compatible with the value $|\alpha| \approx 1$ shown as the optimal value in recent proposals of resource-efficient operations with hybrid qubits [130].

To quantify the entanglement, we can calculate the negativity of entanglement value $\mathcal{N} = 0.37$ when corrected from detection losses (15%), and $\mathcal{N} = 0.27$ without. For a maximally entangled state the negativity of entanglement is 0.5. The fidelity reaches $\mathcal{F} = 0.77$ with the state $|+\rangle_A|\alpha\rangle_B - |-\rangle_A|-\alpha\rangle_B$ with correction from detection losses. This work was the first demonstration of hybrid entanglement of light.

Phase noise sensitivity

The relative phase φ in the generated state, has to be critically kept constant to achieve entanglement. In order to control this phase, a very weak seed beam is injected into each OPO. Depending on the phase of the seed beam with the pump, the resulting signal is either amplified or de-amplified. The phase of the seed beam is locked on the maximum amplification using the photodiodes P1 and P2 in Fig. VI.4 (see Chapter II for more details). Then, the relative phase where the tapped modes are combined is locked using Photodiode P3. This last locking is extremely sensitive. Indeed, it corresponds to a few-meter long interferometer, and occurs after the other locking signals of the OPO cavities and phases. It is therefore sensitive not only to its own path instability but also to all the perturbations of the other upstream locking signals. To model the phase noise of the system, it is possible to plot the negativity of a state resulting from a gaussian phase noise of standard deviation σ:

$$\hat{\rho} = \frac{1}{\sqrt{2\pi}\sigma} \int |\Psi\rangle_{AB}\langle\Psi| e^{-\frac{\varphi^2}{2\sigma^2}}. \tag{VI.1.11}$$

with $|\Psi\rangle_{AB} \propto |0\rangle_A \hat{b}\hat{S}_B|0\rangle_B + e^{i\varphi}|1\rangle_A\hat{S}_B|0\rangle_B$.
The evolution of the negativity of entanglement with the standard deviation σ of the phase noise is given in Fig. VI.6, for different losses. In our experiment, the high quality of our states locates us in the region where the system efficiency is around $\eta_A = \eta_B \approx 0.9$. The negativity is not very sensitive to the phase noise. However we will see later than this noise is nonetheless critical for other entanglement characterization parameters. Finally, it is important to note that as the number of required locking systems increases a lot, the need of automatic relocking systems became crucial for this experiment (see Chapter III for more information).

In summary, we have achieved entanglement between two remote nodes that are using different information encodings [25]. Living in Hilbert space of different dimensionality, the two parties establish heralded hybrid entanglement, which would enable for instance to map discrete qubits onto coherent state ones. The work presented here constitutes the first demonstration of such hybrid entanglement enabling to link computational basis of different nature. In the following section, we will show the generation of a more complex state, reaching potentially higher degree of entanglement by an increased dimensionality of the system.

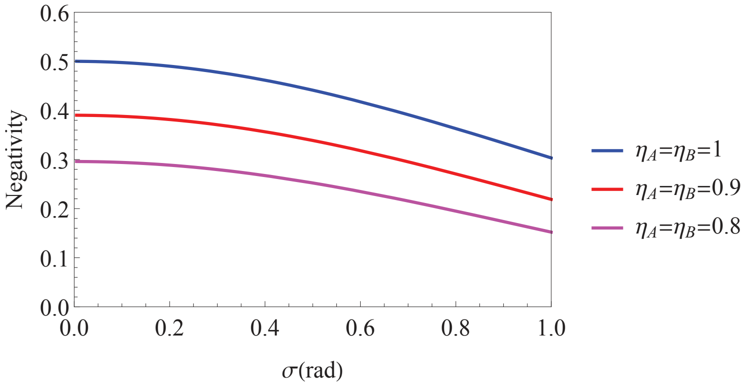

Figure VI.6: Theoretical plot of the evolution of the negativity of the hybrid entangled state under gaussian phase noise of standard deviation σ, for different system efficiencies (symmetric on both sides).

VI.2 Increasing the dimensionality

Systems of higher dimensions, often called qudit, offer many advantages for increased channel capacity [133]. In particular generation of Fock qutrit states of the form:

$$|\Psi\rangle \propto c_0|0\rangle + c_1|1\rangle + c_2|2\rangle \tag{VI.2.1}$$

has been proposed in quantum optics field [134, 135], as well as in superconducting systems [136]. Higher-dimension entangled system, such as discrete qutrit entanglement of the form:

$$|\Psi\rangle \propto |02\rangle + |10\rangle + |20\rangle \tag{VI.2.2}$$

can also find applications in cryptography protocols [137], such as in bit commitment protocols [138], where they can provide higher level of security than qubit entangled states. This is coming from the fact that qutrit states can contain more entanglement than qubit systems. For example, the negativity of entanglement for a maximally entangled state can reach 1, instead of 0.5 for qubit systems. Proposal for discrete qutrit entanglement have been made, such as in optical spatial modes [139], or in superconducting systems [140].

In this section, we will show the generation of hybrid qutrit entangled state, between discrete and continuous encodings, a more complex state than its qubit counterparts in terms of technical difficulties and resulting quantum features.

VI.2.1 Hybrid qutrit entanglement: principle

The goal of our experiment is the generation of a discrete-continuous qutrit entangled state of the form:

$$|\Psi\rangle_{AB} \propto (c_1|0\rangle_A|\psi_1\rangle + c_2|1\rangle_A|\psi_2\rangle + c_3|2\rangle_A|\psi_3\rangle) \tag{VI.2.3}$$

where $|\psi_1\rangle, |\psi_2\rangle, |\psi_3\rangle$ are continuous-variable states.

To implement such a state, we use the same setup as for the hybrid entanglement qubit generation, but we now condition this generation on the detection of two photons.

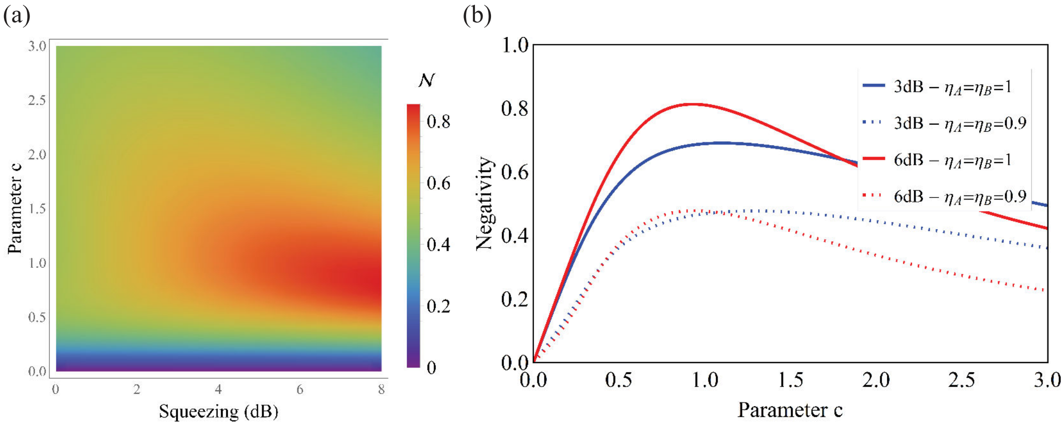

Figure VI.7: (a) Negativity of entanglement of the qutrit hybrid entangled state, for different squeezing amount and different weight parameter c. (b)Negativity of entanglement of the qutrit hybrid entangled state, for different weight parameter c, in the case of 3 dB squeezing and 6 dB squeezing, and for different system efficiencies. The parameter c_{Max}, for which the negativity of entanglement is maximized, slightly changes.

For this purpose, we replace the fiber and the connected SNSPD by a 50/50 fiber beam splitter at which outputs we connect two SNSPDs. Given a double conditioning event happening between 1 ns delay, we can herald the generation of the state:

$$|\Psi\rangle_{AB} = \frac{1}{\sqrt{2+4c^2+c^4}}(\sqrt{2}|2\rangle_A|\text{Sq}\rangle_B - 2ce^{i\varphi}\hat{b}|1\rangle_A|\text{Sq}\rangle_B + c^2e^{i2\varphi}\hat{b}^2|0\rangle_A|\text{Sq}\rangle_B) \tag{VI.2.4}$$

where $|\text{Sq}\rangle_B = \hat{S}|0\rangle_B$, $\hat{b}$ is the annihilation operator on Bob's mode, $c = \frac{\theta t}{\Lambda r}$, and t^2 and r^2 are respectively the transmission and the reflection of the mixing beam-splitter. θ is the angle of the beam splitter enabling the photon-subtraction on the type-I OPO, and Λ is related to the two-mode squeezed state on the type-II OPO : $|TMSS\rangle_{s,i} \propto \sum_n \Lambda^n |n\rangle_s |n\rangle_i$. The phase term φ can be adapted by locking on different points on the fringe resulting from the interference of the two conditioning path. This calculation is fully detailed in Appendix E.

Depending on the choice of the parameter c, it is possible to have different weights for each component of the superposition, resulting in different negativity of entanglement. In figure VI.7(a) is plotted the negativity of entanglement of the system, for different squeezing, and different weight parameters c. The negativity of a qutrit can reach 1 for maximally entangled state. Here, however, due to the fact that $|\text{Sq}\rangle$ and $\hat{b}^2|\text{Sq}\rangle$ are not perfectly orthogonal, it is not possible to reach this value for finite squeezing.

The maximum of the negativity of entanglement is obtained in the ideal case, i.e. in absence of losses, when $\varphi = 0$, for:

$$c^2_{\text{Max}} = \sinh^2|\xi|(1 - \frac{\cosh^2|\xi|}{2}) \tag{VI.2.5}$$

where ξ is the squeezing parameter. This situation corresponds to a two-photon balancing of the count rates, i.e., by blocking one of the conditioning modes, the coincidence counts must be equalized. For infinite squeezing $|\text{Sq}\rangle$ and $\hat{b}^2|\text{Sq}\rangle$ are orthogonal, therefore the negativity tends to a limiting value $\mathcal{N} \approx 0.96$ when the squeezing

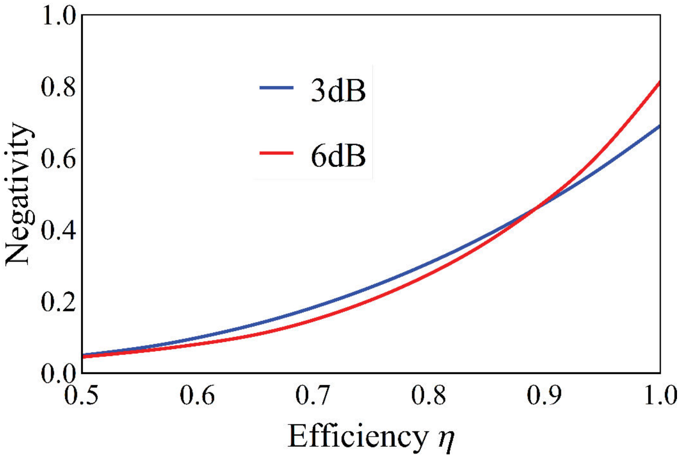

Figure VI.8: Negativity of entanglement of the qutrit hybrid entangled state, in the case of ideal two-photon balancing, for 3 dB (in blue) and 6 dB (in red) of squeezing amount out of the type I OPO, for different system symmetric efficiencies $\eta = \eta_A = \eta_B$.

increases. When losses are added, the balancing value c_{Max} which maximizes the negativity slightly changes depending on the squeezing, as shown in VI.7(b). It is however difficult to give a simple analytical expression. As the change of c_{Max} is very small, we will keep in the following, for simplification of the simulations, the value of the ideal case.

We plot for several values of squeezing, the negativity depending on the efficiency of the system in Fig. VI.8. As it can be seen, The qutrit entangled state is extremely sensitive to losses. In particular for 6 dB squeezing we reach the same amount of negativity as for the 3 dB squeezed qutrit, for an efficiency of $\eta = \eta_A = \eta_B = 0.9$. It will therefore be difficult to surpass the negativity obtained for the hybrid qubit ($\mathcal{N} = 0.37$) and to show experimentally an improvement for 6 dB squeezing. The count rate of this experiment is particularly low, of a few Hz, making it also challenging in terms of path stabilization.

VI.2.2 Results

Figure VI.9 gives the Wigner functions of the reduced density elements $\langle k|\hat{\rho}|l\rangle_A$, of the experimental state $\hat{\rho}$ for a 5 mW pumping power of the type I OPO, leading to a 3 dB squeezed resource. The higher photon number elements are not represented, being below 2%. The fidelity is 73% for $c = 2.3$. The theoretical value of c in order to maximize the negativity is around 1. This means there is still way for improvement in order to balance correctly balance the coincidences counts. However as the count rate is extremely low (around a few Hz), it is difficult to achieve a precise balancing of the two-click coincidences. The achieved negativity is nonetheless 0.38, which is equivalent to ones obtained for the hybrid qubit entanglement, but here for a state much more sensitive to detection losses. This shows the strong entanglement features achieved.

A first attempt has been made for 6 dB of squeezing (30 mW pumping power for the type-I OPO), and the resulting Wigner functions are shown in Fig. VI.10. The achieved negativity is 0.3. The oscillations all over the Wigner functions are coming

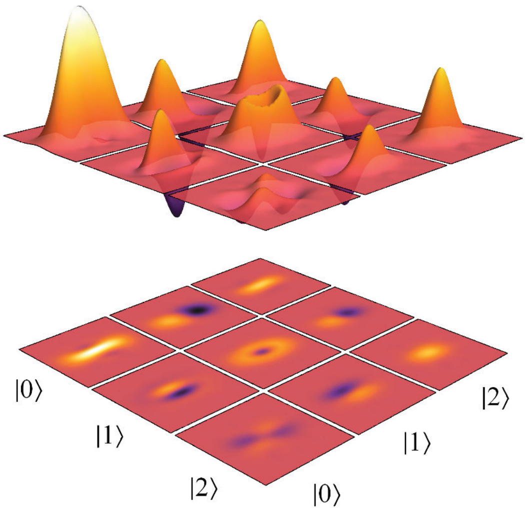

Figure VI.9: Experimental qutrit entangled state $\hat{\rho}$ represented in form of Wigner functions of the reduced density matrices $\langle k|\hat{\rho}|l\rangle_A$ for 3 dB squeezing. The diagonal elements are close to the Wigner functions of $\hat{b}^2|\text{Sq}\rangle$, $\hat{b}|\text{Sq}\rangle$ and $|\text{Sq}\rangle$.

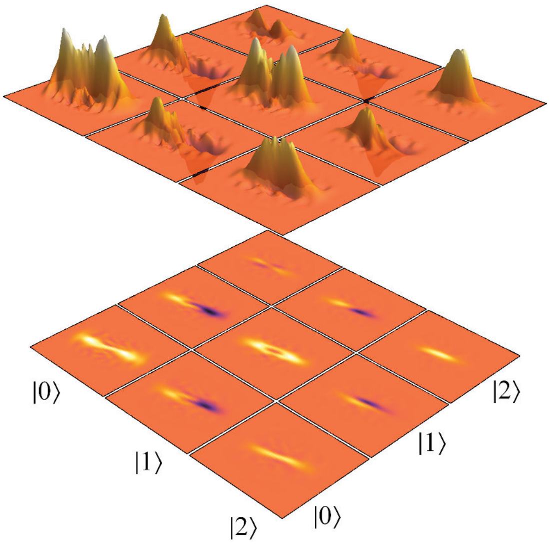

Figure VI.10: Experimental qutrit entangled state $\hat{\rho}$ in form of Wigner functions of the reduced density matrices $\langle k|\hat{\rho}|l\rangle_A$ for 6 dB squeezing. The plotted phase space is twice bigger than the one for the 3 dB case.

from the lack of points (only 70 000 here), due to the low count rate, of a few Hz. When the Hilbert space dimension increases, this effect becomes preponderant. To achieve a better reconstruction, it would require to achieve 200 000 points for the MaxLike tomography. However, such results are only preliminary, as this state is very sensitive to losses, in particular for high squeezing. Additional generations with different weights and phases must also be conducted, for different squeezing, in order to show the tunability of the setup.

In the following section we will see other criteria in order to characterize the degree of entanglement of our system, and in particular its non-locality properties. We will try to apply the following criteria to our hybrid entangled qubit state.

VI.3 Characterization of the hybrid entanglement via steering

Many different criteria are used in order to characterize entanglement. They can be for instance non-separability tests conducted on the density matrix such as negativity or concurrence. We applied one of these criteria, the negativity of entanglement on our hybrid entangled state in the previous section.

Other criterions such as Bell-type measurements where proposed in order to assume fewer hypothesis on the state and still show quantum mechanical features.

In this section we will review "steering" test that we hope to apply on our hybrid entangled state. Steering testing was proposed by Schrödinger as a generalization of the EPR paradox [141]. The idea is the following: Alice and Bob shares two separated modes of an entangled state. Alice is making a measurement on her side, which makes Bob state's wave function collapse. In the steering context, Alice is trying to convince Bob that they share an entangled state. Bob trusts his laboratory, which makes it slightly easier, technically speaking, than Bell-type non-locality tests, where none of the sides can be trusted. It is one of the key tests in order to implement one-sided device-independent protocols in quantum key distribution [35].

Alice can be seen as a black box, where only outcomes $s = +1, -1$ can be shared with Bob. Bob is thus giving a set of parameters j and Alice performs the measurements A_j on its state. She then transmits her answers to Bob, which performs the measurement B_j. As Bob is trusted, he can correct from losses or detection efficiency. In [141] and [142], a steering inequality using homodyne measurement was presented. Such inequality was applied to the case of single-photon entanglement, i.e. state of the form: $\sqrt{R}|0\rangle_A|1\rangle_B + \sqrt{1-R}|1\rangle_A|0\rangle_B$. An experimental violation, following this method has been demonstrated in [143]. In a first place, we will apply the same reasoning to our hybrid entangled qubit state.

VI.3.1 Steering inequality using homodyne detection

In [142] an inequality is provided in order to know if a single-photon entangled state under the losses η is steerable or not:

$$\eta[R + (1-R)2\eta_{HD}] \geq 1 \tag{VI.3.1}$$

where η_{HD} is the efficiency of the homodyne detector used to witness steering. If we consider of our state as a form of single-photon entanglement with: $\eta_{|1\rangle,B} = 78\%$ $\eta_{|1\rangle,A} = 90\%$ By taking $\eta = \sqrt{\eta_{|1\rangle,A}\eta_{|1\rangle,B}}$, we therefore should be able to witness steering.

Here, as a first attempt, we use the inequality derived by Fuwa and co-workers for single-photon entangled state [143], by using it in the $\{\hat{S}|0\rangle, \hat{S}|1\rangle\}$ basis. Alice and Bob share a hybrid entangled state denoted $|\Psi\rangle$:

$$|\Psi\rangle_{AB} = (\sqrt{1-R}\hat{S}|0\rangle_B|1\rangle_A - \sqrt{R}\hat{S}|1\rangle_B|0\rangle_A) \tag{VI.3.2}$$

where R is proportional to the ratio of the count rates and can be tuned by playing with the half-wave plate in front of the mixing beam splitter. To attempt to convince Bob of the veracity of such entanglement, Alice performs quadrature measurement via homodyne detection. Making a quadrature measurement A_j on Alice's side, and getting the result $s \in \{+1, -1\}$ collapses Bob's mode's wave function in the eigenvector $|Q_{\theta_j,A_j}\rangle$ of the measured quadrature:

$$|\psi_B\rangle = \langle Q_{\theta_j,A_j}|\Psi\rangle \tag{VI.3.3}$$

On his side, Bob makes then a full tomography of the state $|\psi_B\rangle$, with correction from detection losses (15%), and apply to it the measurement B_j depending on Alice's result. The idea of the steering inequality is to find measurement on Alice's side to ensure the violation of the following inequality:

$$\frac{1}{n}\sum_{j=1}^{n}\sum_{s} P(s|\theta_j)sTr[\hat{\sigma}_B^{\theta_j}\hat{\rho}_s^{\theta_j}] \leq f(n)\sqrt{1 - Tr[\hat{\sigma}_B^z\hat{\rho}]^2} \tag{VI.3.4}$$

where $\hat{\sigma}_B^{\theta_j} = \sigma_{x,B}\cos\theta_j - i\sigma_{y,B}\sin\theta_j$, and $\hat{\sigma}_B^z$ are the extended spin operators applied to the mode B [33, 34], and $\hat{\rho}_s^{\theta_j}$ Bob's resulting state after Alice's measurement. $f(n)$ is a monotonically decreasing positive function of the number of measurement settings n, and is defined in [142]. This function is close to its asymptotic value $f(\infty) = \frac{2}{\pi}$ for $n = 6$: $f(6) = 0.644$. Therefore 6 measurements should be sufficient to witness a violation. Following the idea developed by Fuwa and co-workers [143], we will apply sign binning on Alice's side, i.e. $s(Q_A^\theta) = sign(Q_A^\theta) \in \{+1, -1\}$. Therefore, $P(s|\theta) = 0.5$. Finally, we can chose a set of angle θ_j in order to cover the full phase space, i.e. $\theta_j = \pi\frac{j}{6}$. This θ_j can be chosen by locking the phase of the local oscillator of Alice's homodyne detection.

For a maximally entangled state, i.e. when $R = 0.5$, and 3 dB of squeezing, Fig. VI.11(a) gives the left and right part of the inequalities members evolution with optical efficiencies (symmetric on both sides). We can see that up to $\eta_A = \eta_B = 0.8$, it is possible to witness a steering violation. This violation is however different when the ratio changes and can be slightly easier to witness. For example, the left and right sides of the inequality for the transmission ratio are given in Fig. VI.11(b), for the typical experimental losses $\eta_A = 0.92 \times 0.85$ (including optical losses and detection efficiency, which are respectively of 8% and 15%) on Alice's side, and $\eta_B = 0.90$ (including optical losses 10%), on Bob's side. The resulting differences between the two sides of the inequality is plotted in Fig. VI.12(a), for the experimental efficiencies and $\eta_B = 0.90$ as a function of the parameter R. Figure VI.12(a) also shows the amount of violation we would get if the considered state was a single-photon entangled state, with the same system efficiencies. Achieving a steering inequality violation is therefore harder, both in terms of transmission ratio R range, and of smaller value Δ, for hybrid entanglement than for single-photon entanglement.

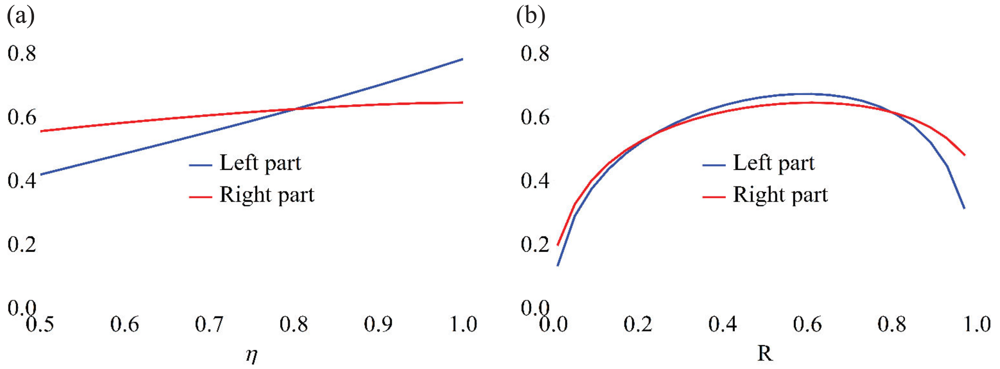

Figure VI.11: (a) Left and right sides of the steering inequality evolution as a function of the efficiency of the system (with $\eta_A = \eta_B = \eta$), for a maximally entangled state (i.e. $R = 0.5$). (b) Left and right sides of the steering inequality evolution for the typical experimental losses $\eta_A = 0.92 \times 0.85$ (including optical losses and detection efficiency, which are respectively of 8% and 15%) and $\eta_B = 0.90$ (including optical losses 10%), with the parameter R.

Both evolutions with losses for the two parameters $R = 0.5$ and $R = 0.6$ are summarized in Fig. VI.12(b).

Given the efficiencies we have in our experiment, i.e. $\eta_A = 0.85 \times 0.92$ and $\eta_B = 0.90$, we should therefore be on the limit to see this steering inequality violation. Experimentally, we found $0.53 < 0.55$ and $0.55 < 0.56$ for $R = 0.5$ and $R = 0.6$ respectively. We could therefore not witness any violation so far while being very close to the limit. Improvements of a few percent of the efficiencies on both sides should therefore be targeted.

Such inequality is very hard to violate, as showed by two recent papers [144] and [145], where it is explained that violating this inequality is the same as violating a CHSH-type inequality, i.e. that the entangled state exhibits strong Bell-type non-

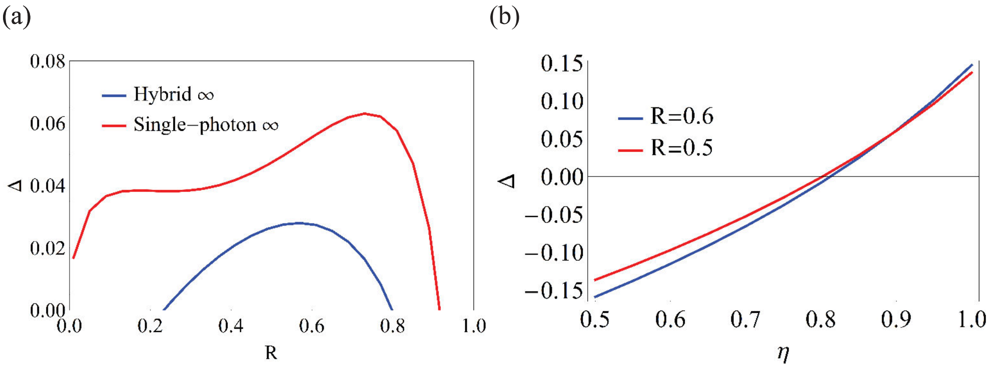

Figure VI.12: (a) In blue is given the value of the theoretical amount of violation observed Δ for $\eta_A = 0.85 \times 0.92$ and $\eta_B = 0.90$ as a function of the parameter R. In red is given the value of the theoretical amount of violation observed in the case of single-photon entanglement, for the same system efficiencies. (b) Value of the amount of violation observed Δ with the efficiency of the system (when $\eta_A = \eta_B = \eta$) for $R = 0.6$ (blue) and $R = 0.5$ (red).

locality features.

In order to show steering-type entanglement, other promising measurements have recently been proposed using for example displacement operation followed by single-photon detection [146]. According to this publication, their steering inequality can be violated for single-photon entanglement provided that the total transmission and detection efficiency is above $\approx 43\%$, which clearly is the case in our experiment.

VI.3.2 Towards Bell-type violation

Following the same idea as steering entanglement witnesses, we also study inequalities for Bell-type non-locality witnesses. A typical scheme of is given in Fig. VI.13. The general principle is to find two operators $\hat{A}$ and $\hat{B}$ hold by Alice and Bob, which give $+1, -1$ outcomes, and two settings of the operators i, i' and j, j' where we can derive the inequality, valid for local systems:

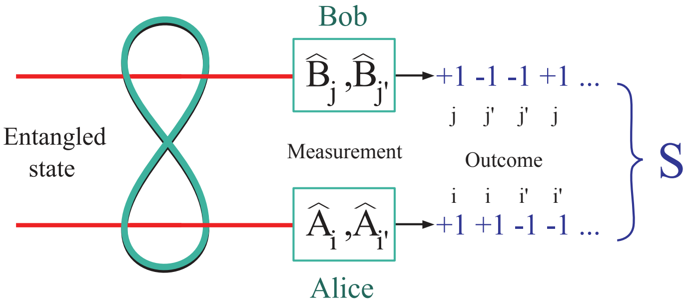

Figure VI.13: Principle of a non-locality witness: Alice and Bob shares entanglement. They randomly perform measurements using operators $\hat{A}$ and $\hat{B}$. Depending on the outcomes of such measurement they calculate correlators of the form $\langle \hat{A}_i, \hat{B}_j \rangle$ and calculate the resulting term S.

$$S = \langle \hat{A}_i \otimes \hat{B}_j \rangle + \langle \hat{A}_{i'} \otimes \hat{B}_j \rangle + \langle \hat{A}_i \otimes \hat{B}_{j'} \rangle - \langle \hat{A}_{i'} \otimes \hat{B}_{j'} \rangle \leq 2 \tag{VI.3.5}$$

Terms of the form $\langle \hat{A}_i, \hat{B}_j \rangle$ are called the correlators, and can be retrieved by the probability to have a certain measurement outcome. Therefore, for a state $\hat{\rho}$:

$$\langle \hat{A}_i \otimes \hat{B}_j \rangle = Tr[\hat{A}_i \hat{B}_j \hat{\rho}] = \sum_{a,b=\{+1,-1\}} p(a=b|\hat{A}_i \otimes \hat{B}_j) - p(a \neq b|\hat{A}_i \otimes \hat{B}_j) \tag{VI.3.6}$$

If $S > 2$ the system exhibits non-locality.

In continuous-variable systems, Milman and co-workers [147] proposed to use the value of the Wigner function, experimentally corresponding to a displacement of the parity operator.

$$\langle \hat{\Pi}_{Alice,\alpha} \otimes \hat{\Pi}_{Bob,\beta} \rangle + \langle \hat{\Pi}_{Alice,\alpha'} \otimes \hat{\Pi}_{Bob,\beta} \rangle + \langle \hat{\Pi}_{Alice,\alpha} \otimes \hat{\Pi}_{Bob,\beta'} \rangle - \langle \hat{\Pi}_{Alice,\alpha'} \otimes \hat{\Pi}_{Bob,\beta'} \rangle \leq 2 \tag{VI.3.7}$$

where $\hat{\Pi}_\alpha = \hat{D}(\alpha)\hat{\hat{\Pi}}\hat{D}^\dagger(\alpha)$ is the displaced parity operator, corresponding to a displacement to the point α. The mean value of this operator corresponds to the value of Wigner function on this point:

$$\langle \hat{\Pi}_\alpha \rangle = W(\alpha). \tag{VI.3.8}$$

First demonstrations using homodyne detection have been proposed [148]. However this method is extremely sensitive to losses and it is impossible to experimentally conduct such test in our setup. The same method haves been applied to two mode-squeezed state in [149–151]. The detection efficiency requirement are usually on the order of $\eta > 95\%$ as shown in [152] or as well as in more recent proposals [153].

Another test procedure we worked on could be to have hybrid types of operators:

$$\langle\hat{\sigma}_{Alice,i}\otimes\hat{\Pi}_{Bob,\beta}\rangle+\langle\hat{\sigma}_{Alice,i'}\otimes\hat{\Pi}_{Bob,\beta}\rangle+\langle\hat{\sigma}_{Alice,i}\otimes\hat{\Pi}_{Bob,\beta'}\rangle-\langle\hat{\sigma}_{Alice,i'}\otimes\hat{\Pi}_{Bob,\beta'}\rangle\leq 2 \tag{VI.3.9}$$

where $\hat{\sigma}_\theta = \hat{\sigma}_X\cos\theta + \hat{\sigma}_Y\sin\theta$. However, for the same reason, the sensitivity of the parity operator measurement to losses, this measurement is very sensitive to losses, and cannot permit to witness any violation at the current experimental efficiencies.

Finally, another proposal by Vlastakis and co-corkers [154], is based on Pauli-type measurement only:

$$\langle\frac{\hat{\sigma}_x+\hat{\sigma}_z}{\sqrt{2}}\otimes\hat{Z}_{Bob}\rangle+\langle\frac{\hat{\sigma}_x-\hat{\sigma}_z}{\sqrt{2}}\otimes\hat{Z}_{Bob}\rangle+\langle\frac{\hat{\sigma}_x+\hat{\sigma}_z}{\sqrt{2}}\otimes\hat{X}_{Bob}\rangle-\langle\frac{\hat{\sigma}_x-\hat{\sigma}_z}{\sqrt{2}}\otimes\hat{X}_{Bob}\rangle\leq 2. \tag{VI.3.10}$$

In this specific case, the Pauli formalism was extended to our continuous qubit basis as:

$$\begin{aligned}\hat{X}_{Bob}&=|\mathrm{Cat}+\rangle\langle\mathrm{Cat}-|+|\mathrm{Cat}-\rangle\langle\mathrm{Cat}+|\\ \hat{Y}_{Bob}&=i|\mathrm{Cat}+\rangle\langle\mathrm{Cat}-|-i|\mathrm{Cat}-\rangle\langle\mathrm{Cat}+|\\ \hat{Z}_{Bob}&=|\mathrm{Cat}+\rangle\langle\mathrm{Cat}+|+|\mathrm{Cat}-\rangle\langle\mathrm{Cat}-|\end{aligned} \tag{VI.3.11}$$

By directly applying such operators to our experimental density matrix, with correction from detection losses, a value slightly above 2 has been obtained, however inside the error bars. Therefore we cannot have conclusions on the non-locality of our state, corrected from detection losses, for the current system efficiencies.

In order to calculate the possible violation for our state we can compute the Bell parameter based on pseudospin operator $(\mathcal{B}_{PS})_{max}$. This parameter enables to quantify the total amount of qubit entanglement in our system. It is the highest that one can reach in a Bell-type test, by using the optimal operators. In this parameter, the Pauli operators for Bob's side used here are the extended formalism of Pauli operators [33, 34], as defined in Chapter I. Such parameter can be simplified [155] if:

$$\langle\hat{\sigma}_i\otimes\hat{\sigma}_j\rangle=0 \tag{VI.3.12}$$

for $i \neq j$. Provided a rotation in phase space of the experimental density matrix in order to fulfill this condition, the maximal amount of Bell-type inequality can be provided as:

$$(\mathcal{B}_{PS})_{max}=2\sqrt{Z^2+X^2} \tag{VI.3.13}$$

where $X = \langle\hat{\sigma}_x\otimes\hat{\sigma}_x\rangle$ and $Z = \langle\hat{\sigma}_z\otimes\hat{\sigma}_z\rangle$. Figure VI.14 gives the evolution of such parameter with losses. By applying this criterion to our density matrix, we got the value $(\mathcal{B}_{PS})_{max} = 2.24$ with correction from detection losses, and $(\mathcal{B}_{PS})_{max} = 1.74$ without correction from detection losses. We are nonetheless stuck to two issues: the first one is that there is not to our knowledge solutions to measure the Pauli Operators

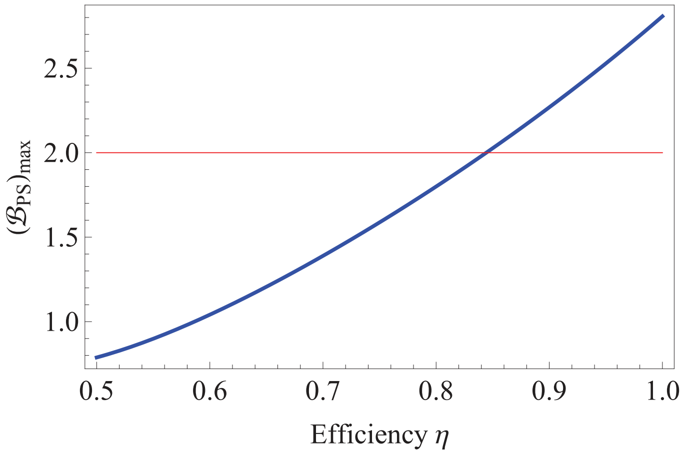

Figure VI.14: Value of the Bell parameter $(\mathcal{B}_{PS})_{max}$ achievable depending on the losses ($\eta_A = \eta_B = \eta$).

via single-shot homodyne measurements. The second one is that we need to correct from detection efficiency from both sides, i.e. we have to open the detection loophole. It is an interesting question to see whether the achieved value of Bell parameter could enable us to violate a steering inequality.

Reaching high fidelity hybrid entangled is important not only for fundamental tests such as presented in this section, but also in order to use it as a toolbox for other protocols. In the context of building heterogeneous networks, the conversion of information from one encoding to the other can be achieved via teleportation. In the following section, we will show the first step of a teleportation scheme, consisting in being able to remotely prepare any continuous-variable qubits by measurement on the discrete-variable side. Such protocol is also interesting on its own as it enables to generate for subsequent protocols any desired CV qubit at a distance.

VI.4 Remote state preparation

As a first application of our hybrid entangled state generation, we will show in this section the preparation at a distance of any continuous-variable qubits. Even though the generation of balanced superposition (i.e. cat states) has been the subject of many studies, being able to fully play on the superposition weights and phases, is more complicated, and requires several conditioning measurement [156]. By using hybrid entanglement, we can implement a quadrature measurement on Alice's DV mode, and therefore generate any coherent-state superpositions on Bob's mode.

VI.4.1 Principle

Following the method developed for single-photon entanglement [157], we start from our hybrid entangled state,

$$|\Psi\rangle_{AB} = |0\rangle_A|\text{Cat}-\rangle_B - |1\rangle_A|\text{Cat}+\rangle_B, \tag{VI.4.1}$$

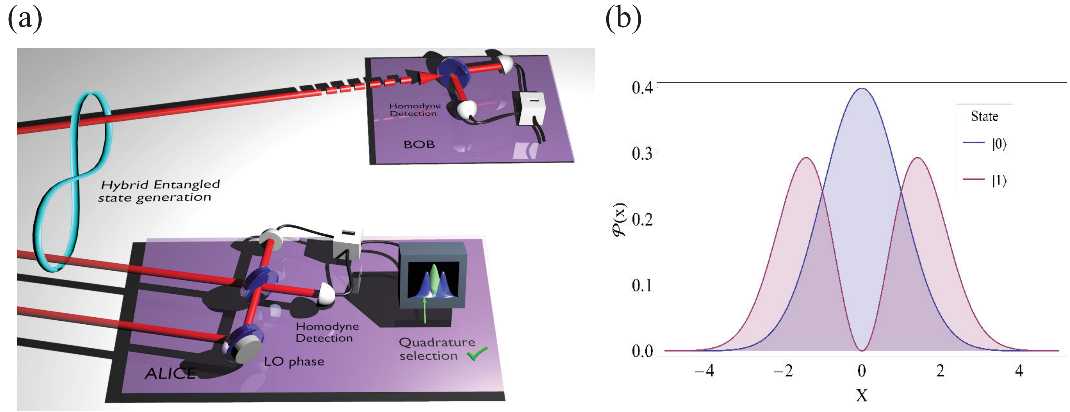

Figure VI.15: (a) Experimental setup for the remote state preparation of continuous-variable qubits via hybrid entanglement. Alice and Bob share an entangled state of the form $|\Psi\rangle_{AB} = |0\rangle_A|\text{Cat}-\rangle_B - |1\rangle_A|\text{Cat}+\rangle_B$. By performing quadrature measurement via homodyne detection on its part of the state, Alice can herald the generation of any continuous-variable state superposition $c_+|\text{Cat}+\rangle_B + e^{i\varphi}c_-|\text{Cat}-\rangle_B$ on Bob side. The quadrature can be chosen by locking the local oscillator of Alice's detection on a certain value θ, and by waiting for an event value Q (within a given acceptance window). Bob then performs homodyne detection in order to check the quality of the generated state.(b) Marginal distributions of vacuum and single-photon states.

and implement, on the discrete-variable side, a quadrature measurement using homodyne detection, as shown in the experimental setup presented in Fig VI.15(a). The marginal distributions corresponding a single photon and vacuum are plotted in VI.15(b), in the ideal case. The measurement of a quadrature outcome close to the value zero on Alice's side will project Bob's state onto the state $|\text{Cat}-\rangle_B$. On the contrary, a large value quadrature outcome will project Bob's state onto the state $|\text{Cat}+\rangle_B$. By measuring quadratures in between, and by playing on the phase of the local oscillator, we can therefore prepare on Bob's side the arbitrary superposition state: $c_-|\text{Cat}-\rangle_B + e^{i\varphi}c_+|\text{Cat}+\rangle_B$. In particular, the measurement of a quadrature value of -1, projects the state onto the balanced case $1/\sqrt{2}(|\text{Cat}+\rangle_B - |\text{Cat}-\rangle_B) \approx |\alpha\rangle_B$, leading to the generation of a coherent state, for $|\alpha|^2 \approx 1$.

The analytical calculation of the coefficients goes as follows. The measurement implemented can be written in the form:

$$\hat{Q}_{\theta,A} = \hat{X}\cos\theta_A + \hat{P}\sin\theta_A. \tag{VI.4.2}$$

The measurement of the quadrature value Q, projects the entangled state onto an eigenstate of the quadrature $|Q_{\theta_A,A}\rangle$:

$$|\Psi\rangle_B = \hat{Q}_{\theta,A}|\Psi\rangle_{AB} \propto \langle Q_{\theta_A,A}|0\rangle_A|\text{Cat}-\rangle_B - \langle Q_{\theta_A,A}|1\rangle_A|\text{Cat}+\rangle_B, \tag{VI.4.3}$$

where

$$\begin{aligned} \langle Q_{\theta_A,A}|0\rangle_A &= \frac{1}{(2\pi)^{1/4}}e^{-\frac{Q^2}{4\sigma_0^2}} \\ \langle Q_{\theta_A,A}|1\rangle_A &= \frac{Qe^{i\theta_A}}{(2\pi)^{1/4}}e^{-\frac{Q^2}{4\sigma_0^2}}. \end{aligned} \tag{VI.4.4}$$

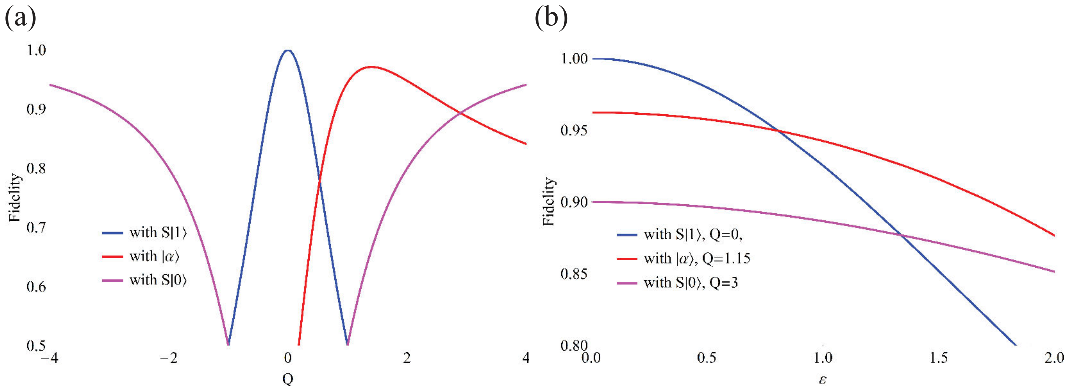

Figure VI.16: (a) Fidelity depending on the measurement results Q for different targeted continuous-variable states ($\theta = 0$). (b) Fidelity as a function of the acceptance band ϵ for different targeted states.

The final state on Bob's side can be written after renormalization as:

$$|\Psi\rangle = \frac{1}{\sqrt{1+Q^2}}(|\text{Cat}-\rangle_B + Qe^{i\theta}|\text{Cat}+\rangle_B). \qquad \text{(VI.4.5)}$$

The closer the measured value is to $Q = 0$, the more the entangled state will be projected onto $|0\rangle_A|\text{Cat-}\rangle_B$. In a nutshell, the value of Q will change the weight of the superposition, while the chosen quadrature will be directly mapped onto the final phase of the superposition. To generate the following states on Bob's side, the following values must therefore be chosen, according to the different fidelity plots in Fig VI.16(a):

- $\hat{S}|1\rangle \approx |\text{Cat}-\rangle$, $Q = 0$, any value of θ
- $\hat{S}|0\rangle \approx |\text{Cat}+\rangle$, $|Q|$ as high as possible, any value of θ
- $|\alpha\rangle$, $Q = 1.15$, $\theta = 0$
- $|-\alpha\rangle$, $Q = -1.15$, $\theta = 0$
- $|\alpha\rangle + i|-\alpha\rangle$, $Q = 1.15$, $\theta = \pi/2$.

The fact that the coherent state's highest fidelity is obtained for $Q = 1.15$ and not at $Q = 1$, as it could be expected in the ideal case, comes from the limited value of $|\alpha| \approx 0.76$.

Experimentally, a strict condition $Q = x$ would lead to zero probability of success. We therefore need to measure a certain band of quadratures of size ϵ that we choose to keep. This would lead to a compromise between the fidelity of the targeted state and the resulting count rate, for the quadrature value $\hat{Q}_{\theta,A}$. The final result can therefore be written as:

$$\hat{\rho}_B \propto \int_{Q-|\epsilon|}^{Q+|\epsilon|} dQ \langle Q_{\theta,A}|\Psi\rangle_{AB}\langle\Psi|Q_{\theta,A}\rangle. \qquad \text{(VI.4.6)}$$

Depending on the acceptance window ϵ, the state fidelity decreases as shown in Fig. VI.16(b). Therefore, we will choose for $Q = 0$ or $Q = 1.15$ the value $\epsilon = 0.1$. To generate $\hat{S}|0\rangle \approx |cat+\rangle$ we will however take $|Q| \geq 2.5$

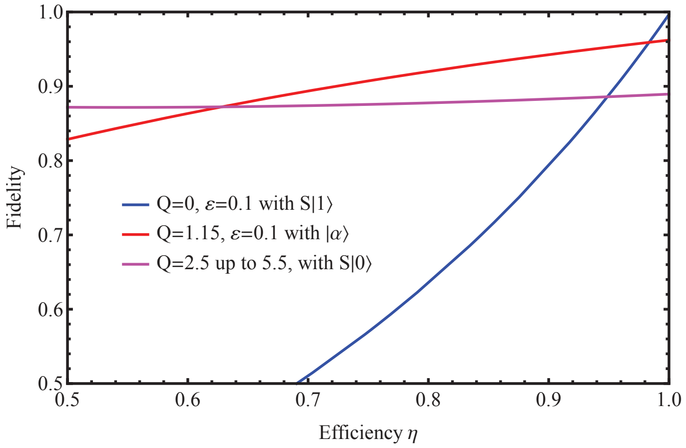

Figure VI.17: Theoretical plot of the fidelity depending on the efficiency of the system $\eta = \eta_{Alice} = \eta_{Bob}$ for different remotely prepared states on Bob's side.

The overall process is obviously sensitive to loss. Indeed, for different bands ϵ we plot the fidelity of each state for symmetric losses $\eta = \eta_{Alice} = \eta_{Bob}$ on both sides in Fig. VI.17. As squeezed vacuum is mostly containing vacuum component, the fidelity is not too much affected by the losses. However, for the odd kitten state generation, the measurement of $Q = 0$ can lead to the generation of unwanted squeezed vacuum, due to the losses on Alice's side. Therefore the fidelity is high for the squeezed vacuum state, and decreases with the increase of the odd kitten state component in the superposition.
.

Experimentally, given a quadrature measurement on Alice's side, we then sample 50 000 quadratures values on Bob side, and reconstruct the full density matrix using a maximum likelihood algorithm.

VI.4.2 Results

Some of the experimentally generated states are presented in Fig. VI.18, in the form of a continuous-variable Bloch sphere, where the poles are defined by the orthogonal states $\hat{S}|1\rangle$ and $\hat{S}|0\rangle$. For each experimental state $\hat{\rho}_{\text{exp}}$, we find the maximal fidelity with the state

$$|\Psi\rangle_{\theta,\varphi} = \cos\frac{\theta}{2}\hat{S}|0\rangle + e^{i\varphi}\sin\frac{\theta}{2}\hat{S}|1\rangle. \tag{VI.4.7}$$

We represented it on the sphere using the coordinates $\{\theta, \varphi\}$. The distance to the center of the Bloch sphere scales with the purity of the state : $d = \sqrt{2Tr[\hat{\rho}^2_{\text{exp}}] - 1}$. We associate each result with a number and we plot next to it the corresponding Wigner function. The generated state corresponding to each number on the Bloch Sphere, and their fidelities can be found in Table VI.1

# Point	Targeted state	Fidelity	$\lvert\alpha\rvert$
1	$\lvert\alpha\rangle$	86%	0.7
2	$\lvert-\alpha\rangle$	85%	0.70
3	$\lvert\text{Cat}+\rangle$	86%	0.5
4	$\lvert\text{Cat}-\rangle$	66%	0.9
5	$\lvert\alpha\rangle - i\lvert-\alpha\rangle$	82%	0.6
6	$\lvert\alpha\rangle + i\lvert-\alpha\rangle$	83%	0.6

Table VI.1: Summary of the different generated states corresponding to each point numbered on the Bloch Sphere given in Fig VI.18. The targeted state is given as well as the experimental fidelity, with correction from detection losses on Bob's side (15%), and the $|\alpha|$ value that maximizes this fidelity. The color of each point corresponds to the coordinate φ of the Bloch sphere, which legend is given.

We achieve fidelities of 70% for the odd cat state (#4), and 80% for the other states for $|\alpha| \sim 0.7$. The fidelity of the odd cat state is smaller than the other ones because it is obtained using the measurement $Q = 0$ which is related to the vacuum component and thus to the losses. $Q = 0$ has therefore a non-negligible probability to be result from the initial component $|1\rangle_A \hat{S}|0\rangle_B$ that has experienced photon losses on Alice's side. This cannot be the case for higher values of Q. The state #1, is the closest to a coherent state. It is not exactly aligned onto the equator of the sphere due to limited values of $|\alpha|$. It is also for the same reason we choose to represent the Bloch sphere in the $\{|\text{Cat}+\rangle, |\text{Cat}-\rangle\}$ basis, instead of the coherent state basis, due to the unperfected orthogonality of the two vectors (the overlap between the two states is here equal to $\langle\alpha| - \alpha\rangle = e^{-4|\alpha|^2} \sim 0.14$).

In summary, we have achieved here the remote state preparation of any CV qubits. This step is the first one towards the teleportation as it enabled us to achieve a full mapping between the discrete- and the continuous-variable encodings. In the following section, we will briefly discuss possible schemes for the implementation of teleportation and discuss about their robustness to optical losses.

VI.5 Encoding conversion by hybrid teleportation

In the near future, quantum technologies might be empowered from the use of different physical platforms. Hybrid systems, between different media, or different encodings, enable to reach out new performances. In the case of the discrete-continuous hybrid quantum information processing, some protocols can be easily achieved in continuous encodings [126], while others benefits from the discrete-variable toolbox [2]. Recently new approaches based on hybrid systems themselves enabled to achieve better performances [9, 10, 130, 158].

The realization of a heterogeneous network taking advantages of the best properties of both worlds requires therefore a transfer of the information between the two

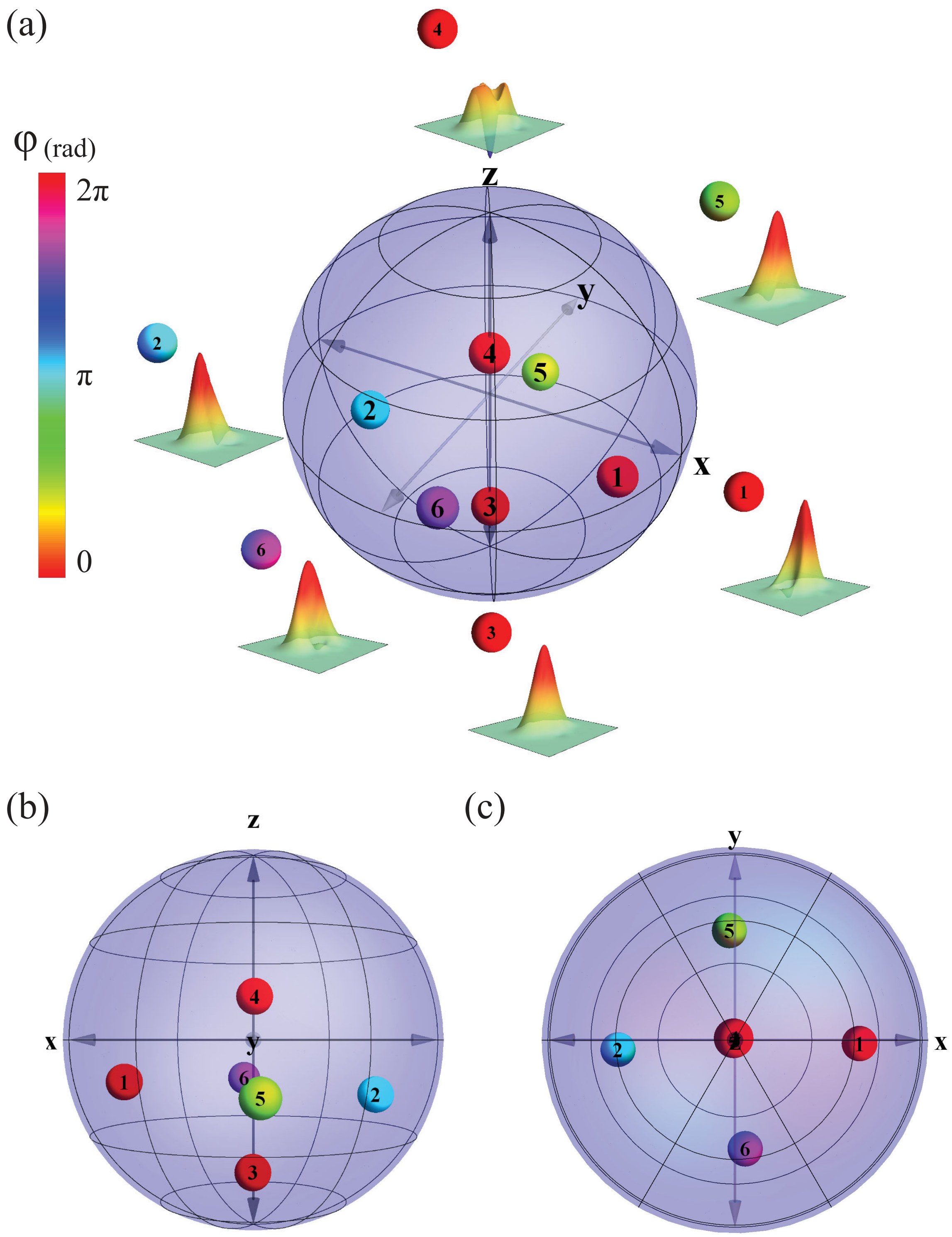

Figure VI.18: (a) Bloch Sphere and associated Wigner functions of several remotely prepared CV qubits. They are corrected from detection losses on Bob's side (15%). (b) Projection on the XZ plane. (c) Projection on the XY plane encodings, which cannot be achieved without quantum teleportation. Such protocol can be seen as a discrete- to continuous-variable converter, as an analogy of digital-to-analog conversion (or the other way round) in classical electronics. In this section we will discuss about possible schemes that would enable us to achieve hybrid quantum teleportation from one encoding to the other in the future.

The goal is to be able to teleport any discrete-variable qubit of the form $c_0|0\rangle + c_1|1\rangle$ to the continuous-variable encoded qubit $c_0|\alpha\rangle + c_1|-\alpha\rangle$, at a distance.

VI.5.1 Finding an optimal Bell measurement

Alice and Bob shares hybrid entanglement of the form $|0\rangle_A|\text{Cat}-\rangle_B - |1\rangle_A|\text{Cat}+\rangle_B$. Charlie sends a discrete-like qubits of the form $c_0|0\rangle_C + c_1|1\rangle_C$. Charlie's qubit is then mixed with Alice's mode on a beam splitter of transmission t and reflection r. $r_{AC} = -r_{CA} = t_{CC} = t_{AA} = \frac{1}{\sqrt{2}}$ gives the following state:

$$\begin{aligned} |\Psi\rangle_{ABC} = \frac{1}{2}\Big(-\frac{c_0}{\sqrt{2}}|0\rangle_A|\text{Cat}+\rangle_B|1\rangle_C - \frac{c_1}{\sqrt{2}}|0\rangle_A|\text{Cat}+\rangle_B|2\rangle_C \\ +c_0|0\rangle_A|\text{Cat}-\rangle_B|0\rangle_C + \frac{c_1}{\sqrt{2}}|0\rangle_A|\text{Cat}-\rangle_B|1\rangle_C \\ -\frac{c_1}{\sqrt{2}}|1\rangle_A|\text{Cat}-\rangle_B|0\rangle_C - \frac{c_0}{\sqrt{2}}|1\rangle_A|\text{Cat}+\rangle_B|0\rangle_C \\ +\frac{c_1}{\sqrt{2}}|2\rangle_A|\text{Cat}+\rangle_B|0\rangle_C\Big) \end{aligned} \tag{VI.5.1}$$

As in usual quantum teleportation protocols, a Bell measurement is required. The detection of a single photon (and only one) on mode A enables the generation of the following state on Bob's mode:

$$|\Psi\rangle_B = \frac{1}{\sqrt{2}}(c_1|\text{Cat}-\rangle_B - c_0|\text{Cat}+\rangle_B). \tag{VI.5.2}$$

Any DV qubit encoded in the $\{|0\rangle, |1\rangle\}$ can therefore be converted to the $\{|\text{Cat}-\rangle, |\text{Cat}+\rangle\}$ basis. The single-photon detectors must, in such case, not only have high efficiency, but they also need to be photon-number resolved. In particular, the contribution of the term $|2\rangle_A|\text{Cat}+\rangle_B|0\rangle_C$ cannot be ignored.

Another way to implement the single-photon resolving detection, can be to use a single-photon subtraction, equivalent to an annihilation operation, followed by a quadrature measurement. The annihilation operation on Alice's mode leads to the heralded state:

$$\hat{a}|\Psi\rangle_{ABC} = \frac{1}{2}\Big(\frac{c_1}{\sqrt{2}}|0\rangle_A|\text{Cat}-\rangle_B|0\rangle_C - \frac{c_0}{\sqrt{2}}|0\rangle_A|\text{Cat}-\rangle_B|0\rangle_C - c_1|1\rangle_A|\text{Cat}+\rangle_B|0\rangle_C\Big). \tag{VI.5.3}$$

The former $|2\rangle_A|\text{Cat}+\rangle_B|0\rangle_C$ component, now become a $|1\rangle_A|\text{Cat}+\rangle_B|0\rangle_C$ term. In order to discard this term, and only keep the $|0\rangle_A$ term, we trigger the teleportation protocol on the detection of the quadrature value $Q = 0$.

The annihilation operation can be realized experimentally by tapping a part of the mode A on a beam splitter, and realizing single-photon detection on it. Thus,

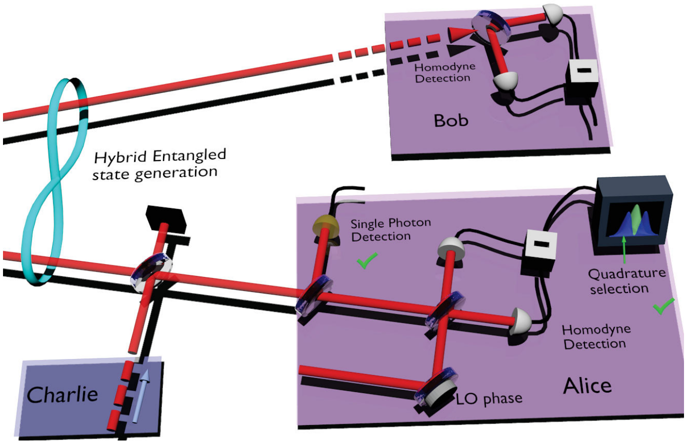

Figure VI.19: Converter scheme. Alice and Bob share a hybrid entangled state. Charlie sends a qubit that is mixed with Alice's mode using a 50/50 beam splitter. One of the outputs of the beam splitter is slightly reflected onto another beam splitter in order to achieve a single-photon subtraction. Alice detects the resulting state using homodyne detection and performs quadrature measurement. The teleportation protocol success is heralded on the detection of a single photon and on the homodyne measurement corresponding to a quadrature value $Q = 0$.

the efficiency of the detector is not a critical parameter as it is only used to herald the teleportation, and thus only the count rate will be affected. One must note that since this click is local, it will not be too costly in terms of success probability and resulting count rate. The quadrature measurement can be implemented by homodyne detection, similarly to the one proposed for steering characterization and remote state preparation of continuous qubits. This measurement efficiency will affect the resulting state and cannot be corrected.

VI.5.2 Implementation and expected results

Alice and Bob firstly generate remote hybrid entanglement, where they share the two modes of the resulting entangled state, by using the scheme described in section VI.1.2, and use the setup illustrated in Fig. VI.19.

Charlie sends its qubit to Alice, who mixes it with her part of the beam, using a 50/50 beam splitter. At one of the outputs, Alice then tap a little part of the beam ($\approx 3\%$), and send it to an SNSPD. Given a detection event, Alice implements homodyne detection and heralds the teleportation by the detection of the quadrature value $Q = 0$. Bob then performs homodyne tomography on its side using a homodyne detector, in order to check the resulting state.

The ideal case, i.e. involving ideal states and no detection losses, is presented in Fig. VI.20, where the fidelity for different measurement outcome Q and for different qubits with a vacuum weight c_0^2. We can therefore confirm that for all c_0^2, the best measurement is for $Q = 0$.

Despite our system losses ($\eta_A = \eta_B = 0.9$) and the homodyne detection losses (15%), we should be able to achieve higher than 70% fidelity, i.e. above the 2/3 limit, for a large variety c_0^2 as shown in Fig. VI.21(a) where the fidelity is plotted for $Q = 0$.

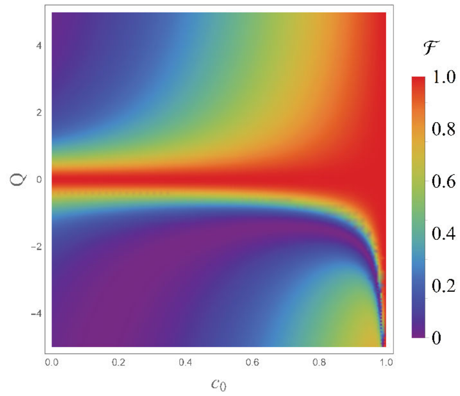

Figure VI.20: Fidelity of the generated continuous-variable qubit with the targeted state, for different homodyne measurement result Q and several weights c_0 of the initial qubit.

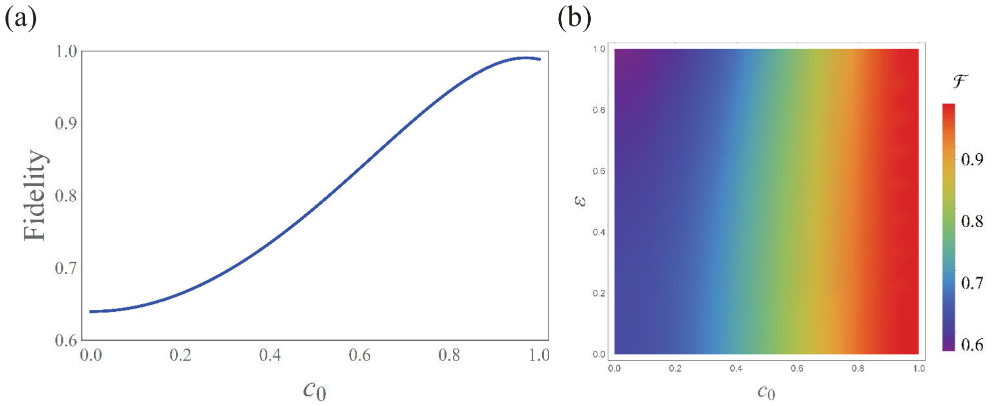

Figure VI.21: (a) Fidelity of the generated continuous-variable state with the targeted state, for $Q = 0$ and several weights of the qubit c_0. The system efficiencies are considered symmetric on each side of the hybrid entangled state, $\eta_A = \eta_B = 0.9$, and the homodyne detection losses (15%). (b) Fidelity of the generated continuous-variable state with the targeted state as a function different acceptance band ϵ of the homodyne detection, and of c_0 the vacuum weight of the qubit.

The fidelity depending on the bandwidth of our quadrature acceptance window ϵ is plotted on Fig. VI.21(b).

Changing the CV basis

For two ideal cat states, with a large $|\alpha|$, the relation between the cat state basis $\{|\text{Cat}+\rangle, |\text{Cat}-\rangle\}$, and the coherent state basis $\{|\alpha\rangle, |-\alpha\rangle\}$ is trivial. The resulting qubit can be written in the ideal case as $a_\alpha|\alpha\rangle_B + a_{-\alpha}|-\alpha\rangle_B$ in the $\{|\alpha\rangle, |-\alpha\rangle\}$, with $a_\alpha = c_1 - c_0$ and $a_{-\alpha} = c_0 + c_1$. In the case of a squeezed vacuum and squeezed single photon as initial resources, the relation between such basis, and the coherent state basis can be a little more complex. The overlap between two qubits is plotted in Fig. VI.22, as a function of c_0 and a_α, for $|\alpha| = 0.7$.

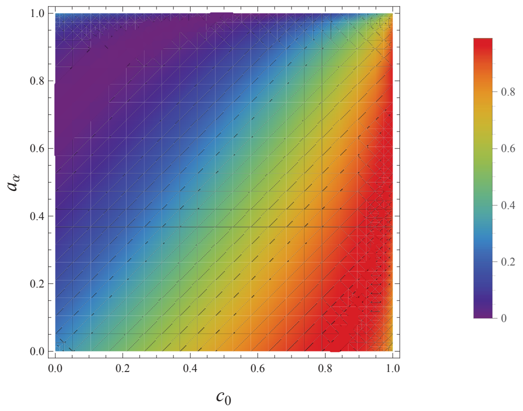

Figure VI.22: Overlap of the qubit encoded in the squeezed Fock basis $\{\hat{S}|0\rangle, \hat{S}|1\rangle\}$, with weight c_0, and encoded in the coherent state basis $\{|\alpha\rangle, |-\alpha\rangle\}$, of weight a_α, for $|\alpha| = 0.7$.

VI.5.3 An analog-to-digital converter?

In this section we will briefly discuss the possibility of using a similar method for the implementation of a continuous-to-discrete-variable teleportation protocol.

Alice and Bob share hybrid entanglement, which can be written as:

$$|\Psi\rangle_{AB} \propto |+\rangle_A|\alpha\rangle_B - |-\rangle_A|-\alpha\rangle_B = \hat{D}_B(\alpha)|+\rangle_A|0\rangle_B - \hat{D}_B(-\alpha)|-\rangle_A|0\rangle_B. \quad \text{(VI.5.4)}$$

Charlie sends this time a continuous qubit of the form :

$$c_\beta|\beta\rangle_C + c_{-\beta}|-\beta\rangle_C \quad \text{(VI.5.5)}$$

Charlie combines his mode with Bob's mode with a 50/50 beam splitter, therefore realizing the transformation:

$$\begin{aligned} \hat{D}_B(\alpha) = e^{\alpha\hat{a}-\alpha^*\hat{a}^\dagger} \rightarrow e^{\alpha\frac{\hat{a}+\hat{c}}{\sqrt{2}}-\alpha^*\frac{\hat{a}^\dagger+\hat{c}^\dagger}{\sqrt{2}}} &= \hat{D}_B(\frac{\alpha}{\sqrt{2}})\hat{D}_C(\frac{\alpha}{\sqrt{2}}) \\ \hat{D}_B(-\alpha) &\rightarrow \hat{D}_B(\frac{-\alpha}{\sqrt{2}})\hat{D}_C(\frac{-\alpha}{\sqrt{2}}) \\ \hat{D}_C(\beta) &\rightarrow \hat{D}_C(\frac{\beta}{\sqrt{2}})\hat{D}_B(\frac{-\beta}{\sqrt{2}}) \\ \hat{D}_C(-\beta) &\rightarrow \hat{D}_C(\frac{-\beta}{\sqrt{2}})\hat{D}_B(\frac{\beta}{\sqrt{2}}) \end{aligned} \quad \text{(VI.5.6)}$$

The resulting state can then be simplified as:

$$\begin{aligned} |\Psi\rangle_{ABC} = c_\beta|+\rangle_A|\frac{\alpha-\beta}{\sqrt{2}}\rangle_B|\frac{\alpha+\beta}{\sqrt{2}}\rangle_C + c_{-\beta}|+\rangle_A|\frac{\alpha+\beta}{\sqrt{2}}\rangle_B|\frac{\alpha-\beta}{\sqrt{2}}\rangle_C \\ -c_\beta|-\rangle_A|\frac{-(\alpha+\beta)}{\sqrt{2}}\rangle_B|\frac{\beta-\alpha}{\sqrt{2}}\rangle_C - c_{-\beta}|-\rangle_A|\frac{\beta-\alpha}{\sqrt{2}}\rangle_B|\frac{-(\alpha+\beta)}{\sqrt{2}}\rangle_C. \end{aligned} \quad \text{(VI.5.7)}$$

For the particular case of $\alpha = \beta$, this can be furthermore simplified in:

$$\begin{aligned} |\Psi\rangle_{ABC} = c_\alpha|+\rangle_A|0\rangle_B|\sqrt{2}\alpha\rangle_C + c_{-\alpha}|+\rangle_A|\sqrt{2}\alpha\rangle_B|0\rangle_C \\ -c_\alpha|-\rangle_A|-\sqrt{2}\alpha\rangle_B|0\rangle_C - c_{-\alpha}|-\rangle_A|0\rangle_B|-\sqrt{2}\alpha\rangle_C. \end{aligned} \tag{VI.5.8}$$

A simple homodyne measurement $Q = 0$ on mode B and tracing of mode C would lead to:

$$|\Psi\rangle_A = c_\alpha|+\rangle_A - c_{-\alpha}|-\rangle_A. \tag{VI.5.9}$$

However if α is too small, this scheme might not work. Detecting a single photon on mode B can therefore also be a way to implement this teleportation scheme, and to get:

$$|\Psi\rangle_A = c_{-\alpha}|+\rangle_A - c_\alpha|-\rangle_A. \tag{VI.5.10}$$

Experimentally speaking, the mode C can be used in order to lock the two seed waves and to maintain the same phase between Alice and Charlie at the mixing point.

VI.6 Conclusion

We have demonstrated hybrid entanglement, i.e. entanglement between particle-like and wave-like optical qubits. This entanglement is produced at a distance, and the two modes can freely propagate and be used in subsequent protocols. We have shown that we can also increase the dimensionality of the state and the amount of entanglement it contains by generating qutrit hybrid entangled state This scheme is based on an additional photon detection. We also studied some theoretical protocols and calculations that could be applied to our system to show entanglement features such as Bell-type non-locality or steering. However it is complicated to find operators robust enough to losses and further investigations should therefore be conducted.

Finally, we gave a first example of the use of hybrid entanglement by remotely generating continuous-variable qubits by measurement on the discrete mode. A second application would be the conversion of discrete-variable states to continuous-variable states, for which we studied a possible scheme.

Hybrid entanglement can also be seen as entanglement between a particle, and between a wave like-qubit, i.e. between a system of 0 or 1 particle, and a system containing several particles. On the next chapter, we will demonstrate that the developed setup is also a versatile way to achieve the exploration in phase space of the entangled state and the realization of "micro-macro entanglement".

VII

Micro-Macro entanglement of light

Introduction

In the previous chapter, we have shown the generation of hybrid entanglement between discrete-like and continuous-like types of optical qubit. However, we will show here that the fidelity to the targeted state remain limited by the approximation done on the initial resource. To enhance this fidelity, an additional local subtraction can be operated, resulting into new effects in phase space. Moreover, the ability to play with the number of photon detections, and the amount of initial squeezing make our setup a versatile platform to study the generation of squeezing-induced micro-macro entanglement, where state of small size, i.e. single-photon states, are entangled with "macroscopic" states. In this chapter, we will detail the realization of such entanglement and study some macroscopicity witnesses that we will apply to our state.

Contents

VII.1 Additional local photon subtraction 128
  VII.1.1 Even kitten state: an approximation 128
  VII.1.2 Experimental setup 129
  VII.1.3 Results 130
VII.2 Squeezing-induced micro-macro entanglement of light . . 132
  VII.2.1 Experimental generation 132
  VII.2.2 Results 133
VII.3 Macroscopicity witnesses 136
  VII.3.1 Pointer in phase space 136
  VII.3.2 Distance in phase space 139
  VII.3.3 Distinguishability in phase space 141
  VII.3.4 Amplitude and frequency of the Wigner fringes and purity decay 143
  VII.3.5 Fisher information based criterion 144
  VII.3.6 Resume 146
VII.4 Conclusion 147

VII.1 Additional local photon subtraction

In Chapter VI, we have demonstrated hybrid entanglement between discrete-like and continuous-like types of qubit of the form:

$$|\Psi\rangle \propto |0\rangle|\mathrm{Cat}+\rangle + |1\rangle|\mathrm{Cat}-\rangle. \tag{VII.1.1}$$

However, due to our approximation consisting in using squeezed vacuum as a starting resource, instead of a real even cat state, the maximum achievable fidelity with the targeted hybrid state was therefore limited to 94%. The *effectively* generated state was therefore of the form:

$$|\Psi\rangle_{AB} \propto \hat{S}_B|0\rangle_A|0\rangle_B + \hat{b}\hat{S}_B|0\rangle_A|0\rangle_B. \tag{VII.1.2}$$

where $\hat{S}_B$ and $\hat{b}$ are the squeezing and annihilation operators on mode B. This effect can be seen directly in the superposition of the generated even and odd cat states $(|\mathrm{Cat}+\rangle_B + |\mathrm{Cat}-\rangle_B)/\sqrt{2}$, i.e. the projection in the rotated basis, which should be a coherent state in the ideal case. Figure VII.1(a) gives the Wigner function of this superposition for the state in Eq. VII.1.2: as it can be seen, it has an imperfect gaussian shape.

In this section, we will show how to go around this approximation by an additional local subtraction and how this can be implemented experimentally.

VII.1.1 Even kitten state: an approximation

In order to improve such fidelity, an additional local photon subtraction enables to generate a two-photon subtracted squeezed vacuum, which has a closer fidelity to an even cat state [81]. Such operation will also lead to an increase in the size of the generated cat state. This operation can be written as:

$$|\mathrm{Cat}+\rangle \approx \hat{a}\hat{a}\hat{S}|0\rangle \propto \left(-\frac{\sinh 2|\xi|}{2}\hat{S}|0\rangle + \sqrt{2}\sinh^2|\xi|\hat{S}|2\rangle\right) \tag{VII.1.3}$$

The fidelity with a targeted even cat state can be found in Fig. VII.2 (a). A value $|\alpha|^2$ up to 1.1 can be obtained with fidelities greater than 98%.

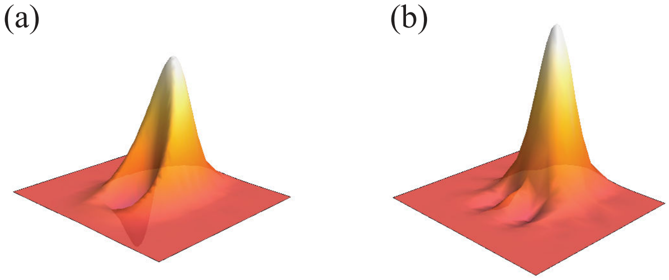

Figure VII.1: Theoretical plot of the Wigner function of the resulting state in the rotated basis (a) without and (b) with additional local photon detection.

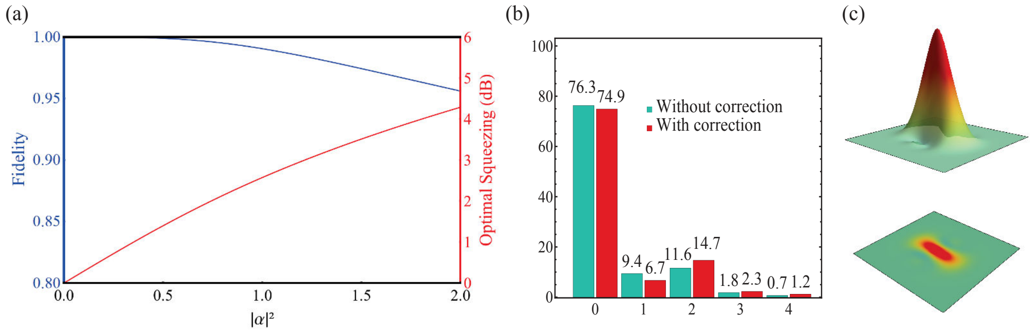

Figure VII.2: (a) The fidelity between an even cat state of size $|\alpha|^2$ and a two-photon-subtracted squeezed vacuum is given in blue, for different optimized squeezing. The optimal squeezing to achieve the maximal fidelity for a given size is plotted in red. (b) Experimental photon-number probabilities with and without correction from detection losses (15%). (c) Experimental Wigner function of two-photon subtracted squeezed vacuum corrected from detection losses (15%).

Experimentally speaking, going from the generation of an odd cat state to an even one requires the addition of another annihilation operation, which can be implemented by an other photon detection on a small part of the beam. For example, at the output of the conditioning path, one can replace the former fiber by a fibered beam splitter and two photon-detectors. Given two conditioning events in an acceptance window smaller than 1 ns, the heralded state is therefore a two-photon subtracted squeezed vacuum. The experimental resulting state is presented in VII.2(b) and (c), and reaches $\mathcal{F} = 88\%$ with an even cat state of size $|\alpha|^2 = 0.8$, and a squeezing of 3 dB out of the type I-OPO.

By this improved approximation, the fidelity of the hybrid entangled state is therefore not limited anymore and can be higher than 99%. The resulting hybrid entangled state can in this case be written as:

$$|\Psi\rangle_{AB} \propto \hat{b}\hat{S}_b|0\rangle_A|0\rangle_B + \hat{b}^2\hat{S}_b|0\rangle_A|0\rangle_B. \tag{VII.1.4}$$

Figure VII.1 (b) gives the Wigner function of the projection in the rotated basis, with an additional subtraction, i.e. when the even cat state is approximated by a two-photon subtracted squeezed vacuum. The fidelity of the superposition with a coherent state is close to unity.

VII.1.2 Experimental setup

The protocol of the resulting hybrid entangled state generation will be the same as the one developed in Chapter VI, at the difference of a single-photon subtracted squeezed vacuum, i.e. an odd kitten state, used as a starting resource on Bob's side, instead of the previous squeezed vacuum state. This additional local photon subtraction is experimentally translated into another conditioning path for the continuous-variable mode, which is the twin of the other as shown in Fig. VII.3. We trigger the homodyne detection on the detection of two events, arriving inside an acceptance window of 1 ns of delay. The beam splitter ratio is chosen in order to balance the coincidences counts:

given a single-photon detection on Bob's first detector, the second detection probability of each path must be equal. The calculation of the generated hybrid entangled state is fully detailed in Appendix F.

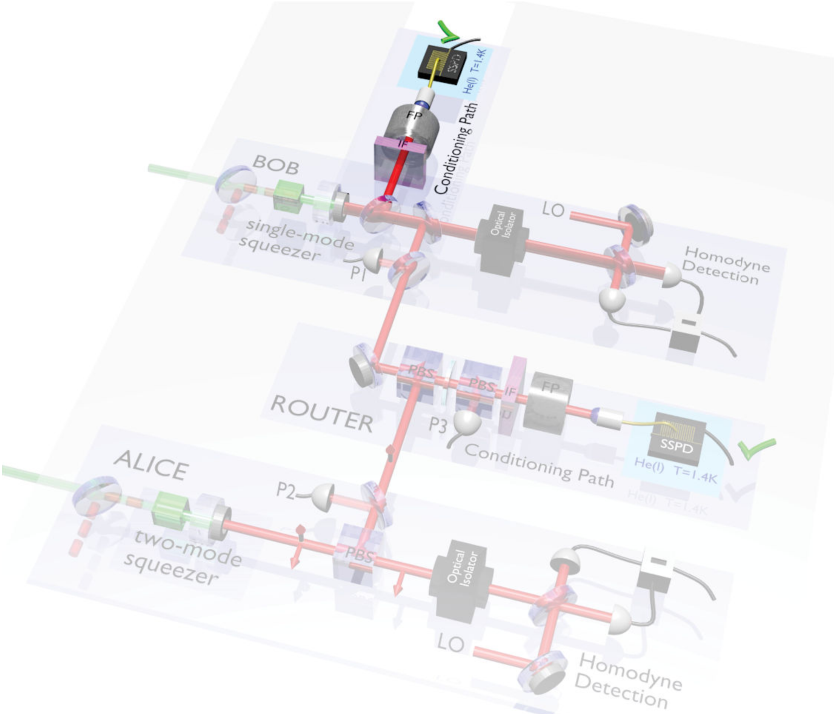

Figure VII.3: Experimental setup. Alice and Bob locally generate the required resources by using continuous-wave optical parametric oscillators operated below threshold. A two-mode squeezer and a single mode-squeezer are used respectively on Alice's and Bob's node. Firstly, a small fraction of Bob's squeezed vacuum is tapped (3%) and send through a first filtering path and to a single-photon detector (SNSPD). This detection is a local operation. A second small fraction of Bob's is the tapped by a second beam splitter and mixed at a central station to the idler beam generated by Alice. The resulting beam is then frequency-filtered (second conditioning path) and detected by a superconducting single-photon detector (SNSPD). Two-photon detection events, one on each detector, separated by less than 1 ns, herald the entanglement generation. The hybrid entangled state is characterized by two high-efficiency homodyne detections. Photodiodes P1, P2 and P3 are used for phase control and stabilization. The beam splitter ratio in the central station enables to choose the relative weights in the superposition. FP stands for Fabry-Pérot cavity, IF for interferential filter, PBS for polarizing beam splitter and LO for local oscillator.

VII.1.3 Results

The results are given in form of the Wigner functions of the reduced density matrices $\langle k|_A\hat{\rho}|l\rangle_A$ in Fig. VII.4. As expected, the elements in the $|\pm\rangle$ basis have Wigner functions closer to gaussian functions. The reached negativity of entanglement is $\mathcal{N} = 0.28$ with correction from detection efficiency ($\eta = 85\%$). The fidelity with the targeted state is $\mathcal{F} = 71\%$, for $|\alpha| = 0.9$.

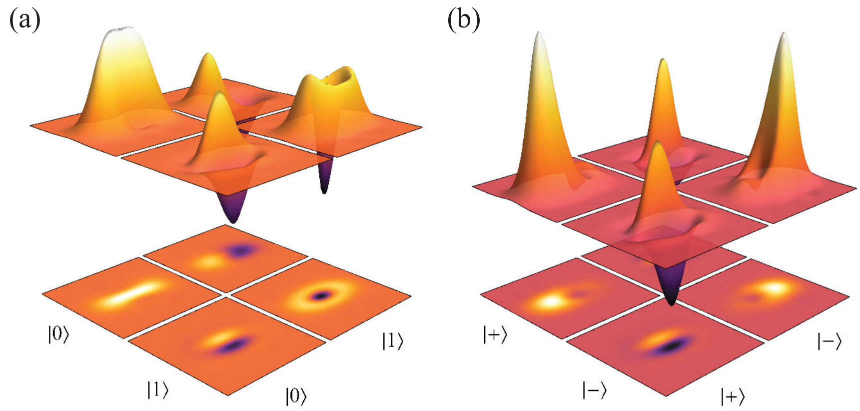

Figure VII.4: Experimental Wigner representation of the hybrid entangled state with an additional local photon detection, with correction from detection losses ($\eta = 85\%$) (a) in the Fock state basis and (b) in the $|\pm\rangle$ rotated basis. The relative phase is set to $\varphi = \pi$ and the beam splitter ratio in the central station is adjusted to generate a maximally entangled state, i.e. with equal superposition weights.

The lack of improvement in the size $|\alpha|^2$ and in the fidelity comes from the fact that this state is more sensitive to losses, due to the multiple heraldings.

The theoretical negativity of entanglement is given as a function of the efficiency of the system in Fig VII.5(a), as well as the one for the single-photon detection hybrid entangled state. Due to the complex structure of the state, it is therefore much more sensitive to optical losses than its "single-detection" counterpart.

This state is also more sensitive to phase noise in its "non-local" conditioning path, as shown in Fig VII.5(b), where the negativity of entanglement is plotted as a function of the gaussian noise standard deviation σ, for different system efficiencies.

In addition to this high sensitivity, the requirement of a two-photon detection event leads to a drastic decrease of the count rate, requiring therefore long-term stability of

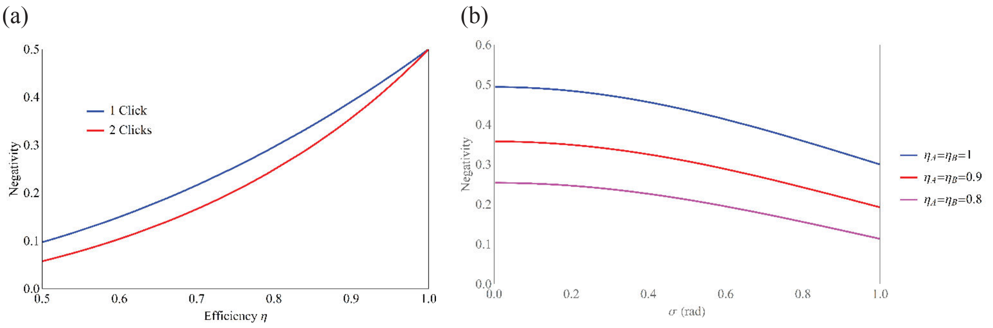

Figure VII.5: (a) Theoretical evolution of the negativity of entanglement with the system efficiency, for the single-photon detection (in blue), i.e. the state generated in Chapter VI, and for the additional photon subtraction (in red). (b) Theoretical plot of the negativity of entanglement as a function of the gaussian phase noise standard deviation σ on its conditioning path for different system efficiencies (symmetric on both sides) the experiment. Efficient photon detectors are therefore required for these cascaded detections and the new generation of SNSPDs, detailed in Chapter III, was used here.

We have shown here a way to increase the quality of our state by the mean of additional single-photon detection operation. We will see in the next section that the setup furthermore enables a larger distance in phase space between the two coherent states, paving the way to the study of squeezing induced micro-macro entangled states [159].

VII.2 Squeezing-induced micro-macro entanglement of light

Hybrid entanglement between continuous and discrete variables can also be seen as entanglement between two waves with opposite phases, and the presence or absence of one particle. By extending this idea to higher photon numbers, hybrid entanglement can therefore be related to entanglement between a small number of particles - 0 or 1, with two "classical" macroscopic systems: two lasers with opposite phase. Such view reminds the historical Schrödinger cat *gedankenexperiment*, where a cat is entangled with an atom [41]. In this experiment, an atom is in a superposition of $|g\rangle + |f\rangle$. The de-excitation of the atom triggers the spreading of a poison, which kills the cat. The cat-atom system is therefore in the superposition: $|g\rangle|dead\rangle + |f\rangle|alive\rangle$. Such state is very close to the targeted hybrid system: $|0\rangle|\alpha\rangle + |1\rangle| - \alpha\rangle$.

If the "micro" aspect is easy to define here, the macroscopicity of a quantum system is a tough question and an active topic, where very recent experiments [160, 161] and measures are still fruits of numerous questions nowadays [162, 163].

This question of macroscopicity has long been related to the absurdity of having a cat alive and dead at the same time and to the collapsing of quantum mechanics at macroscopic scale. Creating macroscopic quantum states is thus an experimental challenge as it allows to probe the border between quantum and classical behavior and to see if a limiting size of system could exist. While the role of decoherence has long been studied to explain the difficulty to have macroscopic states [13], criteria on what precisely is a macroscopic superposition has still not found a universal answer.

In this section we will show the experimental construction of microscopic states entangled to macroscopic states. Unlike previous studies based on displaced single-photon entanglement [164–167], where the mean photon number is signing the macroscopicity of the state, our setup also enables to play with the number of photon detection and initial squeezing, in order to investigate features of macroscopicity in phase space.

VII.2.1 Experimental generation

In order to implement such micro-macro entanglement, we use the same setup as for the hybrid entanglement setup with additional local subtraction, shown in Fig. VII.3 and described in Section VII.1.2. Using a half-wave plate and a polarized beam splitter in front of the local subtraction path, we can choose whether to subtract or not a first single-photon on the squeezed vacuum on Bob's side. In the following of the chapter, the two generated state will be re-named *1-click* and *2-click* states depending on the number of photon detection involved in the setup, for the sake of simplicity. Given the choice of a first photon detection, we then implement the same setup as for the hybrid entanglement, by mixing the two conditioning path and heralding the generation of the entangled state by a second, non-local, detection. Finally, we can change the pump power on Bob's side to increase the initial squeezing.

To simplify the notation, we also re-name the two "macroscopic" states involved in the superposition: $|\Psi_+\rangle$ and $|\Psi_-\rangle$. The hybrid entangled state can this way be written, whatever the squeezing and number of photon detection involved, in the general form:

$$|\Psi\rangle_{AB} \propto |+\rangle_A|\Psi_+\rangle_B - |-\rangle_A|\Psi_-\rangle_B. \tag{VII.2.1}$$

Thanks to the full reconstruction of the density matrix $\hat{\rho}_{AB}$, we can obtain these states by getting the reduced density matrix in the rotated basis: $\rho_{\Psi_\pm} = \langle\pm|_A\hat{\rho}_{AB}|\pm\rangle_A$, where $|\pm\rangle_A = \frac{|0\rangle_A \pm |1\rangle_A}{\sqrt{2}}$.

VII.2.2 Results

Figures VII.6 and VII.7 give the experimental marginal distribution of the states ρ_{Ψ_+} and ρ_{Ψ_-}, and the corresponding Wigner functions, for 1-click and 2-click experiments respectively.

The two states exhibit very different behavior in terms of marginal distributions. For both states, the two marginal blocks seem to enlarge with the increasing squeezing. However their phase-space distance increases much more with the squeezing for the 2-click state. Moreover, the overlap between the two distributions decreases for the 2-click state, while it stays constant for the 1-click state.

The slight oscillations on the Wigner functions and on the marginal distributions of highly squeezed states come from the fact that the Hilbert space spanned by these states is higher. The number of acquired quadrature of 100 000 for the tomography process becomes therefore insufficient in these cases.

Figures VII.8 and VII.9 provide the negativity of entanglement and the mean photon number of the states on Bob's side (since theoretically $\langle\Psi_+|\hat{n}|\Psi_+\rangle = \langle\Psi_-|\hat{n}|\Psi_-\rangle$, we give here the experimental mean value) for an ideal system and for the experimental results.

For 6 dB of squeezing, entanglement is present in the system ($\mathcal{N} \approx 0.20$) between a small number of photon (0 and 1) and a larger mean photon number ($\langle\hat{n}\rangle \approx 5.6$). The mean photon number is higher than the theoretical prediction in the ideal case (i.e. no losses in the system). This discrepancy with the theory comes from the fact that the measured squeezing on the homodyne detection has experienced losses. In order to reach a certain final amount of squeezing, the pumping value must be higher than the theoretical prediction, resulting on a higher mean photon number.

In terms of photon number, we can say that we achieve entanglement between two states of different sizes. But is the macroscopicity, and in particular a micro-macro entangled state, only characterized by the mean photon number? A recently published paper softens this affirmation by showing that the macroscopicity of a system depends more on the effective number of photon truly participating in the entanglement [168]. New criteria, other than the mean photon number, have therefore to be studied in order to fully characterize such entanglement.

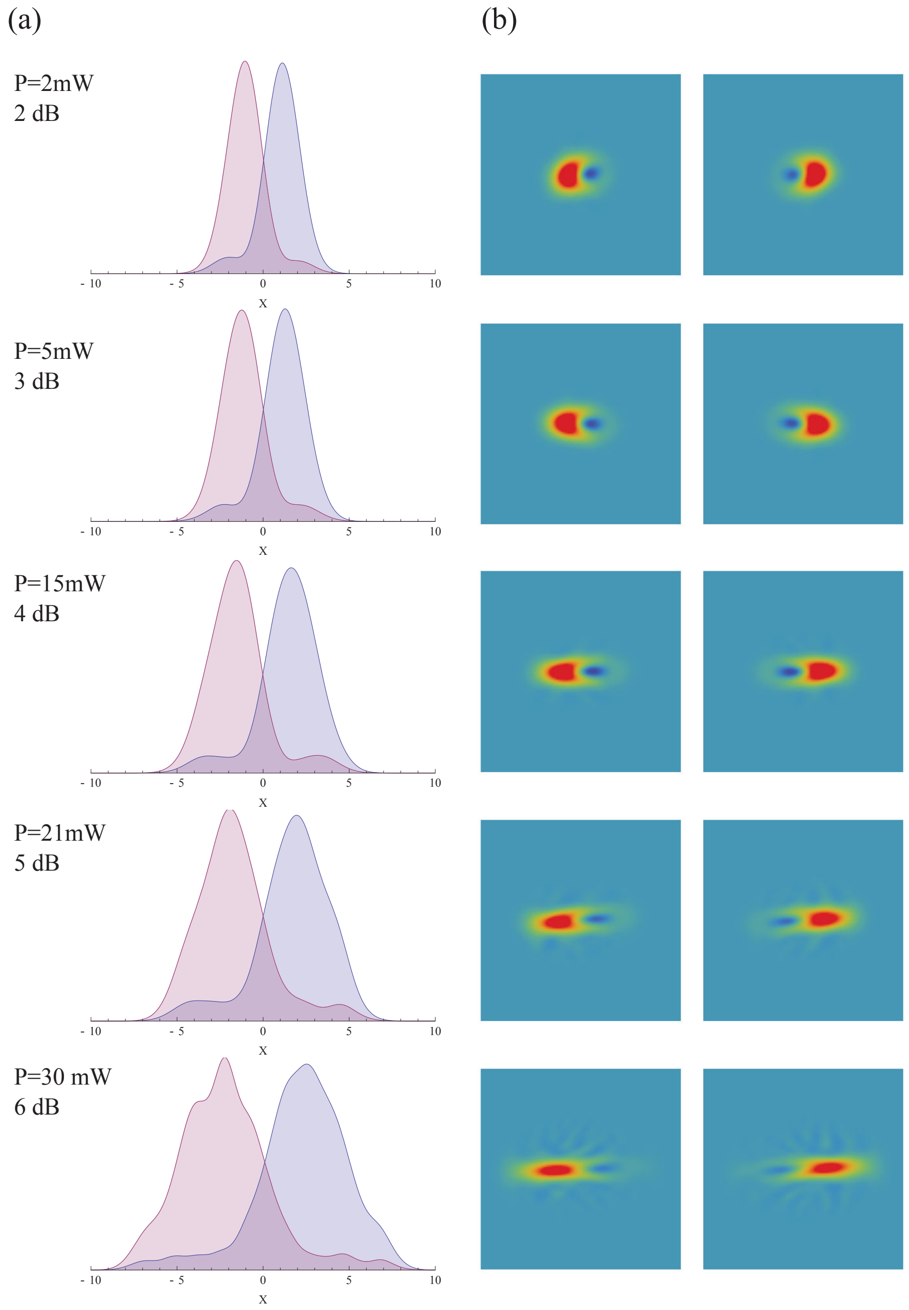

Figure VII.6: Experimental results for the 1-click state. (a) Marginal distributions and (b) Wigner functions of the two reduced density matrices $\rho_{\Psi_\pm} = \langle \pm|_A \hat{\rho}_{AB} |\pm\rangle_A$, for different input pump powers for the type I-OPO, i.e. for different amounts of squeezing on Bob's mode. These results are corrected from detection losses (15%). $|\Psi_-\rangle$ marginal distribution is plotted in purple and the corresponding Wigner function is on the left side.

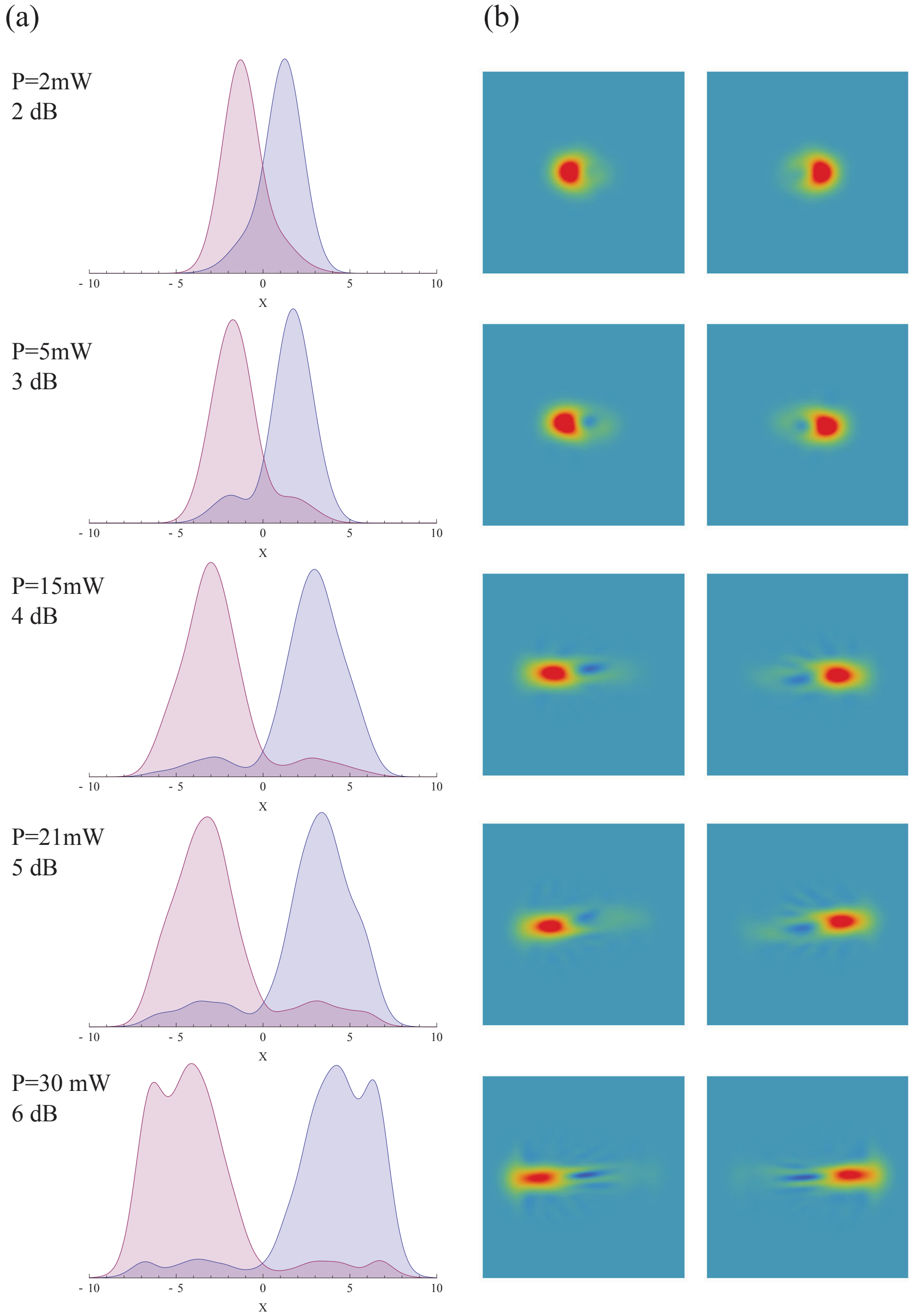

Figure VII.7: Experimental results for the 2-click state. (a) Marginal distributions and (b) Wigner functions of the two reduced density matrices $\rho_{\Psi_\pm} = \langle \pm|_A \hat{\rho}_{AB} |\pm\rangle_A$, for different input pump powers for the type I-OPO, i.e. for different amounts of squeezing on Bob's mode. These results are corrected from detection losses (15%). $|\Psi_-\rangle$ marginal distribution is plotted in purple and the corresponding Wigner function is on the left side.

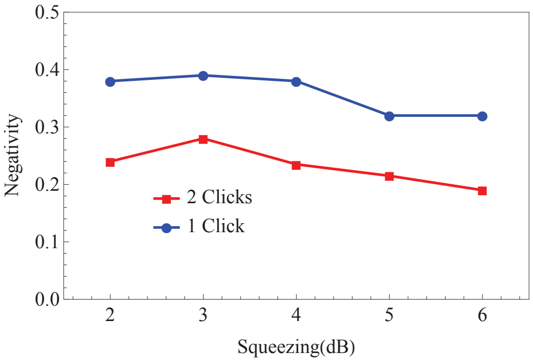

Figure VII.8: Experimental negativity of entanglement as a function of squeezing, corrected from detection losses (15%).

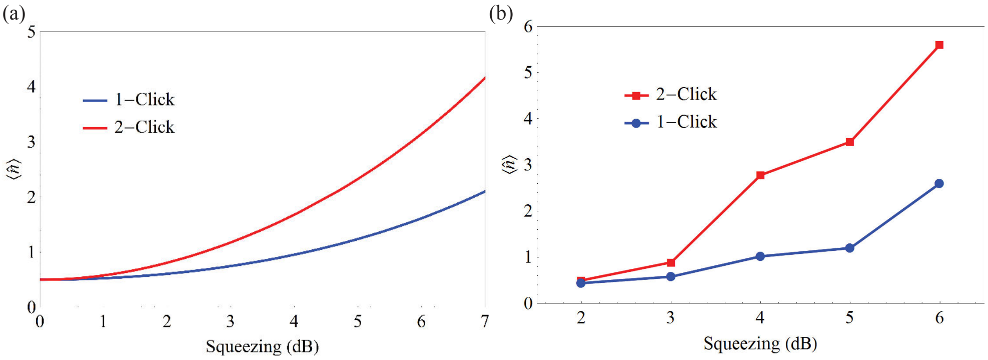

Figure VII.9: (a) Theoretical simulations of the mean photon number with the squeezing for 1-click and 2-click states, for an ideal system without losses, i.e. $\eta = \eta_A = \eta_B = 1$. (b) Experimental values of the mean photon number with the squeezing, as $(\langle\Psi_+|\hat{n}|\Psi_+\rangle + \langle\Psi_-|\hat{n}|\Psi_-\rangle)/2$, corrected from detection losses (15%).

VII.3 Macroscopicity witnesses

In order to quantify the macroscopic aspect of our state we will review a certain number of criteria. Indeed, quantifying in a universal manner the macroscopicity of a quantum state is still not a solved question [168]. H. Jeong *et al.* provide in [169] a review of different criteria used in the literature. However most of the reviewed criteria are only applicable to pure states. In this section we will only consider criteria that are applicable to our state, i.e., applicable to optical mixed states. We will as well apply them to single-photon entanglement, and in particular to displaced single-photon entanglement, where a displacement operation is performed on one of the modes [164]:

$$|\psi\rangle = \frac{1}{\sqrt{2}}(|0\rangle_A \hat{D}_B(\alpha)|1\rangle_B + |1\rangle_A \hat{D}_B(\alpha)|0\rangle_B). \tag{VII.3.1}$$

VII.3.1 Pointer in phase space

This criterion was proposed, as a first approach, by Sekatski and co-workers in [170] and [171]. The macroscopicity is related to the distinguishability of the two states using a noisy classical measurement. A classical pointer on a scale x, interacts with our quantum state, and can shift by a value related to the mean photon number. The final distribution of the pointer can be written as:

$$p_\rho = Tr[p_i(x + \hat{a}^\dagger \hat{a})\hat{\rho}] \tag{VII.3.2}$$

where $p_i(x) = e^{-\frac{x^2}{2\sigma}}$ is a gaussian distribution of the pointer, indicating the classical behavior of the pointer. The probability for the classical pointer to distinguish between the two states therefore depends on the amount of noise of the classical detector and can be written as:

$$P^{\sigma}_{|\Psi_1\rangle,|\Psi_2\rangle} = \frac{1}{2}\left(1 + \frac{1}{2}\int dx |p_{|\Psi_1\rangle}(x) - p_{|\Psi_2\rangle}(x)|\right). \tag{VII.3.3}$$

The size of the superposition is there related to the maximal amount of noise that can be tolerated to distinguish the two states with a certain probability P_g. The more macroscopic a superposition is, the easier it can be distinguished, and therefore the more noise the detector can tolerate. The authors give an example for two Fock states, $|M\rangle$ and $|M+N\rangle$, separated by N photons:

$$P^{\sigma}_{|M\rangle,|N+M\rangle} = \frac{1}{2}(1 + \text{erf}\left(\frac{N}{2\sqrt{2\sigma}}\right)). \tag{VII.3.4}$$

For a given targeted separation P_g, and the related maximal tolerable amount of noise $\sigma^{P_g}_{\text{MAX}}$, the size of any state is defined as the corresponding size N of the equivalent Fock state superposition:

$$\text{Size}_{P_g}[|\Psi_1\rangle, |\Psi_2\rangle] = 2\sqrt{2}\text{erf}^{-1}(2P_g - 1) \times \sigma^{P_g}_{\text{MAX}}[|\Psi_1\rangle, |\Psi_2\rangle]. \tag{VII.3.5}$$

For displaced single-photon entanglement of the form:

$$|\Psi\rangle = \hat{D}_B(\alpha)|0\rangle_A|1\rangle_B + \hat{D}_B(\alpha)|1\rangle_A|0\rangle_B, \tag{VII.3.6}$$

the probability of distinguishing between $\hat{D}_B(\alpha)|1\rangle_B$ and $\hat{D}_B(\alpha)|0\rangle_B$ as a function of the detector noise is plotted in Fig. VII.10. For a targeted value of P_g, for example $P_g = 2/3$, the maximum tolerable noise evolves with α. The Fock state that would lead to the same $\sigma^{2/3}_{\text{MAX}}$ has the size $N \approx 0.86 \times \sigma^{2/3}_{\text{MAX}}$, which is therefore the defined size of the displaced single-photon entangled state.

For states opposite in phase space, as for example in cat-like superposition $|\alpha\rangle \pm |-\alpha\rangle$, the photon number being the same, $|\alpha|^2$, it is required to add a displacement in order to translate their photon number and to "help" the detector: $|0\rangle \pm |2\alpha\rangle$. This criterion is therefore displacement-sensitive. Numerical simulations of the probability $P^{\sigma}_{\Psi_+,\Psi_-}$ for our 1- and 2-click states, are given in Fig. VII.11(a) for 3 dB of squeezing and in (b) for 6 dB of squeezing. Our 2-click state is more "macroscopic" than the 1-click state: the amount of noise that can be tolerated to reach out certain value P_g is higher. For more squeezing, it is possible to target values of P_g for a larger tolerable $\sigma^{P_g}_{\text{MAX}}$. The size therefore rises with the squeezing.

The theoretical prediction of $\sigma^{2/3}_{\text{MAX}}$ as a function of the squeezing, for an ideal state is presented in Fig. VII.12(a). Figure VII.12(b) gives the corresponding experimental

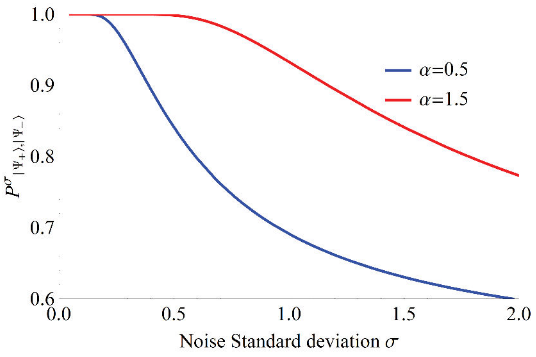

Figure VII.10: Theoretical simulation of the probability $P^{\sigma}_{\hat{D}_B(\alpha)|1\rangle_B,\hat{D}_B(\alpha)|0\rangle_B}$ in function of standard deviation of the detector noise σ for displaced single-photon entanglement, for several values α of the displacement

results with correction from detection losses (15%). The 2-click state can thus be considered more macroscopic for this criterion than the 1-click state. For a given displacement, the macroscopicity is, as predicted, both depending on the squeezing, and on the number of single-photon detection.

However, if we add another displacement on Bob's mode it is possible to theoretically target any values of P_g, showing that this criterion is above all sensitive to the mean photon number. This means also that a displacement operation can lead to the generation of macroscopic superposition, as is featured in displaced single-photon experiments [164–167]. Moreover, such criterion can also be applied to demonstrate the macroscopicity of states such as a coherent state $|\alpha\rangle$, as such state can be re-written as: $|\alpha\rangle = \frac{1}{\sqrt{2}}(D(\alpha)|+\rangle + D(\alpha)|-\rangle)$. Given a large enough displacement to be distinguishable, i.e. its amplitude being large enough, a coherent state can therefore be a macroscopic superposition, which is controversial.

As a conclusion, even though this criterion gives information about the possibility of discriminating two states with a classical detector, it is more related to the photon

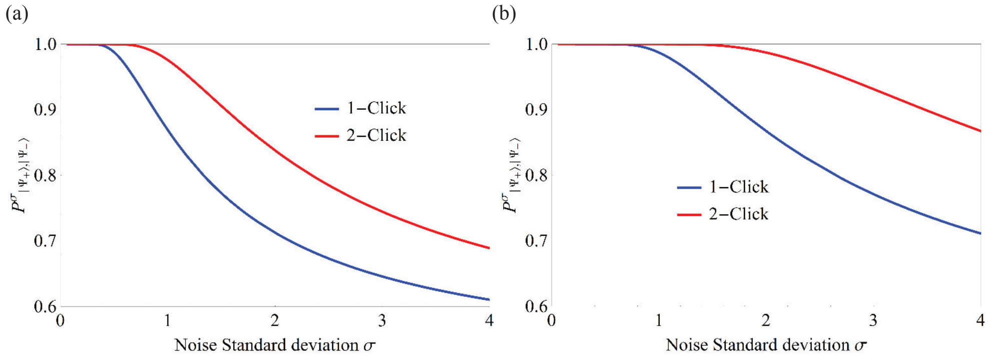

Figure VII.11: Theoretical simulation of the probability $P^{\sigma}_{\Psi_+,\Psi_-}$ as a function of the standard deviation of the detector noise σ (with system symmetric losses of $\eta = \eta_A = \eta_B = 0.9$), for (a) for 3 dB of squeezing, and (b) for 6 dB squeezing. The used displacement value α is related to the mean photon number value of our two states as $\alpha = \sqrt{\frac{Tr[\rho_+\hat{n}]+Tr[\rho_-\hat{n}]}{2}}$.

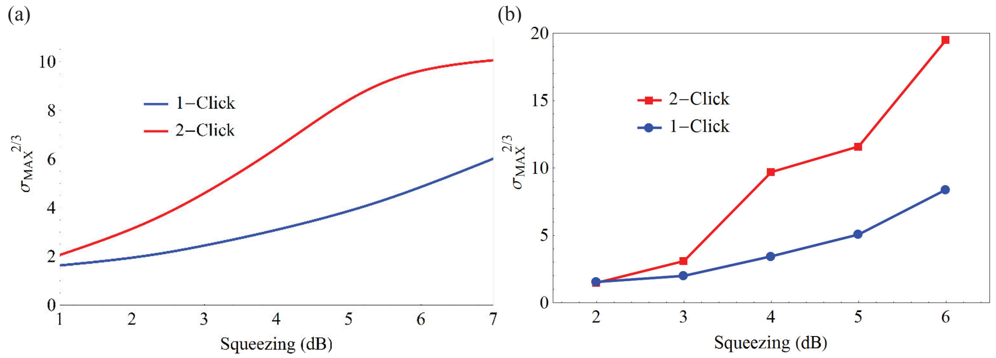

Figure VII.12: (a) Theoretical simulation for an ideal state of $\sigma_{\mathrm{MAX}}^{2/3}$ as a function of the squeezing for (in blue) 1-click state and (in red) 2-click state.(b) Experimental values, with correction from detection losses (15%), for different squeezing amount measured on the homodyne detection. The used displacement value α is related to the mean photon number value of our two states as $\alpha = \sqrt{\frac{Tr[\rho_+\hat{n}]+Tr[\rho_-\hat{n}]}{2}}$.

number than to a separability in phase space. The next criterion will target the ability to distinguish both states in phase space.

VII.3.2 Distance in phase space

In a second approach, the two states must be as distant as possible in phase space, i.e. answering to a criterion defined in [159]. In particular, such distance D can be expressed via the marginal distribution $\mathcal{P}(x)$ as:

$$D = \frac{1}{\sigma_0}|\langle\Psi_+|\hat{x}|\Psi_+\rangle - \langle\Psi_-|\hat{x}|\Psi_-\rangle| = \frac{1}{\sigma_0}|\int_{-\infty}^{+\infty} x\mathcal{P}_+(x)dx - \int_{-\infty}^{+\infty} x\mathcal{P}_-(x)dx|. \quad \text{(VII.3.7)}$$

It can be seen as the "distance" between the two marginal distributions. For displaced single-photon entanglement, this distance does not change with the amplitude of the displacement, and is always equal to 2. Applied to our particular states, it can be written as a function of the squeezing:

$$\begin{aligned} D_{\text{1-click}} &= \frac{2}{\sqrt{s}} \\ D_{\text{2-click}} &= \frac{6-2s}{\sqrt{3s^3-2s^2+3s}} \end{aligned} \quad \text{(VII.3.8)}$$

where $s = e^{-2\xi}$. Figure VII.13 (a) gives the theoretical value of this criterion in the ideal case (i.e. no losses). Both distances increase with the squeezing, but the slope is much more important for the 2-click state than for the single conditioning hybrid state. However, for a certain squeezing amount, a 1-click state could always reach the same D as a 2-click state (for a smaller squeezing though). Moreover, this criterion does not imply anything about the distinguishability of the two states by a measurement, despite the fact it shows some sort of separation in phase space.

The experimental results, given in Fig VII.13(b), with correction from detection losses (15%), are consistent with the theoretical predictions. Due to the losses on the

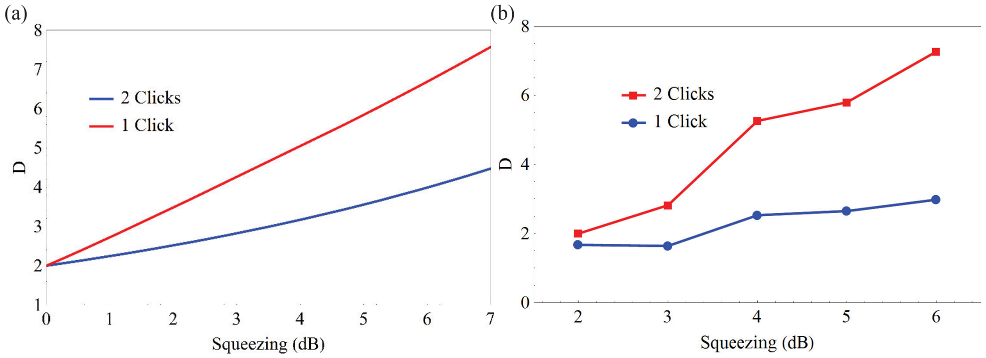

Figure VII.13: (a) Theoretical simulation of the distance D with squeezing for the ideal 1-click state (in blue) and 2-click states (in red). (b) Experimental results, with correction from detection losses (15%).

optical path, to reach 6 dB squeezing on the homodyne detection, we have indeed to furtherly push the pump, leading to a higher number of photon and a higher squeezing at the output of the OPO, as previously explained for the mean photon number. D is therefore higher than its theoretical prediction for 6 dB and is closer to the value it would reach for 7 dB.

All the observed discrepancies can be explained by phase noise and losses, as studied theoretically in the following. We will use squeezing values of 3 dB and 6 dB as examples. Figure VII.14 provides the distance D as a function of the system efficiency, (a) for 3 dB squeezing and (b) for 6 dB squeezing. The discrepancy with losses is slightly more important for 2-click states than for 1-click states, and increases with the squeezing amount. The distance between the two marginal distributions is also affected by the noise on the phase of the entanglement. D therefore varies with the standard deviation σ of a gaussian phase noise of the entanglement path, as shown in VII.15 for different squeezing levels, with the system efficiencies $\eta = \eta_A = \eta_B = 0.9$.

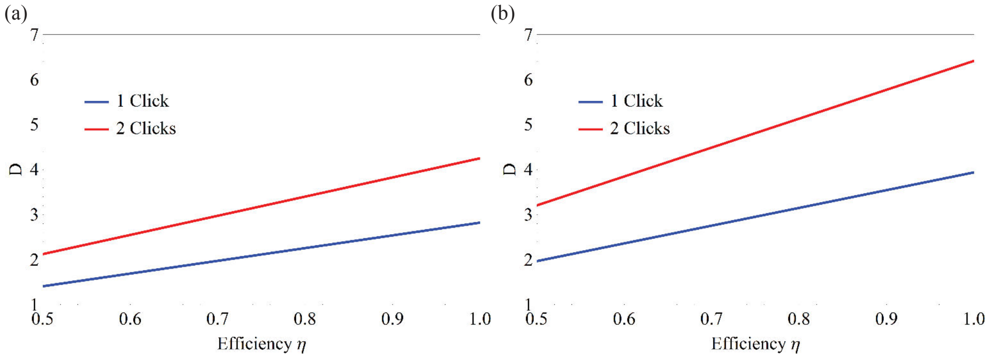

Figure VII.14: Theoretical simulation of D criterion under symmetric system efficiencies ($\eta_A = \eta_B = \eta$) for (a) 3 dB of squeezing and (b) 6 dB of squeezing.

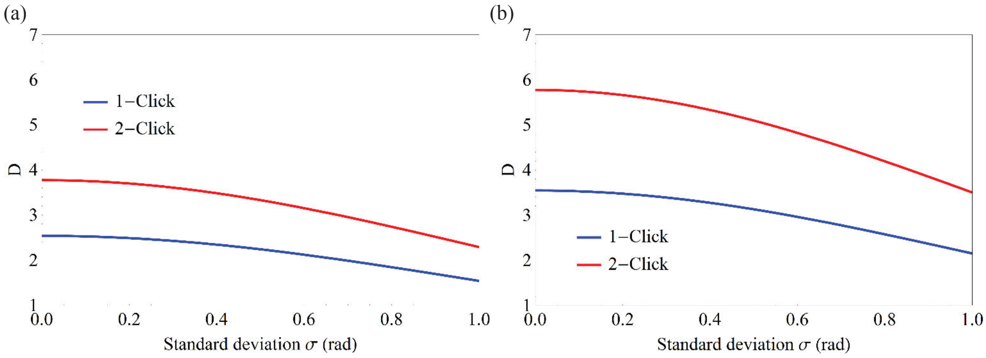

Figure VII.15: Theoretical simulation of D with the standard deviation of the gaussian phase noise of the entangling optical path for (a) 3 dB of squeezing and (b) 6 dB of squeezing, with symmetric efficiencies $\eta = \eta_A = \eta_B = 0.9$.

VII.3.3 Distinguishability in phase space

To quantify the distinguishability between the two states in phase space, Neergard-Nielsen and Andersen introduced criterion P [159] such as:

$$P = \frac{1}{2}(\langle\Psi_+|\hat{\Pi}_+|\Psi_+\rangle - \langle\Psi_+|\hat{\Pi}_-|\Psi_-\rangle) = \frac{1}{2}(\int_0^{+\infty}\mathcal{P}_+(x)dx + \int_{-\infty}^{0}\mathcal{P}_-(x)dx), \quad \text{(VII.3.9)}$$

where

$$\begin{aligned} \hat{\Pi}_+ &= \int_0^{+\infty}|x\rangle\langle x|dx \\ \hat{\Pi}_+ &\int_{-\infty}^{0}|x\rangle\langle x|dx. \end{aligned} \quad \text{(VII.3.10)}$$

This quantity is related to the overlap between the two components of the superposition. Applied to our state, it is possible to re-write the corresponding equations as:

$$\begin{aligned} P_{\text{1-click}} &= \frac{1}{2} + \frac{1}{\sqrt{2\pi}} \approx 0.9 \\ P_{\text{2-click}} &= \frac{1}{2} + \sqrt{\frac{2}{\pi}}\frac{1}{\sqrt{3s^2 - 2s + 3}} \end{aligned} \quad \text{(VII.3.11)}$$

with $s = e^{-2\xi}$. For displaced single-photon entanglement, P does not depend on the amplitude of the displacement and is always equal to 0.9.

In Figure VII.16(a) is given the evolution of P with the squeezing for both states, in the ideal case (i.e. no losses). We can see that whatever the squeezing, for single-click experiments, P stays at 0.9. This is the consequence of the first observation we made about the overlap between the marginal distributions being constant. The two-click state, however, can theoretically reach values impossible to obtain with one click experiment. Moreover displaced single-photon entanglemed states give the same boundary at $P \approx 0.9$. The experimental values that we obtained for our states are given in Fig VII.16(b). Theoretically, according to the losses for 3 dB (Fig VII.17(a)) and for 6 dB-squeezing (Fig VII.17(b)) we should be able to target slightly larger values of P for 1-click and 2-click states and beat the $P_{single} \approx 0.9$ limit. This discrepancy

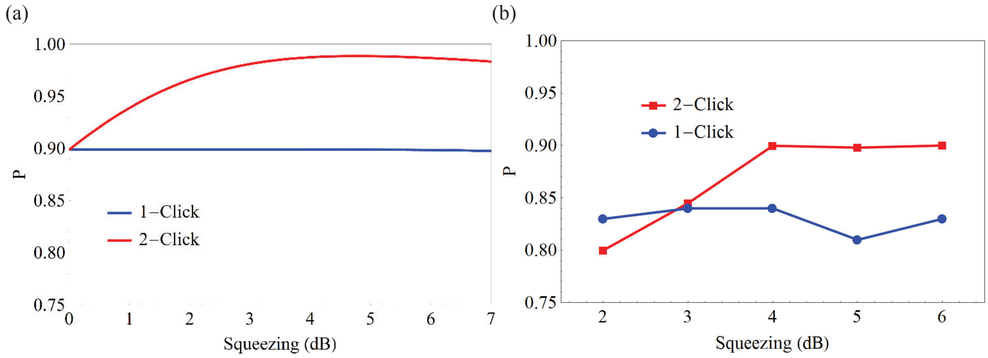

Figure VII.16: (a) Theoretical simulation of P, the distinguishability, with squeezing. (b) Experimental values of P with the squeezing, with correction from detection losses (15%).

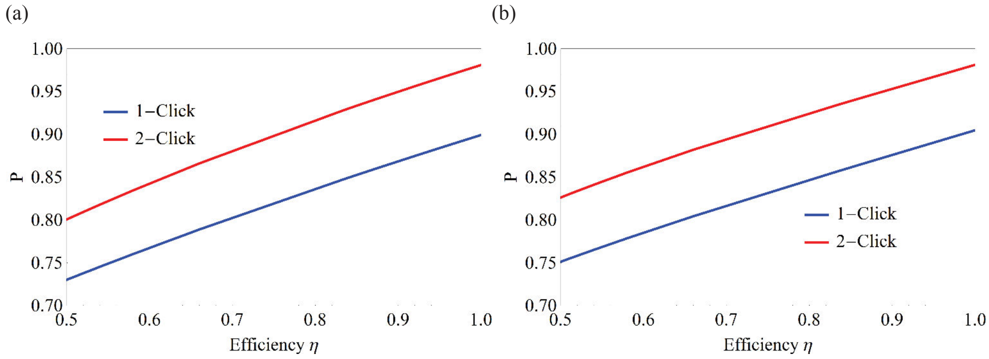

Figure VII.17: Theoretical simulation of P criterion under symmetric losses ($\eta_A = \eta_B = \eta$) for (a) 3 dB of squeezing and (b) 6 dB of squeezing.

might be due to the phase noise we can observe. We saw previously that the negativity of entanglement was not so sensitive to the phase noise of the mixing path, even though this effect was more important for the 2-click state than for the 1-click counterpart. However the distinguishability, shown in Fig. VII.18 for 3 dB (a) and for 6 dB (b), is more sensitive.

This sensitivity is roughly the same whatever the squeezing and the number of click, which would explain the offset effect, of roughly the same amount : $\Delta P \approx 0.05$, for all our experiments. Improvements have therefore to be made in order to furtherly stabilize the optical setup to target higher values of P and beat the "single detection" experiment limit.

As a conclusion, this criterion is above all sensitive on the number of photon detection involved in the system.

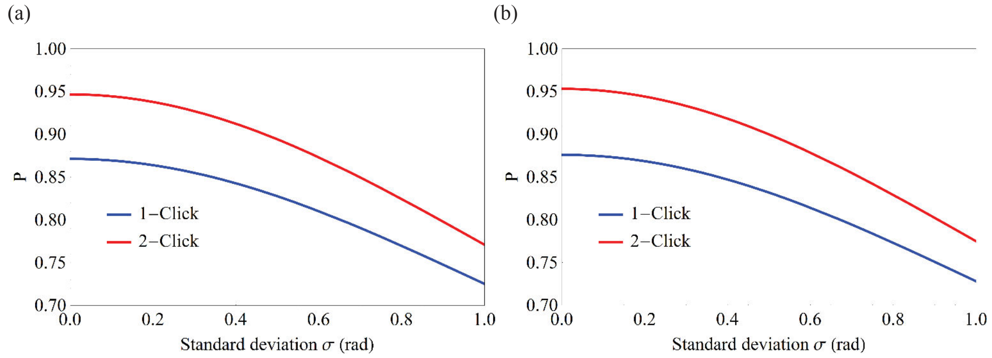

Figure VII.18: Theoretical simulation of P with the standard deviation σ of the gaussian phase noise of the entangling optical path, for (a) 3 dB of squeezing and (b) 6 dB of squeezing. Symmetric efficiencies $\eta_A = \eta_B = \eta = 0.9$ are considered.

VII.3.4 Amplitude and frequency of the Wigner fringes and purity decay

The idea, developed by Jeong et al. [172], is to base a macroscopicity criterion on the measurement of the *amplitude* and the *frequency* of the Wigner function fringes of a superposition, at the same time. Such criterion was developed because of the fringes observed in Schrödinger cat-like superposition of coherent states, where the frequency and observed contrast is directly related to the size and the purity of the superposition.

The Wigner function can be calculated from the characteristic function $\chi(\xi)$ of the state ρ :

$$\chi(\xi) = Tr[\hat{\rho} e^{(\xi \hat{a}^\dagger - \xi^* \hat{a})}]. \tag{VII.3.12}$$

The authors therefore define the criterion as:

$$\mathcal{I}(\hat{\rho}) = \frac{1}{2\pi} \int d\xi [|\xi|^2 - 1] |\chi(\xi)|^2 \tag{VII.3.13}$$

This criterion can also be defined in an alternative way as:

$$\mathcal{I}(\hat{\rho}) = -\frac{1}{2} \frac{d\mathcal{P}(\hat{\rho})}{d\tau} = -Tr[\hat{\rho}\mathcal{L}(\hat{\rho})] \tag{VII.3.14}$$

where $\mathcal{L}(\hat{\rho}) = \hat{a}\hat{\rho}\hat{a}^\dagger - \frac{1}{2}(\hat{\rho}\hat{a}^\dagger\hat{a} + \hat{a}^\dagger\hat{a}\hat{\rho})$ is a Lindblad superoperator for photon losses. If our states were more sensitive to other types of decoherence (such as phase noise for example), another type of operator would be adapted. For single-photon entanglement, this value is equal to 0.5, and does not change even if displacement is applied on one mode.

By simulating the behavior of our two states, we can find out in Fig VII.19 that indeed, the more squeezing is applied, the more macroscopic the system is. Moreover it seems consistent with the idea of phase-space separation as the 2-click state is more macroscopic than the 1-click state. However, no difference can really be obtained experimentally, as shown in Fig. VII.19 (b).

Indeed, this criterion is very sensitive to losses as shown in Fig. VII.20. For 6 dB of squeezing, the state is more fragile and therefore decoheres faster than for 3 dB

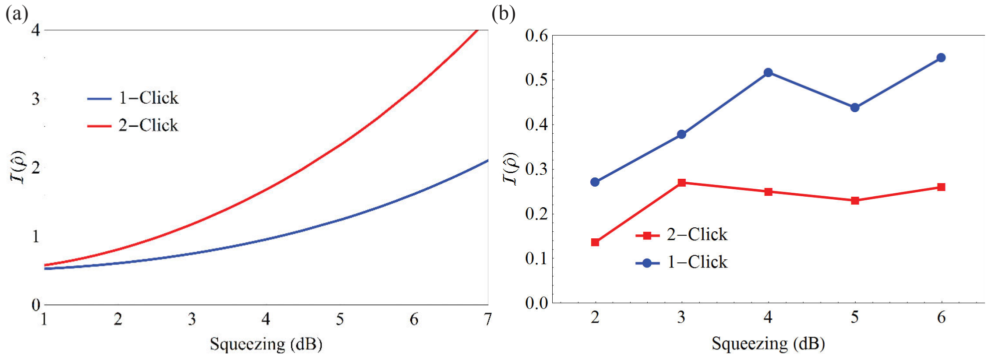

Figure VII.19: (a) Theoretical simulation, in the ideal case, of $\mathcal{I}(\hat{\rho})$ with squeezing for 1-click and 2-click states. (b) Experimental values, of $\mathcal{I}(\hat{\rho})$ with the squeezing, with correction from detection losses (15%).

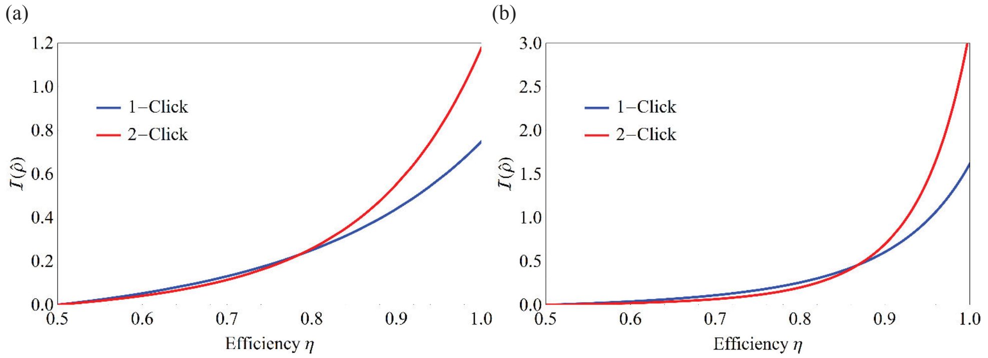

Figure VII.20: Theoretical simulation of $\mathcal{I}(\hat{\rho})$ with the system efficiency, (a) for 3 dB squeezing and (b) for 6 dB squeezing, for 1-click and 2-click states.

of squeezing. However both systems converge towards similar values around 80% of system efficiency. Improvement on the setup must therefore be conducted in order to be able to witness differences with squeezing and photon detections.

This criterion answers to a large number of properties of a "good" measurement of macroscopicity, such as the invariance through *free operations*, an operation which does not create the resource. However, a recently published paper by Yadin and Vedral [173] demonstrated that it fails as a monotone measurement of the macroscopicity, leading to a significant underestimation of the macroscopicity in terms of Fisher information, therefore still considered as the best criterion so far.

VII.3.5 Fisher information based criterion

This criterion, proposed by Fröwis and Dür [174], has been proved to comply with many requirements, such as the impossibility to achieve macroscopic superposition using displacement operation [173]. Originally made for spin systems, it makes a difference between macroscopic quantum states and macroscopic superpositions. The macroscopicity criterion derived here consists in quantifying the maximal Fisher information that can be obtained from a system. The Fisher information quantifies the maximal precision in which a parameter associated with a certain observable $\hat{A}$, can be estimated with a given quantum state $\hat{\rho}$.

The authors also show that this criterion can be related to the fast oscillations of certain observables, which could remind us of the oscillations of the Wigner function fringes for large cat states, developed as a macroscopicity measurement in the previous criterion. By decomposing any state using its spectral decomposition:

$$\hat{\rho} = \sum_a \lambda_a |\psi_a\rangle\langle\psi_a|, \tag{VII.3.15}$$

the Fisher information can be written as:

$$\mathcal{F}(\hat{\rho}, A) = 2\sum_{a,b} \frac{(\lambda_a - \lambda_b)^2}{\lambda_a + \lambda_b} |\langle\psi_a|A|\psi_b\rangle|^2. \tag{VII.3.16}$$

For a pure state, it can be simplified using the variance of the operator A as:

$$\mathcal{F}(|\psi\rangle, A) = 4V(|\psi\rangle, A) = 4(\langle\psi|A^2|\psi\rangle - \langle\psi|A|\psi\rangle^2). \tag{VII.3.17}$$

The size of the system is then defined by the maximal Fisher information for a set of operator A_i:

$$\mathcal{N}_{\mathcal{F}}(\hat{\rho}) = \max_{A_i \in \mathcal{A}} \frac{1}{4N} \mathcal{F}(\hat{\rho}, A_i). \tag{VII.3.18}$$

As in the previous criterion, we will only apply such operation onto Bob's subsystem, therefore $N = 1$ for us. For operators, we can use the set of quadrature operators:

$$x_i(\theta_i) = \mathbb{1} \otimes \sigma_0 (a_B e^{-i\theta_i} - a_B^\dagger e^{i\theta_i}) \tag{VII.3.19}$$

The maximal Fisher information one can get is then to be optimized on θ_i. For any NOON-state type, $|N\rangle|0\rangle + |0\rangle|N\rangle$, the Fisher information can be written as 2^N. In the case of single-photon entanglement, the size is therefore $2/4 = 0.5$. Moreover, for displaced single-photon entanglement, the maximal Fisher information does not depend on the displacement amplitude α that is applied to it.

In contrast, the maximal Fisher information depends on the squeezing and the number of photon subtraction in our case. Figure VII.21(a) provides the theoretical value of the maximized Fisher information with the amount of squeezing on Bob's mode. We can see that the evolution is very similar to the $\mathcal{I}(\hat{\rho})$ criterion for pure states. We apply this criterion to our experimental matrices, corrected from detection losses (15%) and find the results plotted in Fig. VII.21(b).

The results are quite consistent with the theory and show the macroscopicity of our state as being more important than displaced single-photon entanglement, in particular for high squeezing. Already, for 3 dB squeezing, the state is found to be more macroscopic than an ideal displaced single-photon entangled state.

The difference between 2-click and 1-click states tends to be very small experimentally, though existing. Indeed for the losses of our experiments, this criterion drops drastically for the 2-click state, as shown in Fig. VII.22, where the maximal Fisher information is given with the system efficiency for (a) 3 dB and (b) 6 dB squeezing. However, the resulting operation seems quite noisy, probably due to the reconstruction process and the added errors. By increasing the number of sample points for

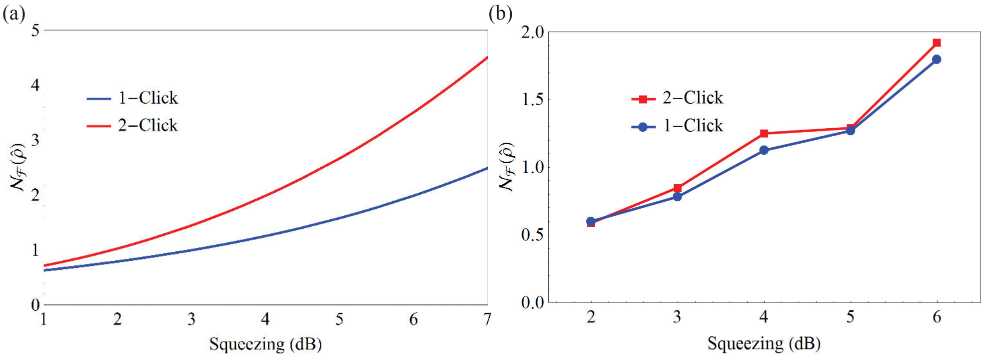

Figure VII.21: (a) Theoretical simulation, in the ideal case, of $\mathcal{N}_{\mathcal{F}}(\hat{\rho})$ with squeezing. (b) Experimental value, of $\mathcal{N}_{\mathcal{F}}(\hat{\rho})$ with the squeezing, with correction from detection losses (15%).

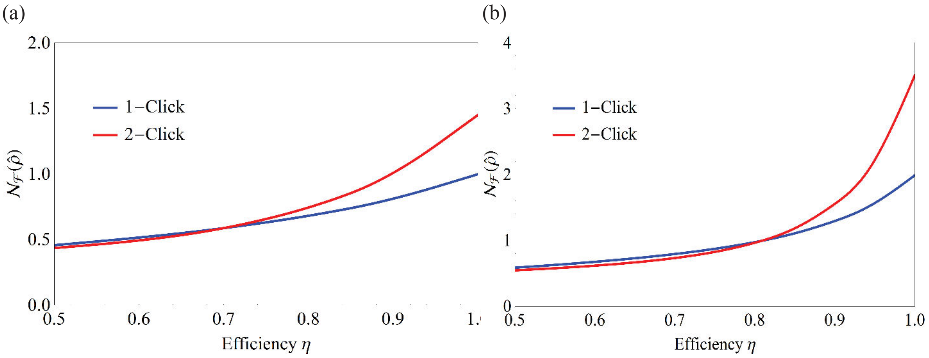

Figure VII.22: Theoretical simulations of $\mathcal{N}_{\mathcal{F}}(\hat{\rho})$ as a function of the system efficiency, (a) for 3 dB squeezing and (b) for 6 dB squeezing.

the tomographic process and the number of iteration of the MaxLike algorithm, we would probably reduce such numerical noise, in particular for larger size. The Fisher information seems more robust to losses than $\mathcal{I}(\hat{\rho})$ for 3 dB of squeezing, but tends to be the same for 6 dB, as shown in Fig. VII.22.

The maximal Fisher information is, up-to-date, the most acknowledged criterion on macroscopicity measurement. In our case, it is sensitive to squeezing operation and to the number of photon detection, but not to displacement operations. As the Fisher information is also a criterion based on the measurement of a quadrature operator, it might probably be possible to translate this macroscopy criterion on a direct homodyne measurement.

VII.3.6 Resume

We resume here the results of the different criteria applied to the 1-click and 2-click states, both theoretically simulated and experimentally realized. The comparison with displaced single-photon entangled state is given. In particular we summarize, by adding a check mark, when a given criterion can be affected by the controllable ingredients of the setup, such as displacement in the single-photon case or squeezing in our case.

Criterion	Disp. Sg.$_{Th}$	1-click$_{Th}$	2-click$_{Th}$	1-click$_{Exp}$	2-click$_{Exp}$
Pointer	✓	✓	✓	✓	✓
Distance	×	✓	✓	✓	✓
Distinguishability	×	×	✓	×	×
Purity decay	×	✓	✓	×	×
Fisher Information	×	✓	✓	✓	✓

Table VII.1: Recapitulative table of the different macroscopicity criteria, for different states: the theoretical 1-click$_{Th}$ and 2-click$_{Th}$ states, their experimental counterparts 1-click$_{Exp}$ and 2-click$_{Exp}$, with correction from detection losses (15%), and the displaced single-photon entangled state, denoted as: Disp. Sg.$_{Th}$.

VII.4 Conclusion

In this chapter, we extended the notion of hybrid entanglement to entanglement between microscopic degree of freedom and macroscopic degrees of freedom. We implemented a scheme in order to generate a new type of optical squeezing-induced micro-macro entanglement, where the macroscopicity can be seen in the phase-space distance between two states.

This new type of "micro-macro" entangled state allows the test of various criteria. The way of qualifying and quantifying this macroscopicity is still an unanswered question and a very active topic. While some criterion can only applied to pure states, some only quantify the separability, as the ability to be detected by a classical detector, or the distance in phase-space. For some criterion, our states can beat the limit achievable with an ideal single-photon entangled state, even with the addition of a displacement operation on this latest, such as phase space distance and separability. In particular, our state can show a macroscopic behavior with respect to the most recognized criteria for macroscopicity which is the maximal Fisher information.

We therefore provided a new platform for playing with these macroscopic features where in addition to the photon number ingredient achieved via squeezing, one can change the number of photon detections applied.

Conclusion

In the work presented here we have demonstrated new applications of the hybrid approach of quantum information processing, such as the engineering of complex optical quantum states. Firstly, by combining large escape efficiency optical parametric oscillators and high-efficiency superconducting single-photon detectors, we demonstrated a high brightness single-photon source. Such source can also be used to generate higher number Fock states as well as large optical Schrödinger cat states. In this endeavor, we used a method that consists in engineering the core state containing all the required non-gaussianity and minimizing therefore the experimental costs. Then, the targeted size can be achieved through a gaussian operation, such as squeezing. We therefore demonstrated the generation of high-fidelity optical large squeezed cat states with a count rate allowing the implementation of subsequent protocols. We also showed that the generated core state contains the same quantum features as a Schrödinger cat states, in terms of negativity of the Wigner function, while being more robust against decoherence. Moreover, the method we developped already provides the optimal core state for transmission purpose.

In a last part, we demonstrated a quantum bridge between discrete and continuous encodings via the generation of remote hybrid entanglement between CV and DV optical qubits. As a first step towards the transfer of information from one encoding to another via quantum teleportation, we reported the remote generation of arbitrary continuous-variable qubits via measurement on the discrete variable side. We finally extended the idea of entanglement between a wave-like qubit and a particle-like qubit to the concept of micro-macro entanglement between Hilbert-spaces of different sizes. After generating squeezing induced micro-macro entanglement on a versatile platform enabling to play with the number of photon detections and photon number via squeezing, we demonstrated that our state should ideally exhibit macroscopic features and scaling through a wide range of criteria. Our experimental results showed in addition macroscopic behavior under the most acknowledged criterion, which is the maximal Fisher information.

Perspectives

Firstly, the robustness of the generated large squeezed cat states to losses opens the question of the necessity of large cat state resources for quantum computation and communication. Indeed, as the changes between a squeezed cat state and a real cat states only consists in the division and multiplication of the quadrature by a certain amount (i.e. unsqueezing), the protocols should remain the same, while showing more robustness to experimental losses. A recent paper by the group of J. Home [124] in the field of circuit QED shows an improvement of the precision of the measured state via squeezing. This effect is due to the reduced sensitivity of the state to the detection inefficiency, showing the large range of application of this question. This would mean that the size of the cat, i.e. its photon number, is therefore not the important parameter for quantum information processing, but it is the overlap related to the contrast of the Wigner central fringes which would enable to overcome classical protocols.

Another immediate perspective of this PhD work is the implementation of a Digital to Analog-like quantum converter via the teleportation of a discrete qubit to a continuous encoding.

It has also been recently suggested that single photon entanglement can be more efficiently distributed over long distances using hybrid entangled state. This potential advantage has to be fully examined [175].

On another side, the limiting factor on the efficiency of our teleportation protocol is coming from its sensitivity to the decoherence [169]. By changing the discrete variable degree of freedom, encoded in presence or absence of a particle to polarization type qubits, as recently proposed by Jeong [176], or to time-bin encoding, would enable to reach better connectivity to DV realizations. It would also change the game for Bell tests implementation. With polarization encoding on the DV side, the hybrid entangled state can also directly be used as the main off-line resource to achieve resource-efficient quantum computation [130].

Finally, another current limitation of our hybrid processes, and in particular of our generation of hybrid entangled state, is the probabilistic nature of the process. This drastically decreases the count rate when one wants to generate more complex states, even with close-to-unity detection efficiencies. A way to achieve deterministic generation of such entanglement would be to implement light-matter interaction, such that, through single-photon operation, a coherent wave would be reflected. The interaction of a single-photon entangled state with this system would directly lead to the deterministic generation of large size micro-macro hybrid entangled state of form $|0\rangle|\alpha\rangle + |1\rangle|-\alpha\rangle$. A first step has been recently realized by our co-workers [177], by the demonstration of a Bragg mirror made of a few atoms coupled to a nanofiber. In order to enhance the light-matter coupling, other platforms such as photonic crystal waveguides should be considered in this endeavor.

Appendix

A Useful mathematical formulas

A.1 Hermite polynomials

We use in the entire manuscript the physicist description:

$$\begin{gathered} H_0(x) = 1, H_1(x) = 2x, H_2(x) = 4x^2 - 2, \\ H_n(x) = 2xH_{n-1}(x) - 2(n-1)H_{n-2}(x) \end{gathered} \tag{A.1.1}$$

A.2 Laguerre polynomials

The definition:

$$L_n^{\alpha} = \sum_{i=0}^{n} (-1)^i \binom{n+\alpha}{n-i} \frac{x^i}{i!}, \tag{A.2.1}$$

and the recurrence relation:

$$L_n^{\alpha} = \frac{\alpha + 1 - x}{n} L_{n-1}^{\alpha+1}(x) - \frac{x}{n} L_{n-1}^{\alpha+1}(x), \tag{A.2.2}$$

therefore give:

$$\begin{gathered} L_0^k = 1, L_1^{k-l} = -x + (k-1) + 1 \\ L_l^{k-l} = \frac{k - l + 1 - x}{l} L_{l-1}^{k-l+1}(x) - \frac{x}{l} L_{l-2}^{k-l+2}(x). \end{gathered} \tag{A.2.3}$$

A.3 Gauss integral

$$\int_{\mathbb{R}} e^{-ax^2+bx} dx = \sqrt{\frac{\pi}{a}} e^{\frac{b^2}{4a}} \tag{A.3.1}$$

B

ADUC7020 code for Maximum searching algorithm

```
#include<aduc7020.h>

#define DIG_OUT_LOCK 0
#define DIG_IN_SWEEP 3
#define DIG_OUT_SWEEP 0

// test
void test(void);
// main functions
void Lock_phase(void);

// auxiliary functions
unsigned long Bound(unsigned long);
void Sweep(void);
void Delay(int);


// functions to simplify code
void init_digital(void);
int Read_Digital(int);
void Write_Digital(int,int);
void ADCpoweron(int);
int ADCtoDAT(unsigned long);
unsigned long DATtoADC(int);

int main(void){
        REFCON = 0x01;     // internal 2.5V reference
        DAC0CON = 0x12;    // AGND-ARef range 0x12 2.5V
        while(1){
                Lock_phase();

        }
}

void test(void){                         // test for adc and dac
                ADCpoweron(20000); // power on ADC
        REFCON = 0x01;     // internal 2.5V reference
        DAC0CON = 0x12;    // AGND-ARef range 0x12 2.5V
        while(1){
                ADCCP = 0x00;      // conversion on ADC0
                ADCCON = 0x6E4;    // continuous conversion
```

```
                while(!ADCSTA){}
                DAC0DAT = ADCDAT;
        }
}


/** This is the basic code for locking phase using fringes signal
    output from the interferometer.**/
void Lock_phase(void){
        // define variables
        int N_step, N_delay, flag, N, sum, k;
        unsigned long Vout, Vin1, Vin2;

        // ADC&DAC setting
        ADCpoweron(20000); // power on ADC
        REFCON = 0x01;     // internal 2.5V reference
        DAC0CON = 0x12;    // AGND-ARef range 0x12 2.5V
        ADCCP = 0x00;      // conversion on ADC0
        ADCCON = 0x6E4;    // continuous conversion

        // IO setting
        init_digital();

        // locking parameters initialization
        N_step = 5;    //  step size
        N_delay = 500; // wait for certain time
        flag = 1;      // indicator for searching direction
        N = 100;       // accumulation number for each locking step
        Vin1 = DATtoADC(0); // initialize the voltage of first step

        // main loop for the locking
        while(1){
                Sweep();
                // switch between sweep mode and locking mode;
                // note that the sweep mode is just for the
                    convenience of the experiment,
                // for locking the phase, it is not necessary.
                Write_Digital(0,1); // Output a high level digital
                    output on pin P1.0 for indicating the locking
                    mode.

                Vout = Vout + flag * DATtoADC(N_step); // calculate
                    the voltage for next step
                Vout = Bound(Vout); // limit the range of V
                DAC0DAT = Vout; // output voltage on DAC0
                Delay(N_delay); //wait for a certain time for the
                    response of PZT

        // input average over N samples in order to filter out
            highest frequencies noise
                sum = 0; // initialization
                for(k = 1; k <= N; k++){
                        while(!ADCSTA){}        // wait for the end
                            of ADC conversion
                        sum += ADCtoDAT(ADCDAT); // read voltage from
                             ADC0
```

```
                }
                Vin2 = DATtoADC(sum/N); // calculate average value
                    for the voltage of second step

                if(Vin2 < Vin1) flag = -1 * flag; // change maximum
                    searching direction if V2 < V1

                Vin1 = Vin2; // update the voltage of first step
        }
}

///***   Simple functions   ***///

void init_digital(void){
    GP1CON = 0x00000000;    // IO initialization
        GP1DAT = 0xFF000000;    // set P1.n as digital output
        GP0CON = 0x00000000;    // IO initialization
        GP0DAT = 0x00000000;    // set P0.n as digital input
}

// read digital value from the pin P0.input_pin
int Read_Digital(int input_pin){
        return ((GP0DAT&0x000000FF) >> input_pin) & 0x1;
}

// write digital value to the pin P1.output_pin
void Write_Digital(int output_pin, int state){
        if(state == 1)
                GP1DAT = (0x00000001<<(output_pin+16))|GP1DAT;
        else
                GP1DAT = ~((0x00000001<<(output_pin+16))|(~GP1DAT));
}

// wait for ADC to be fully powered on
void ADCpoweron(int time){
        ADCCON = 0x620; // power-on the ADC
        while (time >= 0)       time--;
}

// convert ADC/DAC format to integer format
int ADCtoDAT(unsigned long ADC){
        return (ADC&0xFFF0000)>>16;
}

// convert integer format to ADC/DAC format
unsigned long DATtoADC(int DAT){
        unsigned long ADC;
        ADC = DAT;
        return ADC<<16;
}
```

C

Arduino code for Maximum searching algorithm

```
// values of ADC0
unsigned long U0; // before the step
unsigned long U1; // after the step
 // values of DAC0
unsigned long V0;// before the step
unsigned long V1; // after the step

//locking variables
double T=0.05; //waiting delay between two steps in ms
int s=10; // step between two voltages sent to the piezo
unsigned long moy=100; // average x time the analog signal

//user pins
int sweepPin=49;  // pin where we plug the digital input sweep/lock

//other useful variables
int val=0; // a variable to store the state of sweepin
int flag=1; // direction of the correction: +/-1

void setup(){
 analogWriteResolution(12); // 12-bit resolution for the analog!
 pinMode(sweepPin, INPUT); // put the sweep pin as an input
}

void loop(){
  flag=1;
  V0=2048;  // start in the middle
  val=digitalRead(sweepPin); // check if sweeping  or locking mode
 while(val==HIGH){ // sweeping mode
    for(int x=0; x<4096; x=x+s){
      analogWrite(DAC0, x); // use DAC1 for ... DAC1
      delay(T);
    }
    for(int x=4095; x>=0; x=x-s){
      analogWrite(DAC0, x);
      delay(T);
    }
   val=digitalRead(sweepPin); // check if sweeping  or locking mode
```

```
 }
 while(val==LOW){ // locking mode
    for(int i=0; i<moy;i++){  // average ADC
       U0=U0+analogRead(ADC0);
       delay(0.001);
    }
    U0=U0/moy;
    V1=V0+flag*s;  // make a step in one direction
    if(V1>4095||V1<1){ // check the signal is still between max and
        min range, if not, set back the voltage in the middle of the
        range
      V1=2048;
    }
    analogWrite(DAC0,V1); // send the signal to PZT
    delay(0.1);
    for(int i=0; i<moy; i++){  // average ADC
      U1=U1+analogRead(ADC0);
      delay(0.001);
    }
    U1=U1/moy;
    if(U1<U0){ // if the new signal is smaller than the previous one,
         change the direction of the step.
      flag=-flag;
    }
    V0=V1;
    val=digitalRead(sweepPin);// check if sweeping  or locking mode
 }
}
```

D Hybrid entangled qubit state

In the following is detailed the calculation for the generation of hybrid qubit entanglement, where Alice and Bob, on distant nodes, have a type-II and a type-I OPO respectively as shown in Fig.D.1. On the type-I OPO side, a small part of the cat state is tapped onto a beam splitter of reflectivity $r = \sin\theta \approx \theta \ll 1$, resulting in :

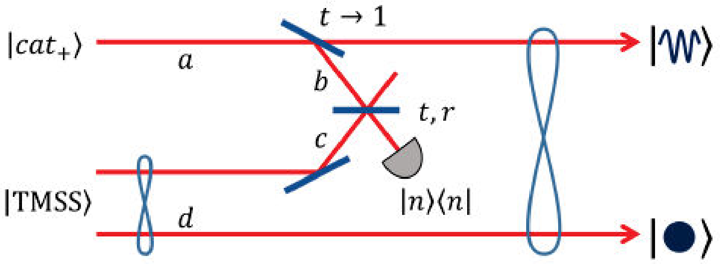

Figure D.1: Scheme for the generation of hybrid entangled qubit state.

$$\hat{B}(r) = e^{\theta(\hat{a}\hat{b}^\dagger - \hat{a}^\dagger\hat{b})}|\text{Cat+}\rangle_a|0\rangle_b \simeq (1 + \theta\hat{a}\hat{b}^\dagger)|\text{Cat+}\rangle_a|0\rangle_b \tag{D.0.1}$$

On the type-II OPO side, a two-mode squeezed state of the form $|TMSS\rangle_{s,i} \propto \sum_n \Lambda^n|n\rangle_s|n\rangle_i$. is generated. By pumping far below threshold, $\Lambda \ll 1$ which can be approximated as:

$$(1 + \Lambda\hat{c}^\dagger\hat{d}^\dagger)|0\rangle_c|0\rangle_d \tag{D.0.2}$$

The mode b and c acquire phase shifts φ_1 and φ_2 respectively, due to their optical propagations, and are then combined on a beam splitter of transmission t and reflection r, which gives the transformation:

$$\begin{aligned}(1 + \theta\hat{a}\hat{b}^\dagger)(1 + \Lambda\hat{c}^\dagger\hat{d}^\dagger)|\text{Cat+}\rangle_a|0\rangle_b|0\rangle_c|0\rangle_d \to \\ (1 + \theta\hat{a}\hat{(}t\hat{b}^\dagger e^{i\varphi_1} + r\hat{c}^\dagger e^{i\varphi_2})) \\ (1 + \Lambda(t\hat{c}^\dagger e^{i\varphi_2} - r\hat{b}^\dagger e^{i\varphi_1})\hat{d}^\dagger)|\text{Cat+}\rangle_a|0\rangle_b|0\rangle_c|0\rangle_d\end{aligned} \tag{D.0.3}$$

Then, by only keeping first order terms in Λ and θ, and the operator $\hat{b}^\dagger$, corresponding to the detection of a single photon on mode b, and tracing out the mode c the resulting state is :

$$|\Psi\rangle_{AB} = (e^{i\varphi_1}\theta t\hat{a}\hat{b}^\dagger - e^{i\varphi_2}\Lambda r\hat{b}^\dagger\hat{d}b^{\dagger})|\text{Cat+}\rangle_a|0\rangle_b|0\rangle_d \tag{D.0.4}$$

By tracing out the mode b, one gets:

$$\theta t|1\rangle_d|\mathrm{Cat}+\rangle_a + \Lambda r e^{i\varphi}|0\rangle_d|\mathrm{Cat}-\rangle_a \tag{D.0.5}$$

where $\varphi = \varphi_2 - \varphi_1 + \pi$. The maximal negativity of entanglement is obtained for a balancing of the probabilities, i.e. for: $\Lambda^2 r^2 = \theta^2 t^2$.

E

Hybrid entangled qutrit state

Here is detailed the calculation for the generation of the hybrid qutrit entangled state. Alice and Bob owns the same OPOs as in Appendix D. A small part of the single-mode squeezed vacuum state is tapped onto a beam splitter of reflectivity $r = \sin\theta \approx \theta \ll 1$, resulting in :

$$\hat{B}(r) = e^{\theta(\hat{a}\hat{b}^\dagger - \hat{a}^\dagger\hat{b})}\hat{S}_a|0\rangle_a|0\rangle_b \simeq (1 + \theta\hat{a}\hat{b}^\dagger + \frac{\theta^2}{2}\hat{a}^2\hat{b}^{\dagger 2})\hat{S}_a|0\rangle_a|0\rangle_b \tag{E.0.1}$$

On the type-II OPO side, a two-mode squeezed state of the form $|TMSS\rangle_{s,i} \propto \sum_n \Lambda^n|n\rangle_s|n\rangle_i$. is generated. By pumping far below threshold, $\Lambda \ll 1$ which can be approximated as:

$$(1 + \Lambda\hat{c}^\dagger\hat{d}^\dagger + \frac{\Lambda^2}{2}\hat{c}^{\dagger 2}\hat{d}^{\dagger 2})|0\rangle_c|0\rangle_d \tag{E.0.2}$$

Following the same procedure as in Appendix D and by only keeping second order terms in Λ and θ, and the operator $\hat{b}^{\dagger 2}$, corresponding to the detection of two photon on mode b, and tracing out the mode c the resulting state is :

$$|\Psi\rangle_{AB} = \frac{\theta^2 t^2}{2}\hat{a}^2\hat{S}|0\rangle_a|0\rangle_b - e^{i\varphi}\theta\Lambda r t\hat{a}\hat{S}|0\rangle_a|1\rangle_b - e^{2i\varphi}\frac{\Lambda^2 r^2}{\sqrt{2}}\hat{S}|0\rangle_a|2\rangle_b. \tag{E.0.3}$$

where $\varphi = \varphi_2 - \varphi_1 + \pi$. Leading to the heralded state:

$$|\Psi\rangle_{AB}\frac{1}{\sqrt{2 + 4c^2 + c^4}}\Big(\sqrt{2}|2\rangle_A|\mathrm{Sq}\rangle - 2ce^{i\varphi}|1\rangle_A|\mathrm{Cat}-\rangle + c^2e^{i2\varphi}|0\rangle_A|\mathrm{Cat}+\rangle\Big) \tag{E.0.4}$$

where $c = \frac{\theta t}{\Lambda r}$.

F Hybrid entangled qubit state with additional photon subtraction

Here is given the calculation of the hybrid qubit entangled state generation, with an additional local subtraction, as shown in Fig. F.1. We consider now the realistic case in which we start with squeezed vacuum on Bob's side. The first local detection enable to reiterate the same calculation but starting with an odd cat state.

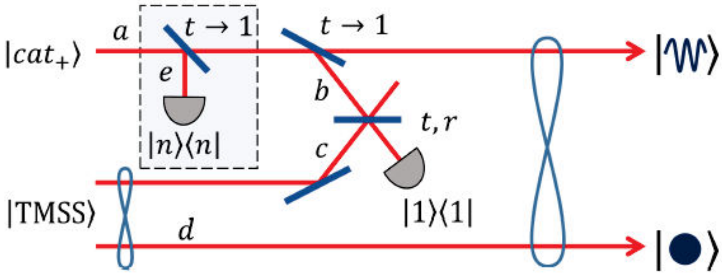

Figure F.1: Scheme for the generation of hybrid entangled qubit state with an additional local photon subtraction.

A small part of the odd cat state is taped onto a beam splitter of reflectivity $r = \sin\theta \approx \theta \ll 1$, resulting in :

$$\hat{B}(r) = e^{\theta(\hat{a}\hat{b}^{\dagger} - \hat{a}^{\dagger}\hat{b})}|\text{Cat}-\rangle_a|0\rangle_b \simeq (1 + \theta\hat{a}\hat{b}^{\dagger}|\text{Cat}-\rangle_a|0\rangle_b \tag{F.0.1}$$

On the type-II OPO side, an two-mode squeezed state of the form $|TMSS\rangle_{s,i} \propto \sum_n \Lambda^n |n\rangle_s |n\rangle_i$. is generated. By pumping far below threshold, $\Lambda \ll 1$ which can be approximated as:

$$(1 + \Lambda\hat{c}^{\dagger}\hat{d}^{\dagger})|0\rangle_c|0\rangle_d \tag{F.0.2}$$

The mode b and c go through phase changing φ_1 and φ_2, and are then combined on a beam splitter of transmission t and reflection r, which gives the transformation:

$$\begin{aligned}(1+\theta\hat{a}\hat{b}^{\dagger})(1+\hat{c}^{\dagger}\hat{d}^{\dagger})|\mathrm{Cat}-\rangle_a|0\rangle_b|0\rangle_c|0\rangle_d \rightarrow \\ &(1+\theta\hat{a}\hat{(}t\hat{b}^{\dagger}e^{i\varphi_1}+r\hat{c}^{\dagger}e^{i\varphi_2})) \\ &(1+\Lambda(t\hat{c}^{\dagger}e^{i\varphi_2}-r\hat{b}^{\dagger}e^{i\varphi_1})\hat{d}^{\dagger})|\mathrm{Cat}-\rangle_a|0\rangle_b|0\rangle_c|0\rangle_d\end{aligned} \tag{F.0.3}$$

Then, by only keeping first order terms in Λ and θ, and the operator $\hat{b}^{\dagger}$, corresponding to the detection of a single photon on mode b, and tracing out the mode c the resulting state is :

$$(e^{i\varphi_1}\theta t\hat{a}\hat{b}^{\dagger}-e^{i\varphi_2}\Lambda r\hat{b}^{\dagger}\hat{d\hat{b}}^{\dagger})|\mathrm{Cat}-\rangle_a|0\rangle_b|0\rangle_d \tag{F.0.4}$$

By tracing out the mode b, one gets:

$$|\Psi\rangle_{AB}=\theta t|1\rangle_d|\mathrm{Cat}-\rangle_a+\Lambda re^{i\varphi}|0\rangle_d|\mathrm{Cat}+\rangle_a \tag{F.0.5}$$

where $\varphi=\varphi_2-\varphi_1+\pi$. The maximal negativity of entanglement is obtained for a balancing of the probabilities, i.e. for: $\Lambda^2r^2=\theta^2t^2$.

Bibliography

[1] Einstein, A. & Infeld, L. *The Evolution of Physics* (Cambridge University Press, 1938). [On page xi.]

[2] Kok, P. *et al.* Linear optical quantum computing with photonic qubits. *Rev. Mod. Phys.* **79**, 135–174 (2007). [On pages xi, 100, and 120.]

[3] Braunstein, S. L. & van Loock, P. Quantum information with continuous variables. *Rev. Mod. Phys.* **77**, 513–577 (2005). [On page xi.]

[4] Ralph, T. & Pryde, G. Optical quantum computation. *Progress in Optics* **54** (2010). [On pages xi and 78.]

[5] Pirandola, S. *et al.* MDI-QKD: Continuous- versus discrete-variables at metropolitan distances. *Nat. Photon.* **9**, 773–775 (2015). [On page xi.]

[6] Takeda, S. & Furusawa, A. *Principles and Methods of Quantum Information Technologies*, chap. Optical Hybrid Quantum Information Processing, 439–458 (Springer, 2016). [On page xi.]

[7] Yokoyama, S. *et al.* Nonlocal quantum gate on quantum continuous variables with minimal resources. *Phys. Rev. A* **90**, 012311 (2014). [On page xi.]

[8] van Loock, P. *et al.* Hybrid quantum computation in quantum optics. *Phys. Rev. A* **78**, 022303 (2008). [On pages xii and 100.]

[9] Qi, G., Liu-Yong., C., Hong-Fu, W. & Shou, Z. Universal quantum computation using all-optical hybrid encoding. *Chin. Phys. B* **24**, 040303 (2015). [On pages xii and 120.]

[10] Andersen, U. L., Neergaard-Nielsen, J. S., van Loock, P. & Furusawa, A. Hybrid discrete- and continuous-variable quantum information. *Nat. Phys.* **11**, 713–719 (2015). [On pages xii, 77, 78, and 120.]

[11] Ourjoumtsev, A., Tualle-Brouri, R., Laurat, J. & Grangier, P. Generating optical Schrödinger kittens for quantum information processing. *Science* **312**, 83–86 (2006). [On pages xii, 78, and 101.]

[12] Neergaard-Nielsen, J. S., Melholt Nielsen, B., Hettich, C., Mølmer, K. & Polzik, E. S. Generation of a superposition of odd photon number states for quantum information networks. *Phys. Rev. Lett.* **97**, 083604 (2006). [On pages xii and 78.]

[13] Deléglise, S. *et al.* Reconstruction of non-classical cavity field states with snapshots of their decoherence. *Nature* **455**, 510–514 (2008). [On pages xii, 78, 87, 94, and 132.]

[14] Bimbard, E. *et al.* Homodyne tomography of a single photon retrieved on demand from a cavity-enhanced cold atom memory. *Phys. Rev. Lett.* **112**, 033601 (2014). [On page xii.]

[15] Nemoto, K. & Munro, W. J. Nearly deterministic linear optical controlled-NOT gate. *Phys. Rev. Lett.* **93**, 250502 (2004). [On page xii.]

[16] Lloyd, S. & Braunstein, S. L. Quantum computation over continuous variables. *Phys. Rev. Lett.* **82**, 1784–1787 (1999). [On page xii.]

[17] Gu, M., Weedbrook, C., Menicucci, N. C., Ralph, T. C. & van Loock, P. Quantum computing with continuous-variable clusters. *Phys. Rev. A* **79**, 062318 (2007). [On page 70.]

[18] Marek, P., Filip, R. & Furusawa, A. Deterministic implementation of weak quantum cubic nonlinearity. *Phys. Rev. A* **84**, 053802 (2011). [On page xii.]

[19] Morin, O. *et al.* Witnessing trustworthy single-photon entanglement with local homodyne measurements. *Phys. Rev. Lett.* **110**, 130401 (2013). [On page xii.]

[20] Takeda, S., Mizuta, T., Fuwa, M., van Loock, P. & Furusawa, A. Deterministic quantum teleportation of photonic quantum bits by a hybrid technique. *Nature* **500**, 315–318 (2013). [On page xii.]

[21] van Loock, P. *et al.* Hybrid quantum repeater using bright coherent light. *Phys. Rev. Lett.* **96**, 240501 (2006). [On page xiii.]

[22] Takeda, S., Fuwa, M., van Loock, P. & Furusawa, A. Entanglement swapping between discrete and continuous variables. *Phys. Rev. Lett.* **114**, 100501 (2015). [Not cited.]

[23] Park, K. & Jeong, H. Entangled coherent states versus entangled photon pairs for practical quantum-information processing. *Phys. Rev. A* **82**, 062325 (2010). [Not cited.]

[24] Zielińska, J. A., Beduini, F. A., Lucivero, V. G. & Mitchell, M. W. Atomic filtering for hybrid continuous-variable/discrete-variable quantum optics. *Opt. Express* **22**, 25307–25317 (2014). [On page xiii.]

[25] Morin, O. *et al.* Remote creation of hybrid entanglement between particle-like and wave-like optical qubits. *Nat. Photon.* **8**, 570–574 (2014). [On pages xiii, 42, 99, 100, and 106.]

[26] Morin, O. *Non-gaussian states and measurements for quantum information.* Ph.D. thesis, UPMC, tel-01066655 (2013). [On pages xiii, 23, 29, and 99.]

[27] Nielsen, M. A. & Chuang, I. L. *Quantum Computation and Quantum Information* (Cambridge University Press, 2000). [On pages 3 and 7.]

[28] Grynberg, G., Aspect, A. & Fabre, C. *Introduction to Quantum Optics: From the Semi-classical Approach to Quantized Light* (Cambridge University Press, 2010). [Not cited.]

[29] Barnett, S. & Radmore, P. *Methods in theoretical quantum optics* (Oxford University Press, 1997). [Not cited.]

[30] Loudon, R. *The quantum theory of light* (Oxford University Press, 2000). [Not cited.]

[31] Haroche, S. & Raimond, J. *Exploring the quantum: atoms, cavities, and photons* (Oxford University Press, 2006). [On page 3.]

[32] Jozsa, R. Fidelity for mixed quantum states. *J. Mod. Opt.* **41**, 2315–2323 (1994). [On page 6.]

[33] Chen, Z.-B., Pan, J.-W., Hou, G. & Zhang, Y.-D. Maximal violation of Bell's inequalities for continuous variable systems. *Phys. Rev. Lett.* **88**, 040406 (2002). [On pages 7, 112, and 115.]

[34] Filip, R. & Mišta, L. Violation of Bell's inequalities for a two-mode squeezed vacuum state in lossy transmission lines. *Phys. Rev. A* **66**, 044309 (2002). [On pages 7, 112, and 115.]

[35] Branciard, C., Cavalcanti, E. G., Walborn, S. P., Scarani, V. & Wiseman, H. M. One-sided device-independent quantum key distribution: Security, feasibility, and the connection with steering. *Phys. Rev. A* **85**, 010301 (2012). [On pages 8 and 111.]

[36] Shalm, L. K. *et al.* Strong loophole-free test of local realism. *Phys. Rev. Lett.* **115**, 250402 (2015). [On pages 8 and 56.]

[37] Giustina, M. *et al.* Significant-loophole-free test of Bell's theorem with entangled photons. *Phys. Rev. Lett.* **115**, 250401 (2015). [Not cited.]

[38] Hensen, B. *et al.* Loophole-free Bell inequality violation using electron spins separated by 1.3 kilometres. *Nature* **526**, 682–686 (2015). [On pages 8 and 56.]

[39] Leonhardt, U. *Measuring the quantum state of light* (Cambridge University Press, 2006). [On pages 10 and 27.]

[40] Hudson, R. L. When is the Wigner quasi-probability density non-negative? *Reports on Mathematical Physics* **6**, 249–252 (1974). [On page 14.]

[41] Schrödinger, E. Die gegenwärtige situation in der quantenmechanik. *Naturwissenschaften* **23**, 807–812; 823–828; 844–849 (1935). [On pages 17, 86, and 132.]

[42] Huang, K., Le Jeannic, H., Ruaudel, J., Morin, O. & Laurat, J. Microcontroller-based locking in optics experiments. *Rev. Sci. Instrum.* **85**, 123112 (2014). [On pages 21, 32, and 39.]

[43] Laurat, J. *Etats non classiques et intrication en variables continues à l'aide d'un oscillateur paramétrique optique.* Ph.D. thesis, Université Paris VI, tel-00007442 (2004). [On page 23.]

[44] Morin, O. *et al.* Quantum state engineering of light with continuous-wave optical parametric oscillators. *J. Vis. Exp.* **87**, e51224 (2014). [On pages 26 and 101.]

[45] Kumar, R. *et al.* Versatile wideband balanced detector for quantum optical homodyne tomography. *Opt. Commun.* **285**, 5259 – 5267 (2012). [On page 28.]

[46] Lvovsky, A. I. Iterative maximum-likelihood reconstruction in quantum homodyne tomography. *J. Opt. B: Quantum and Semiclassical Optics* **6**, S556 (2004). [On page 28.]

[47] Lvovsky, A. I. & Raymer, M. G. Continuous-variable optical quantum-state tomography. *Rev. Mod. Phys.* **81**, 299–332 (2009). [On page 28.]

[48] Morin, O., Fabre, C. & Laurat, J. Experimentally accessing the optimal temporal mode of traveling quantum light states. *Phys. Rev. Lett.* **111**, 213602 (2013). [On pages 30, 39, 58, 63, and 68.]

[49] White, A. D. Frequency stabilization of gas lasers. *IEEE J. Quantum Electron.* **1**, 349–357 (1965). [On page 31.]

[50] Drever, R. W. P. *et al.* Laser phase and frequency stabilization using an optical resonator. *Appl. Phys. B* **31**, 97–105 (1983). [On page 31.]

[51] Shaddock, D. A., Gray, M. B. & McClelland, D. E. Frequency locking a laser to an optical cavity by use of spatial mode interference. *Opt. Lett.* **24**, 1499–1501 (1999). [On page 31.]

[52] Wu, L.-A., Kimble, H. J., Hall, J. L. & Wu, H. Generation of squeezed states by parametric down conversion. *Phys. Rev. Lett.* **57**, 2520–2523 (1986). [On page 42.]

[53] Eberle, T. *et al.* Quantum enhancement of the zero-area sagnac interferometer topology for gravitational wave detection. *Phys. Rev. Lett.* **104**, 251102 (2010). [On page 42.]

[54] Andersen, U. L., Gehring, T., Marquardt, C. & Leuchs, G. 30 years of squeezed light generation. *Phys. Scr.* **91**, 053001 (2016). [On pages 42 and 69.]

[55] Bowen, W. P. *et al.* Experimental investigation of continuous-variable quantum teleportation. *Phys. Rev. A* **67**, 032302 (2003). [On page 42.]

[56] Aasi, J. *et al.* Enhancing the sensitivity of the LIGO gravitational wave detector by using squeezed states of light. *Nat. Photon.* **7**, 613–619 (2013). [On page 42.]

[57] Dell'Anno, F., De Siena, S. & Illuminati, F. Multiphoton quantum optics and quantum state engineering. *Phys. Rep.* **428**, 53 – 168 (2006). [On page 42.]

[58] Huang, K. *et al.* Optical synthesis of large-amplitude squeezed coherent-state superpositions with minimal resources. *Phys. Rev. Lett.* **115**, 023602 (2015). [On pages 42, 63, 69, 77, 79, and 85.]

[59] Walmsley, I. A. Quantum optics: Science and technology in a new light. *Science* **348**, 525–530 (2015). [On page 42.]

[60] Hadfield, R. Single-photon detectors for optical quantum information applications. *Nat. Photon.* **3**, 696–705 (2009). [On page 42.]

[61] Natarajan, C. M., Tanner, M. G. & Hadfield, R. H. Superconducting nanowire single-photon detectors: physics and applications. *Supercond. Sci. Technol.* **25**, 063001 (2012). [On page 42.]

[62] Rosfjord, K. M. *et al.* Nanowire single-photon detector with an integrated optical cavity and anti-reflection coating. *Opt. Express* **14**, 527–534 (2006). [On page 42.]

[63] Rosenberg, D., Kerman, A. J., Molnar, R. J. & Dauler, E. A. High-speed and high-efficiency superconducting nanowire single photon detector array. *Opt. Express* **21**, 1440–1447 (2013). [On page 42.]

[64] Miki, S., Yamashita, T., Terai, H. & Wang, Z. High performance fiber-coupled NbTiN superconducting nanowire single photon detectors with Gifford-McMahon cryocooler. *Opt. Express* **21**, 10208–10214 (2013). [On page 42.]

[65] Baek, B., Lita, A. E., Verma, V. & Nam, S. W. Superconducting a-W_xSi_{1-x} nanowire single-photon detector with saturated internal quantum efficiency from visible to 1850 nm. *App. Phys. Lett.* **98**, 251105 (2011). [On page 43.]

[66] Verma, V. B. *et al.* A three-dimensional, polarization-insensitive superconducting nanowire avalanche photodetector. *App. Phys. Lett.* **101**, 251114 (2012). [On page 43.]

[67] Marsili, F. *et al.* Detecting single infrared photons with 93% system efficiency. *Nature Photon.* **7**, 210–214 (2013). [On page 43.]

[68] Verma, V. B. *et al.* High-efficiency WSi superconducting nanowire single-photon detectors operating at 2.5k. *App. Phys. Lett.* **105**, 122601 (2014). [On page 44.]

[69] Miller, A. J. *et al.* Compact cryogenic self-aligning fiber-to-detector coupling with losses below one percent. *Opt. Express* **19**, 9102–9110 (2011). [On page 44.]

[70] Le Jeannic, H. *et al.* High-efficiency WSi superconducting nanowire single-photon detectors for quantum state engineering in the near infrared. *Opt. Lett.* **41**, 5341–5344 (2016). [On pages 48 and 60.]

[71] Gisin, N. & Thew, R. Quantum communication. *Nat. Photon.* **1**, 165 (2007). [On page 56.]

[72] Knill, E., Laflamme, R. & Milburn, G. J. A scheme for efficient quantum computation with linear optics. *Nature* **409**, 46–52 (2001). [On page 56.]

[73] Eisaman, M., Fan, J., Migdall, A., & Polyakov, S. Invited review article: single-photon sources and detectors. *Rev. Sci. Instrum.* **82**, 071101 (2011). [On page 56.]

[74] Somaschi, N. *et al.* Near-optimal single-photon sources in the solid-state. *Nat. Photon.* **10**, 340–345 (2016). [On pages 57 and 60.]

[75] Morin, O., D'Auria, V., Fabre, C. & Laurat, J. High-fidelity single-photon source based on a type-II optical parametric oscillator. *Opt. Lett.* **37**, 3738–3740 (2012). [On page 59.]

[76] Jin, R.-B. *et al.* Efficient detection of an ultra-bright single-photon source using superconducting nanowire single-photon detectors. *Opt. Commun.* **336**, 47 – 54 (2015). [On page 61.]

[77] Ramelow, S. *et al.* Highly efficient heralding of entangled single photons. *Opt. Express* **21**, 6707–6717 (2013). [On page 61.]

[78] Krapick, S. *et al.* An efficient integrated two-color source for heralded single photons. *New J. Phys.* **15**, 033010 (2013). [On page 61.]

[79] Pomarico, E., Sanguinetti, B., Guerreiro, T., Thew, R. & Zbinden, H. MHz rate and efficient synchronous heralding of single photons at telecom wavelengths. *Opt. Express* **20**, 23846 (2012). [On page 61.]

[80] Ngah, L. A., Alibart, O., Labonté, L., D'Auria, V. & Tanzili, S. Ultra-fast heralded single photon source based on telecom technology. *Laser Photon. Rev.* **9**, L1–L5 (2015). [On page 61.]

[81] Neergaard-Nielsen, J. S., Nielsen, B. M., Takahashi, H., Vistnes, A. I. & Polzik, E. S. High purity bright single photon source. *Opt. Express* **15**, 7940–7949 (2007). [On pages 61, 101, and 128.]

[82] Wakui, K., Takahashi, H., Furusawa, A. & Sasaki, M. Photon subtracted squeezed states generated with periodically poled KTiOPO4. *Opt. Express* **15**, 3568–3574 (2007). [On pages 61 and 78.]

[83] Scholz, M., Koch, L. & Benson, O. Statistics of narrow-band single photons for quantum memories generated by ultrabright cavity-enhanced parametric down-conversion. *Phys. Rev. Lett.* **102**, 063603 (2009). [On page 61.]

[84] Förtsch, M. *et al.* A versatile source of single photons for quantum information. *Nat. Commun.* **4**, 1818 (2013). [On page 61.]

[85] Luo, K.-H. *et al.* Direct generation of genuine single-longitudinal-mode narrowband photon pairs. *New J. Phys.* **17**, 073039 (2015). [On page 61.]

[86] Nielsen, A. E. B. & Mølmer, K. Transforming squeezed light into a large-amplitude coherent-state superposition. *Phys. Rev. A* **76**, 043840 (2007). [On page 63.]

[87] Nielsen, A. E. B. & Mølmer, K. Photon number states generated from a continuous-wave light source. *Phys. Rev. A* **75**, 043801 (2007). [Not cited.]

[88] Sasaki, M., Takeoka, M. & Takahashi, H. Temporally multiplexed superposition states of continuous variables. *Phys. Rev. A* **77**, 063840 (2008). [On page 63.]

[89] Takahashi, H. *et al.* Generation of large-amplitude coherent-state superposition via ancilla-assisted photon subtraction. *Phys. Rev. Lett.* **101**, 233605 (2008). [On pages 63 and 79.]

[90] Takeoka, M., Takahashi, H. & Sasaki, M. Large amplitude coherent-state superposition generated by a time-separated two-photon subtraction from a continuous-wave squeezed vacuum. *Phys. Rev. A* **77**, 062315 (2008). [On page 63.]

[91] Qin, Z. *et al.* Complete temporal characterization of a single photon. *Light Sci Appl* **4**, e298 (2015). [On page 68.]

[92] Menzies, D. & Filip, R. Gaussian-optimized preparation of non-gaussian pure states. *Phys. Rev. A* **79**, 012313 (2009). [On pages 69, 77, and 80.]

[93] Ralph, T., Gilchrist, A., Milburn, G., Munro, W. & Glancy, S. Quantum computation with optical coherent states. *Phys. Rev. A* **68**, 042319 (2003). [On pages 70 and 78.]

[94] Lund, A. P. *et al.* Boson sampling from gaussian states. *Phys. Rev. Lett.* **113**, 100502 (2014). [Not cited.]

[95] Ralph, T. C. & Huntington, E. H. Unconditional continuous variable dense coding. *Phys. Rev. A* **66**, 042321 (2002). [On page 70.]

[96] Brańczyk, A. M. & Ralph, T. C. Teleportation using squeezed single photons. *Phys. Rev. A* **78**, 052304 (2008). [On page 70.]

[97] Bowen, W. P., Schnabel, R., Lam, P. K. & Ralph, T. C. A characterization of continuous variable entanglement. *Phys. Rev. A* **69**, 012304 (2004). [On page 70.]

[98] Polzik, E. S., Carri, J. & Kimble, H. J. Spectroscopy with squeezed light. *Phys. Rev. Lett.* **68**, 3020–3023 (1992). [On page 70.]

[99] Treps, N. *et al.* A quantum laser pointer. *Science* **301**, 940–943 (2003). [On page 70.]

[100] Vahlbruch, H. *et al.* The GEO 600 squeezed light source. *Class. Quantum Grav.* **27**, 084027 (2010). [On page 70.]

[101] Abbott, B. *et al.* Observation of gravitational waves from a binary black hole merger. *Phys. Rev. Lett.* **116**, 061102 (2016). [On page 70.]

[102] Vahlbruch, H., Mehmet, M., Danzmann, K. & Schnabel, R. Detection of 15 dB squeezed states of light and their application for the absolute calibration of photoelectric quantum efficiency. *Phys. Rev. Lett.* **117**, 110801 (2016). [On page 70.]

[103] Leuchs, G., Glauber, R. J. & Schleich, W. P. Intensity–intensity correlations determined by dimension of quantum state in phase space: P-distribution. *Physica Scripta* **90**, 108007 (2015). [On page 70.]

[104] Leuchs, G., Glauber, R. J. & Schleich, W. P. Dimension of quantum phase space measured by photon correlations. *Physica Scripta* **90**, 074066 (2015). [On page 70.]

[105] Scully, M. O. & Zubairy, M. S. *Quantum Optics* (Cambridge University Press, 1997). [On page 73.]

[106] Stiller, B., Seyfarth, U. & Leuchs, G. Temporal and spectral properties of quantum light. *arXiv* 1411.3765 (2013). [On page 75.]

[107] Müller, C. R. *et al.* Evading vacuum noise: Wigner projections or Husimi samples? *Phys. Rev. Lett.* **117**, 070801 (2016). [On page 77.]

[108] Jeong, H. & Kim, M. Efficient quantum computation using coherent states. *Phys. Rev. A* **65**, 042305 (2002). [On page 78.]

[109] Gilchrist, A. *et al.* Schrödinger cats and their power for quantum information processing. *J. Opt. B: Quantum Semiclass. Opt.* **6** (2004). [On page 78.]

[110] Lund, A., Ralph, T. & Haselgrove, H. Fault-tolerant linear optical quantum computing with small amplitude coherent states. *Phys. Rev. Lett.* **100**, 030503 (2008). [On page 78.]

[111] Marek, P. & Fiurášek, J. Elementary gates for quantum information with superposed coherent states. *Phys. Rev. A* **82**, 014304 (2010). [On page 78.]

[112] van Loock, P. Optical hybrid approaches to quantum information. *Laser and Photonics Reviews* **5**, 167–200 (2011). [On page 78.]

[113] Wang, C. *et al.* A Schrödinger cat living in two boxes. *Science* **352**, 1087–1091 (2016). [On pages 78 and 94.]

[114] Gerrits, T. *et al.* Generation of optical coherent-state superpositions by number-resolved photon subtraction from the squeezed vacuum. *Phys. Rev. A* **82**, 031802 (2010). [On page 79.]

[115] Ourjoumtsev, A., Jeong, H., Tualle-Brouri, R. & Grangier, P. Generation of optical Schrödinger cats from photon number states. *Nature* **448**, 784 (2007). [On page 79.]

[116] Etesse, J., Bouillard, M., Kanseri, B. & Tualle-Brouri, R. Experimental generation of squeezed cat states with an operation allowing iterative growth. *Phys. Rev. Lett.* **114**, 193602 (2015). [On page 79.]

[117] Makino, K. *et al.* Synchronization of optical photons for quantum information processing. *Science Advances* **2**, e1501772 (2016). [On page 79.]

[118] Miwa, Y. *et al.* Exploring a new regime for processing optical qubits: Squeezing and unsqueezing single photons. *Phys. Rev. Lett.* **113**, 013601 (2014). [On page 80.]

[119] Filip, R. Gaussian quantum adaptation of non-gaussian states for a lossy channel. *Phys. Rev. A* **87**, 042308 (2013). [On page 86.]

[120] Paavola, J., Hall, M. J. W., Paris, M. G. A., & Maniscalco, S. Finite-time quantum-to-classical transition for a Schrödinger-cat state. *Phys. Rev. A* **84**, 012121 (2011). [On page 87.]

[121] Serafini, A., M. G. A. Paris, F. I. & Siena, S. D. Quantifying decoherence in continuous variable systems. *J. Opt. B: Quantum Semiclass. Opt.* **7**, R19–R36 (2005). [On page 87.]

[122] Vlastakis, B. *et al.* Deterministically encoding quantum information in 100-photon Schrödinger cat states. *Science* **342**, 607 (2013). [On page 94.]

[123] Brune, M. *et al.* Observing the progressive decoherence of the "meter" in a quantum measurement. *Phys. Rev. Lett.* **77**, 4887 (1996). [On page 94.]

[124] Kienzler, D. *et al.* Observation of quantum interference between separated mechanical oscillator wavepackets. *Phys. Rev. Lett.* **116**, 140402 (2016). [On pages 94 and 150.]

[125] Jeong, H. *et al.* Generation of hybrid entanglement of light. *Nat. Photon.* **8**, 564–569 (2013). [On page 99.]

[126] Braunstein, S. L. & Pati, A. K. *Quantum information with continuous variables* (Kluwer Academic, 2003). [On pages 100 and 120.]

[127] Kreis, K. & van Loock, P. Classifying, quantifying, and witnessing qudit-qumode hybrid entanglement. *Phys. Rev. A* **85**, 032307 (2012). [On page 100.]

[128] Rigas, J., Gühne, O. & Lütkenhaus, N. Entanglement verification for quantum-key-distribution systems with an underlying bipartite qubit-mode structure. *Phys. Rev. A* **73**, 012341 (2006). [On page 100.]

[129] Wittmann, C. *et al.* Witnessing effective entanglement over a 2 km fiber channel. *Opt. Express* **18**, 4499–4509 (2010). [On page 100.]

[130] Lee, S.-W. & Jeong, H. Near-deterministic quantum teleportation and resource-efficient quantum computation using linear optics and hybrid qubits. *Phys. Rev. A* **87**, 022326 (2013). [On pages 100, 106, 120, and 150.]

[131] Spiller, T. P. *et al.* Quantum computation by communication. *New J. Phys.* **8**, 30 (2006). [On page 100.]

[132] Dakna, M. *et al.* Generating Schrödinger-cat-like states by means of conditional measurements on a beam splitter. *Phys. Rev. A* **55**, 3184 (1997). [On page 101.]

[133] Fujiwara, M., Takeoka, M., Mizuno, J. & Sasaki, M. Exceeding the classical capacity limit in a quantum optical channel. *Phys. Rev. Lett.* **90**, 167906 (2003). [On page 107.]

[134] Yukawa, M. *et al.* Generating superposition of up-to three photons for continuous variable quantum information processing. *Opt. Express* **21**, 5529 (2013). [On page 107.]

[135] Lanyon, B. P. *et al.* Manipulating biphotonic qutrits. *Phys. Rev. Lett.* **100**, 060504 (2008). [On page 107.]

[136] Hofheinz, M. *et al.* Synthesizing arbitrary quantum states in a superconducting resonator. *Nature* **459**, 546–549 (2009). [On page 107.]

[137] Cerf, N. J., Bourennane, M., Karlsson, A. & Gisin, N. Security of quantum key distribution using *d*-level systems. *Phys. Rev. Lett.* **88**, 127902 (2002). [On page 107.]

[138] Spekkens, R. W. & Rudolph, T. Degrees of concealment and bindingness in quantum bit commitment protocols. *Phys. Rev. A* **65**, 012310 (2001). [On page 107.]

[139] Langford, N. K. *et al.* Measuring entangled qutrits and their use for quantum bit commitment. *Phys. Rev. Lett.* **93**, 053601 (2004). [On page 107.]

[140] DiCarlo, L. *et al.* Preparation and measurement of three-qubit entanglement in a superconducting circuit. *Nature* **467**, 574–578 (2010). [On page 107.]

[141] Wiseman, H. M., Jones, S. J. & Doherty, A. C. Steering, entanglement, nonlocality, and the Einstein-Podolsky-Rosen paradox. *Phys. Rev. Lett.* **98**, 140402 (2007). [On page 111.]

[142] Jones, S. J. & Wiseman, H. M. Nonlocality of a single photon: Paths to an Einstein-Podolsky-Rosen-steering experiment. *Phys. Rev. A* **84**, 012110 (2011). [On pages 111 and 112.]

[143] Fuwa, M., Takeda, S., Zwierz, M., Wiseman, H. M. & Furusawa, A. Experimental proof of nonlocal wavefunction collapse for a single particle using homodyne measurement. *Nat. Commun.* **6**, 6665 (2015). [On pages 111 and 112.]

[144] Cavalcanti, E. G., Foster, C. J., Fuwa, M. & Wiseman, H. M. Analog of the Clauser-Horne-Shimony-Holt inequality for steering. *J. Opt. Soc. Am. B* **32**, A74–A81 (2015). [On page 113.]

[145] Girdhar, P. & Cavalcanti, E. G. All two-qubit states that are steerable via clauser-horne-shimony-holt-type correlations are Bell nonlocal. *Phys. Rev. A* **94**, 032317 (2016). [On page 113.]

[146] Guerreiro, T. *et al.* Demonstration of Einstein-Podolsky-Rosen steering using single-photon path entanglement and displacement-based detection. *Phys. Rev. Lett.* **117**, 070404 (2016). [On page 114.]

[147] Milman, P. *et al.* A proposal to test Bell's inequalities with mesoscopic non-local states in cavity qed. *Eur. Phys. J. D* **32**, 233–239 (2005). [On page 114.]

[148] García-Patrón, R. *et al.* Proposal for a loophole-free Bell test using homodyne detection. *Phys. Rev. Lett.* **93**, 130409 (2004). [On page 115.]

[149] Nha, H. & Carmichael, H. J. Proposed test of quantum nonlocality for continuous variables. *Phys. Rev. Lett.* **93**, 020401 (2004). [On page 115.]

[150] Kuzmich, A., Walmsley, I. A. & Mandel, L. Violation of Bell's inequality by a generalized Einstein-Podolsky-Rosen state using homodyne detection. *Phys. Rev. Lett.* **85**, 1349–1353 (2000). [Not cited.]

[151] Jeong, H. Testing Bell inequalities with photon-subtracted gaussian states. *Phys. Rev. A* **78**, 042101 (2008). [On page 115.]

[152] D'Angelo, M., Zavatta, A., Parigi, V. & Bellini, M. Tomographic test of Bell's inequality for a time-delocalized single photon. *Phys. Rev. A* **74**, 052114 (2006). [On page 115.]

[153] Etesse, J., Blandino, R., Kanseri, B. & Tualle-Brouri, R. Proposal for a loophole-free violation of Bell's inequalities with a set of single photons and homodyne measurements. *New J. Phys.* **16**, 053001 (2014). [On page 115.]

[154] Vlastakis, B. *et al.* Characterizing entanglement of an artificial atom and a cavity cat state with Bell's inequality. *Nat. Commun.* **6**, 8970 (2015). [On page 115.]

[155] Park, J., Lee, S.-Y., Lee, H.-W. & Nha, H. Enhanced Bell violation by a coherent superposition of photon subtraction and addition. *J. Opt. Soc. Am. B* **29**, 906–911 (2012). [On page 115.]

[156] Neergaard-Nielsen, J. S. *et al.* Optical continuous-variable qubit. *Phys. Rev. Lett.* **105**, 053602 (2010). [On page 116.]

[157] Babichev, S. A., Brezger, B. & Lvovsky, A. I. Remote preparation of a single-mode photonic qubit by measuring field quadrature noise. *Phys. Rev. Lett.* **92**, 047903 (2004). [On page 116.]

[158] Ulanov, A. E., Fedorov, I. A., Sychev, D., Grangier, P. & Lvovsky, A. I. Loss-tolerant quantum enhanced metrology and state engineering via the reverse Hong-Ou-Mandel effect. *Nat. Commun.* **7**, 11925 (2016). [On page 120.]

[159] Andersen, U. L. & Neergaard-Nielsen, J. S. Heralded generation of a micro-macro entangled state. *Phys. Rev. A* **88**, 022337 (2013). [On pages 132, 139, and 141.]

[160] Hoff, U. B., Kollath-Bönig, J., Neergaard-Nielsen, J. S. & Andersen, U. L. Measurement-induced macroscopic superposition states in cavity optomechanics. *arXiv* 1601.01663 (2016). [On page 132.]

[161] Laghaout, A., Neergaard-Nielsen, J. S. & Andersen, U. L. Assessments of macroscopicity for quantum optical states. *Opt. Commun.* **337**, 96 – 101 (2015). [On page 132.]

[162] Kwon, H., Park, C.-Y., Tan, K. C. & Jeong, H. Disturbance-based measure of macroscopic coherence. *arXiv* 1608.01122 (2016). [On page 132.]

[163] Lee, C.-W. & Jeong, H. Quantification of macroscopic quantum superpositions within phase space. *Phys. Rev. Lett.* **106**, 220401 (2011). [On page 132.]

[164] Bruno, N. *et al.* Displacement of entanglement back and forth between the micro and macro domains. *Nat. Phys.* **9**, 545–548 (2013). [On pages 132, 136, and 138.]

[165] Ghobadi, R. *et al.* Optomechanical micro-macro entanglement. *Phys. Rev. Lett.* **112**, 080503 (2014). [Not cited.]

[166] Lvovsky, A. I., Ghobadi, R., Chandra, A., Prasad, A. S. & Simon, C. Observation of micro-macro entanglement of light. *Nat. Phys.* **9**, 541–544 (2013). [Not cited.]

[167] Tiranov, A. *et al.* Demonstration of light-matter micro-macro quantum correlations. *Phys. Rev. Lett.* **116**, 190502 (2016). [On pages 132 and 138.]

[168] Tichy, M. C., Park, C.-Y., Kang, M., Jeong, H. & Mølmer, K. Macroscopic entanglement in many-particle quantum states. *Phys. Rev. A* **93**, 042314 (2016). [On pages 133 and 136.]

[169] Jeong, H., Kang, M. & Kwon, H. Characterizations and quantifications of macroscopic quantumness and its implementations using optical fields. *Opt. Commun.* **337**, 12 – 21 (2015). [On pages 136 and 150.]

[170] Sekatski, P., Sangouard, N. & Gisin, N. Size of quantum superpositions as measured with classical detectors. *Phys. Rev. A* **89**, 012116 (2014). [On page 136.]

[171] Sekatski, P., Gisin, N. & Sangouard, N. How difficult is it to prove the quantumness of macroscropic states? *Phys. Rev. Lett.* **113**, 090403 (2014). [On page 136.]

[172] Jeong, H. *et al.* Generation of hybrid entanglement of light. *Nat. Photon.* **8**, 564–569 (2014). [On page 143.]

[173] Yadin, B. & Vedral, V. A general framework for quantum macroscopicity in terms of coherence. *Phys. Rev. A* **93**, 022122 (2016). [On page 144.]

[174] Fröwis, F. & Dür, W. Measures of macroscopicity for quantum spin systems. *New J. Phys.* **14**, 093039 (2012). [On page 144.]

[175] Lim, Y., Joo, J., Spiller, T. P. & Jeong, H. Loss-resilient photonic entanglement swapping using optical hybrid states. *arXiv* 1608.04882 (2016). [On page 150.]

[176] Kwon, H. & Jeong, H. Generation of hybrid entanglement between a single-photon polarization qubit and a coherent state. *Phys. Rev. A* **91**, 012340 (2015). [On page 150.]

[177] Corzo, N. V. *et al.* Large Bragg reflection from one-dimensional chains of trapped atoms near a nanoscale waveguide. *Phys. Rev. Lett.* **117**, 133603 (2016). [On page 150.]

Résumé :

La dualité onde-particule a conduit à deux façons d'encoder l'information quantique. Dans la première approche dite "continue", l'information est encodée sur les quadratures du champ lumineux tandis que la seconde dite "discrète" repose par exemple sur des photons uniques. L'approche hybride a récemment émergé, et consiste à utiliser les concepts et boites à outils de ces deux approches, afin de contourner les limitations individuelles.

Dans ce travail de thèse, nous avons, dans une première partie, utilisé des protocoles hybrides pour générer des états quantiques non-gaussiens de la lumière. A l'aide d'oscillateurs paramétriques optiques, et de détecteur de photons supraconducteurs de haute efficacité, nous avons généré des photons uniques extrêmement purs très efficacement, ainsi que des états chats de Schrödinger de large amplitude, qui permettent d'encoder l'information en variables continues. Nous avons également étudié comment des opérations continues telles que la compression de bruit peuvent aider à cette génération. La méthode utilisée, basée sur la génération "d'états-noyaux" rend en outre ces états plus robustes à la décohérence.

Dans une seconde partie, dans le contexte d'un réseau quantique hétérogène basé sur différents encodages, connecter les deux approches nécessite une intrication hybride de la lumière. Nous avons introduit une telle ressource entre des états continus et discrets, et nous avons montré une première application : la génération à distance de bits quantiques continus. Le système expérimental développé au cours de cette thèse est également une plateforme polyvalente permettant la génération d'états « micro-macro » intriqués.

Mots clés : Optique quantique, approche hybride en information quantique, chat de Schrödinger, photon unique, intrication, intrication micro-macro, macroscopicité

Abstract:

In quantum information science and technology, two traditionally-separated ways of encoding information coexist -the continuous and the discrete approaches, resulting from the wave-particle duality of light. The first one is based on quadrature components, while the second one involves single photons. The recent optical hybrid approach aims at using both discrete and continuous concepts and toolboxes to overcome the intrinsic limitations of each field.

In this PhD work, first, we use hybrid protocols in order to realize the quantum state engineering of various non-Gaussian states of light. Based on optical parametric oscillators and highly-efficient superconducting-nanowire single-photon detectors, we demonstrate the realization of a high-brightness single-photon source and the quantum state engineering of large optical Schrödinger cat states, which can be used as a continuous-variable qubit. We show how continuous-variable operations such as squeezing can help in this generation. This method based on so-called core states also enables to generate cat states that are more robust to decoherence.

Second, in the context of heterogeneous networks based on both encodings, bridging the two worlds by a quantum link requires hybrid entanglement of light. We introduce optical hybrid entanglement between qubits and qutrits of continuous and discrete types, and demonstrate as a first application the remote state preparation of continuous-variable qubits. Our experiment is also a versatile platform to study squeezing-induced micro-macro entanglement.

Keywords : Quantum optics, hybrid quantum information, Schrödinger cat states, single photon, entanglement, micro-macro entanglement, macroscopicity